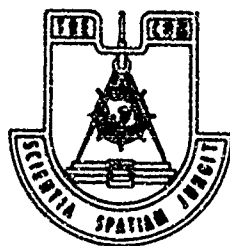


UNCLASSIFIED

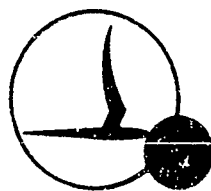
AD NUMBER
AD819970
NEW LIMITATION CHANGE
TO Approved for public release, distribution unlimited
FROM Distribution authorized to U.S. Gov't. agencies and their contractors; Administrative/Operational Use; 28 JUN 1963. Other requests shall be referred to Army Air Mobility Reseacrch and Development Lab., Fort Eustis, VA.
AUTHORITY
USAAMRDL ltr, 4 May 1971

THIS PAGE IS UNCLASSIFIED

AD819970



CAL/TRECOM SYMPOSIUM



PROCEEDINGS Vol I

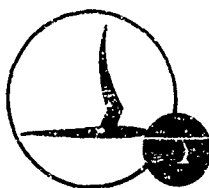
Dynamic
Load Problems
Associated
with
Helicopters
and V/STOL
Aircraft

*

JUNE 26-28
STATLER HILTON BUFFALO N.Y.



CAL/TRECOM SYMPOSIUM



PROCEEDINGS Vol I

**Dynamic
Load Problems
Associated
with
Helicopters
and V/STOL
Aircraft**

*

JUNE 26-28

STATLER HILTON BUFFALO N.Y.

STATEMENT #2 UNCLASSIFIED
This document is subject to special export controls and each
transmission to foreign government or organization may be
made only with prior approval of *SP-1*
St. Austin, Va.



Statements and opinions contained herein are those of the authors and are not to be construed as reflecting the views of the Department of the Army or the cosponsors of this Symposium--The U. S. Army Transportation Research Command or Cornell Aeronautical Laboratory, Inc.

FOREWORD

Rapid advances made in helicopter and V/STOL aircraft development during the past few years have created many new and unique design requirements. In the field of dynamic loads, in particular, an increasing number of problems have required fundamental research in mechanics, aeromechanics, and physics to acquire the understanding necessary for the development of satisfactory methods of solution. Specific research has resulted in significant advances in the "state of the art" of prediction techniques for dynamic loads on helicopter and V/STOL aircraft. The objectives of this Symposium are to aid the dissemination of the latest research results and to provide a timely opportunity for open discussion among specialists in the field of current and future "dynamic load problems associated with helicopters and V/STOL aircraft".

In keeping with these objectives, the first two days of the Symposium are devoted to the presentation and discussion of specific technical papers on various aspects of dynamic load problems which run the entire gamut from basic research to design methods. In addition, a third day is provided for a review of the current and future dynamic load problems by panels composed of outstanding representatives from the helicopter and V/STOL aircraft industries.

The proceedings of this Symposium have been bound in three volumes — one volume for each day of the general meetings, and one for the panel meetings. We are indebted to the authors for preparing their final manuscripts in a form that could be directly reproduced. This material was published herein as provided by the authors and was neither checked nor edited by CAL or TRECOM.

The sponsors of the Symposium are grateful to the many people who contributed to its success. In particular, our thanks go to Colonel N. A. Gage, Jr., Commanding Officer, U. S. Army Transportation Research Command, and Mr. H. A. Cheilek, Vice President - Technical Director, Cornell Aeronautical Laboratory, Inc., who opened the sessions; to Major General W. J. Ely, Deputy Commanding General, U. S. Army Materiel Command, for his address at the Symposium dinner; to the four session chairmen —

Mr. B. Kelley, Bell Helicopter Company

Mr. W. Gerstenberger, Sikorsky Aircraft Division of the
United Aircraft Corporation

Mr. R. Boswinkle, National Aeronautics and Space Administration,
Langley Field

Dr. A. Hohenemser, McDonnell Aircraft Corporation

and to the two panel chairmen —

Mr. J. G. McHugh, Chief, Aeromechanics Group, U. S. Army
Transportation Research Command

Mr. T. R. Baldwin, Development Division, Army Materiel Command

and most especially, of course, to the authors and panel members without
whom there could not have been a symposium on dynamic loads.

SYMPOSIUM CHAIRMEN

Richard P. White, Jr. (CAL)

John E. Yeates (TRECOM)

TABLE OF CONTENTS

Volume I

1. Dynamic Loads in a Rigid Rotor from Full-Scale Wind-Tunnel Tests
J. F. Johnston, J. E. Rhodes, and R. H. Cotton, Lockheed California
2. An Aeroelastic Study of Helicopter Rotor Systems in High-Speed Flight
E. R. Wood, K. D. Hilzinger, and A. C. Buffalano, Sikorsky
3. In-Flight Measurement of Steady and Oscillatory Rotor Shaft Loads
R. Gabel, Vertol Division, Boeing Aircraft
4. Full-Scale Flight Test Data Relating to Rotor Unsteady Aerodynamics
Mr. Charles W. Ellis, Kaman Aircraft
5. Experimental and Theoretical Study of Local Induced Velocities Over a Rotor Disc
S. Tararine, Giravions Dorand, Paris, France
6. Rotor Airloads
R. Piziali, H. Daughaday, F. DuWaldt, Cornell Aeronautical Laboratory, Inc.
7. Comparison of Flight Measured Helicopter Rotor Blade Chordwise Pressure Distributions and Two-Dimensional Airfoil Characteristics
James Scheiman and Henry Kelley, NASA, Langley Field, Hampton, Virginia
8. A Discussion of Rotor Blade Harmonic Airloading
R. H. Miller, MIT
9. An Experimental Investigation of the Effect of a Non-Rigid Wake on Rotor Blade Airloads in Transition Flight
Norman Ham, MIT

**DYNAMIC LOADS IN A RIGID ROTOR
FROM FULL-SCALE WIND-TUNNEL TESTS**

J.F. Johnston, J.E. Rhodes, and R.H. Cotton

Lockheed, California

DYNAMIC LOADS IN A RIGID ROTOR FROM FULL SCALE WIND TUNNEL TESTS

J. F. Johnston, Manager, Flight Dynamics Department
J. E. Rhodes, Group Engineer, Helicopter Dynamic Loads
R. H. Cotton, Research Specialist, Flight Analyses

INTRODUCTION

In setting up the high speed rigid rotor research program on the XH-51A, it was soon recognized that a wind-tunnel test program prior to flight would expedite and increase the safety of the flight test program. With the aid of BuWeps, TRECOM, and NASA personnel, it was decided that a full-scale test using as much as possible of the flight hardware would be most advantageous. In addition to verifying and/or improving the loads, control, and performance prediction methods for the rigid rotor, such a test would also provide a good checkout of the flight components. Accordingly, these tests were conducted in the NASA Ames 40 x 80 foot wind-tunnel in two phases during February and August, 1962. This paper discusses the dynamic stability and dynamic loads aspects of those tests.

Additional material relative to the XH-51A rigid rotor research helicopter is available in References 1, 2, and 3. Reference 1 covers some of the basic design considerations, particularly in the dynamics area, Reference 2 the loads prediction methods, and Reference 3 is an overall progress report on the research program up to May 1963.

BACKGROUND

During the CL-475 program a whirl tower test method for the rotor system had been evolved which contained fuselage pitch and roll representation, Figure 1. In essence the rotor was mounted on an inertia frame which represented the fuselage. This simulated fuselage contained all the rotor controls and a pilot's seat from which the rig could be controlled in a manner similar to that on the actual flying machine. Power to the rotor was fed from an external source. The inertia frame was gimbaled to a fixed frame rigidly attached to the deck. The pilot on the whirl tower was thus able to apply given lifts, pitch and roll about the gimbal. While this proved an excellent tool for checking rotor stability and control characteristics in hover the essential element of forward velocity was missing.

The rotor blade was fully instrumented and it was proposed to go up in speed on the vehicle in small increments carefully monitoring loads and stability trends at each step.

The problem presented in this approach was the fact that one of the more critical areas, transition, was approached almost instantaneously in the 15 mph to 35 mph range (Figure 2 shows the typical cyclic load plot vs. speed). To provide coverage in this range an Electra turboprop aircraft was run in front of the whirl tower. This gave up to a 40 mph slipstream which although somewhat turbulent provided the necessary assurance. The pilot was able to fly the rig in this turbulence without difficulty. It was from these early experiments that the potential of ground testing in the wind tunnel became apparent.

NASA AMES 40 X 80 WIND

TUNNEL TEST PROGRAM

CL-475 experience had indicated one very important factor. In-plane and higher-frequency loading levels and stability characteristics depended on the rotor-body interrelationship. The more dynamic analysis would progress the greater the realization that the rotor was not an entity on its own. The dynamic system was interdependent (Reference 1). With the help and guidance of NASA, TRECOM and BUWEPS personnel an ambitious program for testing the XH-51A rotor-body system was evolved. The ground rules were as follows:

- (a) The rotor-body dynamic relationship should be simulated to the degree to make load level measurements meaningful.
- (b) The control system including the prime stability items should be represented.
- (c) The complete system would be flown with only translation movement restricted. The control system was to be similar to that of the vehicle.
- (d) Provisions should be made for varying prime control characteristics.
- (e) Complete load measuring instrumentation would be provided.
- (f) The rig would be designed to allow its complete functional check out before installation at AMES.

The success of the program was dependent on three prime items.

- (1) Aerodynamic simulation
- (2) Dynamic simulation
- (3) Ability of the control personnel to be able to fly the rig from a remote station.

The only question with respect to aerodynamic simulation was the effect of the tunnel walls and possible free stream turbulence. This problem can best be understood by comparison of the item to be tested to the tunnel size. Figure 3 shows the rig mounted in the tunnel. In retrospect, aerodynamic simulation proved to be excellent except at very low speeds and hover. In hover the rotor tunnel wall effects created considerable turbulence. This problem was overcome by tilting the rotor in a 10-degree nose down attitude to provide down stream flow.

Dynamic simulation, at first very ambitious, had to be modified for practical reasons and for some of special stability problems associated with the test rig. These will be discussed later.

DESCRIPTION OF TEST RIG

Figure 4 shows the final test rig. This rig could be mounted either on a support structure for whirl tower testing or on the AMES tripod electric driven shaft system. The pitch, roll and collective control systems were operated by electric actuators; the control of these actuators was outside the tunnel in a control station. The mount system freedom was of prime importance for dynamic simulation. Figure 5 shows the initial objectives and those finally used.

A fuselage having the external shape of the XH-51A was mounted on the inertia frame, the object being to obtain as much information on aero characteristics as possible from the tunnel tests.

INSTRUMENTATION

The blade was instrumented to obtain the blade flap moments at seven spanwise stations and the chord or in-plane moments at five stations. At any one time the complete spanwise bendings on one blade were obtained along with the root bending moments on the other two blades. All blades were strain gauged so they could be hooked up at any time. Figure 6 shows the locations of the loads measurements on the hub and blades.

TEST PROGRAM

The test program was planned to cover the areas shown in Figure 7.

DYNAMIC STABILITY CONSIDERATIONS

Early consideration of whirl-tower and wind-tunnel testing indicated two distinct areas in which the stability of the gyro-controlled rigid rotor would be compromised by the conditions of test. These problems were confirmed during the testing and a third was found. Fortunately, solutions were available for each problem that would not compromise obtaining valid rotor dynamic loads data.

Whirl-Tower Mode - The first problem area was dubbed the "whirl-tower mode". It arose from the use of a remote power source to drive the rotor. A universal joint coincident with the body gimbal center was provided in the rotor drive shaft to permit the body to pitch and roll.

If the body and rotor are moved in roll (for example) the resulting moment system due to the drive torque is shown in Figure 8.

The displaced rotor shaft absorbs the lower shaft drive torque partly as torque in the displaced plane of rotation and partly as a moment bending the upper shaft forward - a pitching moment if the rotor and shaft are displaced in roll, or a rolling moment if the rotor is pitched. Since the rotor is flexible, the upper shaft will tend to pitch in the direction of the unbalanced moment. This will slowly precess the gyro in pitch, due to friction and other moments which are always at work tending to erect the control gyro normal to the rotor shaft. Thus the gyro and rotor will have an angular velocity in phase with the applied moment. If the body is free in both pitch and roll about the gimbals, the system is spirally unstable in an advancing mode, the rate of spiral divergence being proportional to the rotor torque and the characteristic erection time of the gyro.

Inasmuch as this "whirl-tower mode" did not show up in the whirl-tower tests of the rotor system for the lower-powered CL-475, it was hoped that the higher-powered XH-51A system would also be relatively free of it. However, the spiral instability occurred during early high-lift, high-power tests. Recovery was made by caging the body. Further difficulty was avoided by stiffening the body mounting in roll, leaving it free to pitch. The roll control inputs were thereafter based on roll moments rather than roll attitude indication.

It should be reiterated that the "whirl-tower mode" is associated with a remote drive, and cannot occur in free flight.

Wind-Tunnel Pitch-Up - The second area in which the difference of test conditions from free flight introduced stability problems was the pitch stability in the wind tunnel at forward speed.

In the wind tunnel, pitch attitude is synonymous with angle of attack, whereas in free flight the freedom in plunge makes it necessary to maintain a pitch rate in order to maintain an angle of attack other than that for steady flight.

Pitch stability in the Lockheed rigid rotor system is obtained from the fact that the control gyro tends to remain fixed in space, so that a change in rotor attitude produces a corrective feathering input. The gyro will however, precess slowly to erect normal to the shaft, slowly removing the corrective input. In free flight this erection rate is small compared to the rate of pitch required to maintain an out-of-trim angle of attack, with the result that the vehicle is stable with respect to angle of attack. In the wind tunnel, however, this erection rate produces a slow divergence. It was assumed that the operator controlling rotor attitude could handle this slow divergence satisfactorily. The control rates available were slow enough, however, to cause the operator considerable trouble. During a 75-knot run it became necessary to cage the system due to a pitch-up. The remainder of the tests at and above 75 knots were run with the system caged, although it later became necessary to reduce the caging stiffness in pitch in order to provide the solution to the third potential dynamic instability associated with the wind tunnel test conditions.

Regressive Whirl Mode - The characteristic wobble of a gyroscope will be in an advancing or regressing mode depending on whether the forces acting on it are destabilizing or stabilizing, respectively. A toy gyroscope spinning atop a table (force of gravity destabilizing) will wobble in the same direction as its rotation, whereas the same gyroscope suspended below a string (force of gravity stabilizing) will wobble in a direction opposite its rotation after a disturbance.

In changing by stages from a system free in both roll and pitch to a system restrained about both axes, the characteristic dynamic motion of the rotor had

changed from an advancing mode characteristic of free flight to a regressive mode. The effect of this change began to appear in testing at 100 knots at a 10-degree nose down attitude, when a beat frequency began to appear in the traces of the blade chord bending. A typical trace is shown in Figure 9. Inasmuch as the beat frequency was very close to the regressive chord bending frequency as seen in the non-rotating system, it was concluded that the trace indicated an incipient dynamic instability. The boundaries for these occurrences, in terms of rotor attitude versus speed, are shown in the lower part of Figure 9.

Fortunately, dynamic analyses of the wind tunnel test conditions were in process at the same time. These analyses showed the possibility of such an instability. More importantly, they showed how to cure the instability. The results are given in Figure 10, showing the system stability as a function of the body pitching frequency against the wind tunnel balance tripod. The system is stable for all body pitch frequencies below 1.6 cps, and unstable for all higher frequencies. The cut-off frequency of 1.6 cps is the regressive chord bending frequency as seen by the body. At support frequencies below 1.6 cps, the body would pitch out of phase with the chord bending, and the regressive whirl mode pattern would be broken up. The support stiffness was then modified by placing rubber blocks on the balance tripod platform against which the body was pulled by the caging cylinders, and adjusting the spacing of the rubber blocks until the body pitch frequency was reduced to 1.5 cps. This minimum margin of 0.1 cps was selected in order to maintain the maximum possible pitch stiffness (approximately 150,000 ft. lb. per radian), and because the physical relationships indicated by the dynamic analysis made good sense. From this point testing proceeded up to the maximum speed with no further dynamic problems.

Adequacy of Simulation - From these experiences it can be concluded that the low-frequency dynamics of the rigid-rotor helicopter cannot be simulated with a restrained model in the wind tunnel. The simulation improves for frequencies above the body restraint frequencies, inasmuch as the phase of the body response becomes similar to free flight. The relative amplitudes of body-rotor interactions are normally satisfactorily simulated at frequencies above twice the body restraint frequency.

With respect to the rotor dynamic loads for steady flight conditions - level flight at any simulated gross weight, drag, or longitudinal or lateral c. g. displacement - the simulation is very good. The IP vertical bending accurately reflects the blade loads due to steady body moments. The IP in-plane bending

requires no body reaction and is thus independent of the conditions of restraint. The 2P and 4P vertical and in-plane blade loads in a 3-blade rotor are reflected as 3P to the body, which is well above the body restraint frequency. Normally these blade loads will be well simulated if the body-rotor springing is simulated, although the body responses are more open to question.

The 3P blade loads are collective in a 3-blade rotor. The vertical bending is most important, inasmuch as the aerodynamic input is appreciable and the blade second bending frequency is near 3P. Analyses indicated that as long as the body appeared massive to the rotor, the degree of massiveness had little effect on the blade 3P responses in the range investigated, which was from one-quarter to full effective body mass. Vertical springiness between the rotor shaft and the body may, however, have a strong effect on the blade loads. Proper simulation is important if this connection is relatively flexible.

The 3P in-plane responses were not properly simulated because of the high inertia of the drive mechanism, but these have proved negligible both in flight and in the wind tunnel.

ROTOR DYNAMIC LOADS

The methods used in loads prediction work was based on Reference 2. The level flight loads are dependent on:

1. Body moment due to center of gravity offset and aerodynamic pitching moment.
2. Vehicle attitude and speed which dictate collective and cyclic blade angles.

In the Ames tunnel the attitude of the vehicle was set by tilting the tripod mount. The attitude was based on an assumed drag for the vehicle. A check on this drag from tunnel balance measurement was difficult due to the large tare drag of the tripod. In order to provide a complete coverage the vehicle attitude was varied at each speed point up to 120 knots.

In comparing predicted, in-flight, and Ames data it should be realized that obtaining a vehicle condition which is identical for all three in terms of body moment, lift, speed, drag, etc. is not always possible. The load levels therefore,

can only be thought of as general trends as a function of speed. At Ames, for example, the operators had to trim out both pitch and roll moments using an indicator linked to the load cells. At the instant of taking the record, there was often quite a high level of body moment left untrimmed.

In spite of these variables the plot of cyclic in-plane moments at the hub versus speed, Figure 11, shows good agreement with predicted values. These values are predominantly one per revolution and first mode.

Good agreement with the one per revolution first mode flapping and steady flapping was obtained when full consideration was taken of the body moment and lift for the particular condition. Figure 12 shows the 1P flapping moment distribution comparison between measured and predicted values.

Loads prediction for the 2P, 3P, and higher harmonics was less sophisticated at the time the wind tunnel tests were made, inasmuch as the levels extrapolated from CL-475 experience indicated that they were of less importance to rotor fatigue than the effects of c.g. offset and fuselage aerodynamic moments. The early analyses did not include considerations of vortex shedding at low speed or of the energy admittance of the harmonic airloads into the higher modes of blade bending.

Figure 13 shows comparisons of the hub 2P and 3P flapping moments vs. speed. The 2P moments measured in the tunnel were generally higher than predicted. These moments were effectively removed in the flight article by providing a shaft mounting frequency below 3P. This resulted in a 17% reduction of the pitch stiffness of the body relative to the rotor plane. This elimination of the 2P blade loading is an example of the importance of the body-rotor dynamic interactions, Reference 1.

The 3P hub flapping moments were found to be of consequence throughout the flight regime. The flight results are in general agreement with the wind-tunnel up to 100 knots, and indicate a higher rate of increase above that speed.

Body-rotor dynamic interaction is prime importance in the 2P and 3P dynamic response. The XH-51A Rotor has a second mode flapping frequency very near 3P as shown in Figure 14. The exact phasing and combined frequency is dependent on the mass springing below the rotor. Figure 15 which is extracted from Reference 1 shows this relationship.

A reasonable tolerance on the higher frequency loadings is acceptable, as they contribute less than 50% of the total cyclic moments causing fatigue damage. Figure 16 shows the total cyclic flapping moment at the hub versus speed measured at Ames, and the contribution of the 3P component.

FULL SCALE VS. MODEL TESTING

The prime advantage of full-scale wind-tunnel rotor testing as compared with testing at model scale is that actual flight hardware is tested, minimizing the difficulties in interpretation from wind tunnel to flight results.

Aside from the obvious advantages of testing at true Reynolds and Mach numbers, the full scale hardware has the further advantage of including the true effects of the non-linearities due to friction and dynamics of the various mechanisms. Mechanical malfunction is often the trigger for catastrophic failure. A good overall dynamic design can be ruined by poor mechanical detail. Full scale testing is the only way to cover this important area. The Ames test uncovered two important problems in this category.

The first was the failure of a blade due to the separation of a poorly bonded leading edge balance as described in Reference 3. This failure led to complete redesign of the blade to provide redundancy and inspectability in the blade-hub system. The discovery of this weakness alone justified the full scale wind tunnel program.

A second less catastrophic discovery involved the feathering bearings. In surveying the records, the feathering angle trace showed a flat top to the sine curve. Examination of the bearings showed that they tended to seize due to locking of the needles in the roller bearings. The design was immediately improved to correct the situation.

The bearing sticking would have shown up in the flight vehicle as poor and erratic dynamic characteristics. The true cause might have been difficult to trace in flight tests because of the reduced instrumentation possible in the flight vehicle.

The prime disadvantage of full-scale rotor testing lies in the large rotational energy in the rotor, making the tests always somewhat hazardous. For this reason, no testing in known hazardous areas, such as fully developed retreating blade stall, was planned. The exploration of hazardous areas is better done at model scale where the danger to test personnel can be orders of magnitude less, and the cost of the many replacement parts likely to be required is correspondingly less.

CONCLUDING REMARKS

In reviewing this experience of testing the XH-51A rigid rotor up to 160 knots in the NASA Ames 40 x 80 foot wind tunnel, it was concluded that the prime objectives had been achieved. The hardware had been wrung out and important mechanical deficiencies had been found and corrected. Proof and further understanding of the fundamental dynamic behavior of the system, within the limits imposed by the necessary wind tunnel restraints, had been obtained. The blade dynamic loads associated with steady flight had been determined.

Should all new rotor systems be tested in this manner? There is probably no general answer to this question. Full-scale wind tunnel testing is not a substitute for the necessary development flight testing; it is rather a means of increasing the safety of the flight work and of getting an early lead on some of the problems likely to be encountered in flight. It is more valuable and more costly than model testing and thus will command more attention and higher-grade personnel. Inasmuch as flight hardware is involved, details that might be passed off as "bugs in the model" cannot be ignored in full-scale testing.

In short, each situation must be judged on its merits. In this particular case, full-scale testing had paid off handsomely.

ACKNOWLEDGEMENTS

The work reported herein was done under a combined Army-Navy contract for research on a high-performance rigid rotor system, the XH-51A. The NASA cooperated fully in the wind tunnel tests.

Full credit is due the personnel of the NASA Ames 40 x 80 foot wind tunnel, who provided advice and consultation before and during the test program, and who conducted the tests with the aid of Lockheed personnel.

REFERENCES

1. Culver, L. H., Designing The High Speed Rigid Rotor Helicopter. Astronautics and Aerospace Engineering, June 1963.
2. Rhodes, J. E., and Gaidelis, J. A., Loads Prediction For Structural Rigid Rotor Systems. 19th Annual American Helicopter Society Meeting, May 1963.
3. Statler, W. H., Heppe, R. R., and Cruz, E. S., Results Of The XH-51A Rigid Rotor Research Helicopter Program. 19th Annual American Helicopter Society Meeting, May 1963.



FIGURE 1 CL-475 WHIRL TEST RIG

FIGURE 2
TYPICAL CYCLIC LOAD
VARIATION WITH SPEED

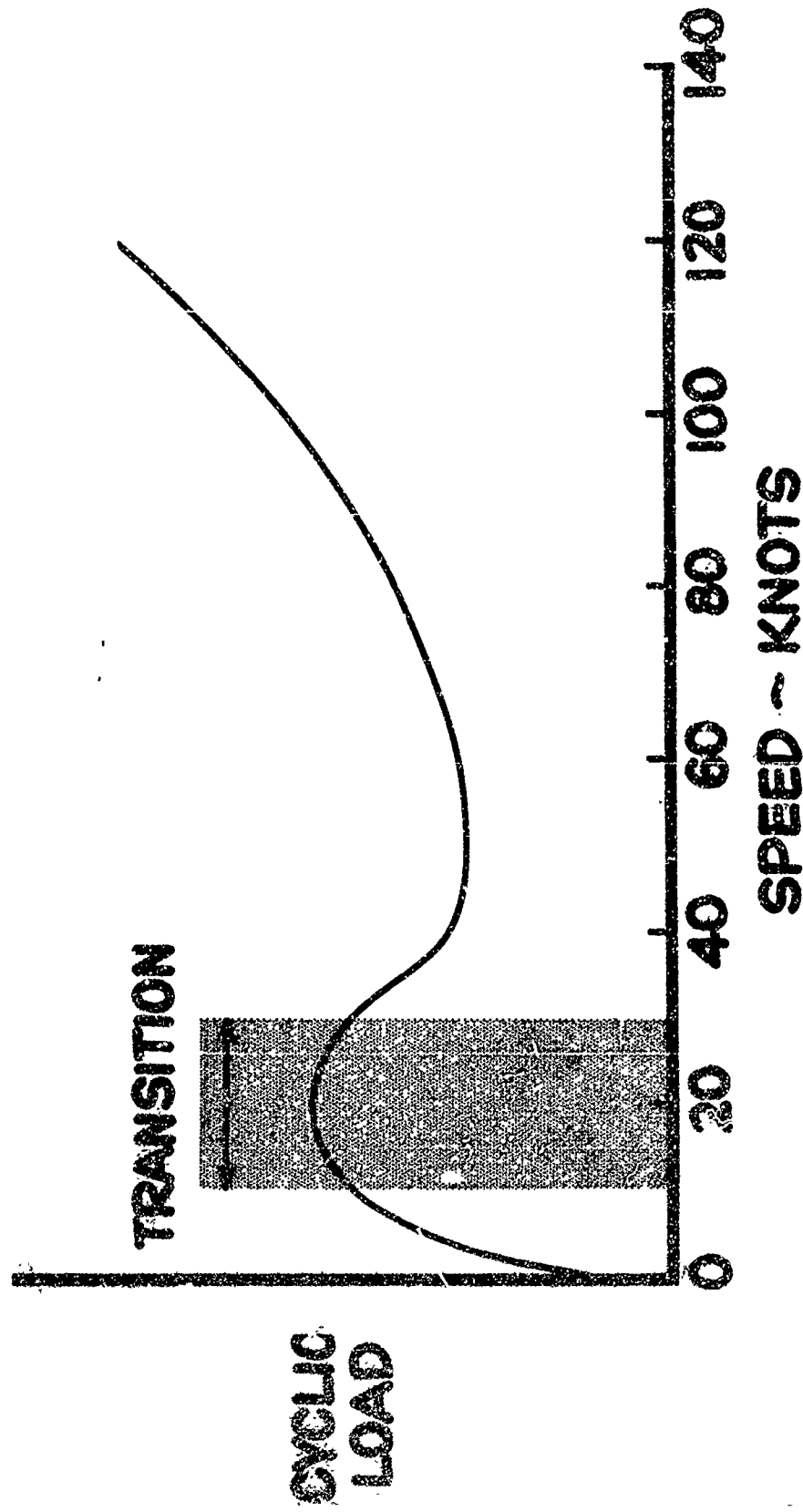
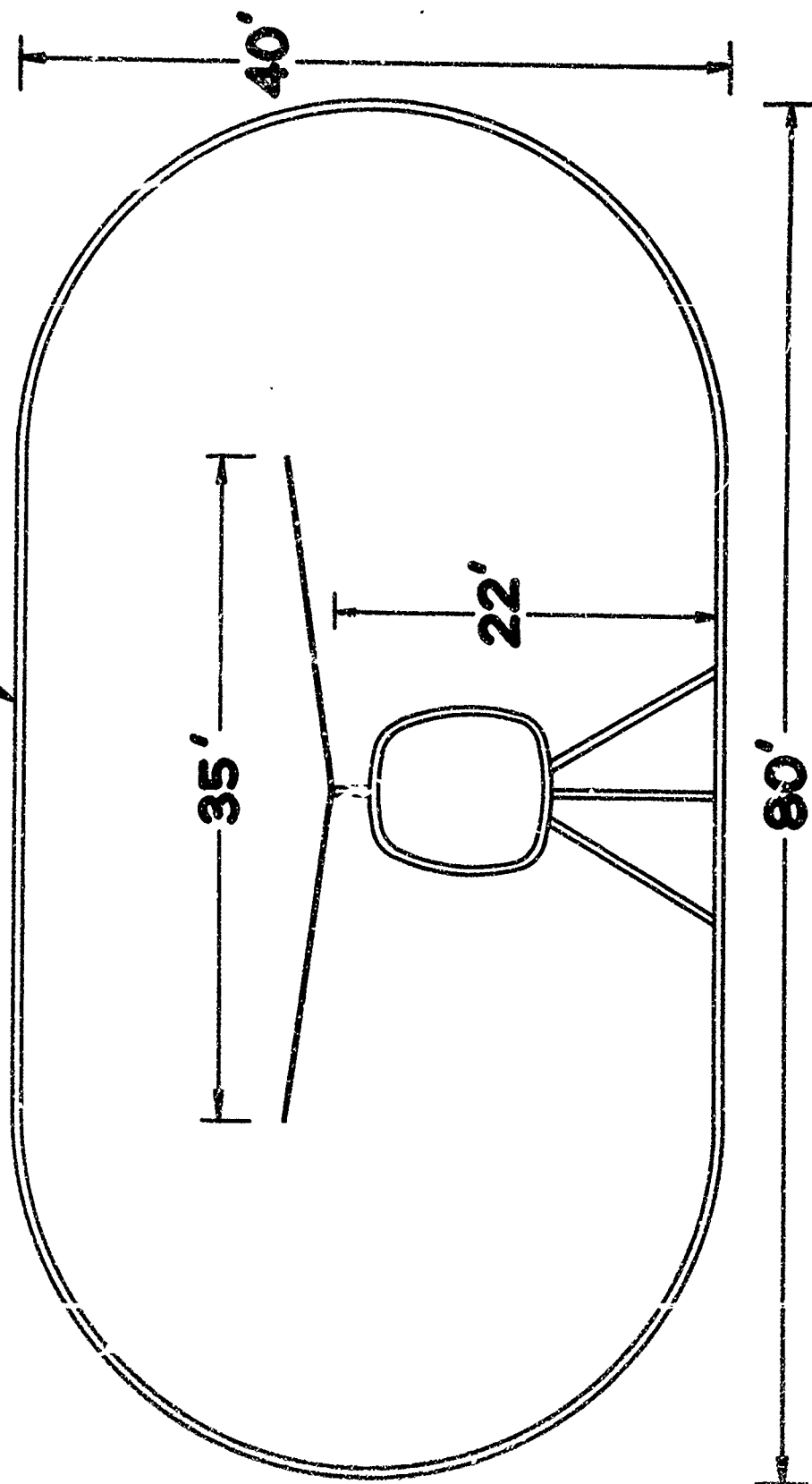


FIGURE 3

TUNNEL SECTION

TUNNEL WALL



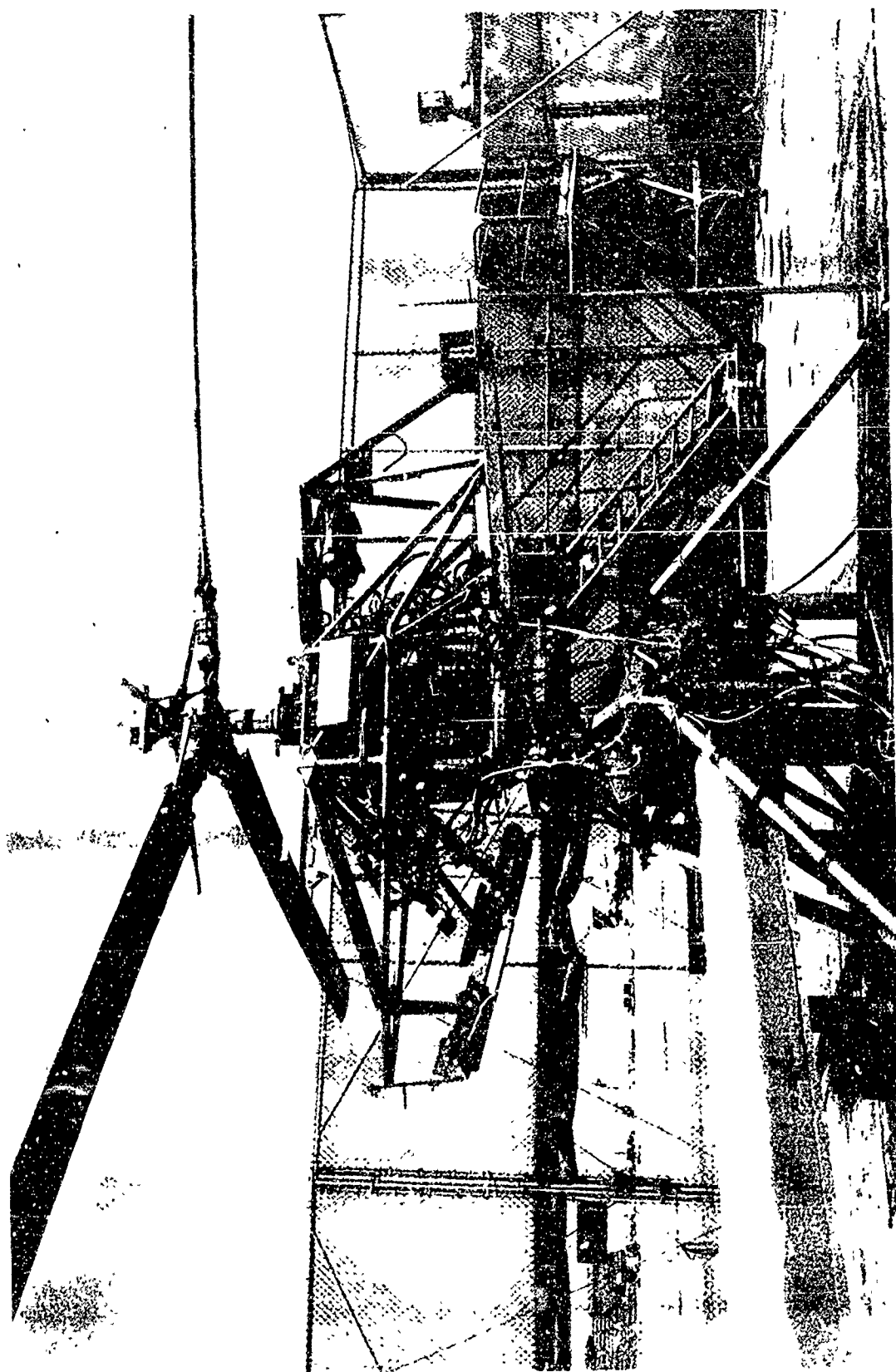


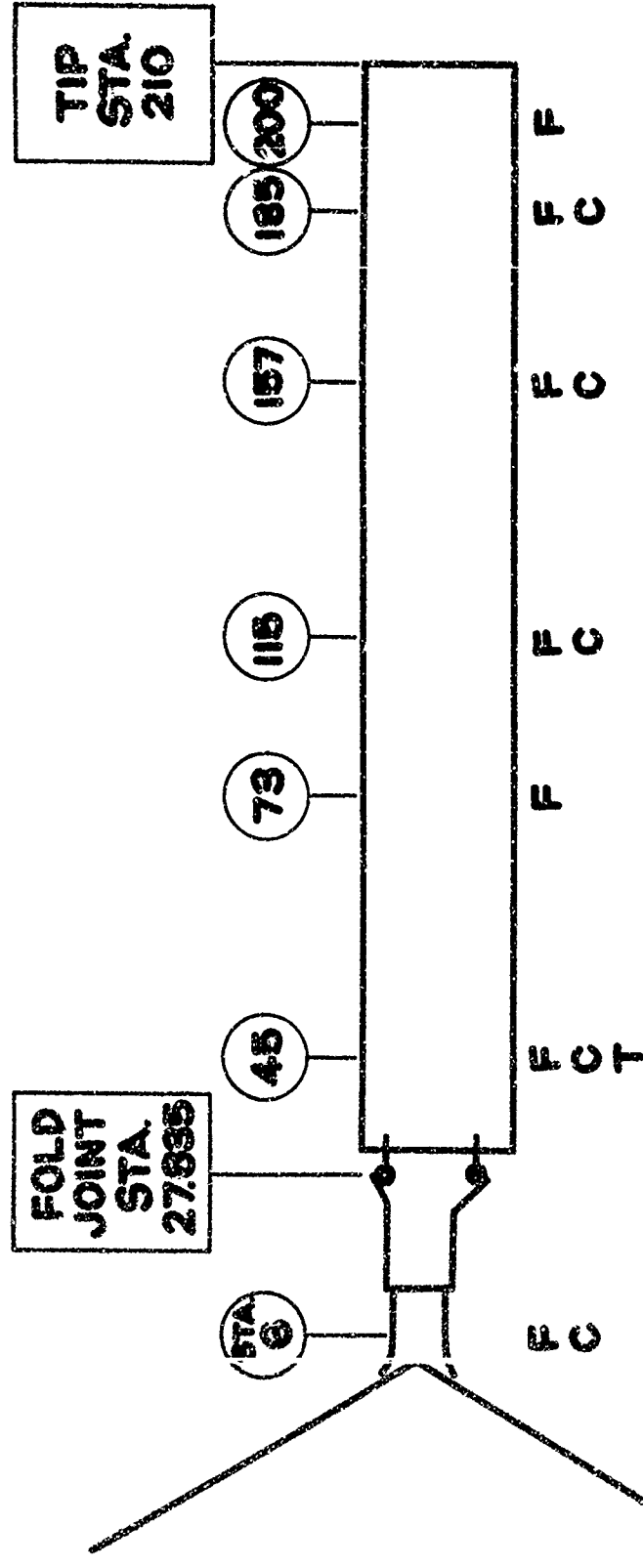
FIGURE 4 XH-51A WHIRL TEST RIG

FIGURE 5

BODY RESTRAINTS IN WIND TUNNEL

	OBJECTIVE	FINAL
PITCH	0	150,000 FT LBS/RAD ~ .25 PER REV.
ROLL	0	600,000 FT LBS/RAD ~1.35 PER REV.
YAW	150,000	150,000
FORIE & AFT	30,000 LB/FT ~ .45 PER REV.	100,000 LB/FT ~ .8 PER REV.
LATERAL	30,000 ~ .45 PER REV.	STIFF
VERTICAL	30,000 ~ .45 PER REV.	700,000 LB/FT ~ .2 PER REV.

FIGURE 6 STRAIN GAGE MEASUREMENTS ON ROTOR



NOTE: F = FLAPWISE BENDING
 C = CHORDWISE BENDING
 T = TORSION

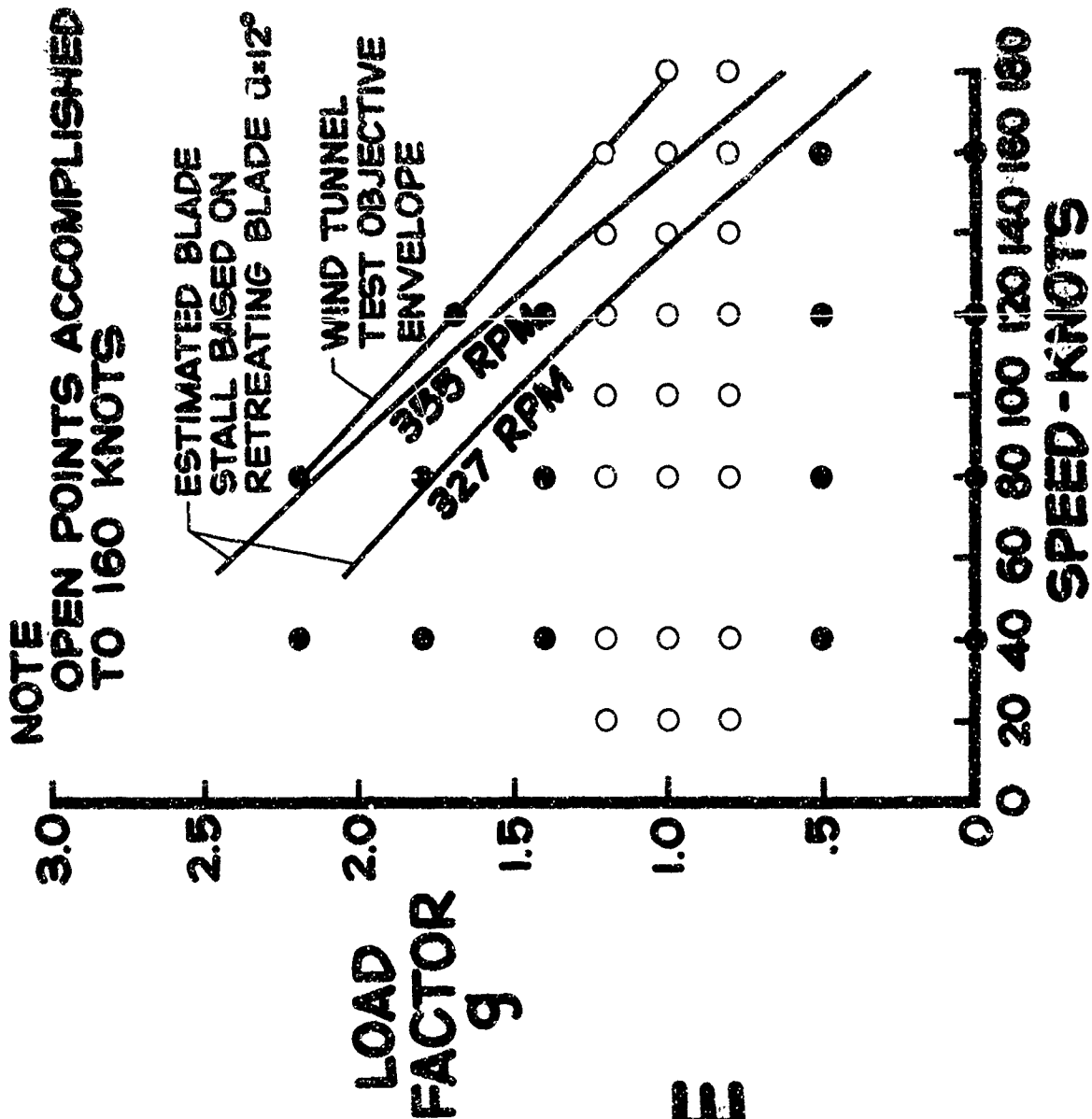


FIGURE 7
V-G
SCHEDULE
3500 LBS. G.W.

FIGURE 8
MOMENTS INVOLVED IN
WHIRL TOWER MODE

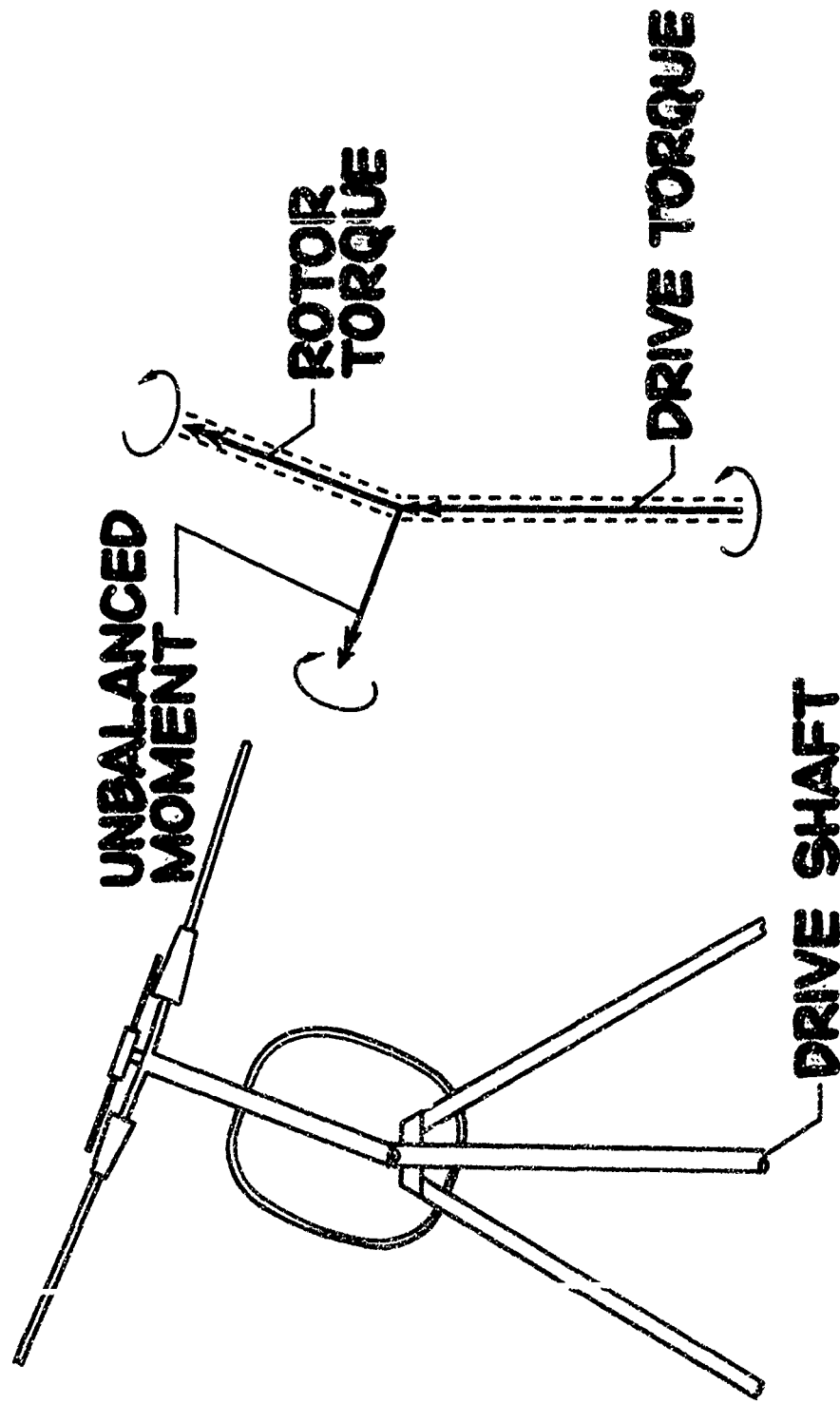


FIGURE 9 **REGRESSIVE WHIRL MODE** **DUE TO BODY RESTRAINT**

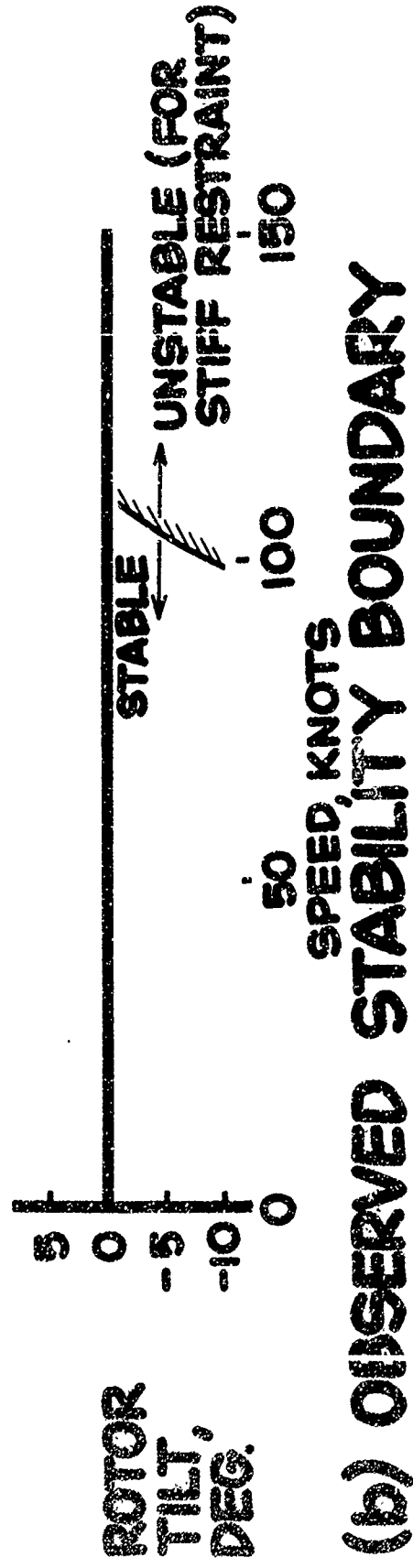
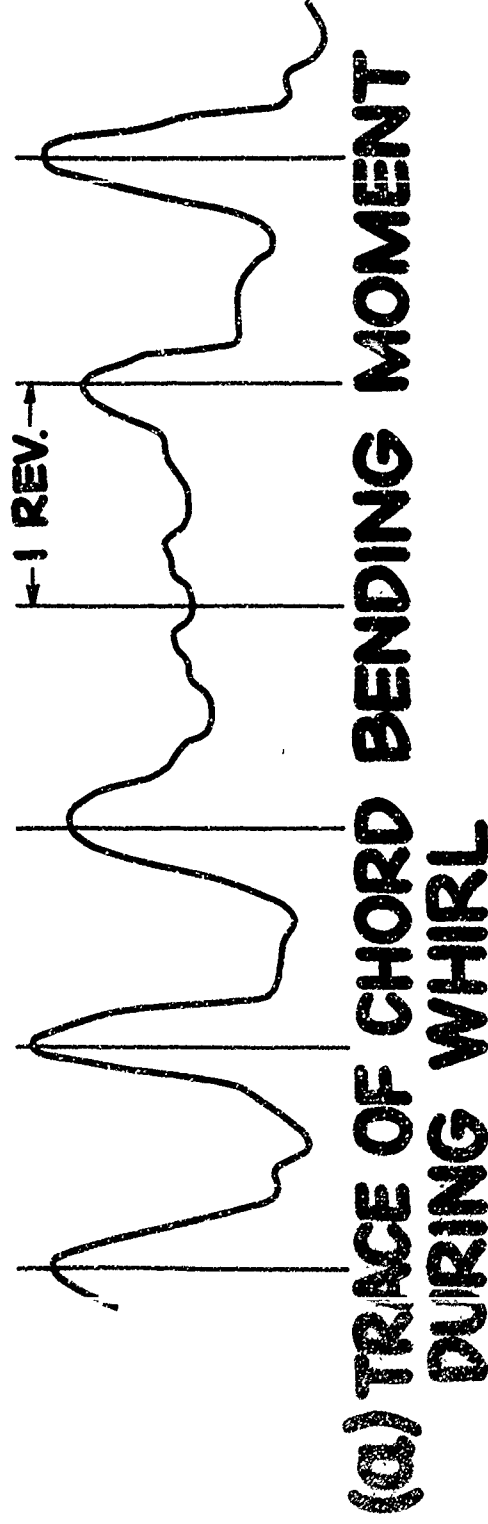
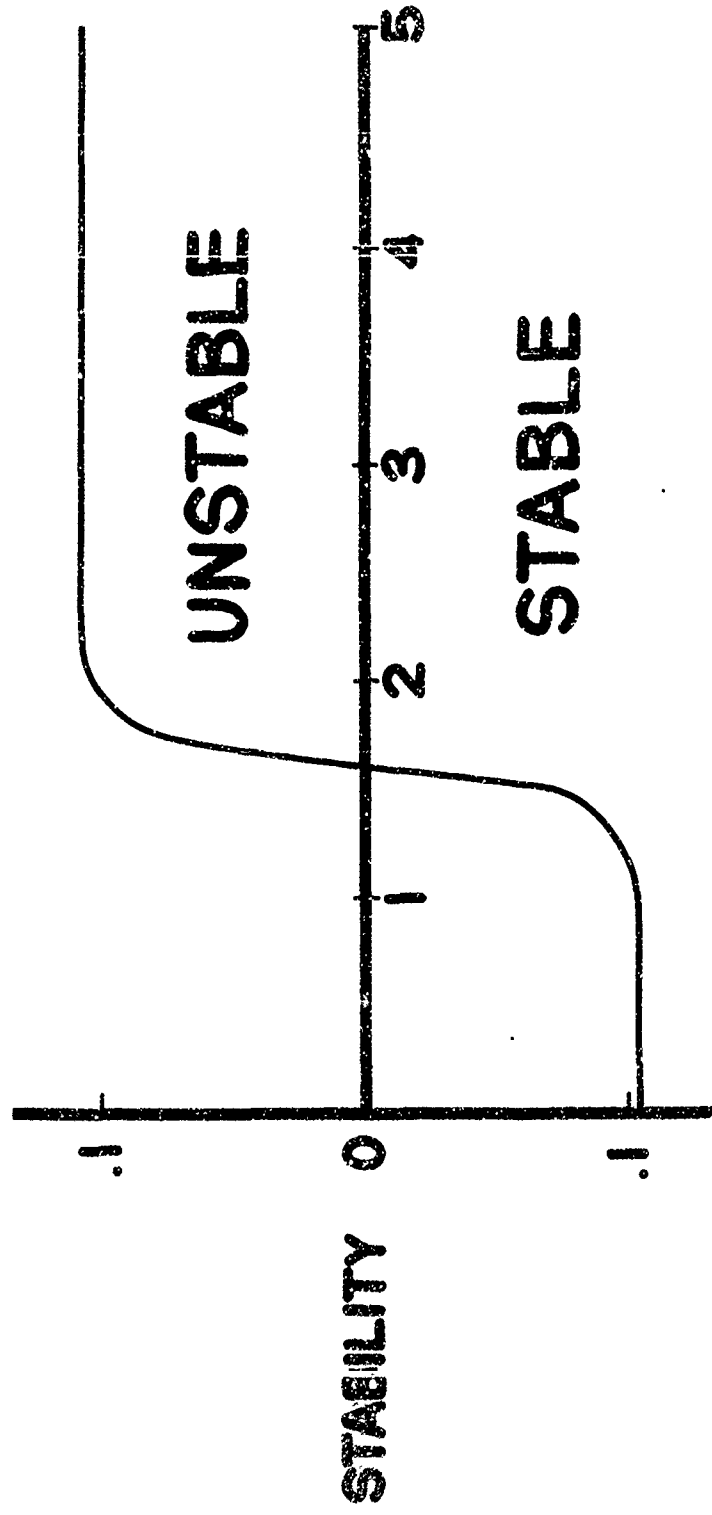


FIGURE 10
EFFECT OF PITCH FREQUENCY
ON WHIRL MODE STABILITY



BODY PITCH FREQUENCY ON TRIPOD, CPS

FIGURE 11

CYCLIC CHORDWISE BENDING AMPLITUDE VS. SPEED

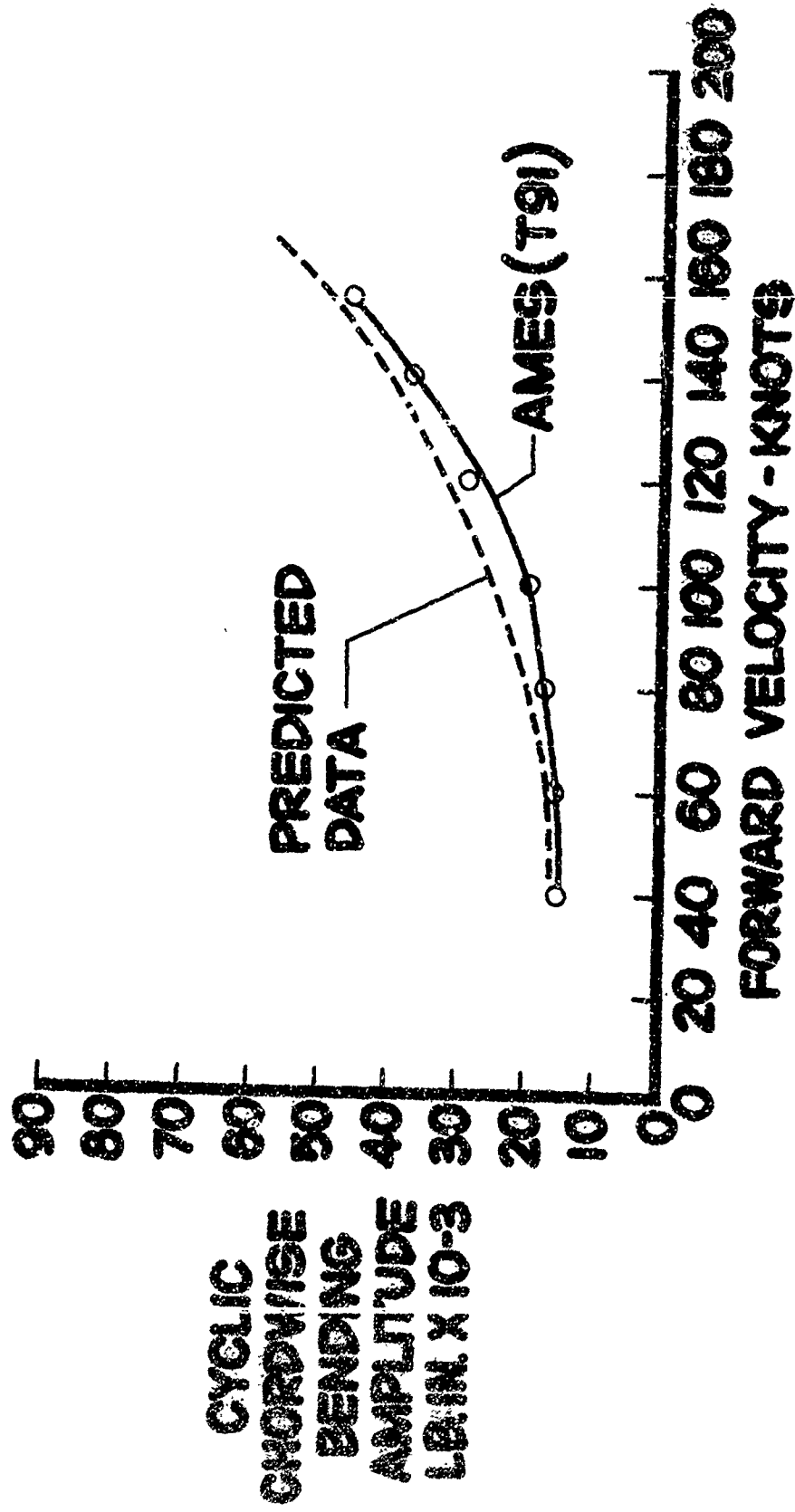


FIGURE 12

SPANWISE BENDING MOMENT DISTRIBUTION

1ST MODE-1ST HARMONIC CYCLIC
FLAPWISE BENDING MOMENT -
SPANWISE DISTRIBUTION TYPICAL
CORRELATION BETWEEN CALCULATED
AND TEST MEASUREMENTS, FOR
= 7.5" c.g. OFFSET

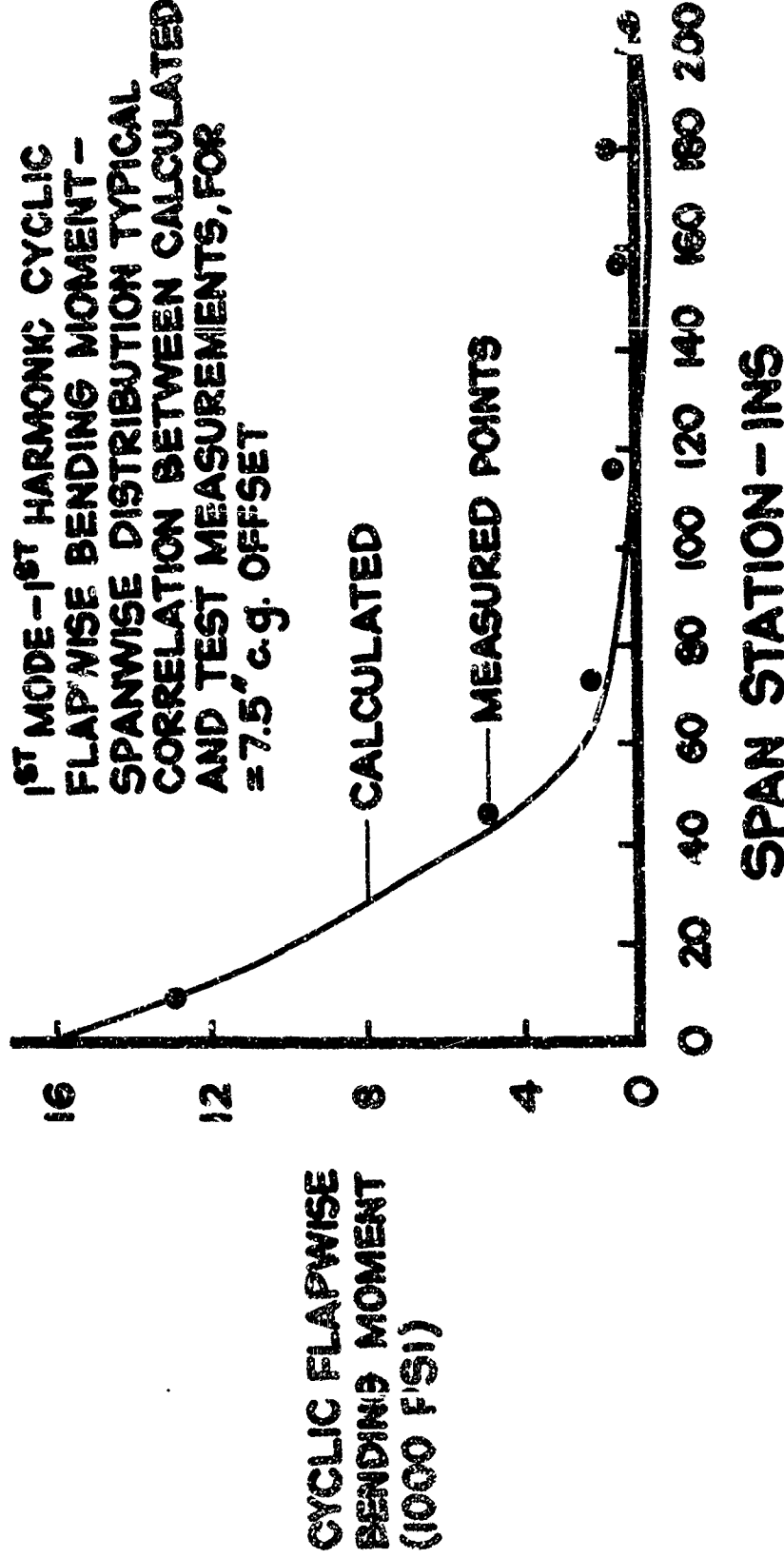


FIGURE 13

HUB FLAP BENDING LOADS 2 PER REV & 3 PER REV

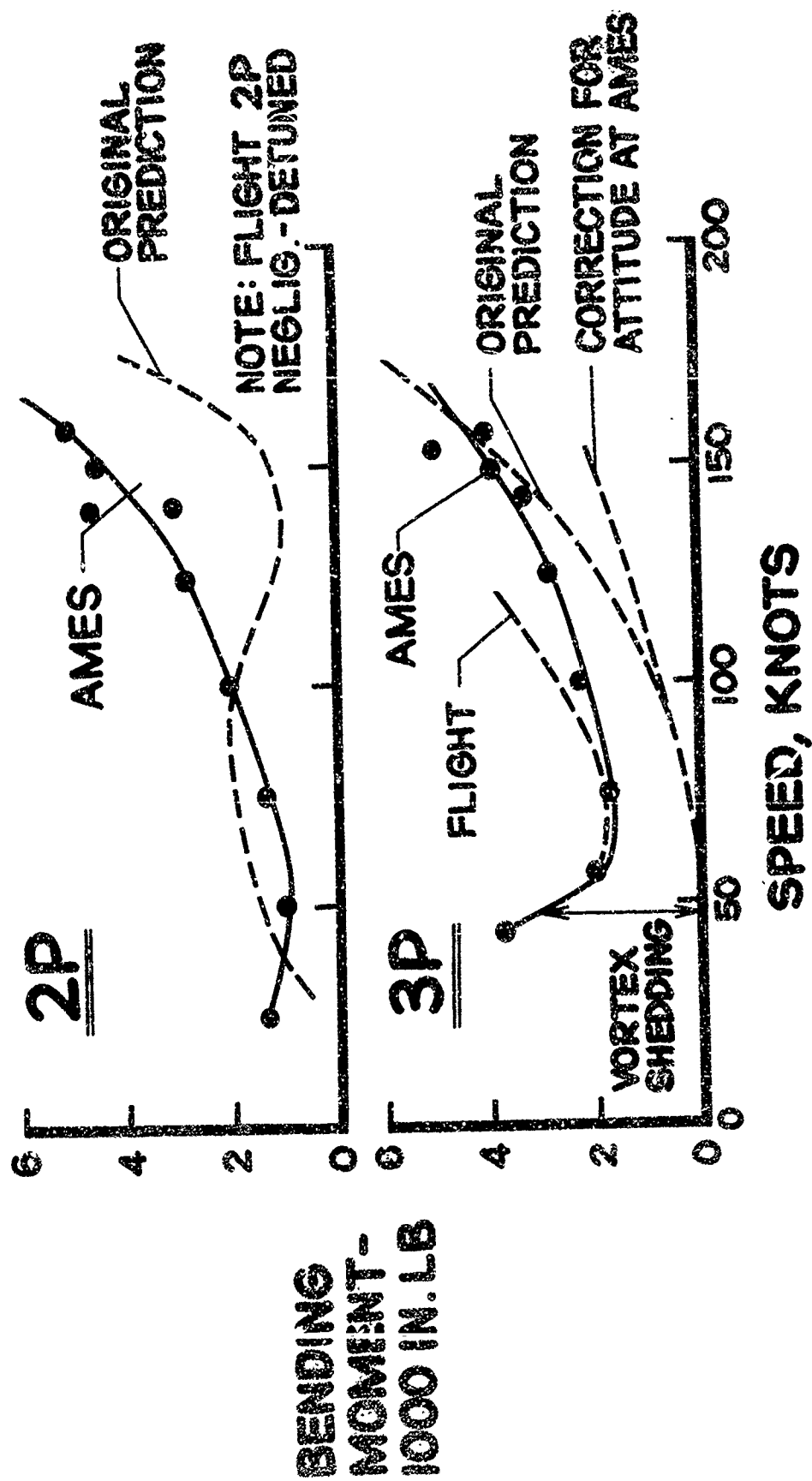


FIGURE 14
**MODEL
 XH-51A
 COUPLED
 BLADE
 FREQ.**

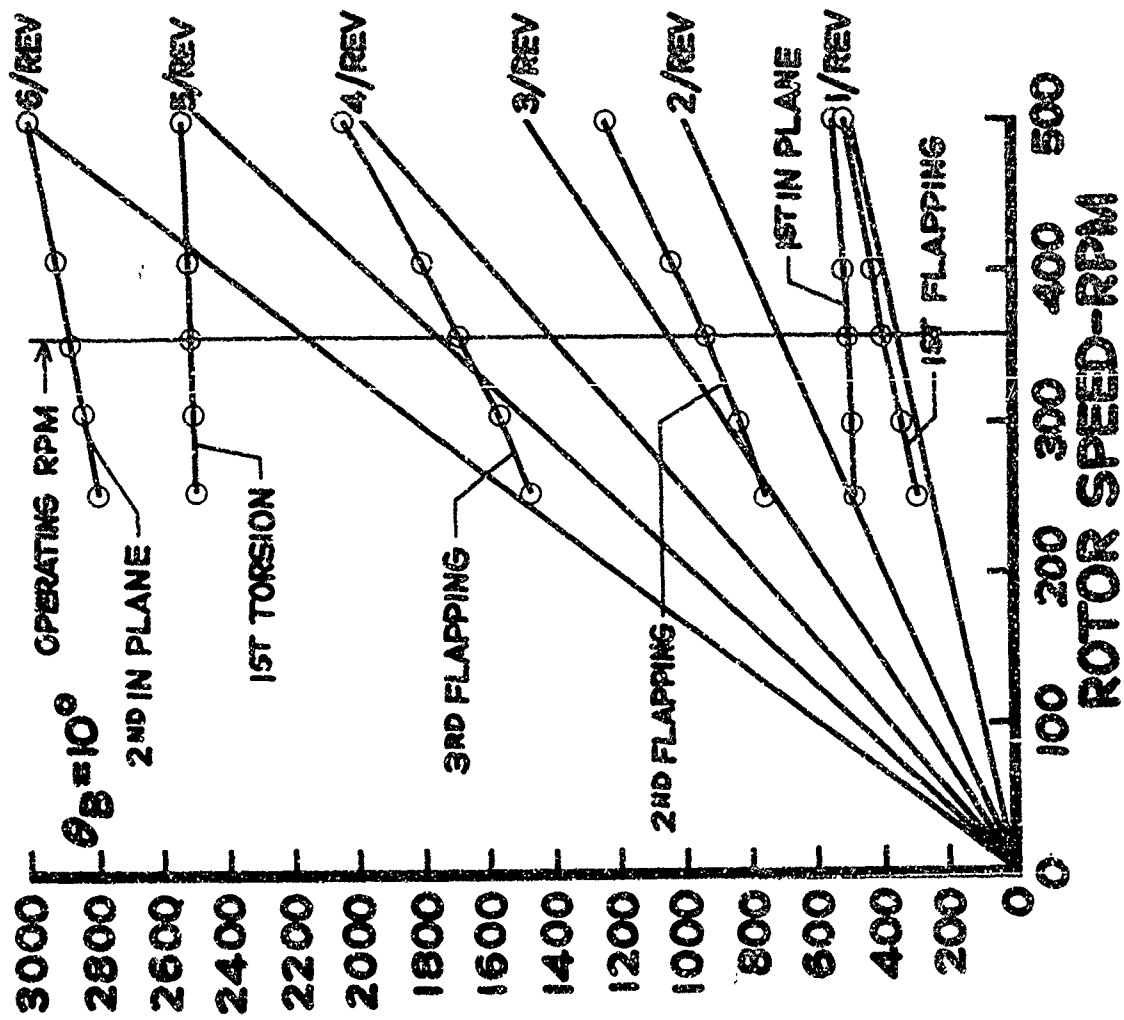


FIGURE 15 EFFECT OF MOUNT STIFFNESS ON BLADE FREQUENCY

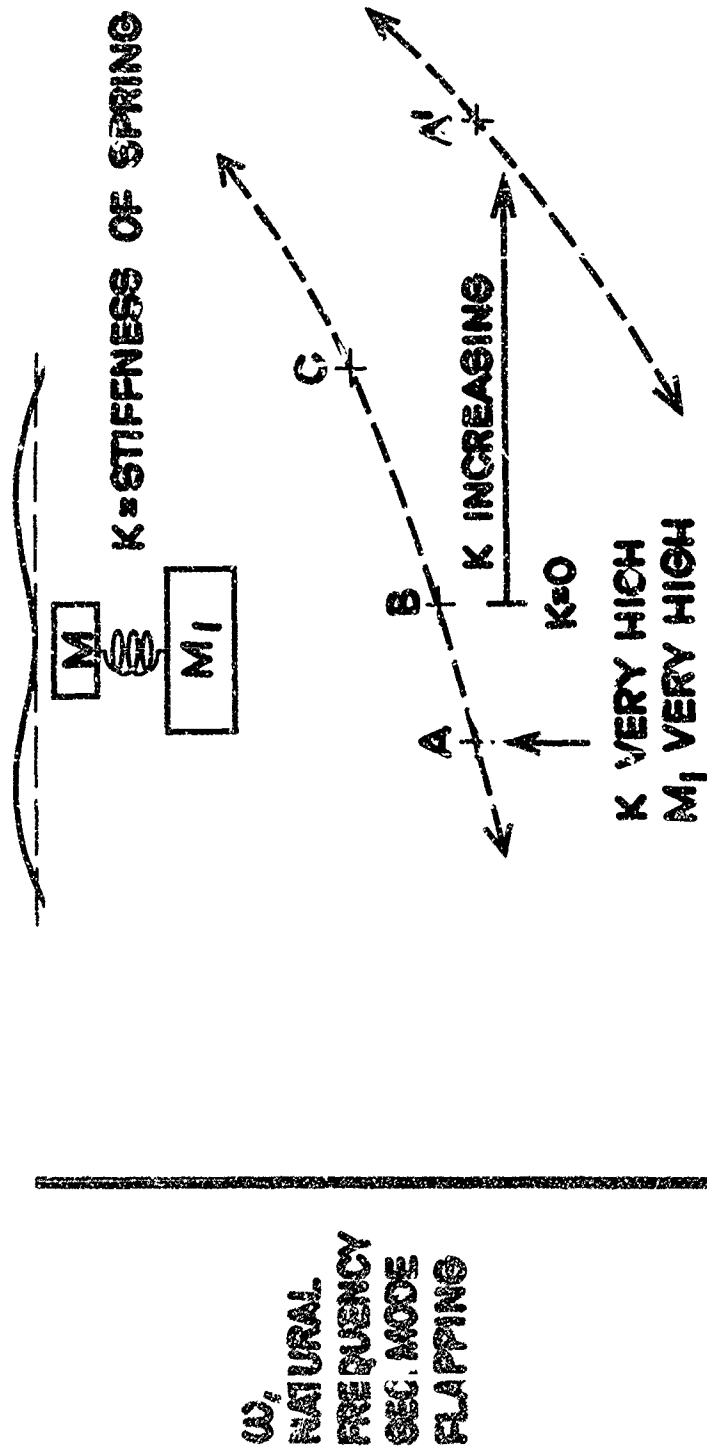
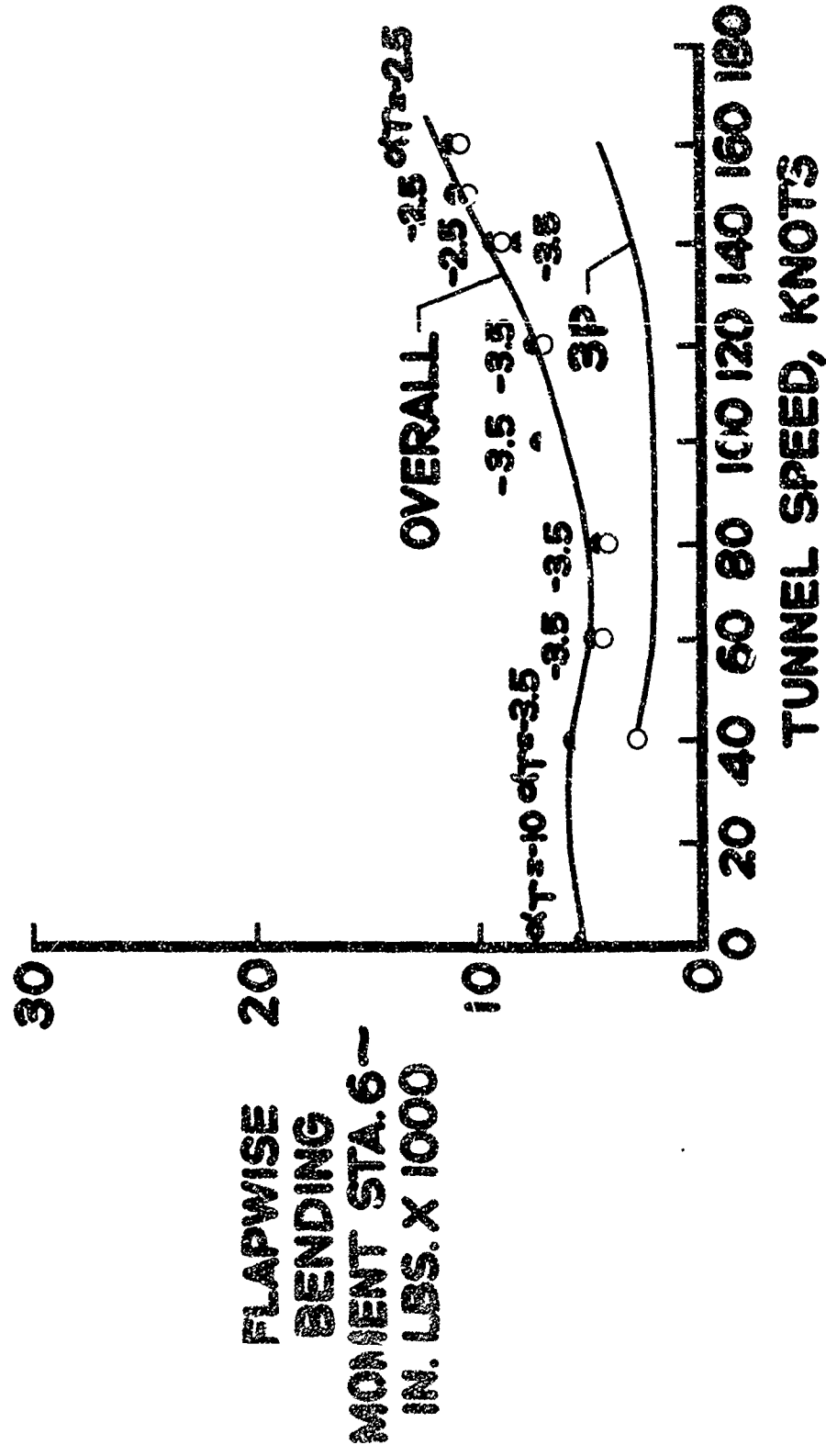


FIGURE 16 CYCLIC HUB FLAP MOMENTS



**AN AEROELASTIC STUDY OF HELICOPTER
ROTOR SYSTEMS IN HIGH-SPEED FLIGHT**

E.R. Wood, K.D. Hilzinger, and A.C. Buffalano

Sikorsky

AN AEROELASTIC STUDY OF HELICOPTER ROTOR SYSTEMS IN HIGH-SPEED FLIGHT

E. R. Wood, K. D. Hilzinger, and A. C. Buffalano

Sikorsky Aircraft Division, United Aircraft Corporation
Stratford, Connecticut

SUMMARY

Presented are results of an aeroelastic investigation to explore effects of flight, rotor, and blade parameters on blade stresses and performance of articulated and rigid rotor systems in high-speed flight. Variations in blade planform and twist, rotor lift and propulsive force, blade stiffness and mass distribution, are investigated for helicopters and compound helicopters at several gross weights for speeds from 150 to 300 knots. The analysis takes into account the fully coupled flatwise-edgewise-torsional response of the rotor blades. Work was performed under U. S. Army TRECOM Contract DA 44-177-TC-831.

INTRODUCTION

Design of helicopters and compound air vehicles for higher airspeeds requires greater knowledge of rotary wing dynamics and performance than is presently available from published analyses and investigations. For fuller understanding of advanced flight regimes, a research program is required, which will explore effects of forward speed, blade planform, blade twist, rotor lift and propulsive force, blade stiffness and mass distribution on resulting blade stresses and performance of articulated rigid rotor systems.

To provide this information, Sikorsky Aircraft last year undertook a study for the U. S. Army Transportation Research Command. This paper gives preliminary results of that study. The work was achieved by a joint effort of the company's Aerodynamic, Blade Design, and Dynamics Sections. Three well developed analytical programs were used in the program. These were: (1) an Advanced Performance Analysis, which was used to determine the basic rotor parameters to be studied; (2) a Horvay-type Blade Design Analysis, which has been responsible for Sikorsky's present-day successful blade designs; and (3) a Coupled Blade Flatwise-Edgewise-Torsional Aeroelastic Analysis, which yields the full spectrum of blade dynamic information. The aeroelastic analysis is general and well suited for studies of a wide range of helicopters and VTOL-type aircraft with rotor blades and propellers of all types. As will be shown in the paper, good correlation has been achieved with the method for both rigid and articulated rotor systems.

1. DESCRIPTION OF AIRCRAFT CONSIDERED

The aeroelastic research program is being carried out under U. S. Army TRECOM Contract DA 44-177-TC-831. Included in the overall TRECOM study are eight basic aircraft, four in the 12,000-lb. class and four in the 33,000-lb. class. There are two 150-knot helicopters, two 200-knot helicopters, two 200-knot wingless compounds, and two 300-knot winged compounds. Four planform variations are considered in each case, and blades are taken as both rigid and articulated. Planform variations are given in Figure (1). A total of 470 flight conditions will be explored in the contract.

Results presented in this paper are taken from initial investigations of the program. Considered are the 150-knot helicopters at 12,000 and 33,000 lb. gross weights. Also shown are some results for the 12,000-lb. winged compound. Substantiation for the method of analysis is based upon correlation studies with flight test data from the Lockheed CL-475 rigid rotor helicopter, and Sikorsky's S-58 and S-61 articulated helicopters. Basic data for the five aircraft considered here are presented in the following table:

TABLE I
BASIC DATA FOR AIRCRAFT INVESTIGATED

	Lockheed CL-475	Sikorsky S-58	Sikorsky S-61	12000-lb. Helicopter	33000-lb. Helicopter	12000-lb. Compound
Blade Radius (ft.)	16	28	31	31	36	28
Offset (inches)	11. *	12	12.625	12.625	24	12.63
Number of Blades	3	4	5	5	6	5
Chord (inches)	12.0	16.4	18.25	18.25	23.65	18.25
Design Taper	1:1	1:1	1:1	1:1	1:1	1:1
Design Twist (degrees)	0	-8	-8	(-8 artic. (0 rigid	(-6 artic. (0 rigid	(-4 artic. (-4 rigid
Airfoil Section	0012	0012	.0012	.0012	0012	0012
Solidity	.0596	.062	.07804	.07804	.1046	.086
Tip Speed (fps)	504	620	660	660	696	493 cruise
Rotor Speed (rpm)	300	216	203	203	185	168
Gross Weight (lbs.)	1970	11300	17000	12000	33000	12000
Percent G. W. Carried by Rotor	100	100	100	100	100	100

*Pitch Bearing Center Line

Tabulated in the Appendix is a set of representative data for blade stiffness, and mass distribution taken from this program. Rigid and articulated blade data are shown for the 150-knot 33,000-lb. helicopter. Also given are fuselage lift and drag characteristics for this aircraft.

2. BLADE DESIGN CRITERIA

Individual blade designs were determined as follows. Initially, an Advanced Performance Analysis was used to obtain basic rotor parameters. These include tip speed, rotor diameter, blade chord, number of blades, and design twist. Based on these parameters, the Blade Design Section then developed structural characteristics for the articulated 1:1 planform blade for each aircraft studied. Blades were designed by standard Sikorsky procedures and met basic load requirements. Characteristics of separate planform blades were then extrapolated from 1:1 planform designs by the following criteria.

1. At corresponding blade radial stations cross-sectional area was held equivalent. By this means blade weights and centrifugal stresses were kept equal. The only deviation permitted was when extrapolated wall thickness became small. Here, to avoid local spar buckling a minimum value of 0.15 inches was set.
2. Section properties were extrapolated based on the ratio of spar wall thickness to chord. Knowing chord and section area, this value could be determined, then used to calculate flatwise, chordwise, and torsional stiffness assuming a typical D-spar blade.

For rigid rotor systems the blade root had to be specifically designed to meet Lockheed's criteria as set forth in Reference (1):

1. For planforms of aspect ratio greater than 18 a soft inplane system was used. This required the first inplane bending frequency to be between .6 Ω and .7 Ω . The inplane frequency was achieved by reducing root stiffness by removing material and attributing 15% of the frequency decrease to bearing flexibility.
2. For planforms of less than 18 a stiff inplane system was used. Here, blades were tuned so that the first inplane bending mode was near 1.4 Ω .
3. Flatwise flexibility of rigid blades was designed so that the second flatwise bending mode was sufficiently removed from n/rev.

4. Prelag and precone angles were selected based on zero steady bending moment at the blade root in cruise flight condition.

3. DESCRIPTION OF AEROELASTIC ANALYSIS

The method of aeroelastic analysis is based upon superposition of separate harmonics of blade forced response, which results from response of the blade to individual harmonics of airloads. A detailed description of the method has been given in References(2) and (3). A brief description follows.

a. Calculation of Aerodynamic Loads

For the helicopter to be analyzed, the gross weight, drag, speed, and rotor rpm must be given. Also for the blades, steady-state two-dimensional airfoil characteristics, structural stiffnesses, mass distribution, twist, and root retention must be specified. The rotor disk is considered to be moving at the proper forward tilt to provide enough propulsive force to overcome the net drag of the aircraft. It must also support the aircraft, and there must be sufficient cyclic pitch to keep the rotor in equilibrium. Certain simplifying assumptions are made to initiate the calculation; such as the approximate coning angle, an estimate of the rotor drag, and an estimate of the radial position of the resultant thrust vector. These approximations do not affect the final accuracy, for if they are too far in error, this can be remedied by a second or third iteration.

For a high-speed condition, constant inflow is taken. The blade is subdivided into twenty-four elements. For each of 36 ten-degree azimuth intervals, the blade is considered set at two blade angles. These angles bracket the expected blade angles. Blade-element aerodynamic lifts are then computed, from which the moment of the thrust about the flapping hinge is calculated as a function of blade angle and azimuth position. The cyclic pitch necessary to maintain the rotor system in equilibrium is then calculated by an iteration to enforce the condition that the first harmonic thrust moment about the flapping hinge is zero.

For calculation of aerodynamic loads, two-dimensional 0012 airfoil data is used. Compressibility effects are taken into account by using separate C_L , C_D , and C_m versus α curves for angles of attack from 0 to 30 degrees for Mach numbers up to 0.95 in 5% increments. To define stall regions above angles-of-attack of 30 degrees, single C_L , C_D , and C_m versus α curves are taken from data in Reference (8).

Final determination of cyclic pitch yields angle-of-attack distribution, rotor drag, power required, location of resultant thrust vector, thrust moments, and provides pitching moments, and resolved thrusts

and drags on twenty-four blade elements for ten-degree azimuth intervals. A harmonic analysis is performed on this loading and the steady plus the first seven harmonics of blade element loading (pitching moments, thrusts, and drags) are obtained in complex form.

b. Blade Dynamic Response

Individual harmonics of airloads are next introduced into the coupled blade dynamic analysis. This method is based upon an extension of Myklestad's analysis for rotating beams. There is provision for up to twenty-four flatwise, edgewise, and torsional degrees-of-freedom with coupling due to twist. Equations are in complex form to allow for aerodynamic damping and phasing of aerodynamic loads. Boundary conditions at the tip of the blade require that shears, moments, and torque are zero. At the root of the blade boundary conditions are applied consistent with blade root restraint, whether articulated, teetering, or rigid. There is provision for a lag damper. Also, with torsion added, provision has been made for control system flexibility and damping.

Analysis for flexible blade dynamics with torsional coupling is done in three steps. In the first step, the blade is treated as infinitely rigid, and rigid body coning, lagging, and twisting calculated. In the second step using an iterative relaxation-type method, steady coupled flatwise-edgewise-torsional bending is computed. The iteration is initiated by using the blade slopes and deflections determined in the first step. In the third step, the first through the seventh harmonics of blade coupled responses are determined. Steady response values from the second step are used so that torsional coupling of vibratory forces times steady deflections and steady forces times vibratory deflections can be included.

Total forced response of the blade is next determined by superposition of separate harmonics of blade dynamic response. This yields the azimuthwise distribution of moments, torques, deflections, twist, and stresses at each of twenty-four blade stations for ten-degree azimuth intervals.

4. CORRELATION WITH FLIGHT TEST DATA

Using constant inflow, the method of analysis described shows good agreement with measurements in predicting performance. This is illustrated by Figure (2). Here, calculated and measured power are shown to compare favorably for the S-61 at two gross weight conditions. The computed values include power required for the tail rotor and accessory drives. Coefficients of drag for the blades were incremented by a $\Delta C_D = .002$ to account for additional roughness of the actual blade over a highly polished wind-tunnel

specimen. Note that good agreement is achieved even at low airspeeds where effects of variable inflow have been shown to be large. Comparisons also indicate that the method described provides performance results consistent with standard performance calculations in use.

Figures (3) and (4) compare calculated blade vibratory bending moments and stresses with flight test values for an articulated rotor helicopter. Given in Figure (3) is a comparison of the radial distribution of one-half peak-to-peak bending moments against flight test data for the S-58 (H-34) helicopter. Data is shown for 110 knots. The test helicopter was instrumented by Sikorsky Aircraft under U. S. Army TRECOM contract. Flight tests were conducted by NASA at Langley Field, and preliminary results of tests were released in Reference (5).

Effect of forward speed on vibratory blade stresses and results of correlation are shown in Figure (4). Here, flight test data taken at Sikorsky Aircraft is compared with calculated values for the S-58 at speeds above 100 knots. Each test point shown on the plot represents an averaging of data taken in three separate flights. Data was obtained from Reference (6).

Correlation studies for a rigid rotor helicopter were based on data furnished by the Lockheed-California Company for the CL-475 helicopter (Reference (1)). Data included detailed information on blade stiffness and mass distribution. Also provided was a blade resonance diagram, a curve showing blade static deflection, and flight-measured vibratory bending moments along the blade at a number of airspeeds.

Results of earlier studies (Reference (2) and (3)) have shown good correlation on predicting one-half peak-to-peak stresses at higher airspeeds using constant induced velocity. Thus, for correlation purposes the highest airspeed was selected for which complete CL-475 data had been furnished. This was 100 mph. The blade was subdivided into twenty segments in the fully coupled flatwise-chordwise-torsional analysis, allowing sixty degrees-of-freedom. First step in the analysis was to run the calculation as a non-rotating beam to check analytical stiffness and weight characteristics against Lockheed's data for static deflection. Good agreement was achieved as shown by Figure (5).

Second step in the rigid rotor correlation program was to determine flexibility of spindle bearings at the blade root. This was achieved by varying the flatwise and chordwise root springs in the analysis until there was good agreement with Lockheed's blade resonance diagram as shown in Figure (6). From this, effective springs of 1.75 million inch lbs. per radian and 4.00 million inch lbs. per radian were determined for respective flatwise and edge-wise root stiffness. Differences between calculated and measured third flatwise modes shown by Figure (6) attributed to motion of the rotor head. Test results had been obtained by shaking the hub with non-rotating blades where motion of the hub would tend to increase the natural frequency.

The third step in the correlation was to run the complete aeroelastic analysis at 100 mph using constant inflow. Here, the rotor was trimmed, cyclic pitch determined and aerodynamic loads calculated. Harmonics of aerodynamic loads were then applied, and individual harmonics of blade response superimposed. The radial distribution of calculated blade vibratory bending moments are shown to compare favorably with Lockheed's flight-measured values in Figure (7).

5. RESULTS OF ANALYSIS

a. Variation of Blade Root Stiffness

Proper treatment of blade root flexibility is of prime importance in design of rigid rotor systems. Rigid rotor designers point out that the term "rigid" is a misnomer and that "hingeless" is a preferred definition. In truth, the root region of these blades is far from being a mathematical cantilever. Designed flexibility contributes to a root restraint, which is between a theoretical rigid and hinged condition.

Effects of root flexibility on vibratory bending moments and stresses are shown in Figures (8), (9), (10), and (11). Presented are results of calculations for the Lockheed CL-475 helicopter at 100 mph. For the first three figures, flatwise root flexibility has been varied, while edgewise restraint is held to a value representative of the actual CL-475 design.

The first plot, Figure (8), gives the distribution of flatwise vibratory bending moments along the blade for an articulated version of the CL-475. The curve is typical of articulated blades in that the maximum vibratory moment occurs at about two-thirds blade radius. Maximum value is ± 2100 inch lbs. The second plot, Figure (9) shows corresponding flatwise vibratory moments for a theoretically rigid root restraint. In this case the outboard blade moment is seen to increase to ± 2700 inch lbs., while at the root, moments reach a value in excess of ± 8000 inch lbs. Finally, shown in Figure (10) are calculated moments for a blade with selected flatwise root restraint. For this condition, outboard blade moments are reduced to ± 650 inch lbs. while root vibratory moments increase to about double the maximum level for the articulated blade. Since more blade area is required at the root to carry centrifugal loads, a section modulus can be selected for the semi-rigid blade that will yield vibratory stress levels comparable to those of an articulated design.

Sensitivity of edgewise stresses to proper tuning is illustrated by Figure (11). Reference (7) recommends a frequency ratio of 1.4 which is apparent from the plot where vibratory stresses are seen to become excessively large as the first edgewise mode of the blade approaches one

per rev. Results given are for a neutral c. g. fuselage trim condition. Center-of-gravity shifts can increase edgewise stresses due to increased first harmonic blade bending and associated Coriolis forces.

b. Twist and Planform Variations

Shown in Figures (12) through (17) are results of varying blade twist and planform for the 12,000 and 33,000 lb. helicopters at 150 knots. The effect of blade twist on performance is given in Figures (16) and (17). Only one power curve is shown for both rigid and articulated helicopters of the same gross weight. Calculated power was the same for each type helicopter, since the rigid rotor was preconed for this airspeed, giving both articulated and rigid systems the same coning angle. Power shown is that required by the rotor and does not take into account tail rotor power and accessory drives. Coefficients of drag for the blade were incremented by $\Delta C_D = .002$ to account for blade roughness. The non-linear planform blade gave the best performance results for both gross weight machines, but was the first to stall out at low twists or if forward speed was increased. The marked increase in power for the non-linear blades from -8 to -4 degrees in Figure (17) is attributed to a near stall condition and associated high drags. From Figures (16) and (17) it can be seen that change in blade twist can result in a maximum power gain of about 500 hp for the 33,000-lb. helicopter, about 200 hp for the 12,000-lb. aircraft.

Presented in Figures (12) through (15) are maximum flatwise vibratory bending moments versus twist for the four blade planforms. Results are given for both rigid and articulated rotor systems. It is interesting to note that the planform order from lowest to highest bending moments is fairly consistent between both gross weights and rigid and articulated systems. For both gross weight machines highest blade bending moments were for the relatively stiff 3:1 planform blade; lowest were for the unloaded-tip, non-linear blade. The relatively flexible 1:2 blade while showing low moments would present root design problems as a rigid rotor.

c. Variation of Blade Stiffness

A requirement of the aeroelastic investigation was to explore effects of blade stiffness on vibratory bending moments. Figures (21), (22), (23), and (24) give results of this study for the 150-knot 33,000-lb. helicopter. In Figures (21) and (22), flatwise stiffness of the basic blade has been both doubled and reduced to one-half. Plots for both rigid and articulated blades are essentially what would be expected. For the articulated case the entire moment envelope is seen to increase almost proportionately with increase in stiffness. The same is observed for the rigid blade in the root region. For this case it is interesting to note that the point of minimum bending moment moves inboard as the blade becomes more flexible.

Effects of linear variation of stiffness about the basic blade design are given by Figures (23) and (24). Here, for both articulated and rigid blades, flatwise stiffness has been multiplied by factors ranging linearly from 2 at the root to 1/2 at the tip or vice versa. Lowest vibratory moments are achieved for the articulated blade of standard design as given by Figure (23). Here, stiffened outboard blade section and softened cuff appear most detrimental. For rigid blades (Figure (24)), where the critical region is at the root, the reverse is true. Low root stiffness contributes to lower moments, and the stiffer outboard section does not have a significant detrimental effect.

d. Blade Mass Distribution

Given in Figures (18) and (19) are effects on vibratory stress for the 33,000-lb. helicopter by separately introducing a concentrated 36-lb. weight at five radial locations along the blade. Radial stress envelopes for the five positions for an articulated blade are presented in Figure (18). The standard unweighted blade (not shown) had a maximum vibratory stress of 4600 p. s. i. Results shown in Figure (18) indicate: (1) a significant reduction in vibratory stress by introducing a weight at the blade tip; (2) an increase in vibratory stress for weights at the .75R and .50R positions; and (3) little effect on vibratory stress for concentrated weight added to blade inboard regions. Effect on flatwise and edgewise maximum stress by varying the amount of weight added to the blade tip is given by curves shown to the right of Figure (20). Here, vibratory stress reduction is greatest with the first 10 lbs. added, then levels off in the 30-40 lb. region.

Effects of added concentrated weights for rigid blade stresses are plotted in Figure (19). In this case the root region is most critical. Vibratory stress for the standard blade (not shown) was 8750 p. s. i. Here, the tip weight again produced a significant reduction, but weights at other locations gave either a slight decrease or an increase. The left-hand plot of Figure (20) shows results of varying tip weight on rigid blade stresses. Flatwise stress reduction follows the same trend as the articulated system. The sharp continuous reduction shown for edgewise stresses is attributed to detuning the first edgewise mode. The rigid blade in this case (aspect ratio > 18) was designed for $W_T = .65 \Omega$. Added weight brings this mode further below one per rev. Were a stiff inplane design used, increased added tip weight would have the opposite effect. Edgewise stresses would increase for the first edgewise mode would be reduced from 1.4Ω in the direction of one per rev.

e. Compound Helicopters

Interest centers today in extending the speed frontier of helicopters to the 200-300 knot region. The compound helicopter is a possible configuration to meet this requirement. Here, the rotor is substantially unloaded in high-speed flight by external wings, and jet or prop-jet

engines provide the necessary propulsive force. At the time of writing this paper some preliminary work had been done under the contract on this type of design. Results are presented to show early trends, while it is recognized that many questions still remain to be answered.

The basic aircraft is defined in Table I. For the high-speed flight condition the rotor was required to carry 1500-lbs. of lift. Rotor rotational speed was reduced to 168 rpm, which gave an advancing blade Mach number of 0.90 at 300 knots. For first studies, both rigid and articulated blades were taken with -4 degrees of twist. Were the design to be further optimized, it is recognized that additional stress relief could be achieved for both rotor systems by a backoff in blade twist.

An important variable in compound design is rotor angle-of-attack. This can range from having the rotor tilt well forward to provide propulsive force as for the helicopter, to an aft-tilted windmilling rotor which extracts energy from the air stream. For the results shown here the rotor has been placed at zero angle-of-attack. This gives a very low coning angle, blades at relatively flat pitch, and requires some power from the engines to drive the rotor.

Since coning angles were similar, power and drag plots are the same for both rigid and articulated systems. These are shown in Figures (23) and (24). In Figure (23), rotor power required is observed to be only 412 hp at 300 knots. The rotor drag or H-force plotted in Figure (24) is seen to be approaching 1000 lbs. at this airspeed. While this value may be considered high, it is reduced over the drag of a pure helicopter configuration through holding rotor angle-of-attack flat and blade pitch low.

Some interesting trends are noted in the plot showing flatwise vibratory bending moments versus airspeed (Figure (25)). Maximum vibratory moments are seen to increase more sharply with airspeed for the rigid than for the articulated case. This trend is partially explained by the diagrams given on the plot showing spanwise distribution of bending moments for both rotor systems at 200 and 300 knots. Here, it can be seen that outboard moment envelopes are similar for both systems and build up at the same rate with airspeed. However, root moments, which govern rigid blade design, are seen to digress more rapidly.

6. CONCLUSIONS

Early results have been presented from an analytical program to explore effects of parametric variations on blade stress and performance of rigid and articulated rotor systems. The analysis considers the high-speed condition and takes into account the fully coupled flapwise-edgewise-torsional response

of the rotor blades. For the studies constant inflow was taken. Conclusions which may be drawn from the results include:

- a. Calculated performance and one-half peak-to-peak stresses are shown to give good agreement with flight measured values. Good stress correlation is shown for both rigid and articulated rotor helicopters at higher airspeeds. Flight measured data is taken for the Sikorsky S-58 and Lockheed CL-475 helicopters.
- b. Rigid rotor flatwise and edgewise vibratory stresses are observed to be highly sensitive to design of the blade root region. For this rotor system properly designed flexibility gives a root restraint, which is between a theoretical rigid and hinged condition.
- c. For the articulated blade, maximum flatwise vibratory stress generally occurs at about two-thirds blade radius. Location will vary with planform, twist, and whether the aircraft is a helicopter or compound. For the rigid rotor, maximum flatwise vibratory stress occurred at the blade root for all cases studied.
- d. Results of calculations for planform-twist variation indicate a rapid rise in vibratory bending moments with increase in blade twist for both rigid and articulated rotor systems. Highest vibratory bending moments were noted for the 3:1 tapered blade.
- e. Studies on variation of blade stiffness indicate that outboard blade stiffening is detrimental for an articulated blade, whereas inboard blade stiffening shows the largest increase in vibratory moments for a rigid blade.
- f. Reduction in vibratory bending moments was observed for both rigid and articulated blades by introducing a concentrated weight at the blade tip. For the 33,000-lb. helicopter considered, greatest reduction was achieved for both systems with the first 10 lbs. added, lesser reduction thereafter.
- g. Preliminary analysis for compound helicopters indicates a more marked increase in flatwise vibratory bending moments with air-speed for the rigid than for the articulated rotor system.

7. ACKNOWLEDGEMENT

The authors wish to express their appreciation to Mr. Frank Rizzo of Sikorsky Aircraft whose efforts on coordinating blade designs and processing data have contributed significantly to the program. The authors are also grateful to Mr. James McHugh, U. S. Army Transportation Research Command, for guidance on the project, and to Mr. I. Culver, Lockheed-California Co., for technical assistance on rigid rotor systems.

8. REFERENCES

1. Information on Non-Articulated Rotor Systems for the Army-Sikorsky High-Speed Flight Investigation, Lockheed - California Company, Lockheed Letter LAC/391526, Sept. 25, 1962.
2. Gerstenberger, W., and Wood, E. R., Analysis of Helicopter Aeroelastic Characteristics in High Speed Flight, I. A. S. Paper No. 63-72, January 1963.
3. Wood, E. R., and Hilzinger K. D., A Method for Determining the Fully Coupled Aeroelastic Response of Helicopter Rotor Blades, American Helicopter Society, May 1963.
4. Myklestad, N. O., Vibration Analysis, McGraw-Hill, 1956.
5. Information and Preliminary Data on Helicopter Rotor Blade Dynamic Airloads and Moments as Measured in Flight, U. S. Army TRECOM by N. A. S. A., May 24, 1961.
6. Gaieski, T., Stress Survey of the S-58 Main Rotor Blade Rear Web Section, Sikorsky Engineering Report 58251, Aug. 15, 1959.
7. Hibbard, H. L., and Heppe, R. R., Concept and Development of a Simple Stable, and Economical VTOL Vehicle, Aerospace Engineering, Feb. 1962.
8. Critzos, C., and Heyson, H., and Boswinkle, R., jr., Aerodynamic Characteristics of N. A. C. A. 0012 Airfoil Section at Angles of Attack from 0° to 180°, N. A. C. A. TN 3361, 1955.

APPENDIX I

Helicopter Basic Blade Data

Gross Weight 33,000 lbs., 150-Knot Design

Articulated Blade

<u>Radii (In.)</u>	<u>Weight Per Segment (Lb.)</u>	<u>Blade Twist (Deg.)</u>	<u>Blade Chord (In.)</u>	<u>Midline Area (Sq. In.)</u>
432.0	6.97	-1.79	23.65	9.55
410.4	19.60	-1.52	23.65	19.20
388.8	14.51	-1.22	23.65	19.40
367.2	15.77	-0.91	23.65	19.73
345.6	15.74	-0.74	23.65	19.86
324.0	17.14	-0.30	23.65	20.12
302.4	10.29	0.00	23.65	20.15
280.8	17.63	.30	23.65	20.26
259.2	17.02	.60	23.65	20.23
237.6	18.04	.91	23.65	20.28
216.0	17.71	1.2	23.65	20.30
194.4	16.61	1.51	23.65	20.36
172.8	16.42	1.81	23.65	20.40
151.2	16.42	2.13	23.65	20.43
129.6	17.33	2.39	23.65	20.57
108.0	18.46	2.59	9.71	21.00
86.4	38.11	2.59	9.71	24.60
64.8	124.62	2.59	9.71	100.00
43.2	77.12	2.59	9.71	100.00
24.0	84.59	2.59	9.71	100.00

APPENDIX I (contd.)

Articulated Blade

<u>Spar Wall Thickness (in.)</u>	<u>Flatwise Ixx (in⁴)</u>	<u>Edgewise Iyy (in⁴)</u>	<u>Torsion J (in⁴)</u>	<u>Section Zxx (in³)</u>	<u>Modulus Zyy (in³)</u>
.081	1.87	19.9	5.90	1.38	3.8
.162	3.75	39.8	12.70	2.92	7.8
.183	4.20	42.9	15.00	3.24	8.5
.204	4.75	53.0	14.90	3.62	9.8
.212	5.05	55.3	16.55	3.80	10.2
.216	5.42	64.8	18.00	4.15	11.3
.221	5.58	65.3	19.05	4.20	11.5
.224	5.68	66.0	19.30	4.28	11.6
.228	5.80	66.8	19.70	4.35	11.7
.232	5.95	67.3	20.00	4.40	11.9
.237	6.05	68.0	20.30	4.48	12.0
.241	6.18	68.8	20.75	4.55	12.1
.245	6.25	69.3	21.05	4.60	12.3
.249	6.40	70.1	21.40	4.70	12.4
.258	6.45	72.0	21.85	4.90	12.8
.290	8.10	80.8	23.40	5.80	14.3
.375	24.10	124.0	48.80	13.20	22.2
3.0	100.00	100.0	100.00	25.00	25.0
3.0	100.00	100.0	150.00	25.0	25.0
3.0	100.00	100.0	150.00	25.0	25.0

APPENDIX I (contd.)

<u>Rigid Blade</u>				
<u>Radil (in.)</u>	<u>Weight Per Segment (Lb.)</u>	<u>Blade Twist (Deg.)</u>	<u>Blade Chord (In.)</u>	<u>Midline Area (Sq. In.)</u>
432.0	6.97	0.	23.65	9.55
410.4	19.60	0.	23.65	19.20
388.8	14.51	0.	23.65	19.40
367.2	15.77	0.	23.65	19.73
345.6	15.74	0.	23.65	19.86
324.0	17.14	0.	23.65	20.12
302.4	10.29	0.	23.65	20.15
280.8	17.63	0.	23.65	20.20
259.2	17.02	0.	23.65	20.23
237.6	18.04	0.	23.65	20.28
216.0	17.71	0.	23.65	20.30
194.4	16.61	0.	23.65	20.36
172.8	16.42	0.	23.65	20.40
151.2	16.42	0.	23.65	20.43
129.6	17.33	0.	23.65	20.57
108.0	18.46	0.	9.71	21.00
86.4	38.11	0.	9.71	24.60
64.8	124.62	0.	9.71	100.00
43.2	77.12	0.	9.71	100.00
24.0	84.59	0.	9.71	100.00

APPENDIX I (contd.)

Rigid Blade

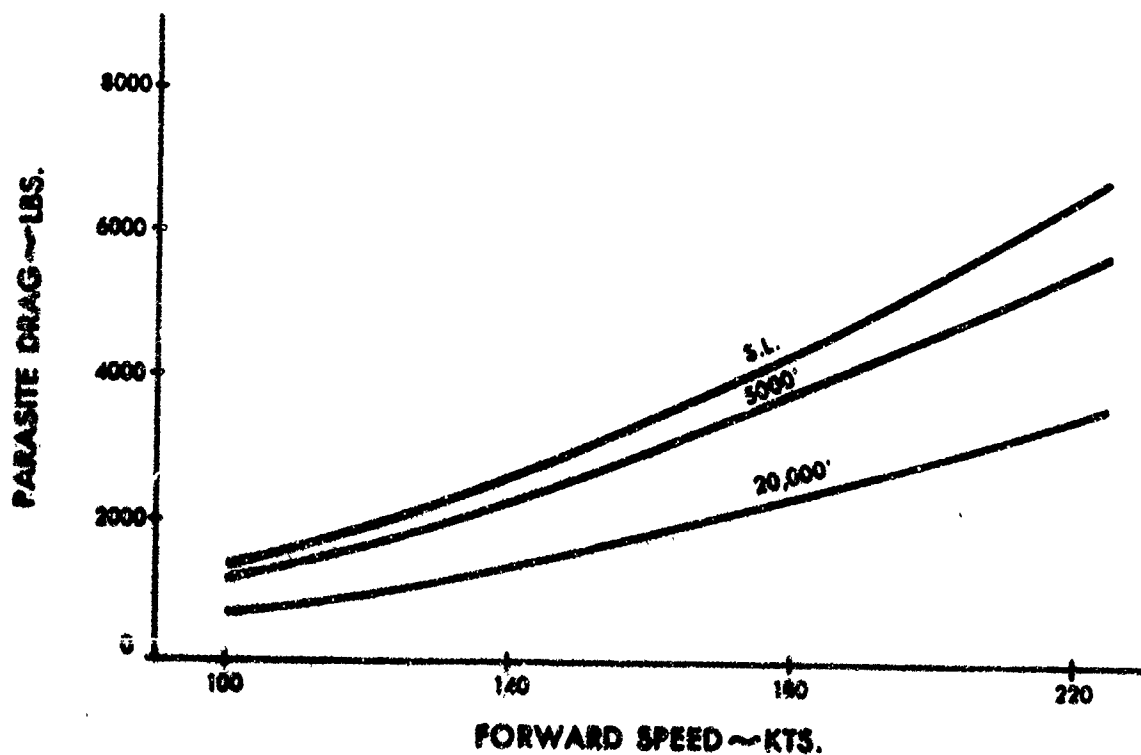
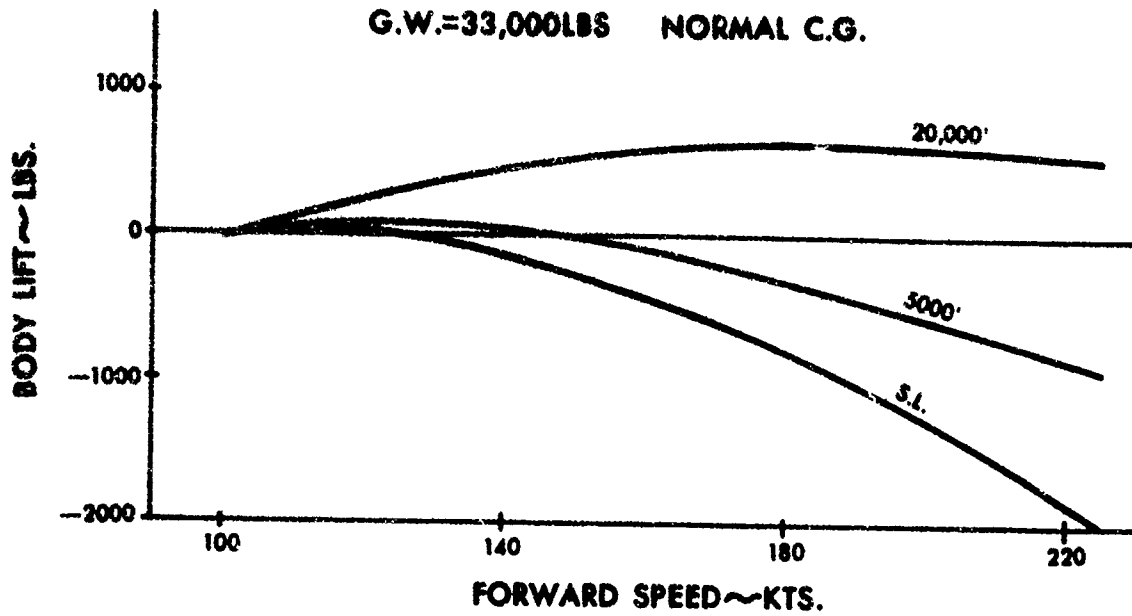
<u>Spar Wall Thickness (In.)</u>	<u>Flatwise Ixx (In⁴)</u>	<u>Edgewise Iyy (In⁴)</u>	<u>Torsion J (In⁴)</u>	<u>Section Zxx (In³)</u>	<u>Modulus Zyy (In³)</u>
.081	1.87	19.2	5.9	1.38	3.8
.162	3.75	39.8	12.7	2.92	7.8
.183	4.20	42.9	15.0	3.24	8.5
.204	4.75	53.0	14.9	3.62	9.8
.212	5.05	55.3	16.6	3.80	10.2
.216	5.42	64.8	18.0	4.15	11.3
.221	5.58	65.3	19.1	4.20	11.5
.224	5.68	66.0	19.3	4.28	11.6
.228	5.80	66.8	19.7	4.35	11.7
.232	5.95	67.3	20.0	4.40	11.9
.237	6.05	68.0	20.3	4.48	12.0
.241	6.18	68.8	20.8	4.55	12.1
.245	6.25	69.3	21.1	4.60	12.3
.249	6.40	70.1	21.4	4.70	12.3
.258	6.45	72.0	21.9	4.90	12.8
.290	8.10	80.8	23.4	5.80	14.3
.375	10.00	124.0	48.8	6.00	22.2
3.0	10.00	43.0	100.0	7.00	10.0
3.0	10.00	43.0	150.0	7.00	10.0
3.0	10.00	43.0	150.0	7.00	10.0

APPENDIX I

LIFT AND DRAG VS TRUE AIRSPEED

STD. DAY $\Omega R=696$ FPS $f=44$ FT²

G.W.=33,000LBS NORMAL C.G.



BLADE PLANFORMS FOR AEROELASTIC STUDY

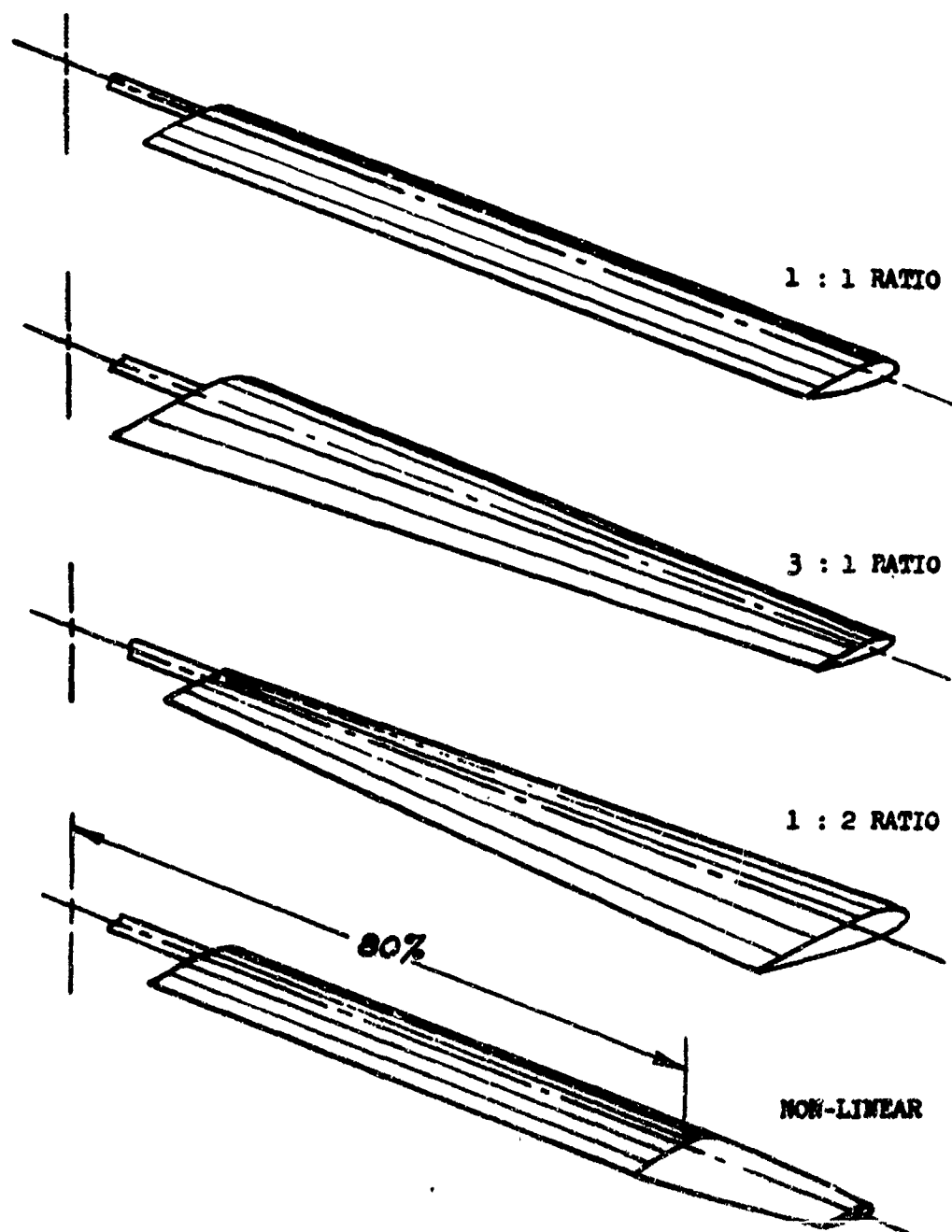


FIGURE 1

**S-61 HELICOPTER
PERFORMANCE COMPARISON
GROSS WEIGHT AS SHOWN $\Omega = 203$ RPM**

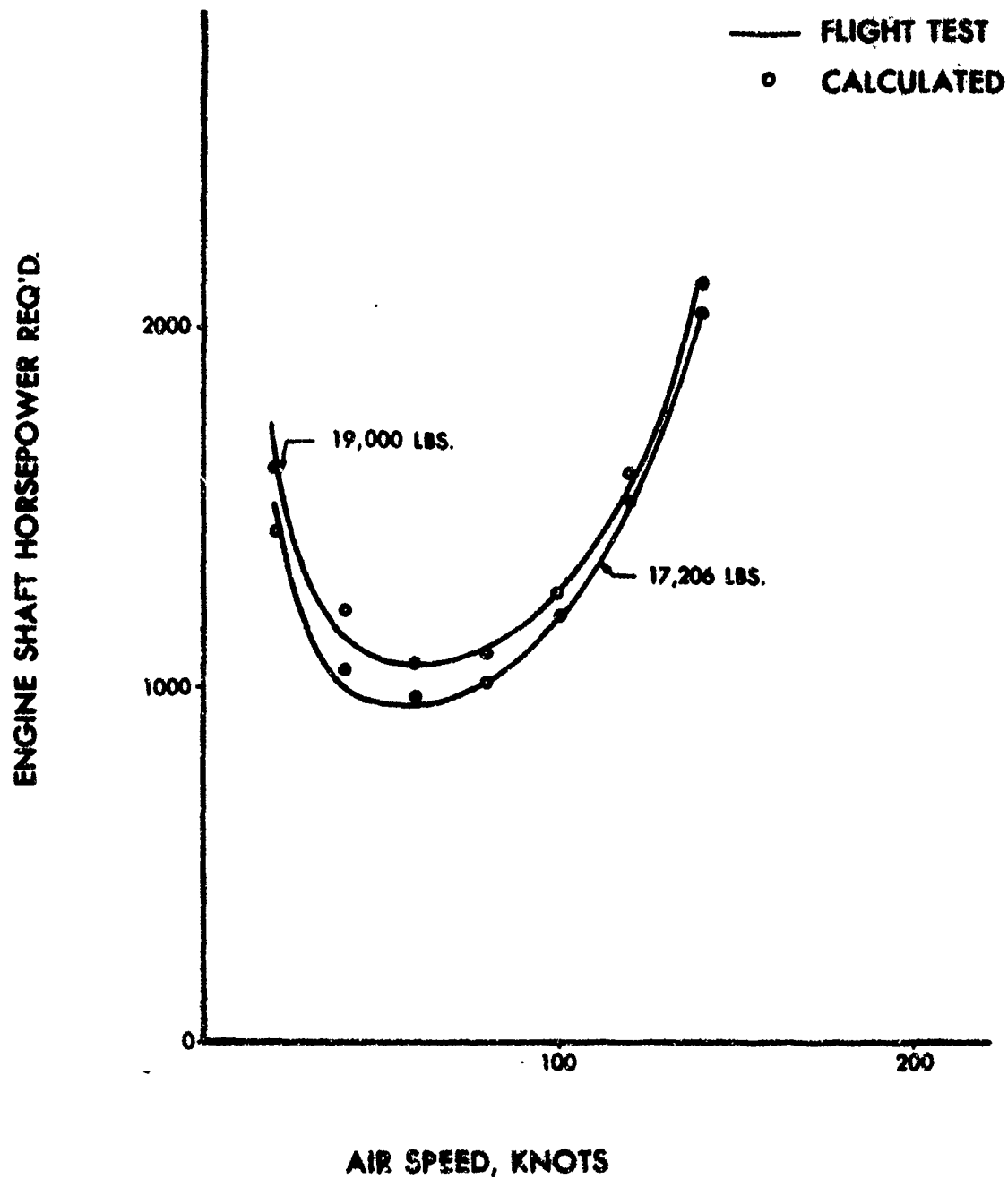


FIGURE 2

S-58 FLATWISE VIBRATORY BENDING MOMENT vs NORMALIZED BLADE RADIUS

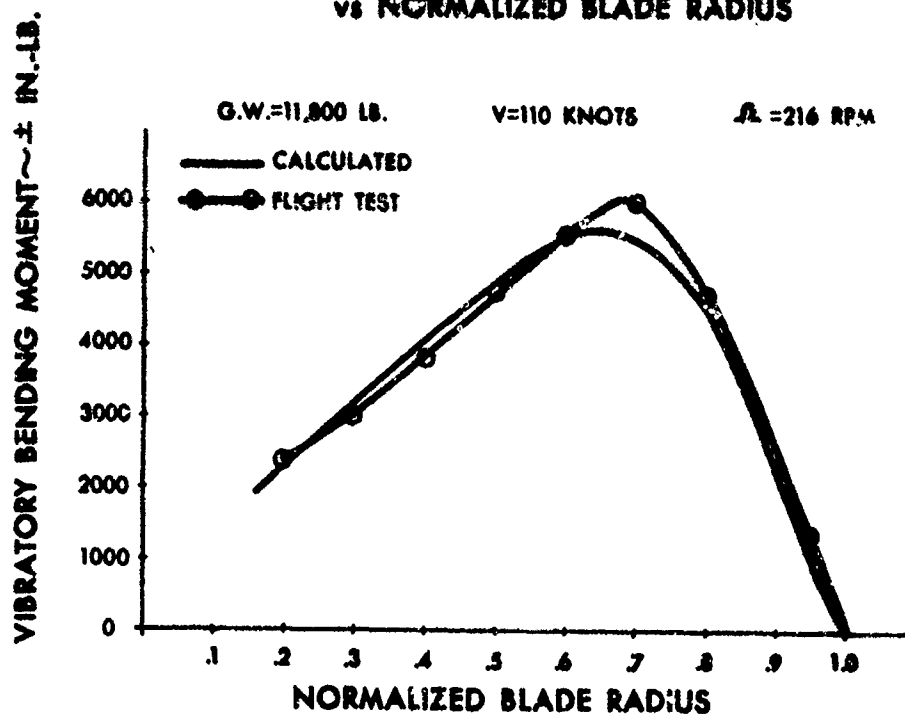


FIGURE 3

MAXIMUM FLATWISE VIBRATORY STRESS vs FORWARD SPEED

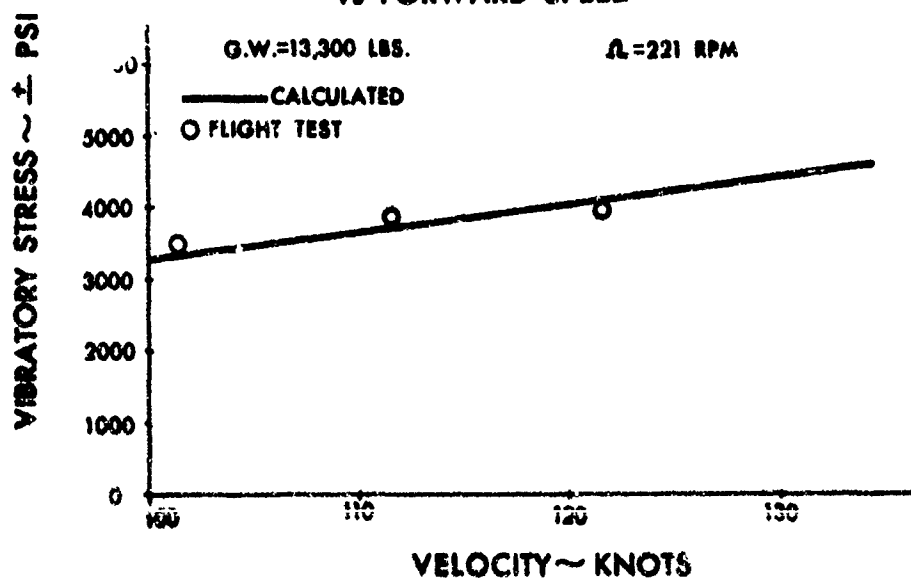


FIGURE 4

BLADE STATIC DEFLECTION CURVE

LOCKHEED CL-475

5.5 lb. wt. AT TIP

△--SIKORSKY PROGRAM

○--LOCKHEED

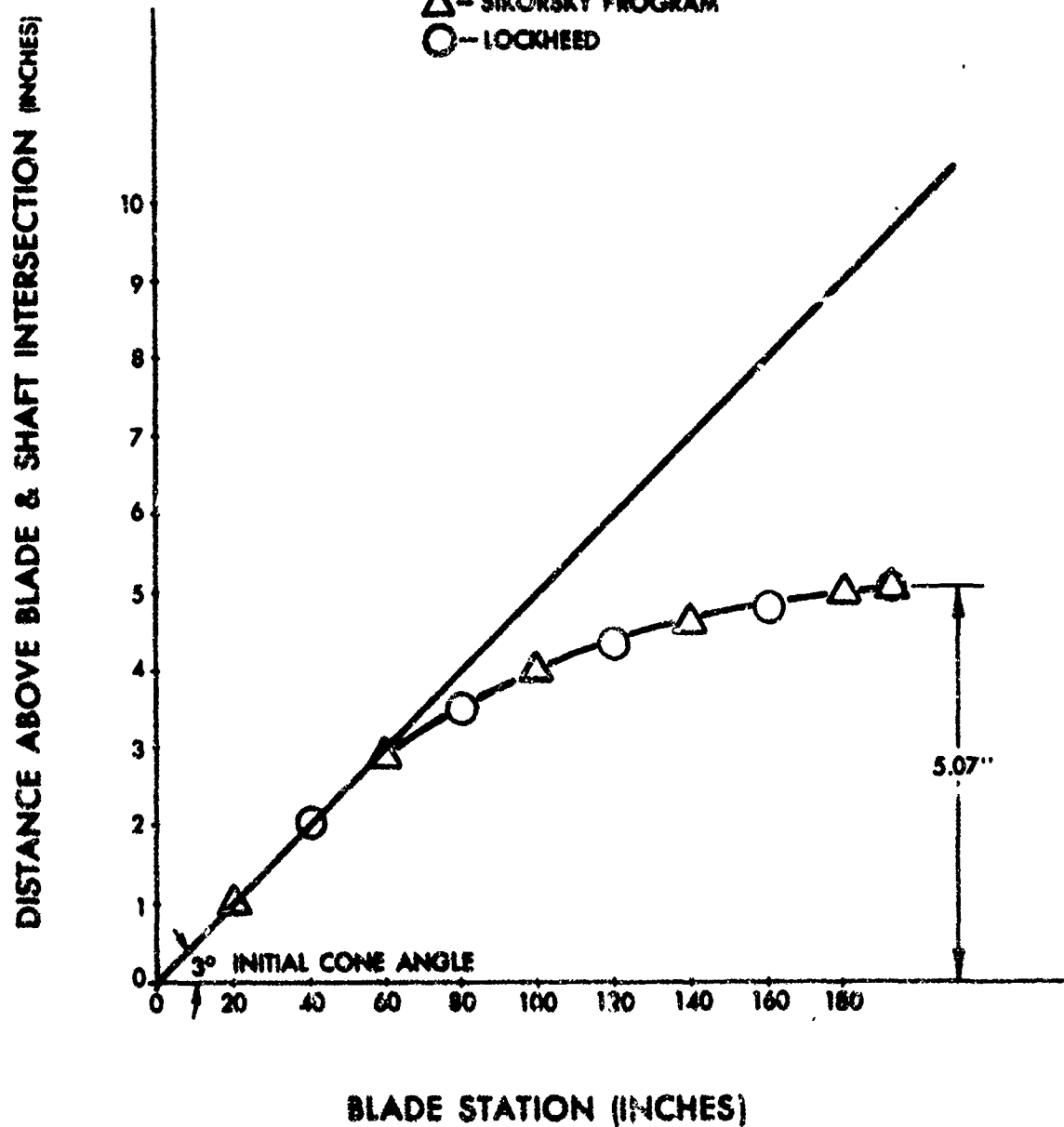


FIGURE 5

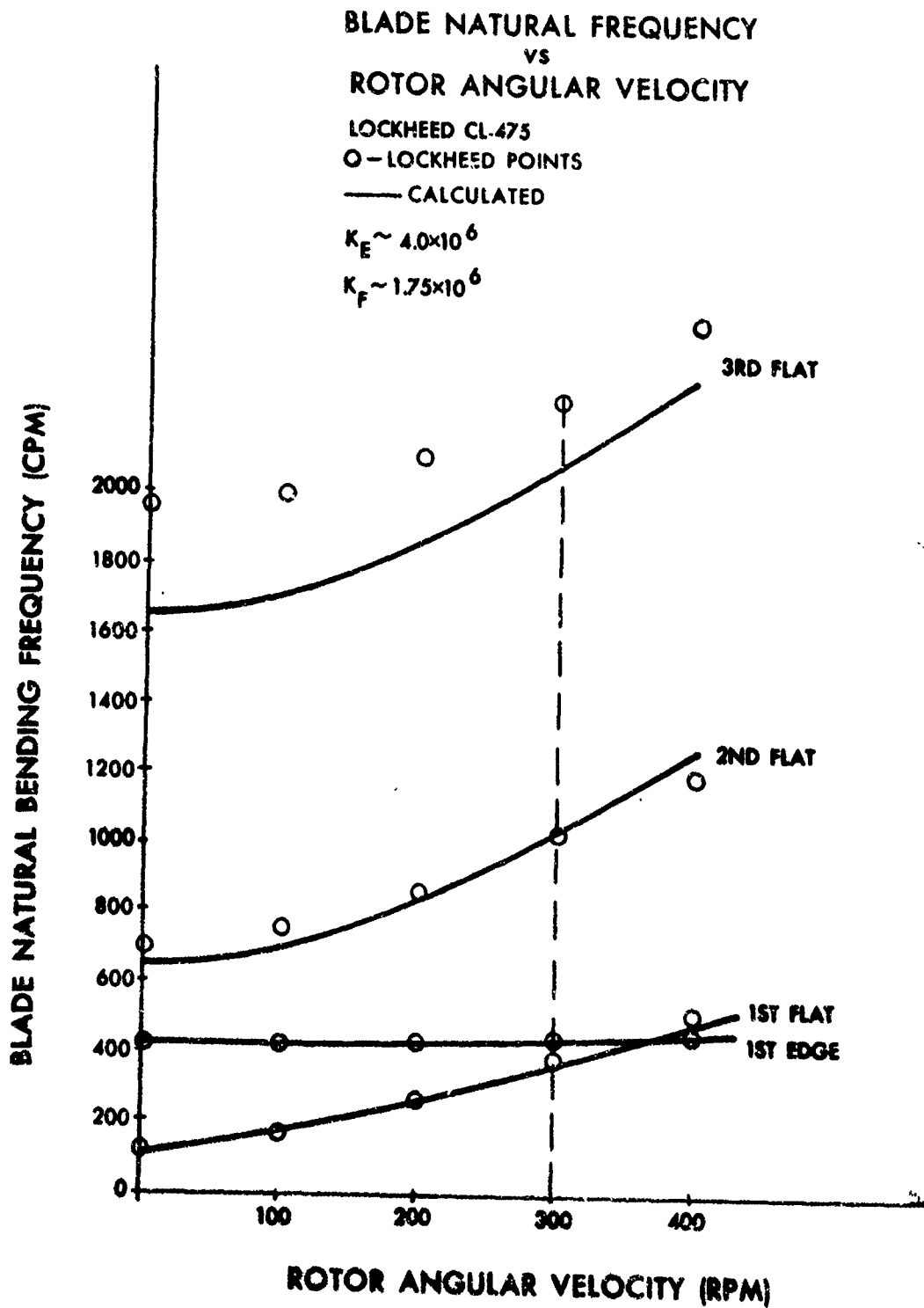


FIGURE 6

FLATWISE BENDING MOMENT vs

BLADE STATION

LOCKHEED CL-475

V=86.84 KNOTS $\Omega=300$ RPM

GROSS WEIGHT= 1975 LB.

— LOCKHEED DATA

--- SIKORSKY PROGRAM

$K^F \sim 1.75 \times 10^6$

$K^E \sim 4.0 \times 10^6$

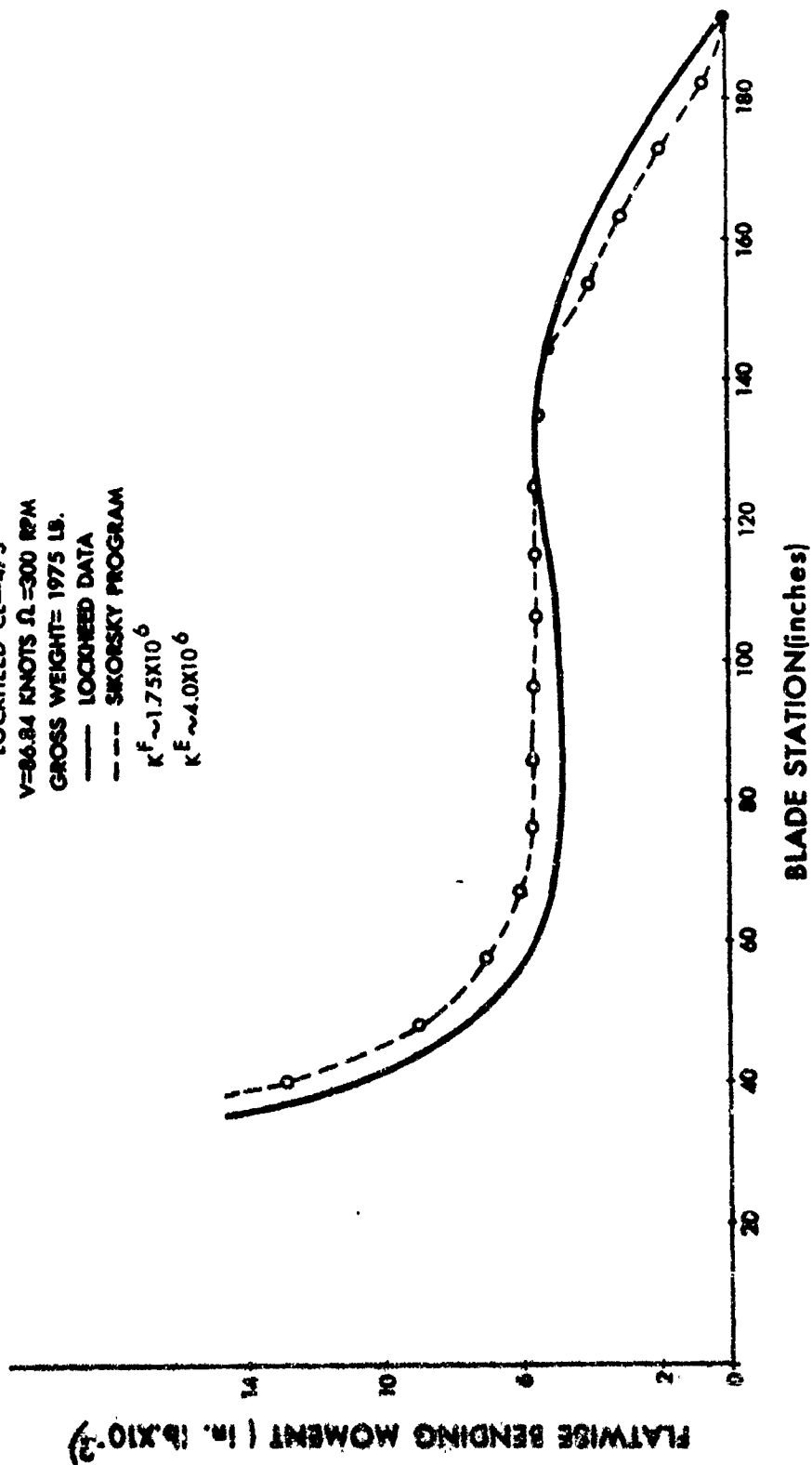


FIGURE 7

EFFECT OF ROOT FLEXIBILITY ON BENDING MOMENTS AND STRESSES CALCULATED FOR LOCKHEED CL-475 HELICOPTER

FLATWISE BENDING MOMENT VS. BLADE RADIUS

ARTICULATED FLATWISE
EDGEWISE SPRING = 4.0×10^6

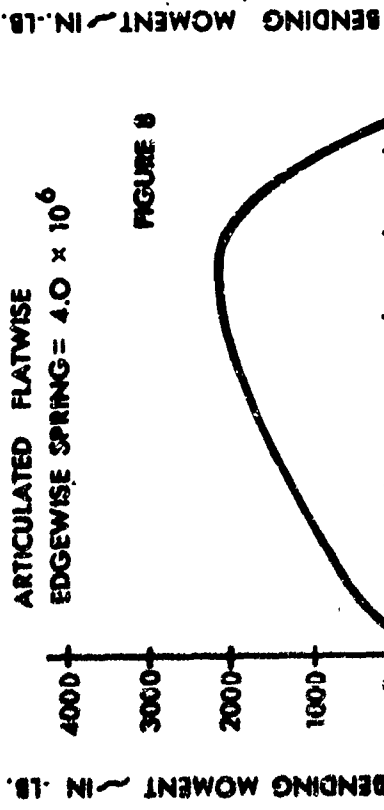


FIGURE 8

FLATWISE BENDING MOMENT VS BLADE RADIUS

FLATWISE SPRING = 2.0×10^5
EDGEWISE SPRING = 4.0×10^6

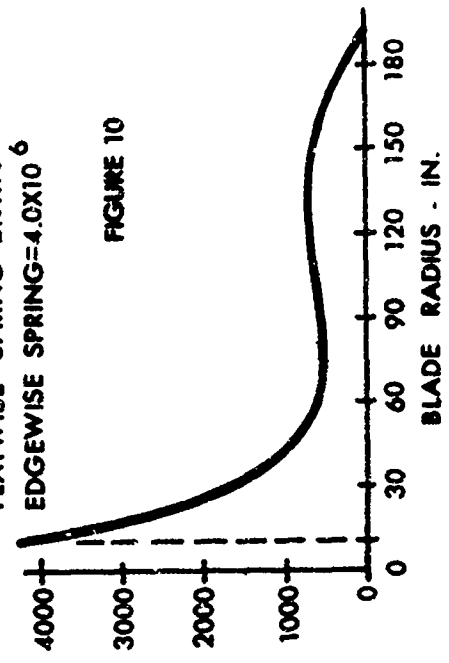


FIGURE 10

FLATWISE BENDING MOMENT VS BLADE RADIUS

CANTILEVERED FLATWISE
EDGEWISE SPRING = 4.0×10^6

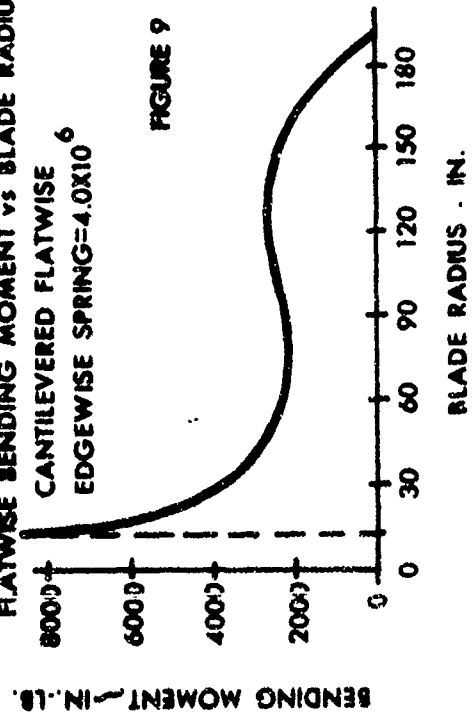


FIGURE 9

EDGEWISE VIBRATORY STRESS VS FREQUENCY RATIO

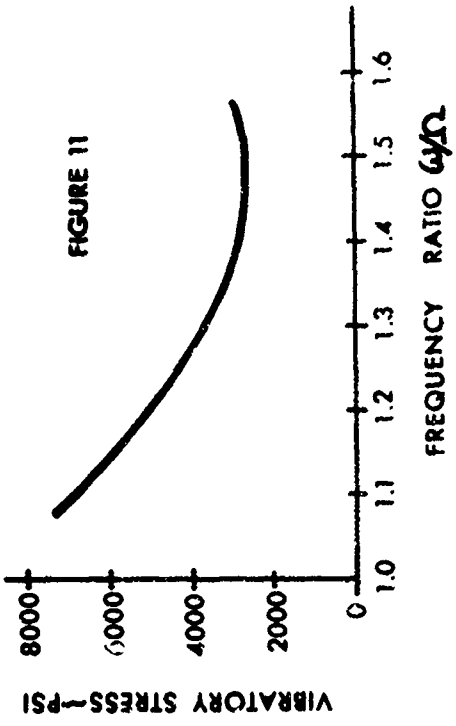


FIGURE 11

13,000 LB. HELICOPTER
ARTICULATED ROTOR
V=150 KT. Ω =203 RPM

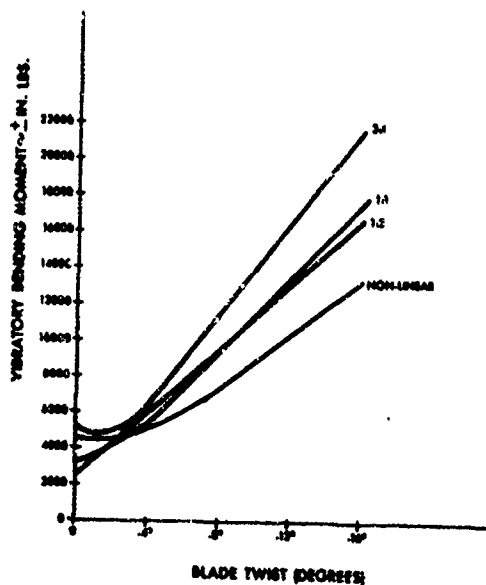


FIGURE 12

12,000 LB. HELICOPTER
RIGID ROTOR
V=150KT. Ω =203 RPM

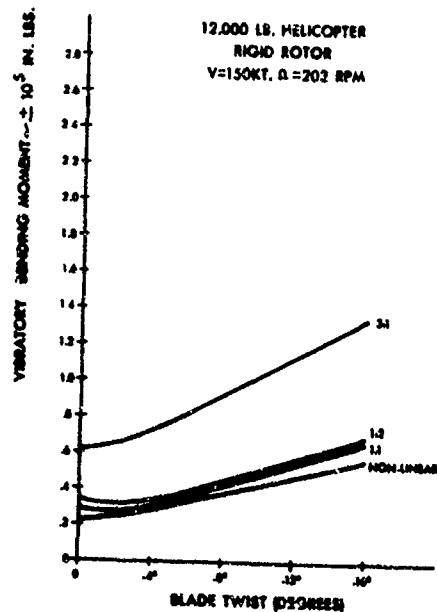


FIGURE 13

33,000 LB. HELICOPTER
ARTICULATED ROTOR
V=180 KT. Ω =165 RPM

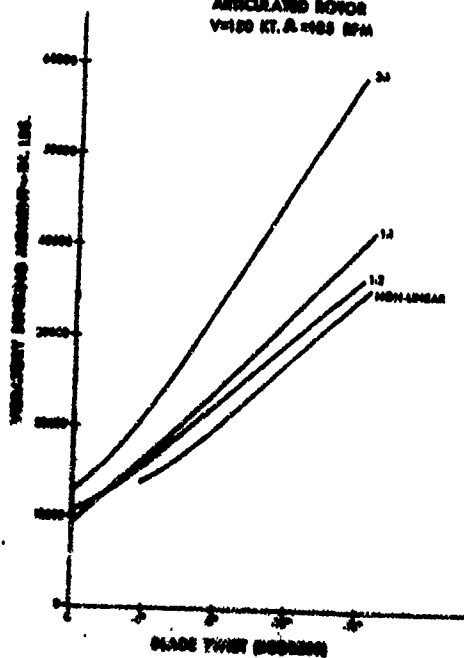


FIGURE 14

33,000 LB. HELICOPTER
RIGID ROTOR
V=180 KT. Ω =165 RPM

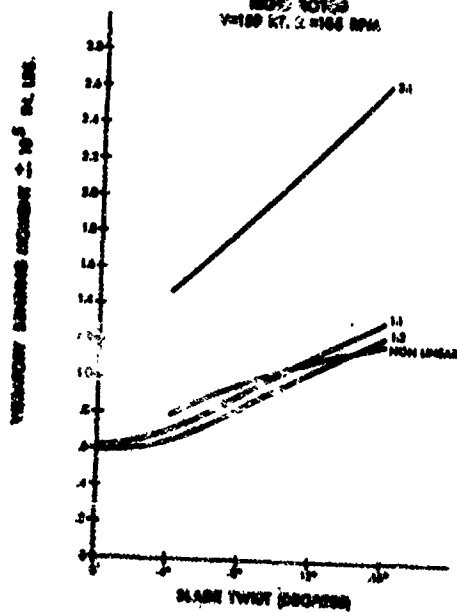


FIGURE 15

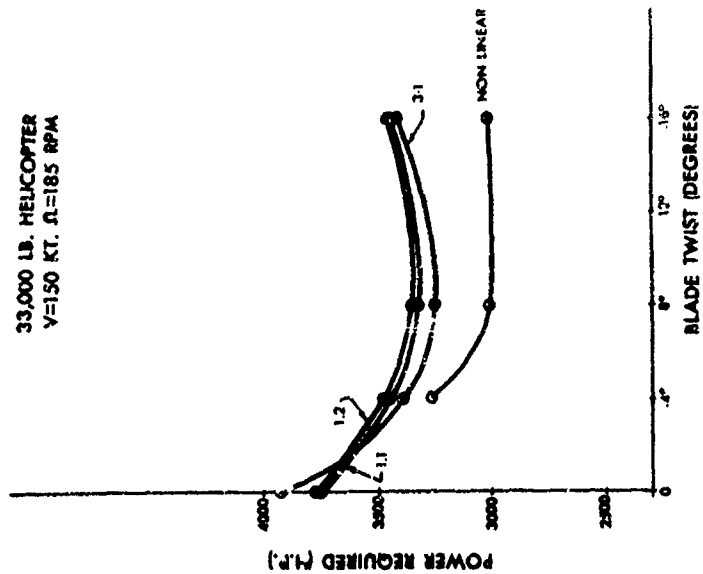


FIGURE 17

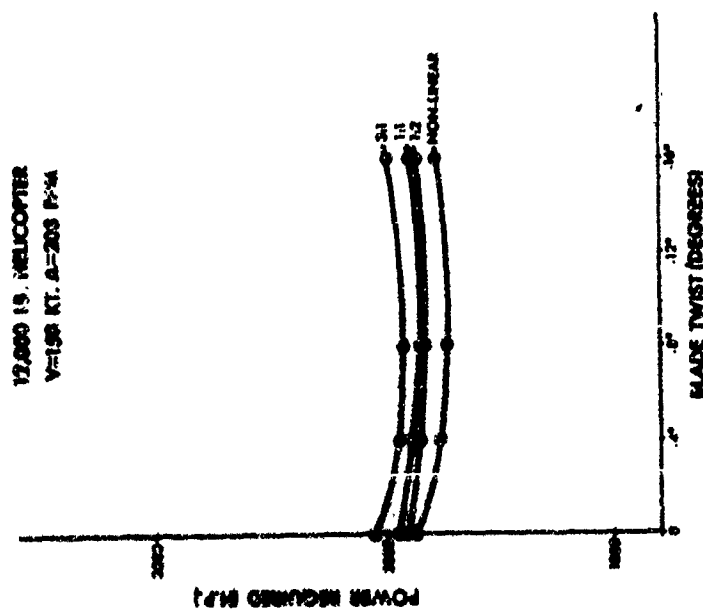
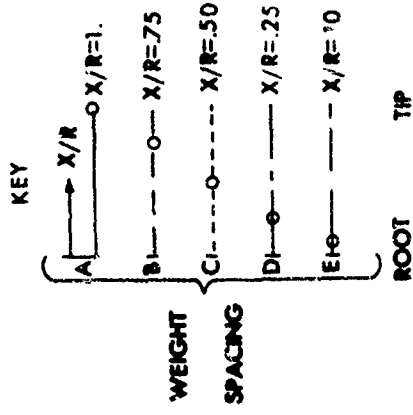
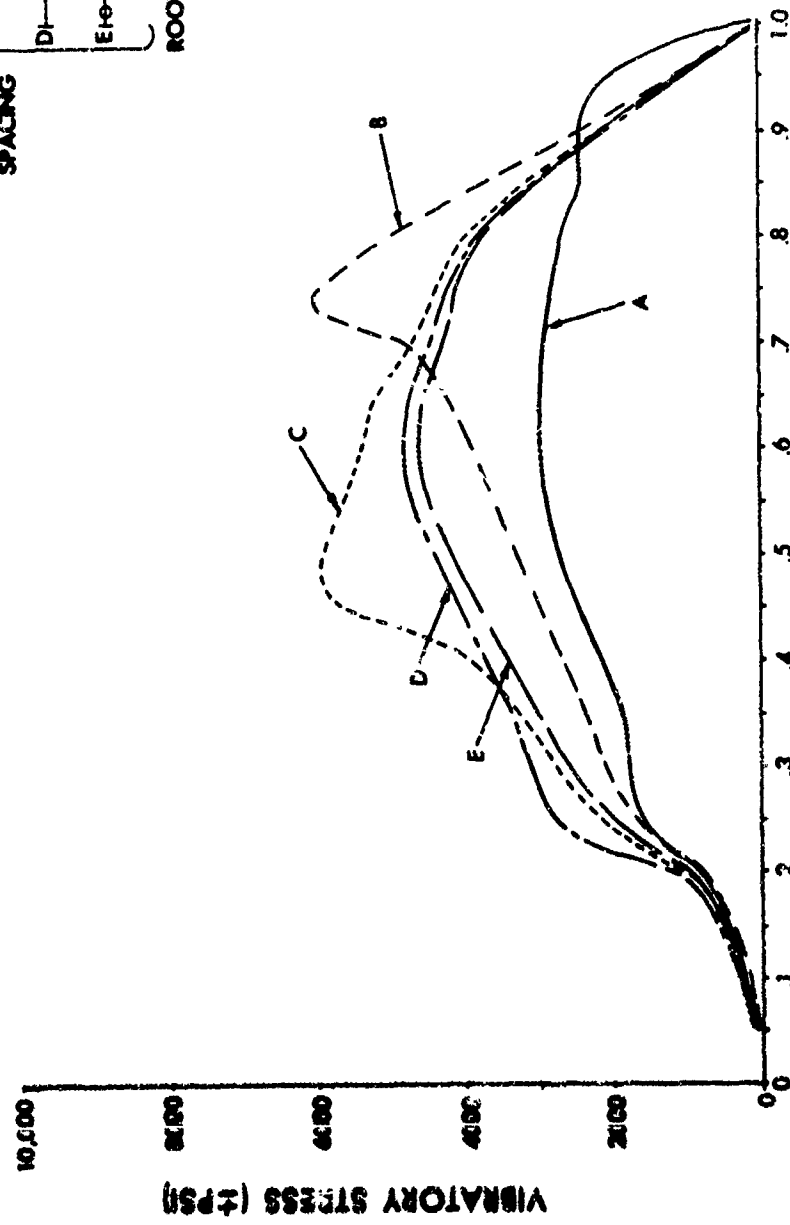


FIGURE 18

EFFECT OF SINGLE 36-LB. WEIGHT ON 1/2 PEAK TO PEAK STRESS

33,000 LB. ARTICULATED HELICOPTER V=150 KNOTS $\Omega=185$ RPM
FLATWISE BENDING



NORMALIZED BLADE RADIUS

FIGURE 18

EFFECT OF SINGLE 36-LB. WEIGHT ON 1/2 PEAK TO PEAK STRESS

33,000-LB. RIGID HELICOPTER V=150 KNOTS $\Omega=185$ RPM
FLATWISE BENDING

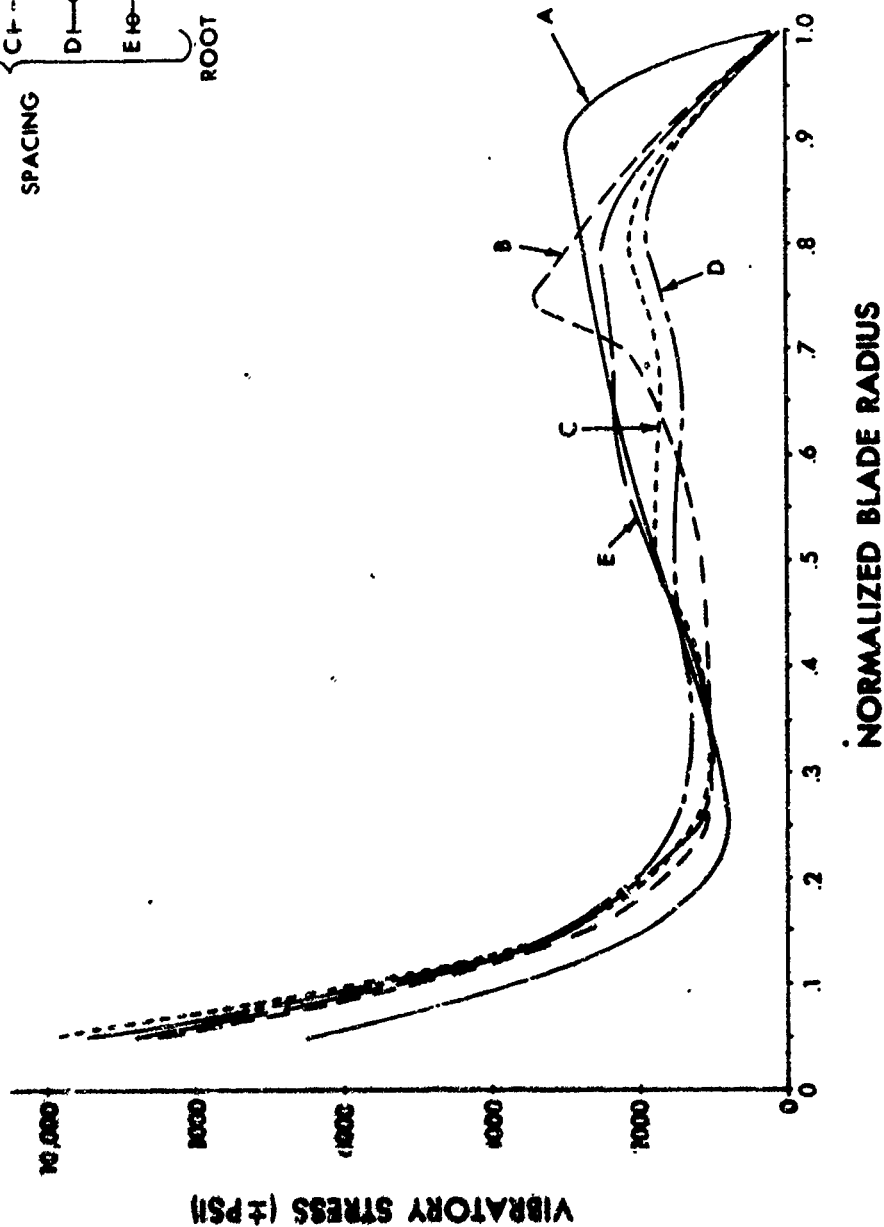
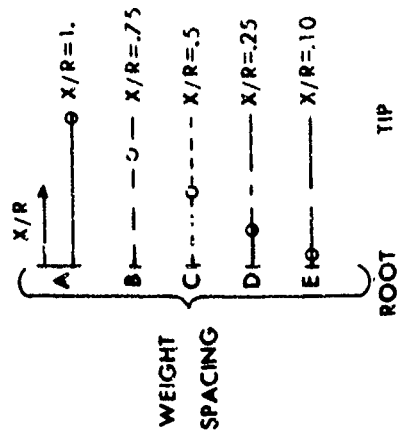


FIGURE 19

VIBRATORY STRESS VS. WEIGHT ADDED AT THE BLADE TIP

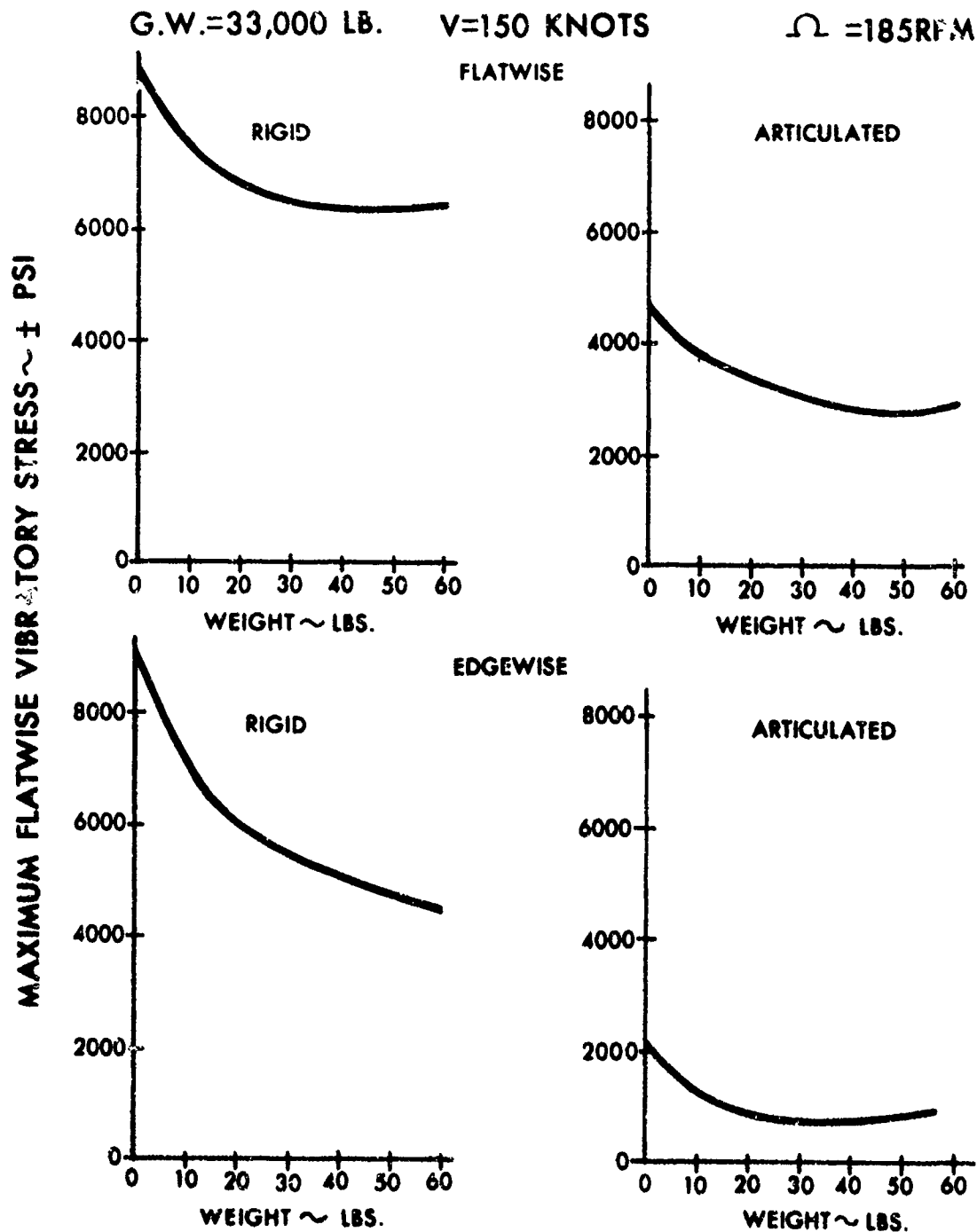


FIGURE 20

EFFECT OF VARIABLE FLATWISE STIFFNESS
ON BENDING MOMENT
V=150 KNOTS G.W.=33,000 LB. Δ =185 RPM
ARTICULATED ROTOR

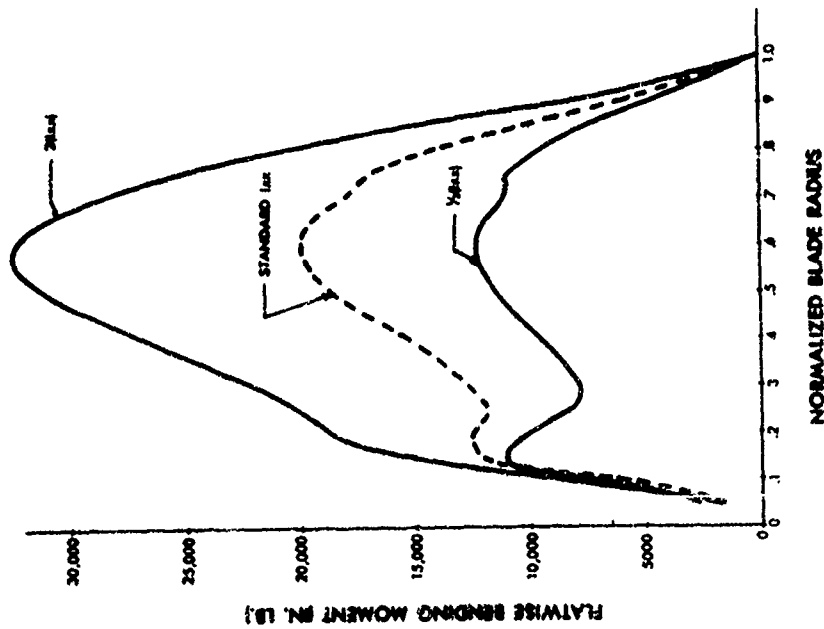


FIGURE 21

EFFECT OF VARIABLE FLATWISE STIFFNESS
ON BENDING MOMENT
V=150 KNOTS G.W.=33,000 LB.
 Δ =185 RPM
RIGID ROTOR

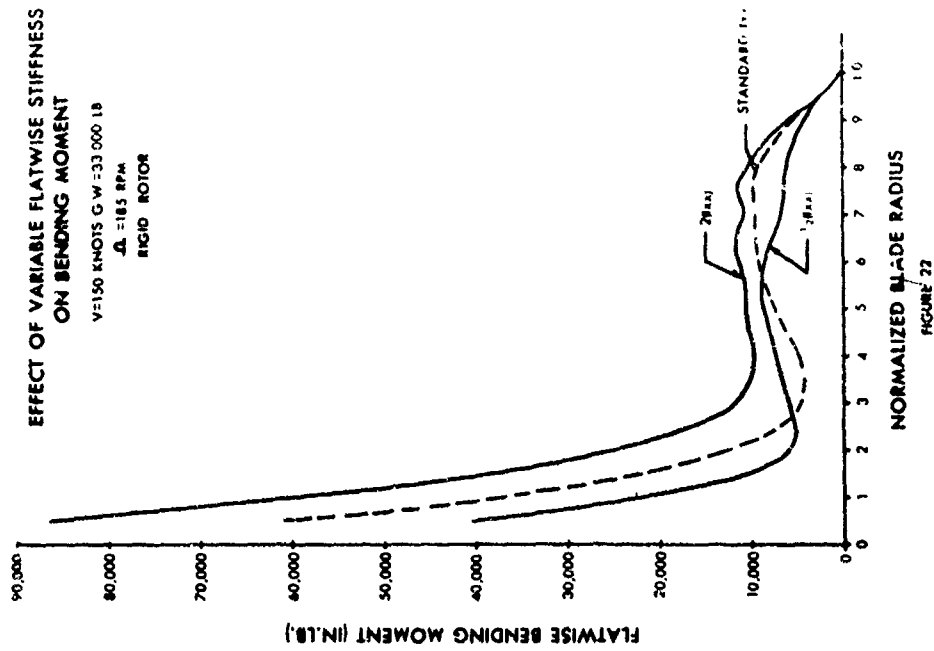


FIGURE 22

EFFECT OF VARIABLE FLATWISE STIFFNESS ON BENDING MOMENT

V=150 KNOTS G.W.=33,000 LB
A=185 MPH
ARTICULATED ROTOR

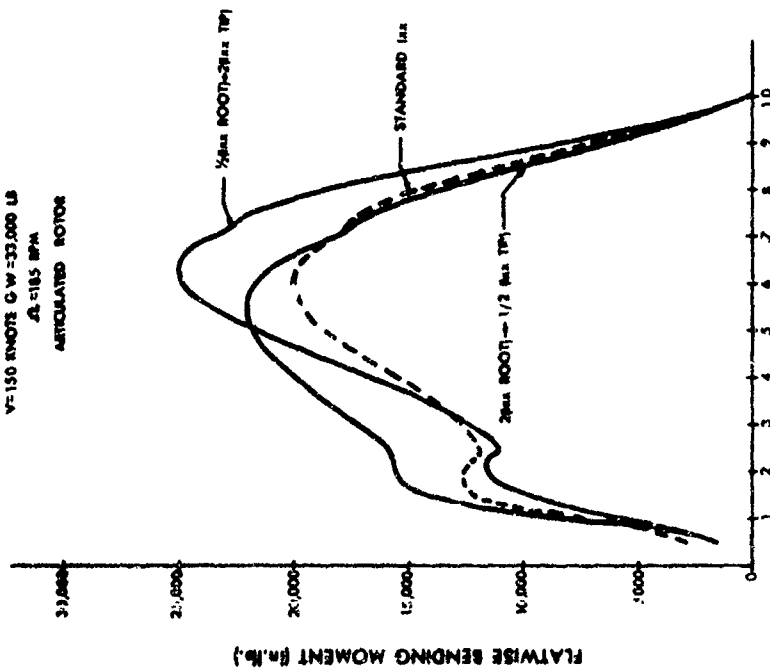


FIGURE 23

EFFECT OF VARIABLE FLATWISE STIFFNESS ON BENDING MOMENT

V=150 KNOTS G.W.=33,000 LB
A=185 MPH
RIGID ROTOR

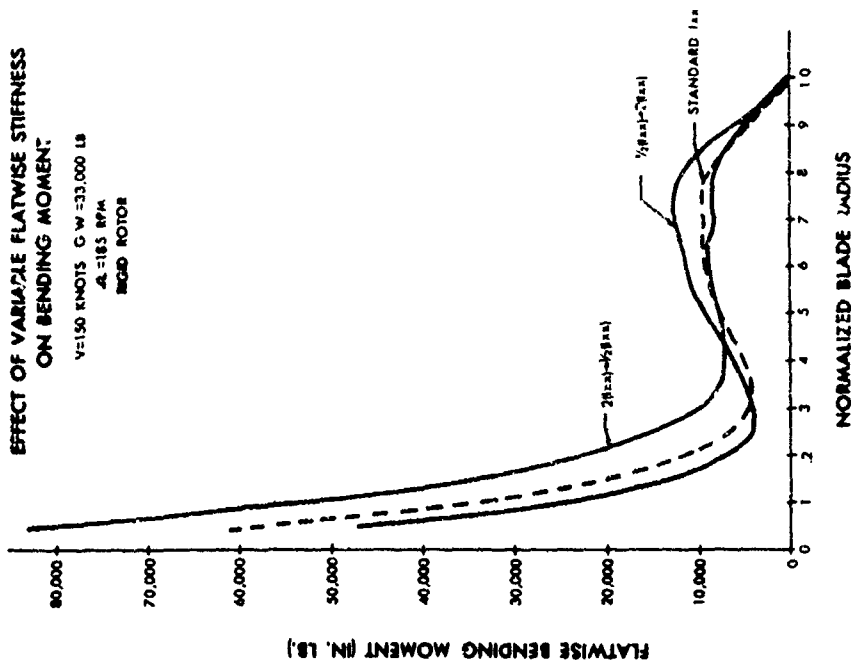


FIGURE 24

COMPOUND HELICOPTER
G.W.=12,000 LB. A=168 RPM

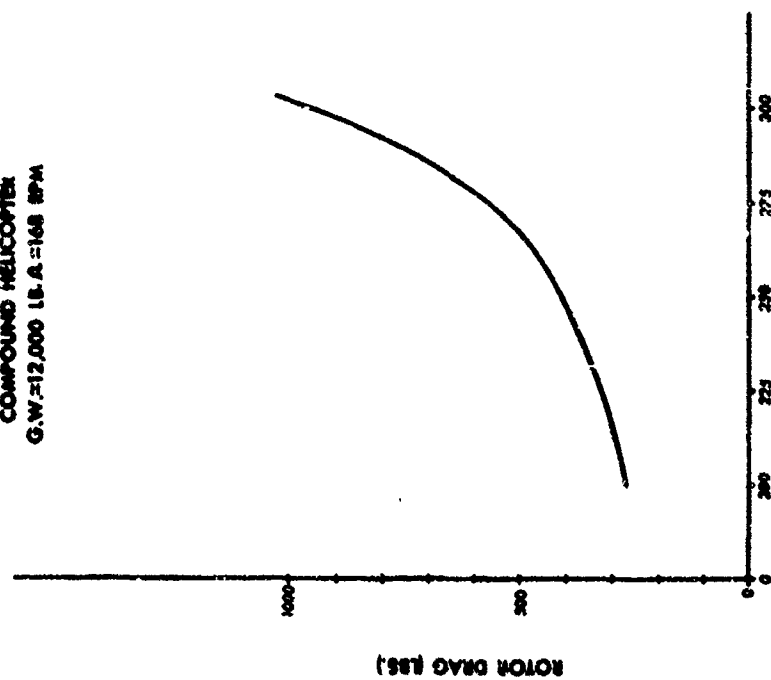


FIGURE 24

COMPOUND HELICOPTER
G.W.=12,000 LB. A=168 RPM

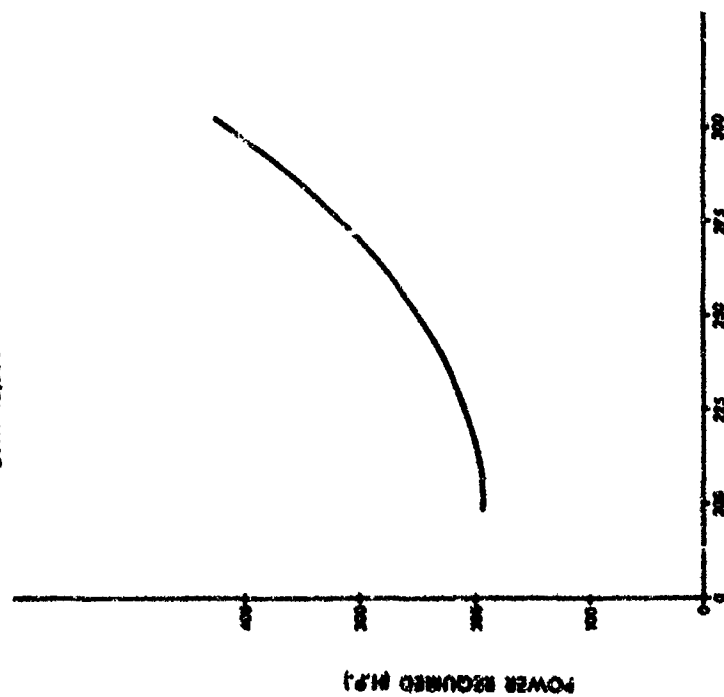


FIGURE 25

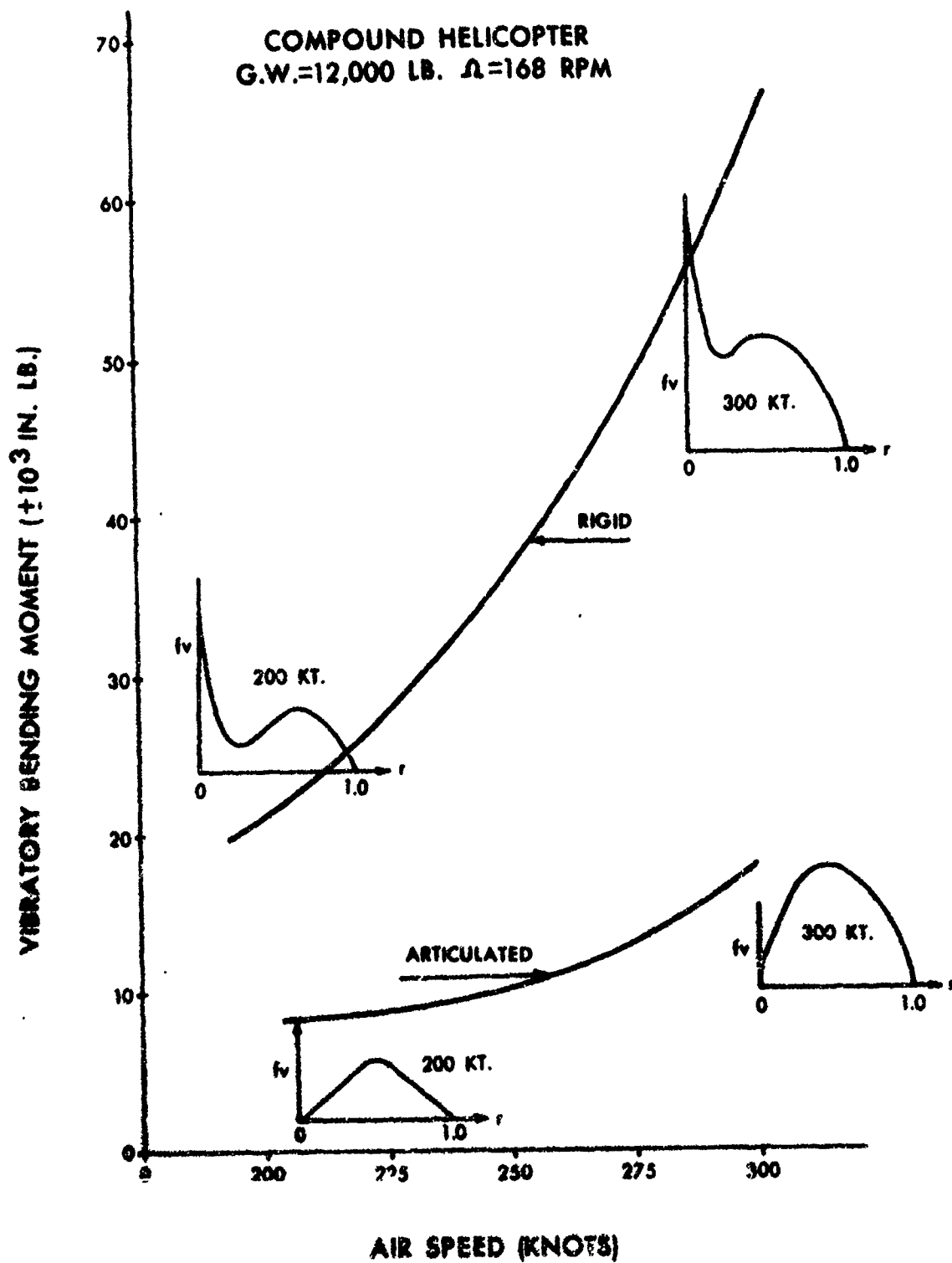


FIGURE 27

**IN-FLIGHT MEASUREMENT OF STEADY AND
OSCILLATORY ROTOR SHAFT LOADS**

R. Gabel

Vertol Division, Boeing Aircraft

IN-FLIGHT MEASUREMENT OF STEADY AND OSCILLATORY ROTOR SHAFT LOADS

Introduction

A set of comprehensive test data on alternating shaft loads is an obvious necessity in the development of improved methods for calculating such loads. A program of in-flight shaft load measurement was conducted as part of an overall vibration research effort sponsored by the Army and Air Force under Contract AF 33(616)-5240 and published as ASD-TDR-62-284. This paper describes the load measurement system and the results obtained from the flight tests.

Load Measurement System

This development of a shaft load measurement system represented a culmination of several previous attempts with very limited success. However, from the results of the previous pioneering attempts it was evident that the best approach lay in further development of the shaft strain measurement system which had been used previously. Additional work indicated that through the use of (1) strain gages with high sensitivity, (2) high voltage in the strain gage bridges, (3) an improved bridge network, and (4) separate load measuring systems for the steady and alternating components of both lift and torque, the desired sensitivity and accuracies could be achieved.

An H-21 helicopter was equipped with strain gages, as illustrated in Figure 1, to measure the following loads.

Forward and aft transmission and rotor shafts:

1. F_x , shear in the rotor plane in the direction of the master spline.
2. F_y , shear in the rotor plane in the direction normal to the master spline.
3. M_x , moment in the rotor plane, about the rotating X axis.
4. M_y , moment in the rotor plane, about the rotating Y axis.
5. F_z , lift force in the shaft vertical direction.
6. M_z , torque about the shaft axis.

A developed view of the rotor shaft strain gage instrumentation is shown in Figure 2.

Load Calibration

Load calibration of the instrumented forward and aft rotor shaft was performed in a specially constructed fixture, and known loads were applied individually at the hub in all directions. Incremental loads were applied

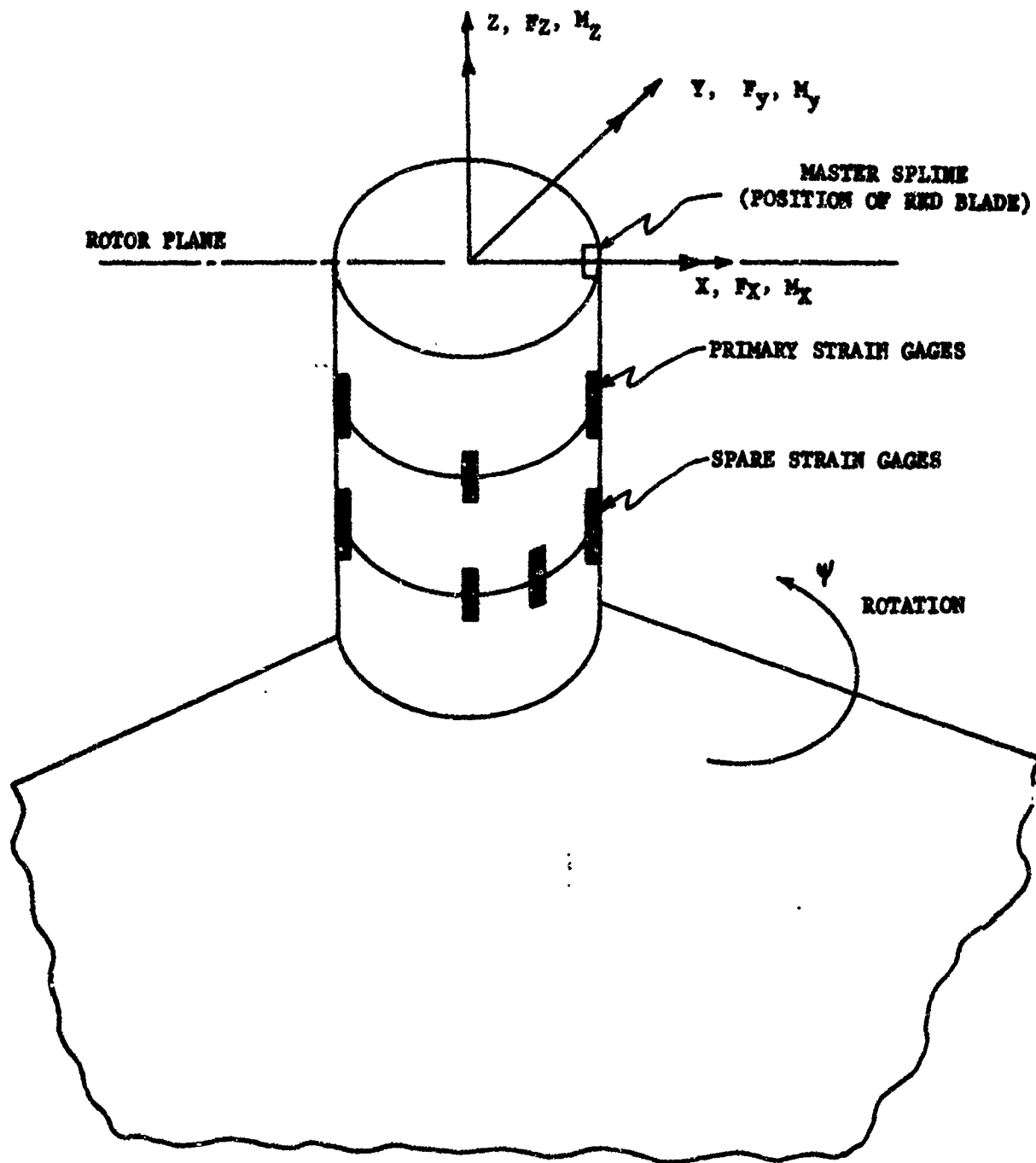


FIGURE 1. SHAFT STRAIN GAGES

DEVELOPMENT OF SHAFT

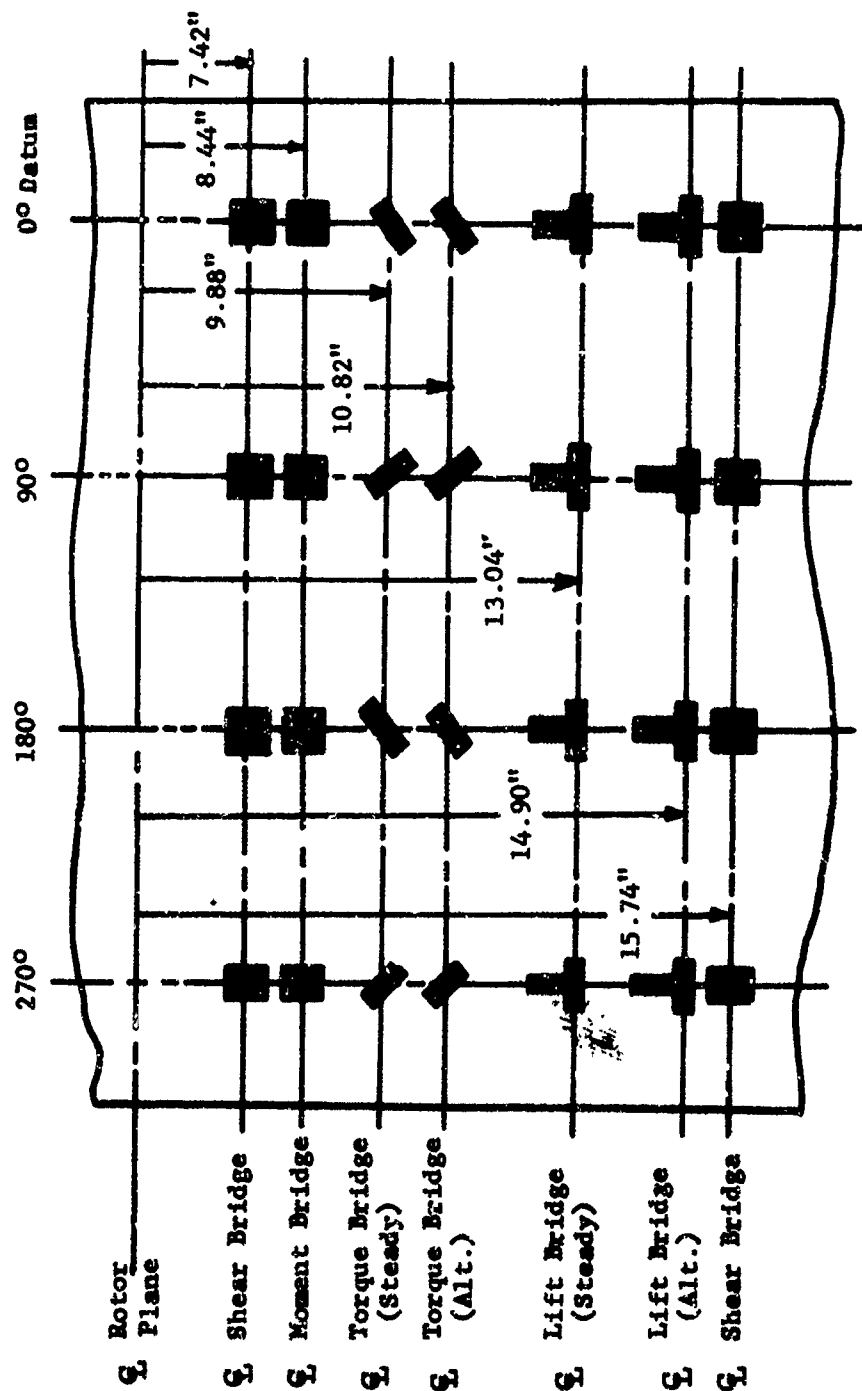
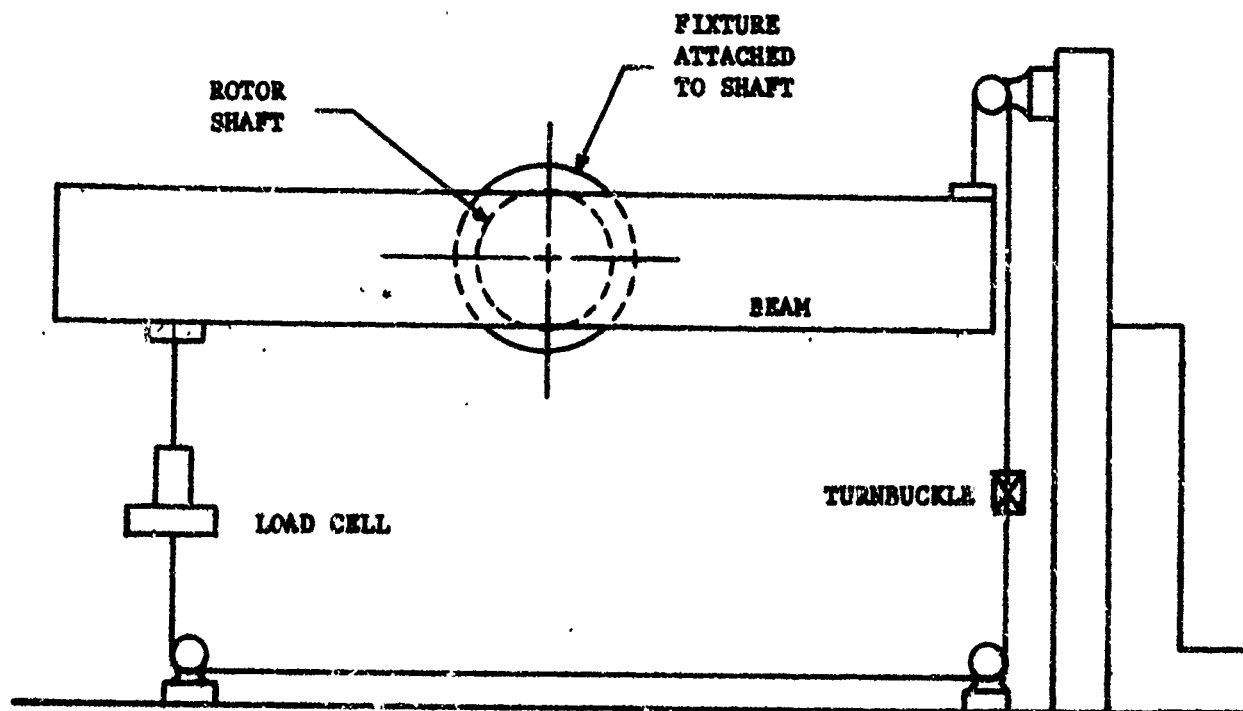


FIGURE 2. ROTOR SHAFT STRAIN INSTRUMENTATION

to the shaft and the output of all gages to each load was recorded, regardless of the direction of the loads, in order to obtain interaction as well as primary load calibration factors.

Torque - Initially, the torque calibration used a load balance system as shown in the lower half of Figure 3, but this system was replaced by a closed loop system to improve the accuracy. Final torque calibration was performed using the test setup shown in the upper half of Figure 3. A schematic of this loading system showing the closed loop cable arrangement is given below.



The torque calibration was performed using the turnbuckle to apply the incremental cable tension in combination with a load cell for measuring the applied load.

Lift - Lift calibration loads were applied with the hydraulic jack shown in Figure 4. Accurate alignment of the load through the center of the shaft was established using an optical system consisting of a sighting scope and target. In the calibration, the incremental loads applied to the shaft were in addition to the mean lift load simulating the aircraft weight.



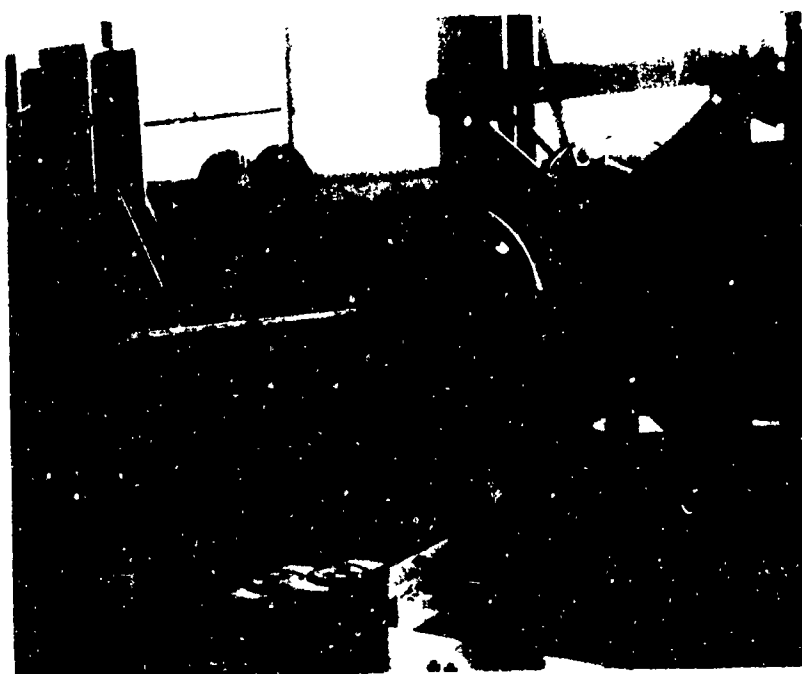
TORQUE LOADING
CLOSED LOOP CABLE LOAD SYSTEM



TORQUE LOADING
EXTERNAL WEIGHT COUPLE LOAD SYSTEM
FIGURE 3. ROTOR SHAFT CALIBRATION
TORQUE LOADING



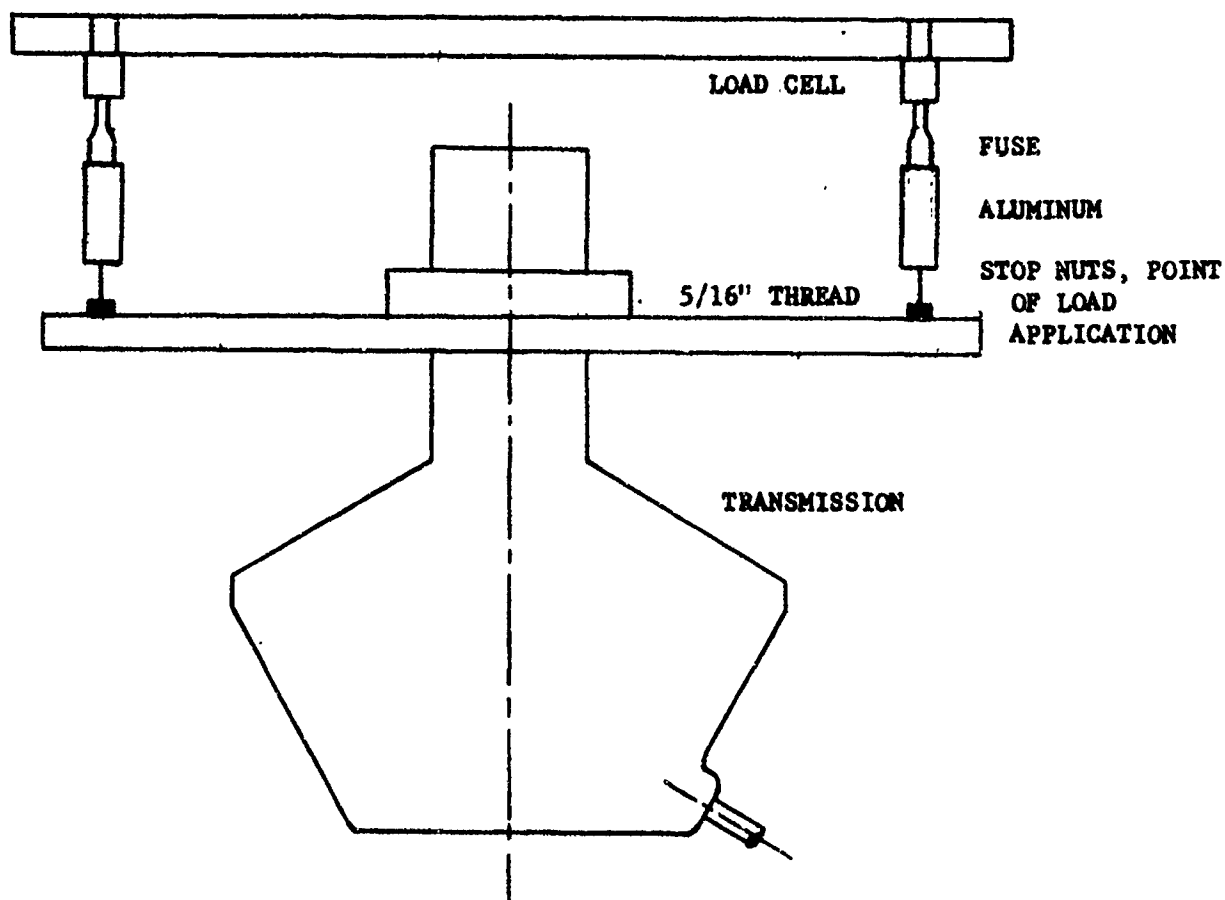
LIFT LOADING
HYDRAULIC JACK



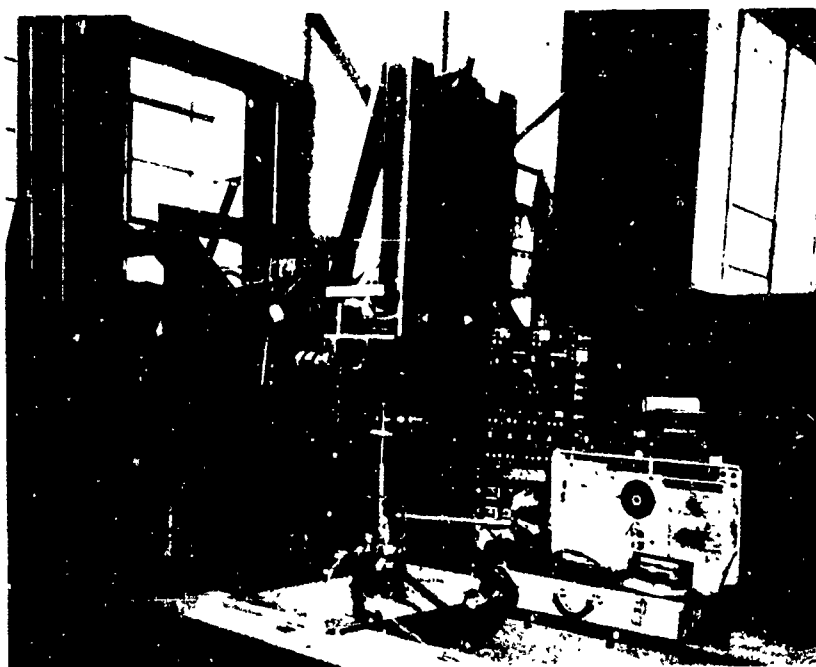
LIFT LOADING
LIFT LOAD AT ROTOR SHAFT
FIGURE 4. ROTOR SHAFT CALIBRATION
LIFT LOADING

Shear - Application of shear loads for calibration of the strain gage bridges was performed as shown in Figure 5. Rotor shaft shear loads were applied using a hydraulic jack mounted at its base on a ball-joint to insure loading through the center line of the shaft. In order to obtain calibration curves for both of the shear bridges used in the test, the shaft was loaded on the 0° - 180° axis in addition to the 90° - 270° axis.

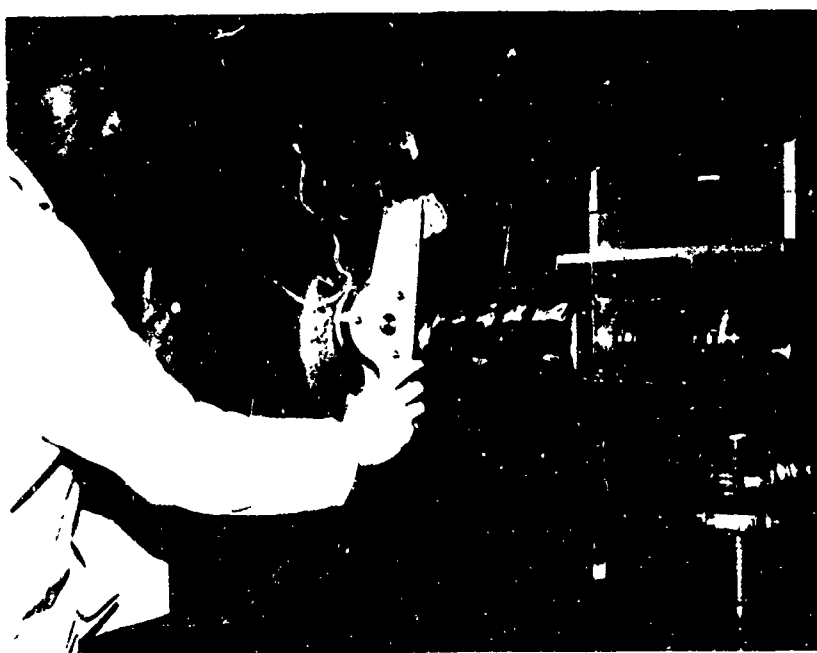
Moment - Calibration loads for bending moment were imposed on the rotor shaft using the test arrangement shown below,



Using the load cells located at each end of the moment arm permitted one side to be loaded in tension while the other was in compression, thus producing a pure moment at the centerline of the shaft. Calibrations were performed for the M_{xx} bending bridges by applying equal tension and compression loads along the axis; the M_{yy} bending bridges were calibrated in the same manner after the shaft had been rotated 90° .



SHEAR LOADING
HYDRAULIC JACK LOAD SYSTEM AND LOAD CELL



SHEAR LOADING
INCLINOMETER CHECK
FIGURE 5. ROTOR SHAFT CALIBRATION
SHEAR LOADING

Load Interaction - A typical calibration chart is illustrated in Figure 6 for shear load. The calibration constant for shear load (90° - 270°) is obtained by dividing the load variation (1200# - 0) by the trace deflection (364-210) counts.

$$K = \frac{1200\#}{154 \text{ cts}} \times \frac{131 \text{ cts}}{\text{in. trace}} = 1040 \#/\text{in.}$$

This chart indicates that, as intended, the predominant gage response occurs between the applied shear load and the strain gage bridge representing shear. This is the pair of bending gages which are wired together to measure differential moment, and designated as a shear bridge. It is also apparent that other gages respond which are not in the direction of the calibration load. Such side effect may be due to an unfavorable location of a particular gage with respect to a load direction it is not intended to measure, or due to Poisson's ratio effect. These side effects are accounted for by an "Interaction Matrix" which also contains the main load calibration. This matrix is the complete relationship between the measurement and the loads on the shaft in all directions at the rotor plane. This result is an interaction matrix of the form,

$$\begin{bmatrix} \bar{F}_X \\ \bar{F}_Y \\ \bar{F}_Z \\ \bar{M}_\alpha \\ \bar{M}_\beta \\ \bar{M}_\gamma \end{bmatrix} = \begin{bmatrix} i_{ax} & i_{ay} & i_{az} & i_{a\alpha} & i_{a\beta} & i_{a\gamma} \\ i_{bx} & i_{by} & i_{bz} & i_{b\alpha} & i_{b\beta} & i_{b\gamma} \\ i_{cx} & i_{cy} & i_{cz} & i_{c\alpha} & i_{c\beta} & i_{c\gamma} \\ i_{dx} & i_{dy} & i_{dz} & i_{d\alpha} & i_{d\beta} & i_{d\gamma} \\ i_{ex} & i_{ey} & i_{ez} & i_{e\alpha} & i_{e\beta} & i_{e\gamma} \\ i_{fx} & i_{fy} & i_{fz} & i_{f\alpha} & i_{f\beta} & i_{f\gamma} \end{bmatrix} \cdot \begin{bmatrix} F_X \\ F_Y \\ F_Z \\ M_\alpha \\ M_\beta \\ M_\gamma \end{bmatrix}$$

F_X, F_Y, F_Z = actual loads in the X, Y, Z direction

M_X, M_Y, M_Z = actual moments about the X, Y, Z axes

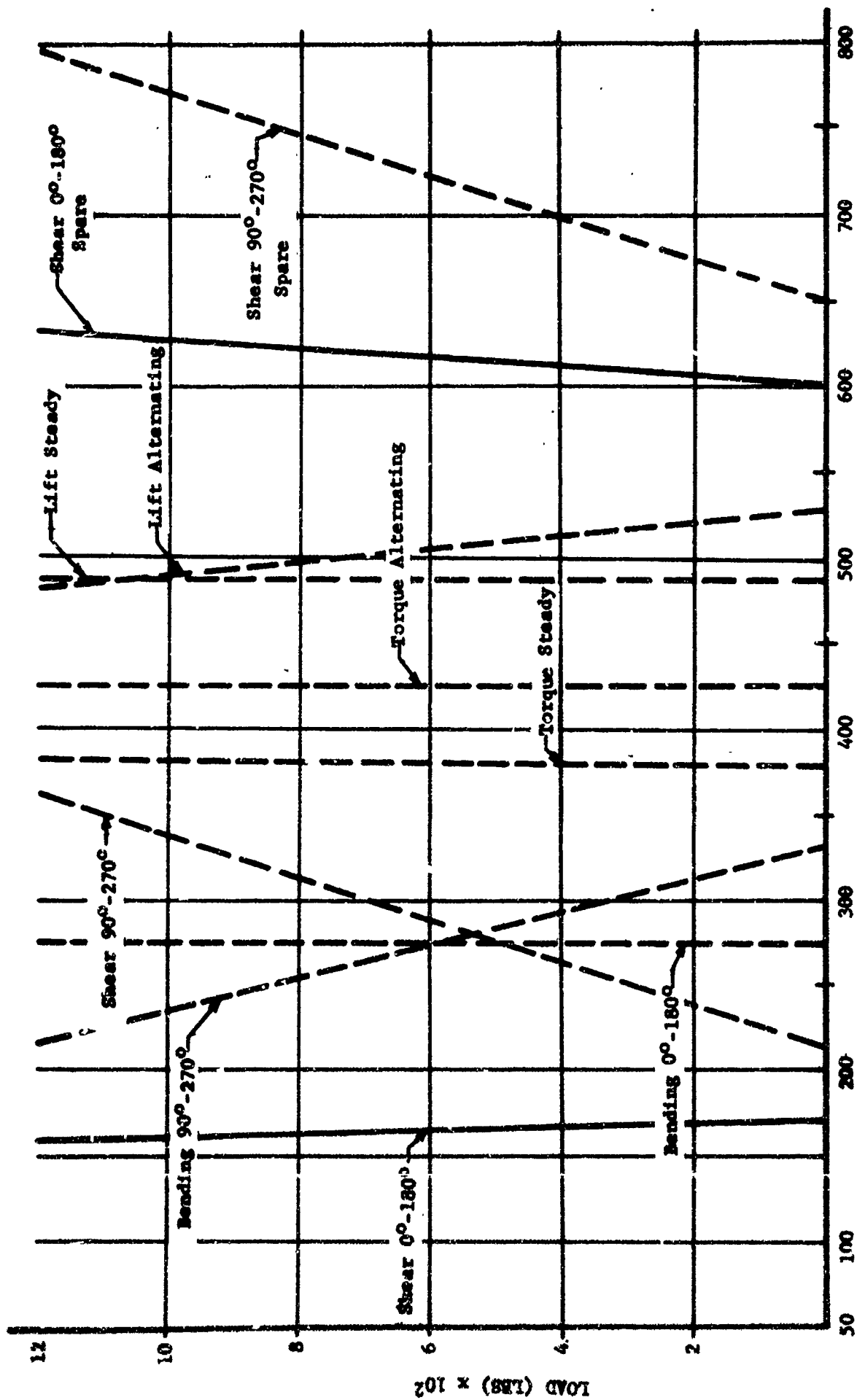
i_{ax}, i_{ay}, i_{az} = interaction of gage "a" to unit X, Y, Z forces

$i_{a\alpha}, i_{a\beta}, i_{a\gamma}$ = interaction of gage "a" to unit α, β, γ moments

$\bar{F}_X, \bar{F}_Y, \bar{F}_Z$ = apparent forces from the strain measurements

$\bar{M}_\alpha, \bar{M}_\beta, \bar{M}_\gamma$ = apparent moments from the strain measurements

The numerical interaction matrices from the load calibration are shown below.



TRACE DEFLECTION IN COUNTS 131 COUNTS = ONE INCH

FIGURE 6. ROTOR SHAFT LOADS CALIBRATION
SHEAR (90° - 270°)

Steady Loads

$$\begin{bmatrix} F_X \\ F_Y \\ F_Z \\ M_X \\ M_Y \\ M_Z \end{bmatrix}_{\text{Measured}} = \begin{bmatrix} 1 & +0.0633 & +0.0021 & +0.0001 & -0.0089 & -0.0016 \\ -0.1171 & 1 & +0.0010 & +0.0067 & -0.0030 & +0.0006 \\ -0.0379 & +0.0416 & 1 & +0.0015 & +0.0091 & -0.0151 \\ 0 & -9.517 & -0.0124 & 1 & -0.0104 & +0.0005 \\ +9.415 & -0.0256 & +0.0881 & +0.0156 & 1 & +0.0074 \\ -0.0858 & -0.0144 & -0.0068 & -0.0205 & -0.0331 & 1 \end{bmatrix} \cdot \begin{bmatrix} F_X \\ F_Y \\ F_Z \\ M_X \\ M_Y \\ M_Z \end{bmatrix}_{\text{Actual}}$$

Alternating Loads

$$\begin{bmatrix} F_X \\ F_Y \\ F_Z \\ M_X \\ M_Y \\ M_Z \end{bmatrix}_{\text{Measured}} = \begin{bmatrix} 1 & +0.0633 & +0.0021 & +0.0001 & -0.0089 & -0.0016 \\ -0.1171 & 1 & +0.0010 & +0.0067 & -0.0030 & +0.0006 \\ +0.0583 & +0.1008 & 1 & +0.0052 & -0.0088 & +0.0029 \\ 0 & -9.517 & -0.0124 & 1 & -0.0104 & +0.0005 \\ +9.415 & -0.0256 & +0.0881 & +0.0156 & 1 & +0.0074 \\ -0.1567 & +0.1142 & -0.0343 & -0.0289 & -0.0467 & 1 \end{bmatrix} \cdot \begin{bmatrix} F_X \\ F_Y \\ F_Z \\ M_X \\ M_Y \\ M_Z \end{bmatrix}_{\text{Actual}}$$

It is noted that the interaction matrices for the steady and alternating loads are composed of the same elements in the rows and columns involving interaction between the shear and bending moment. However, the elements associated with lift and torque loads usually exhibit unlike elements, partly resulting from the nonlinear load characteristics existing between the steady and alternating load ranges used in the calibration, and partly because independent strain gage bridges were used for the steady and alternating lift and torque loads.

Instrumentation Evaluation

Rotor Test Stand - Following the load calibration, the aft transmission was installed on the rotor stand with a standard H-21 hub, wood rotor blade, and complete upper control system. The purpose of this test was to evaluate the reliability and accuracy of the system under operating conditions.

With the full strain recording system operative, the rotor was whirled through a full range of rotor speeds from 240 to 278 rpm, varying collective pitch setting from flat pitch to 12°, with three cyclic pitch settings. The data obtained from this test showed that the strain gage system was operating satisfactorily.

Accuracy Estimate - The results of the primary load calibration are tabulated below, along with an estimate of the load through-record accuracy based on an assumed oscillograph trace reading error of ± 0.02 inches.

Item	Trace Calibration Factor	Estimated Reading Accuracy @ ± 0.02 "	Estimated Overall Accuracy	Typical Load Value	% Accuracy
F _X	1,000 lb/in.	± 20 lb	± 36 lb	1,000 lb	4
F _Y	1,115 lb/in.	± 22 lb	± 36 lb	1,000 lb	4
F _Z Steady	6,050 lb/in.	± 120 lb	± 360 lb	7,000 lb	5
F _Z Alt.	721 lb/in.	± 20 lb	± 30 lb	500 lb	6
M _X	22,050 $\frac{\text{in. lb}}{\text{in.}}$	± 440 in. lb	± 500 in. lb	5,000 in. lb	10
M _Y	19,290 $\frac{\text{in. lb}}{\text{in.}}$	± 400 in. lb	± 450 in. lb	5,000 in. lb	9
M _Z Steady	92,500 $\frac{\text{in. lb}}{\text{in.}}$	$\pm 1,860$ in. lb	$\pm 2,400$ in. lb	100,000 in. lb	3
M _Z Alt	14,710 $\frac{\text{in. lb}}{\text{in.}}$	± 300 in. lb	350 in. lb	5,000 in. lb	7

Fixed System Loads from Measured Strain Data

As noted above, strain gage bridges on the forward and aft rotor shafts measure axial shaft loads and torque, and shear and bending moments in two directions. A square matrix of numerical coefficients, from the load calibration, is then applied to the data to account for interaction, i.e., apparent response of a load measuring device to loads it should not theoretically respond to. The corrected loads in the rotating shaft are next transferred into equivalent loads in the fixed coordinate system of the fuselage.

Figure 7 presents a flow diagram illustrating the steps used in converting the measured strain data to the correct Fourier coefficients for the steady and first four harmonics of rotating shaft loads. Measured flight data was harmonically analyzed using a 24 ordinate analysis programmed on a digital computer to obtain the steady and harmonic load components. Following the harmonic analysis, each steady term of the series was adjusted to correct for the difference between the base line used in the harmonic analysis and the zero load position from the flight calibrations.

Continuing to the right on the flow diagram, the harmonic components are converted to shaft loads by applying the amplitude and, in some cases, phase calibration constants obtained from the load calibration test. Following these corrections, the measured data is regrouped into steady and alternating terms in Items 1-4, alternating terms only in Items 5 and 6, and steady coefficients in Items 7 and 8. The next step in the processing consists of an interaction correction using the interaction matrices obtained during the load calibration. After the inversion of the steady and alternating interaction matrices, the corrected coefficients for steady and alternating loads can be obtained by adjustment of the Fourier coefficients using,

$$\begin{array}{c} \begin{bmatrix} F_X \\ F_Y \\ F_Z \\ M_{ax} \\ M_{ay} \\ M_{az} \end{bmatrix} \\ \text{Actual Loads} \end{array} = \begin{array}{c} \begin{bmatrix} i_{ax} & i_{ay} & i_{az} & i_{ax\alpha} & i_{a\beta} & i_{a\gamma} \\ i_{bx} & i_{by} & i_{bz} & i_{bx\alpha} & i_{b\beta} & i_{b\gamma} \\ i_{cx} & i_{cy} & i_{cz} & i_{cx\alpha} & i_{c\beta} & i_{c\gamma} \\ i_{dx} & i_{dy} & i_{dz} & i_{dx\alpha} & i_{d\beta} & i_{d\gamma} \\ i_{ex} & i_{ey} & i_{ez} & i_{ex\alpha} & i_{e\beta} & i_{e\gamma} \\ i_{fx} & i_{fy} & i_{fz} & i_{fx\alpha} & i_{f\beta} & i_{f\gamma} \end{bmatrix} \\ \text{Inversion of Interaction Matrix} \end{array} \begin{array}{c} \begin{bmatrix} F_X \\ F_Y \\ F_Z \\ M_{ax} \\ M_{ay} \\ M_{az} \end{bmatrix} \\ \text{Measured Loads} \end{array}$$

The rotor system is represented by the schematic diagram of Figure 8 which shows the rotating and fixed axes systems. Fixed system loads can be written as trigonometric functions of the relative angle Ωt between the rotating axis system and fixed axis system as shown in Figure 9. Forward rotor steady, first harmonic and third harmonic fixed system coefficients in terms of rotating system coefficients are shown in Figure 10. Similar expressions for the fixed system shaft loads of the aft rotor derived using a negative direction of rotation are included in the data processing computer program.

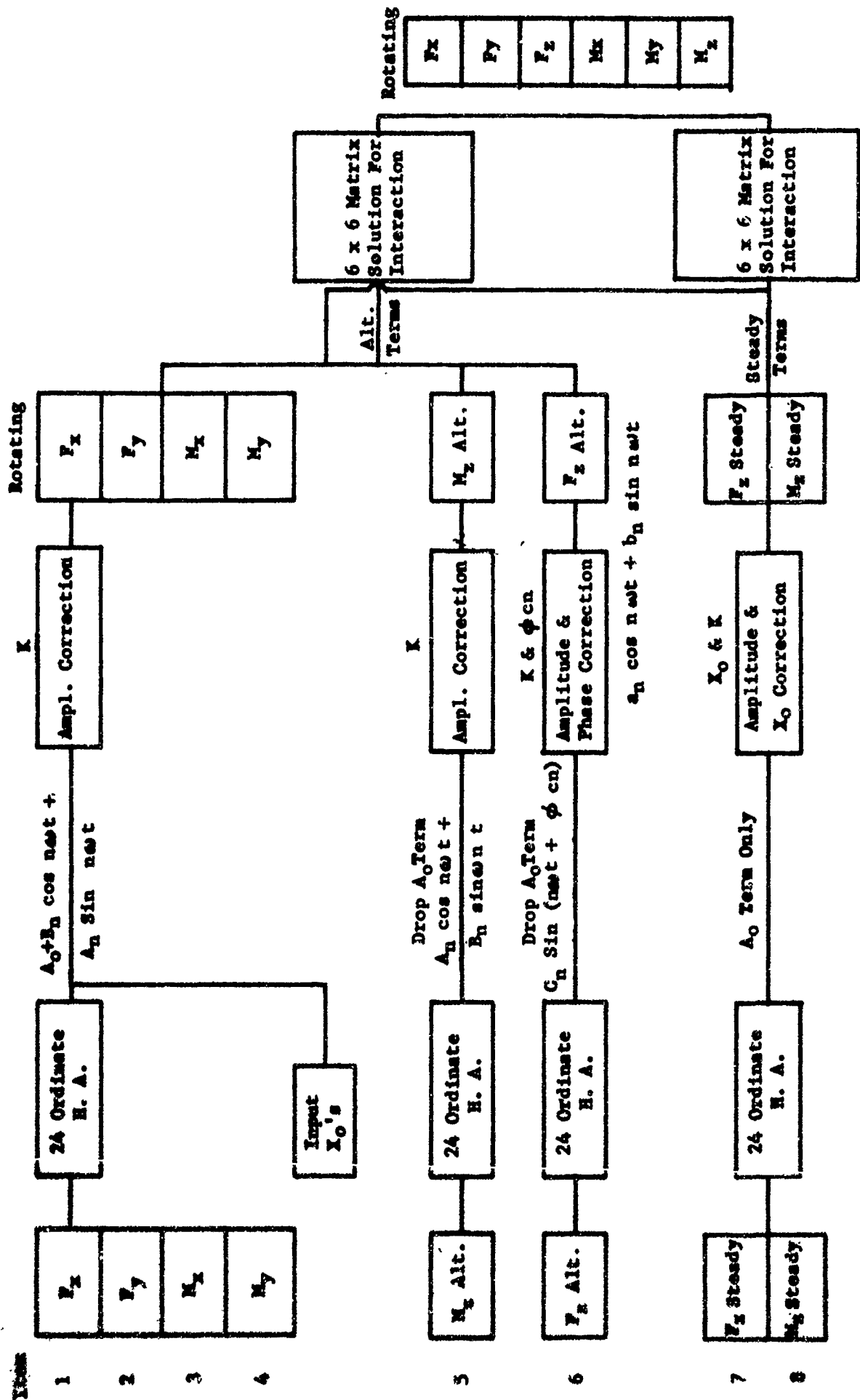


FIGURE 7. FLOW DIAGRAM FOR CONVERTING DATA TO SHAFT LOADS

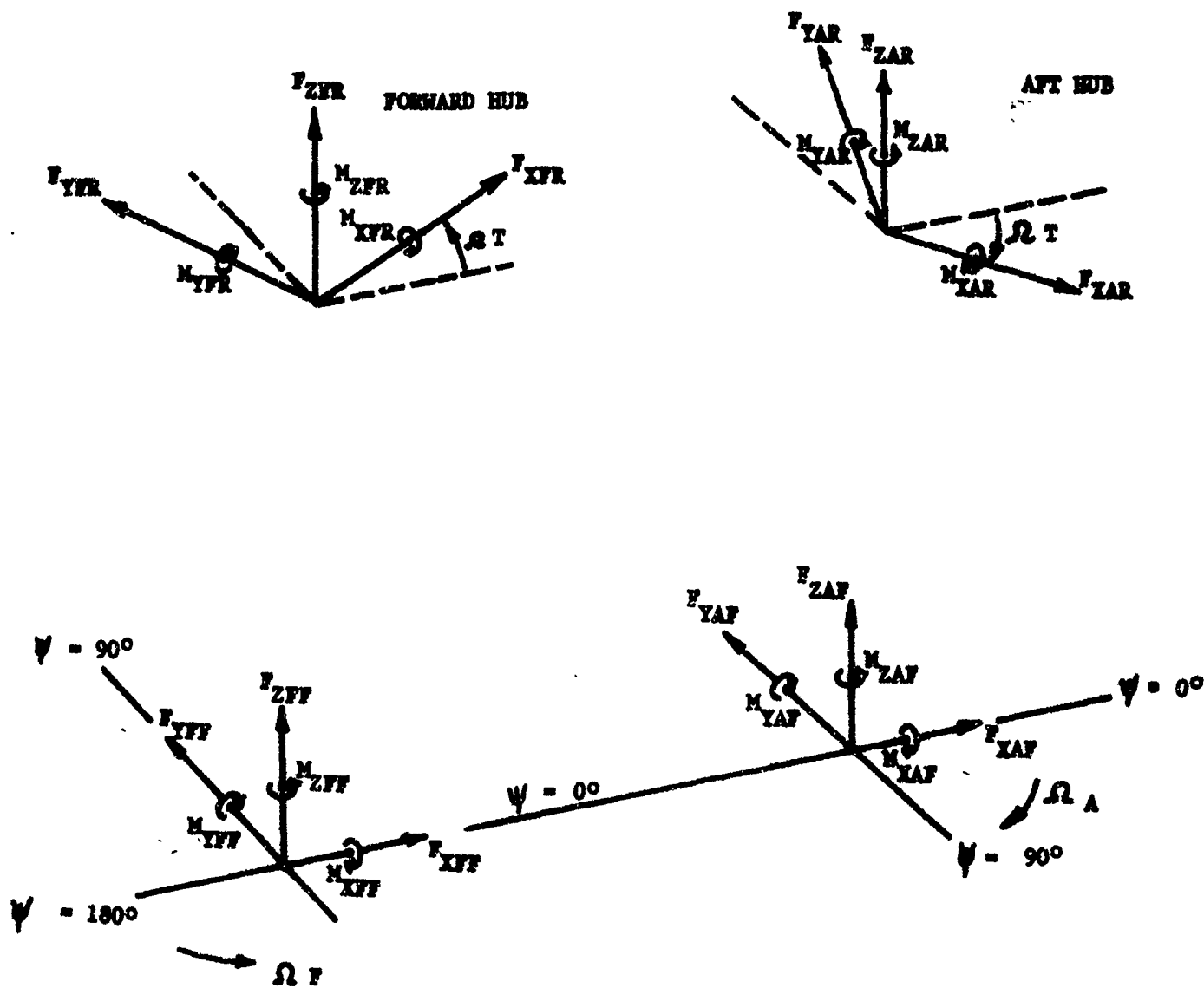


FIGURE 8. SIGN CONVENTION FOR FIXED AND ROTATING SYSTEM HUB LOADS

$$\begin{bmatrix} F_{XF} \\ F_{YF} \\ F_{ZF} \\ M_{XF} \\ M_{YF} \\ M_{ZF} \end{bmatrix} = \begin{bmatrix} \cos\Omega t & -\sin\Omega t & & & & \\ \sin\Omega t & \cos\Omega t & & & & \\ & & 1 & & & \\ & & & \cos\Omega t & -\sin\Omega t & \\ & & & \sin\Omega t & \cos\Omega t & \\ & & & & & 1 \end{bmatrix} \begin{bmatrix} F_{XR} \\ F_{YR} \\ F_{ZR} \\ M_{XR} \\ M_{YR} \\ M_{ZR} \end{bmatrix}$$

FIXED SYSTEM
ROTATING SYSTEM

ROTATING SYSTEM LOADS

- F_{XR} , Shear in the rotor plane in the direction of the master spline
- F_{YR} , Shear in the rotor plane in a direction normal to the master spline
- F_{ZR} , Lift force in the shaft vertical direction
- M_{XR} , Moment in the rotor plane, about the rotating x axis
- M_{YR} , Moment in the rotor plane, about the rotating y axis
- M_{ZR} , Torque about the shaft axis

FIXED SYSTEM LOADS

- F_{XF} , Shear in the rotor plane in the aft direction
- F_{YF} , Shear in the rotor plane in the lateral direction
- F_{ZF} , Lift force in the shaft vertical direction
- M_{XF} , Moment in the rotor plane, about the fixed x axis
- M_{YF} , Moment in the rotor plane, about the fixed y axis
- M_{ZF} , Torque about the shaft axis

FIGURE 9. MEASURED LOADS TO FIXED SYSTEM LOADS

Steady

$$A_{0X} = 1/2A_{1X} - 1/2B_{1Y}$$

$$A_{0Y} = 1/2B_{1X} + 1/2A_{1Y}$$

$$A_{0Z} = A_{0Z}$$

$$A_{0\alpha} = 1/2A_{1\alpha} - 1/2B_{1\beta}$$

$$A_{0\beta} = 1/2B_{1\alpha} + 1/2A_{1\beta}$$

$$A_{0\gamma} = A_{0\gamma}$$

(Fixed) (Rotating)

Legend

First Subscript Denotes Rotor Harmonic

Second Subscript Denotes Load Direction as Shown Below,

X, Force Along X Axis

Y, Force Along Y Axis

Z, Force Along Z Axis

α , Moment About X Axis

β , Moment About Y Axis

γ , Moment About Z Axis

First HarmonicCos Terms

$$A_{1X} = A_{0X} + 1/2A_{2X} - 1/2B_{2Y}$$

$$A_{1Y} = A_{0Y} + 1/2A_{2Y} + 1/2B_{2X}$$

$$A_{1Z} = A_{1Z}$$

$$A_{1\alpha} = A_{0\alpha} + 1/2A_{2\alpha} - 1/2B_{2\beta}$$

$$A_{1\beta} = A_{0\beta} + 1/2B_{2\alpha} + 1/2A_{2\beta}$$

$$A_{1\gamma} = A_{1\gamma}$$

(Fixed) (Rotating)

Sin Terms

$$B_{1X} = -A_{0Y} + 1/2B_{2X} + 1/2A_{2Y}$$

$$B_{1Y} = A_{0X} - 1/2A_{2X} + 1/2B_{2Y}$$

$$B_{1Z} = B_{1Z}$$

$$B_{1\alpha} = -A_{0\alpha} + 1/2B_{2\alpha} + 1/2A_{2\beta}$$

$$B_{1\beta} = A_{0\beta} - 1/2A_{2\alpha} + 1/2B_{2\beta}$$

$$B_{1\gamma} = B_{1\gamma}$$

(Fixed) (Rotating)

Third HarmonicCos Terms

$$A_{3X} = 1/2A_{2X} + 1/2B_{2Y} + 1/2A_{4X} - 1/2B_{4Y}$$

$$A_{3Y} = -1/2B_{2X} + 1/2A_{2Y} + 1/2B_{4X} + 1/2A_{4Y}$$

$$A_{3Z} = A_{3Z}$$

$$A_{3\alpha} = 1/2A_{2\alpha} + 1/2B_{2\beta} + 1/2A_{4\alpha} - 1/2B_{4\beta}$$

$$A_{3\beta} = -1/2B_{2\alpha} + 1/2A_{2\beta} + 1/2B_{4\alpha} + 1/2A_{4\beta}$$

$$A_{3\gamma} = A_{3\gamma}$$

(Fixed) (Rotating)

Sin Terms

$$B_{3X} = 1/2B_{2X} - 1/2A_{2Y} + 1/2B_{4X} + 1/2A_{4Y}$$

$$B_{3Y} = 1/2A_{2X} + 1/2B_{2Y} - 1/2A_{4X} + 1/2B_{4Y}$$

$$B_{3Z} = B_{3Z}$$

$$B_{3\alpha} = 1/2B_{2\alpha} - 1/2A_{2\beta} + 1/2B_{4\alpha} - 1/2A_{4\beta}$$

$$B_{3\beta} = 1/2A_{2\alpha} + 1/2B_{2\beta} - 1/2A_{4\alpha} + 1/2B_{4\beta}$$

$$B_{3\gamma} = B_{3\gamma}$$

(Fixed) (Rotating)

FIGURE 10. FIXED SYSTEM COEFFICIENTS

Rotor Shaft Load Results

Using the measurement technique described above, H-21 rotor loads were obtained at a normal gross weight of 13,500 lb for (1) an airspeed sweep at normal 258 rpm, (2) a rotor sweep at 40 knots airspeed and (3) a rotor speed sweep at 90 knots airspeed. Load plots are shown herein for the steady and third harmonic fixed system results, and second and fourth harmonic rotating results. Each set of force data contains forward and aft rotor loads as sine and cosine components and their resultants. The sine and cosine time reference is when the red blade and the rotor hub master spline are in trail position.

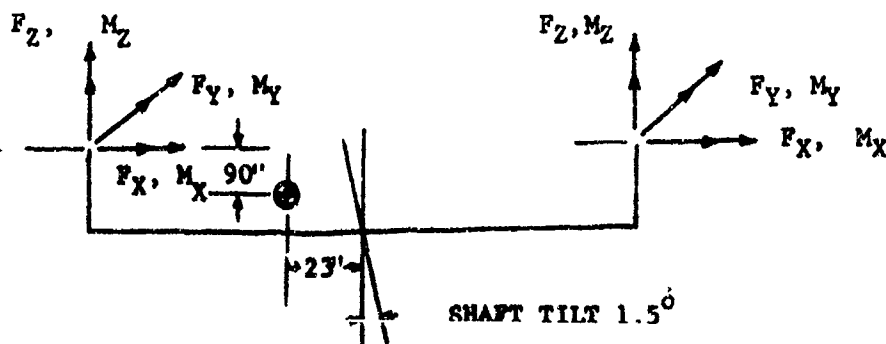
Steady Loads, Instrumentation Check - No rational method was known for positively defining the accuracy of the measured loads. Apart from an examination of the reasonableness of the flight data compared with calculated shaft loads, the best check of the flight data was a steady load balance. This provides a gross check, but does not, of course, provide a check down into the reading accuracy of the data. Even this is appropriate because, in addition to the measured loads and the aircraft weight, other unknown loads act on the helicopter, namely, rotor downwash and aerodynamic drag. Further, the actual cg location at any instant during a flight when data is recorded is not known exactly but is estimated from the takeoff cg location.

To illustrate, a steady load balance is performed below using measured data from a hover condition in which the unknown factors are minimized.

FLT. C96 X-121

RPM = 258

HOVER



RUN 1

G.W. 13,500 lb

Fwd.

$$F_X = +476\#$$

$$F_Y = +5\#$$

$$F_Z = +7691\#$$

$$M_X = +2268 \text{ in-}\#$$

$$M_Y = +8821 \text{ in-}\#$$

$$M_Z = -124001 \text{ in-}\#$$

Aft.

$$F_X = -174\#$$

$$F_Y = +28\#$$

$$F_Z = +5569\#$$

$$M_X = +1103 \text{ in-}\#$$

$$M_Y = -1451 \text{ in-}\#$$

$$M_Z = +122866 \text{ in-}\#$$

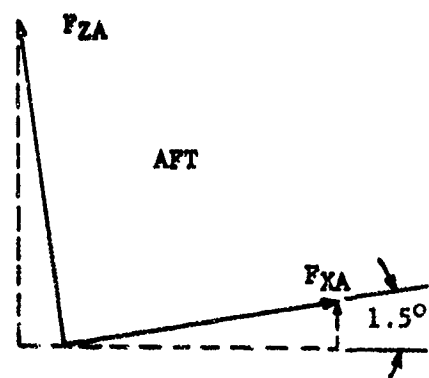
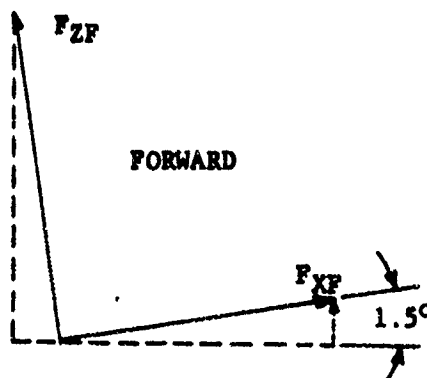
For the gross weight and cg condition shown and assuming vertical trim and no wind the rotor shafts are 1.5° forward of the vertical in the pitch direction. For force balance in either the lateral or longitudinal directions, the appropriate forces from each rotor are combined to obtain the total force acting on the helicopter in each direction which should, of course, be zero. In the vertical direction, the total should equal the helicopter given weight plus any download due to rotor downwash impinging on the fuselage and pitch link compressive loads but minus the rotor weights.

Summing the loads in the lateral direction,

$$\sum F_Y = F_{Y \text{ Fwd}} + F_{Y \text{ Aft}}$$

$$\sum F_Y = 5\# + 28\# = 33\#$$

In the longitudinal direction, the components of lift and shear are combined as illustrated below:



$$\begin{aligned} \sum F_{\text{Long}} &= (F_{ZF} + F_{ZA}) \sin 1.5^\circ - (F_{XF} + F_{XA}) \cos 1.5^\circ \\ &= (7691 + 5569) .0262 - (476 - 176) .9997 \\ &= +44\# \end{aligned}$$

Similarly, for the vertical force at each rotor

$$F_{\text{Vert}} = F_{ZF} \cos 1.5^\circ + F_{XF} \sin 1.5^\circ$$

$$\text{Fwd} \quad 7691(.9997) + 476(.0262) = 7703\#$$

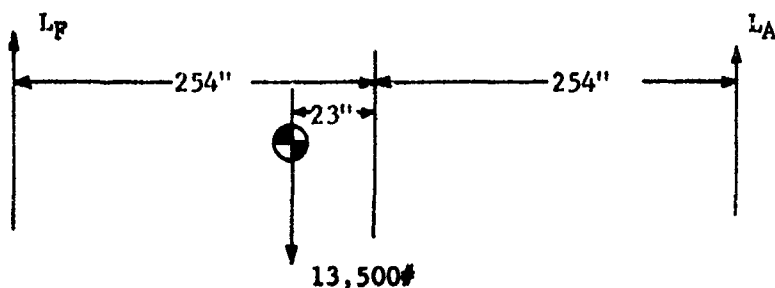
$$F_{\text{Vert}} = F_{ZA} \cos 1.5^\circ + F_{XA} \sin 1.5^\circ$$

$$\text{Aft} \quad 5569(.9997) - 174(.0262) = 5574\#$$

Further, combining the vertical loads at each rotor,

$$\sum F_{\text{Vert}} = 7703 + 5574 = 13,277$$

Before considering the comparison of measured forces and known forces acting on the helicopter, the unknown lift load at each rotor is estimated from the cg location.



Forward Rotor,

$$L_P = \frac{254 + 23}{508} \times 13,500 = 7350\#$$

Aft Rotor,

$$L_A = \frac{254 - 23}{508} \times 13,500\# = 6150\#$$

From this distribution, the steady lifts are defined by adding the estimated downwash and pitch link compressive load, and then subtracting the rotor weight.

$$L_P' = 7350 + 13,500 (.02) + 3(70) - 667 = 7163\#$$

Est. Downwash

Pitch Link
Loads

Rotor
Weight

$$L_A' = 6200 + 13,500 (.02) + 3(70) - 667 = 6003\#$$

The table below presents a comparison of the measured forces and the estimated steady loads:

Load Direction	<u>Forward Rotor</u>			<u>Aft Rotor</u>			<u>Forward & Aft Rotor</u>		
	<u>Measured</u>	<u>Est.</u>	<u>Error</u>	<u>Measured</u>	<u>Est.</u>	<u>Error</u>	<u>Measured</u>	<u>Est.</u>	<u>Error</u>
Longitudinal	-	-	-	-	-	-	44	0	+44
Lateral	-	-	-	-	-	-	33	0	+33
Vertical	7703	7163	-540	5574	6003	+429	13169	13277	+108

Lateral and longitudinal loads are close to the estimated accuracy shown previously. Further, the difference between the estimated total vertical load and the measured loads are within estimated accuracy of 360 lb. Individually, the forward and aft rotors are slightly above the specified accuracy, but this variation reflects some inaccuracy resulting from estimation of the cg location and downwash distribution.

From the measured torque the shaft horsepower is calculated as:

Fwd Rotor	508 H.P.
Aft Rotor	503 H.P.
Total Shaft Power	1011 H.P.

This measured power shows reasonable agreement with a calculated power requirement of 1100 H.P. for the same flight condition.

From the results of this steady load check, it was concluded that the accuracy of the steady load measurement was adequate for the flight program.

Fixed System Steady Loads - Figure 11 presents the fixed system hub forces and moment as an airspeed sweep at 258 rpm and rpm sweeps for 40 and 90 knots.

For reference, the H-21 forward and aft rotor shafts are parallel, but the rotor is rigged to produce a dihedral effect which promotes better speed stability. A side effect of this feature is that in order to maintain a hover attitude, the combination of longitudinal cyclic and differential collective pitch control must provide a greater aft longitudinal force at the forward rotor than the aft rotor. This is illustrated in Figure 11a showing a 500 lb aft force at the forward rotor, and a 200 lb forward force at the aft rotor in hover. As speed increases, the forward force at the aft rotor decreases, and above 80 knots reverses direction. The aft longitudinal force at the forward rotor increases with airspeed.

G.W. = 13,300 LBS.
C.G. = 13 IN. FWD.

FLT. H-21CMX121
ROTOR SPEED = 258 RPM

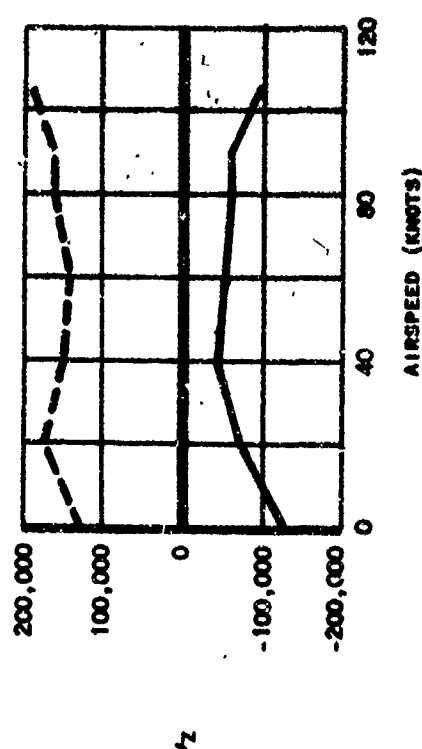
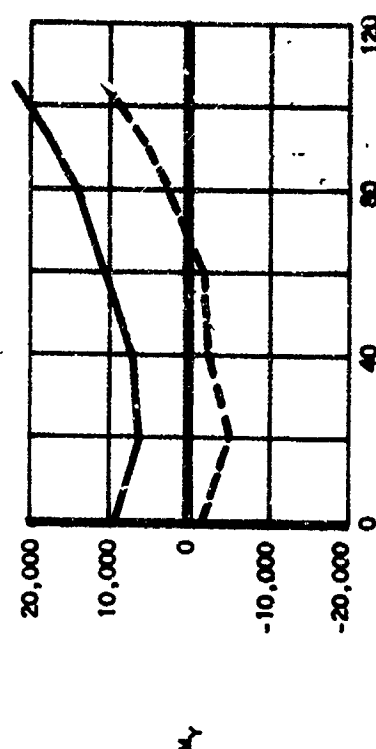
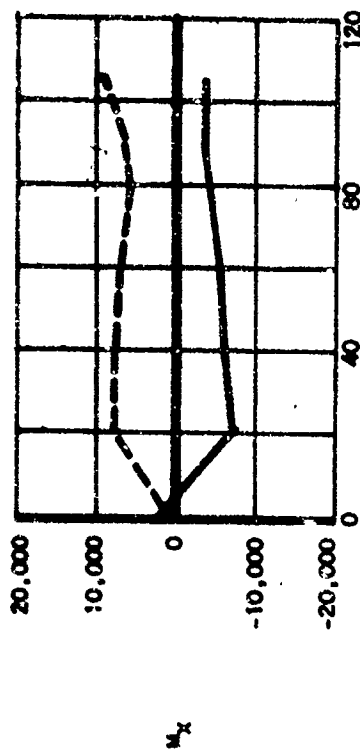
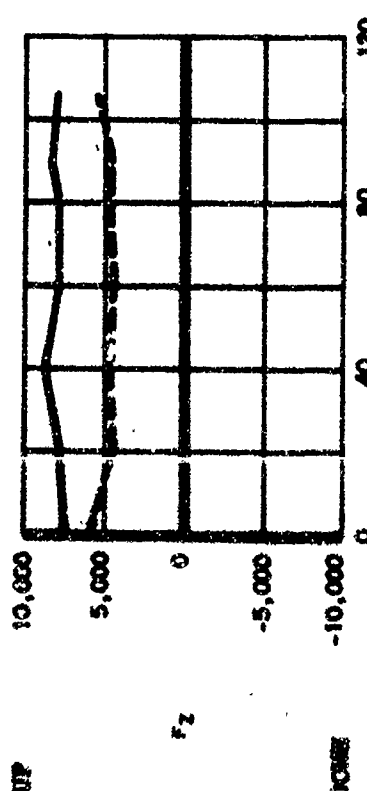
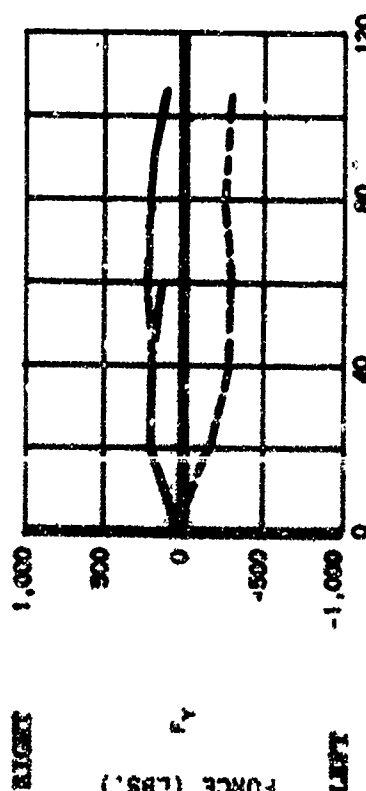
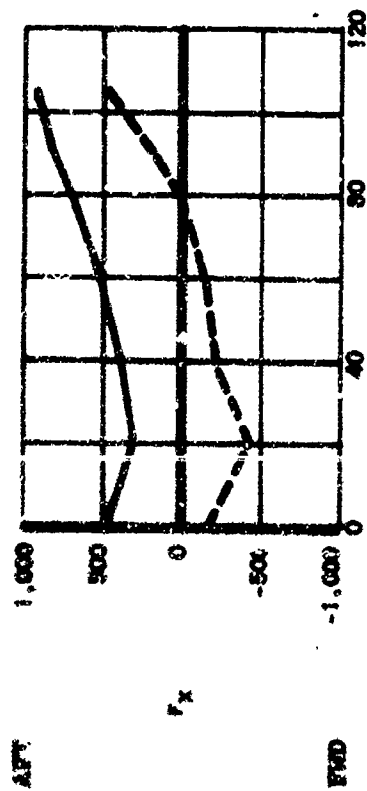


FIGURE 11a. FLIED SYSTEM STEADY LOADS
AIRSPEED SWEEP AT 258 RPM

S.T. = 13,500 LBS.
C.G. = 19 IN. FWD.

FLT. H-21C98X121
IAS = 40 KNOTS

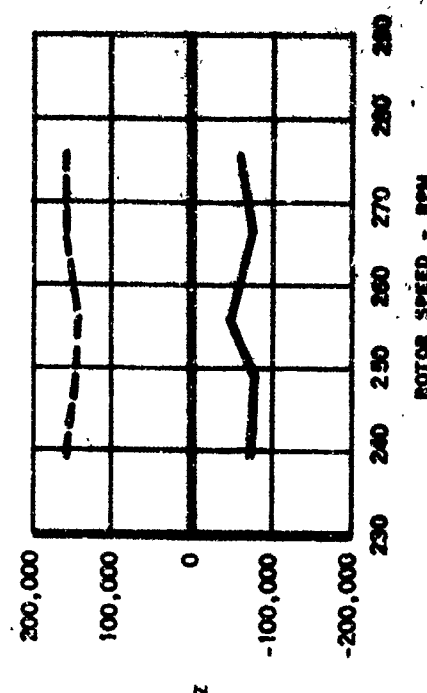
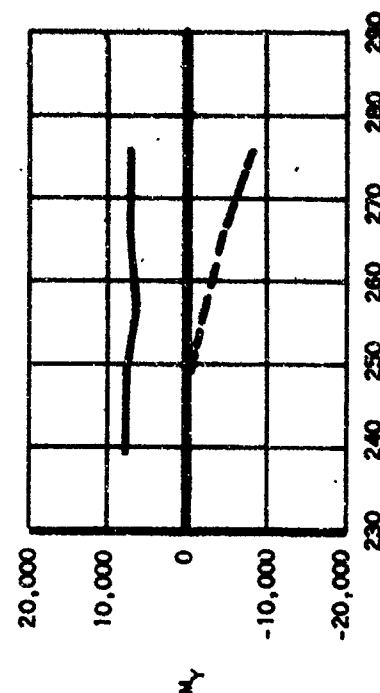
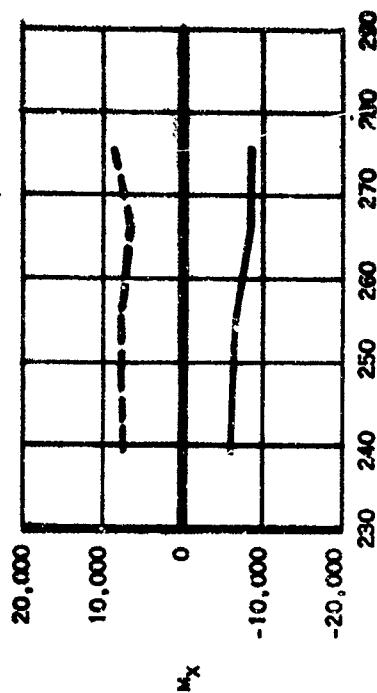
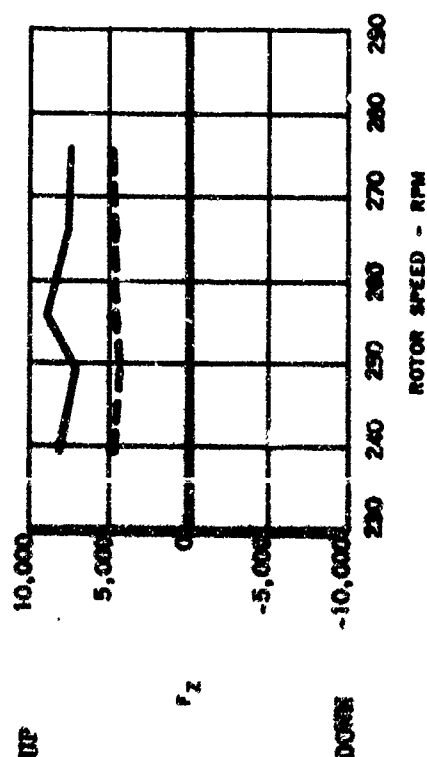
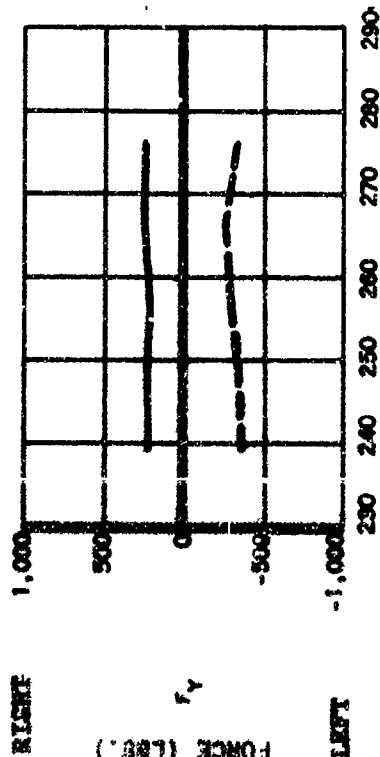
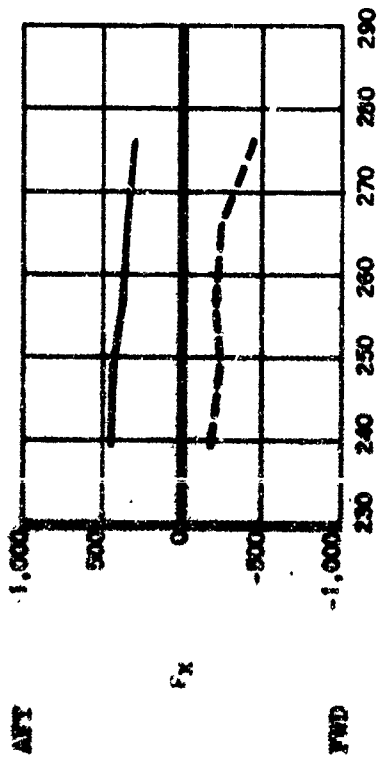


FIGURE 11b. FIXED SYSTEM STEADY LOADS
RPM SWEEP AT 40 KNOTS

FLT. H-21C96X121
IAS = 90 KNOTS

G.W. = 13,500 LBS.
C.G. = 19 1/4" FWD.

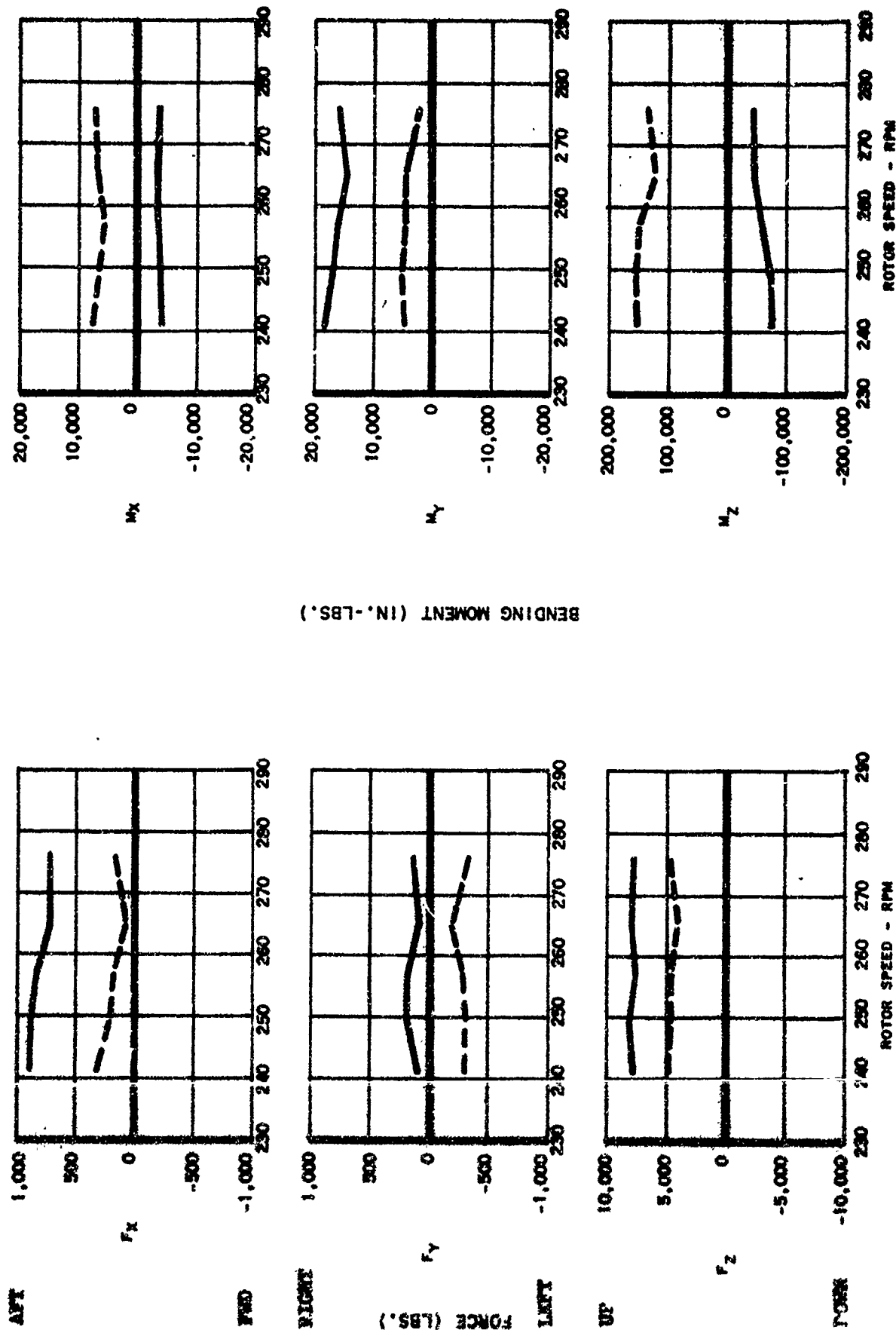


FIGURE 11c. FIXED SYSTEM STEADY LOADS
RPM SWEEP AT 90 KTS

Rotor shaft torque, M_z in Figures 11b and 11c averages about 160,000 inch-lb for the aft rotor and about 60,000 inch-lb for the forward rotor. The rotor directions are as shown in Figure 12. The torque differential of 100,000 in-lb due to the larger aft rotor torque acts counter clockwise on the aircraft, and must be balanced by approximately equal and opposite lateral loads at both rotors. The necessary load magnitude is approximately 200 lb. In Figures 11b and 11c it is seen that these loads do occur in the measured F_y , averaging about 200 lb to the right at the forward rotor and to the left at the aft rotor. Roll moment M_x is also related to this effect since the forward rotor roll moment is roll right, and the aft rotor roll moment is roll left. In hover, the rotor torques, become nearly equal.

Third Harmonic Fixed System Loads - With a three bladed helicopter, third harmonic vibration levels are usually the dominant portion of the vibration environment. Figure 13 presents the measured third harmonic fixed system loads. The second and fourth harmonic rotating shaft loads from which the third harmonic in-plane loads result are presented in Figures 15 and 16.

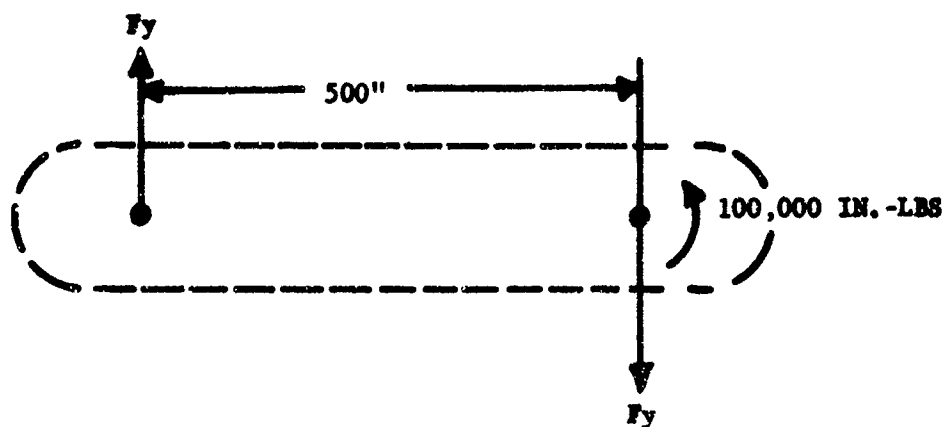
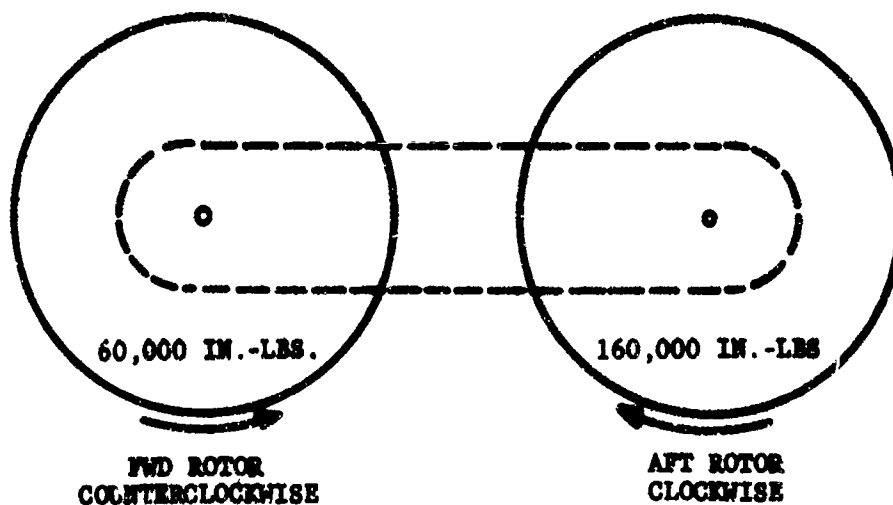
Figure 13a, the 3Ω airspeed sweep, shows that shaft force resultants average,

Rotor	F_x lb	F_y lb	F_z lb
	<u>Longitudinal</u>	<u>Lateral</u>	<u>Vertical</u>
Forward	800	250	200
Aft	1300	300	400

The longitudinal loads are easily the larger, and the aft rotor loads are larger than those at the forward rotor. This is particularly marked at 60 knots where the aft load is almost three times the forward load. No clear general trend with airspeed is evident. The vertical force peaks at 60 knots on the aft rotor, however, the forward rotor vertical has a minimum in this speed region and shows a rapid, fairly steep rise to 103 knots.

Figures 13b and 13c, rotor speed sweeps at 40 knots and 90 knots, indicate an extremely rapid load buildup with rpm for longitudinal load at both rotors and for vertical load at the aft rotor. The sine component is largely responsible for this trend at 40 knots, while both the sine and cosine contribute at 90 knots aft rotor longitudinal load was nearly twice as large as the corresponding forward rotor load.

Third harmonic vertical loads arise from direct addition of third harmonic blade root vertical shears. Third harmonic in-plane loads result from second and fourth harmonic blade root horizontal shears as shown in Figure 14.



DIFFERENTIAL TORQUE

$160,000 - 60,000 = 100,000 \text{ IN.-LBS}$
Acting On Aircraft

$$F_y = \frac{100,000 \text{ IN.-LBS}}{500 \text{ INCHES}} = 200 \text{ LBS}$$

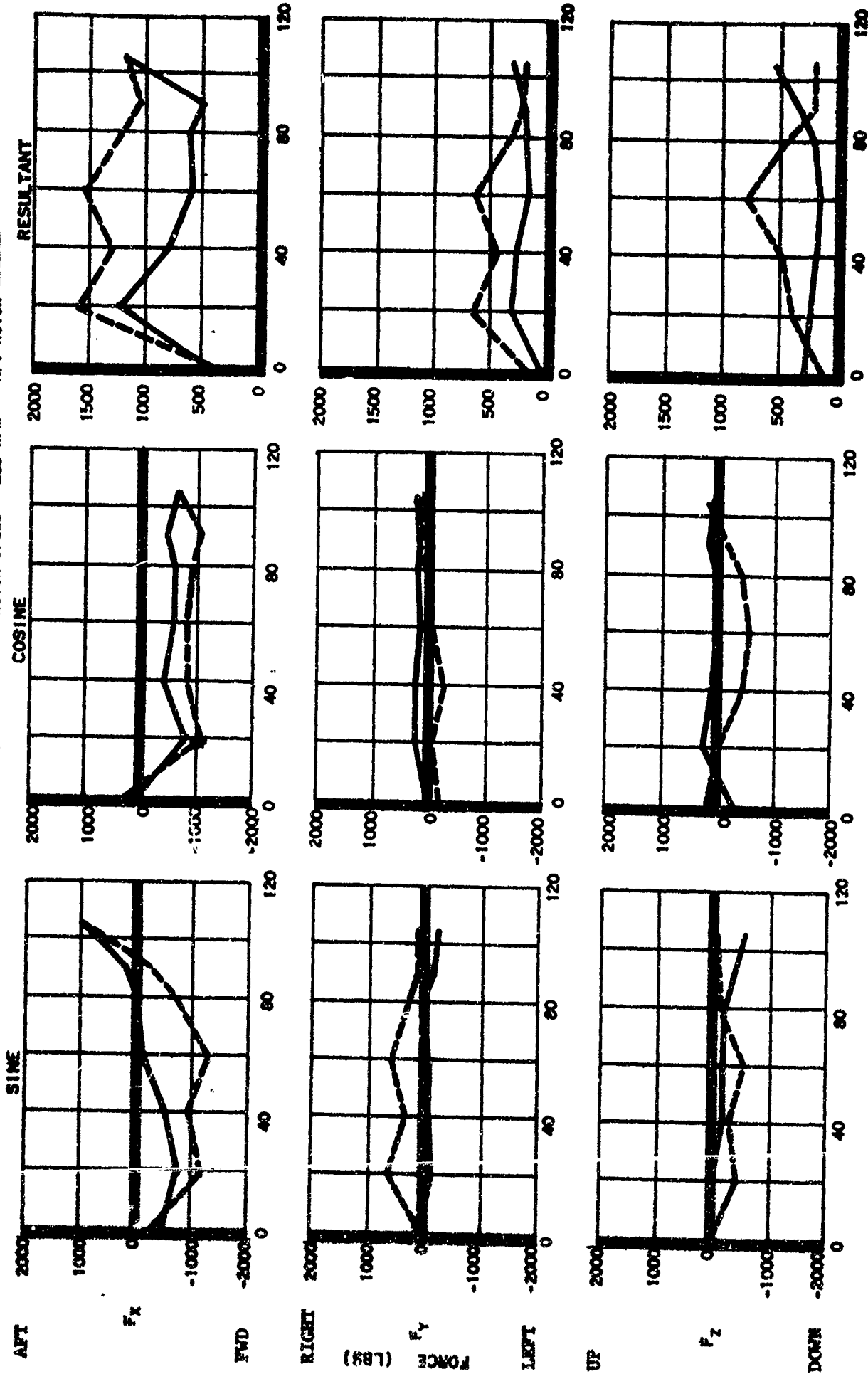
FIG. 12. MEASURED TORQUE DISTRIBUTION

G.W. = 13,500 LBS.
C.G. = 19 IN. FWD.

FLT. H21C-96X121
WOOD BLADES

3RD HARMONIC
ROTOR SPEED = 258 RPM

FWD ROTOR
AFT ROTOR



AIRSPEED (KNOTS)

FIGURE 13a. FIXED SYSTEM THIRD HARMONIC LOADS
AIRSPEED AT 258 RPM

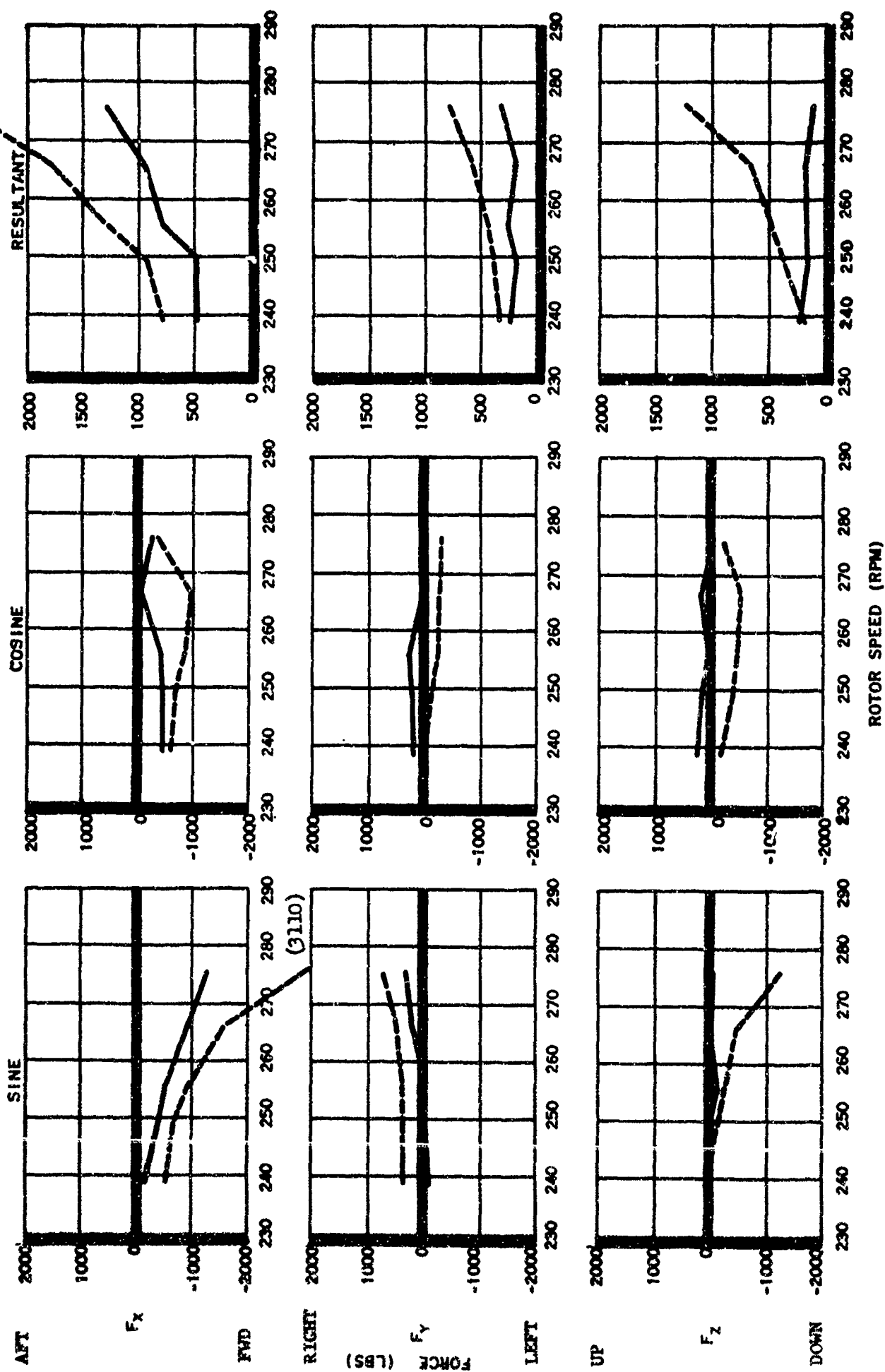


FIGURE 13b. FIXED SYSTEM THIRD HARMONIC LOADS
RPM SWEEP AT 40 KNOTS

G.W. = 13,500 LBS.
C.G. = 19 IN. FWD.
FLT. H21C-96X121
WOOD BLADES
3RD HARMONIC
IAS = 90 KTS

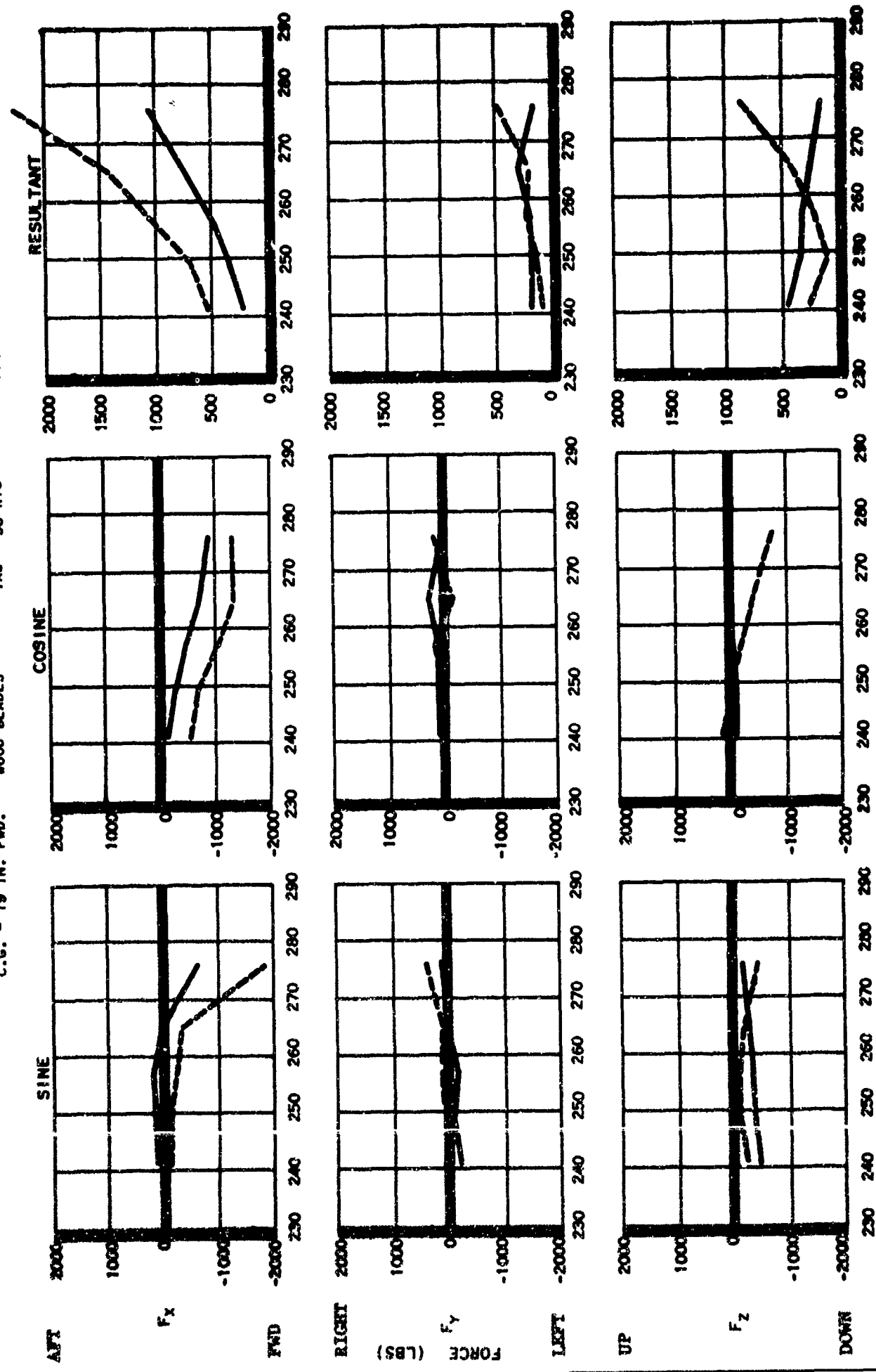


FIGURE 13c. FIXED SYSTEM THIRD HARMONIC LOADS
RPM SWEEP AT 90 KNOTS

COMMENT	Fx3 LONGITUDINAL FIXED SYSTEM LOAD	Fy3 LATERAL FIXED SYSTEM LOADS
$\cos 3\psi$	$\frac{1}{2} [Fx2C + Fx2S + Fx4C - Fx4S]$	$\frac{1}{2} [Fy2C - Fx2S + Fy4C + Fx4S]$
$\sin 3\psi$	$\frac{1}{2} [-Fy2C + Fx2S + Fy4C + Fx4S]$	$\frac{1}{2} [Fx2C + Fy2S - Fx4C + Fy4S]$

WHERE $Fx2S, Fx2C =$ Second and fourth harmonic rotating sine and cosine in-plane
 $Fx4S, Fx4C$ Loads acting in the direction of the master spline
 $Fy2S, Fy2C =$ Second and fourth harmonic rotating sine and cosien in-plane
 $Fy4S, Fy4C$ Loads acting in the direction normal to the master spline

NUMERICALLY, FOR THE FORWARD ROTOR AT 20 KNOTS, 258 RPM

$\cos 3\psi$	$\frac{1}{2} [\frac{(-510) + (-438) + (-340) - (338)}{-474 - \frac{339}{\text{Second}} - \frac{213}{\text{Fourth}}}]$	$\frac{1}{2} [\frac{(515) - (-497) + (-234) + (-232)}{+506 - \frac{233}{\text{Second}} - \frac{273}{\text{Fourth}}}]$
$\sin 3\psi$	$\frac{1}{2} [\frac{-(-515) + (-497) + (-234) + (-232)}{-506 - \frac{233}{\text{Second}} - \frac{739}{\text{Fourth}}}]$	$\frac{1}{2} [\frac{(-510) + (-438) - (-340) + (338)}{-474 + \frac{339}{\text{Second}} - \frac{135}{\text{Fourth}}}]$
RESULTANT	$813 \rightarrow -739 = 1099$	$273 \rightarrow -135 = 305$

FIGURE 14. THIRD HARMONIC IN-PLANE LOADS

Second and Fourth Harmonic Rotating System Loads - Figures 15 and 16 present the rotating second and fourth harmonic in-plane loads. The second harmonic resultant loads show a tendency toward the high hover, low cruise characteristics in the forward rotor, but not in the aft rotor. The fourth harmonic airspeed sweep produces relatively constant resultants within most cases, a tendency to increase sharply at high forward speed.

Numerical combination of these loads into the fixed system third harmonic is illustrated in Figure 14 for the forward rotor at 20 knots. The second and fourth harmonic rotating loads are additive in forming the longitudinal fixed system third harmonic load, subtractive in forming the lateral fixed system harmonic load, hence longitudinal loads are in almost all instances larger than lateral loads.

It is of interest to note certain similarities among the second harmonic airspeed sweep curves in Figure 15a. The F_x sine curve of the forward rotor is the negative of the F_y cosine curve; the F_y sine curve is the same as the F_x cosine curve of the forward rotor. The aft rotor shows similar characteristics, however the pattern differs in sign relation because of the opposite direction of shaft rotation. The fourth harmonic airspeed sweep illustrates its own pattern, Figure 16a. The F_x sine curve is the negative of the F_y cosine curve. The same similarity patterns between longitudinal and lateral second and fourth harmonic loads are also evident in the rpm sweeps.

G.W. = 13,500 LBS.
C.G. = 19 IN. FWD.

FLT. H21C-96X121
WOOD BLADES

2ND HARMONIC
RPM - 258

FWD ROTOR
AFT ROTOR

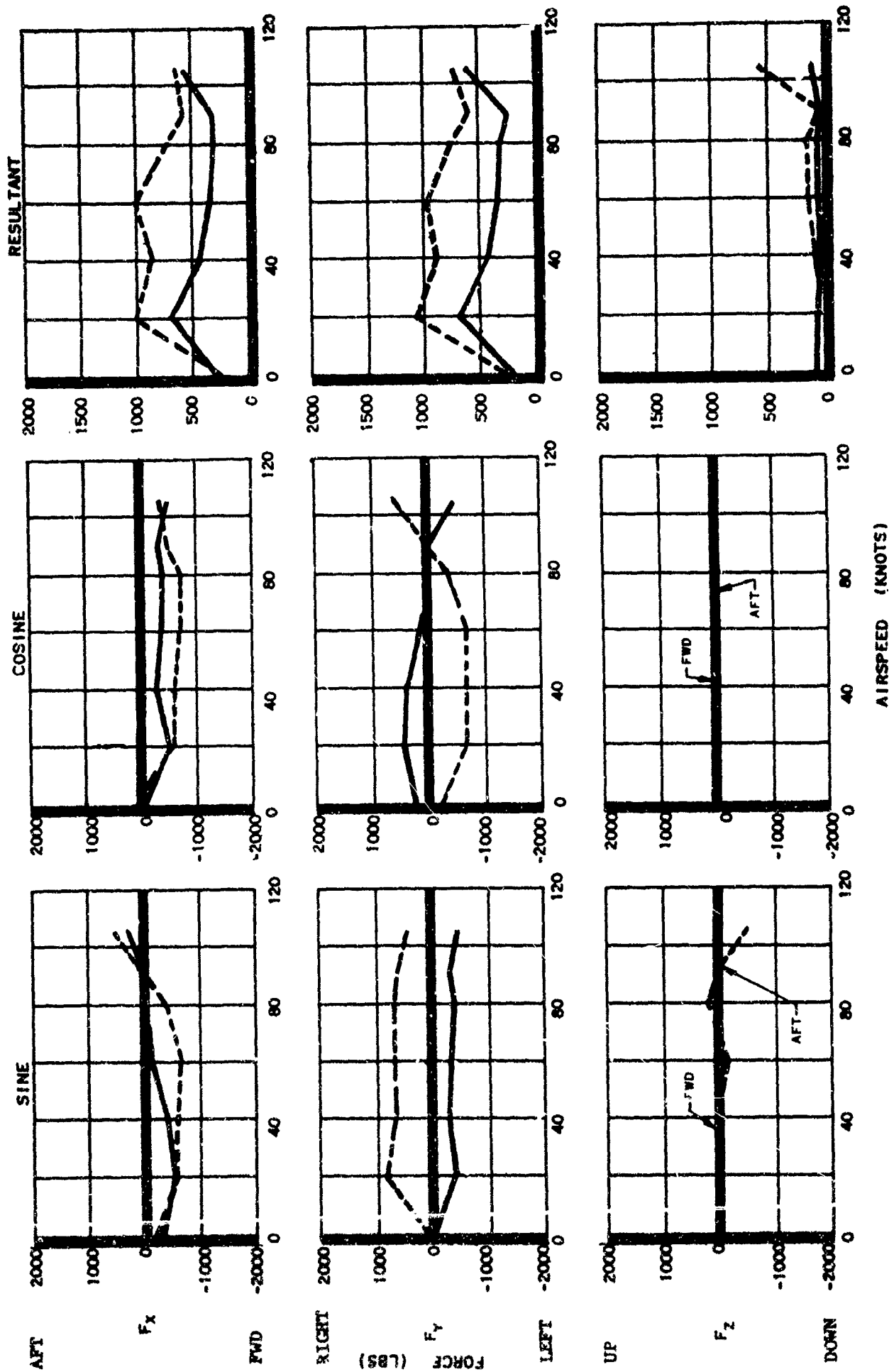


FIGURE 15a. ROTATING SYSTEM SECOND HARMONIC SHAFT LOADS
AIRSPEED SWEEP AT 258 RPM

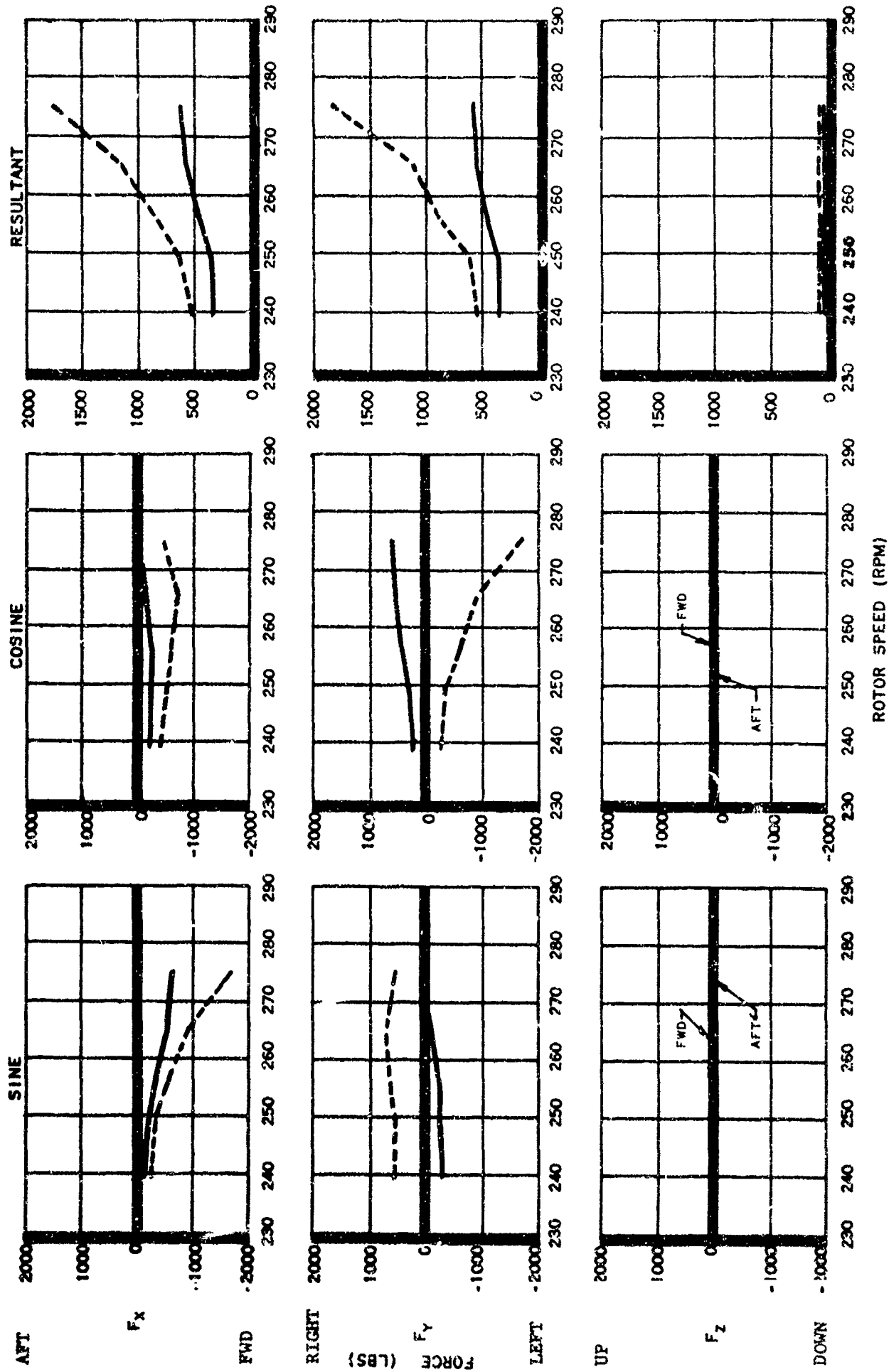


FIGURE 15b. ROTATING SYSTEM SECOND HARMONIC SHAFT LOADS
RPM SWEEP AT 40 KNOTS

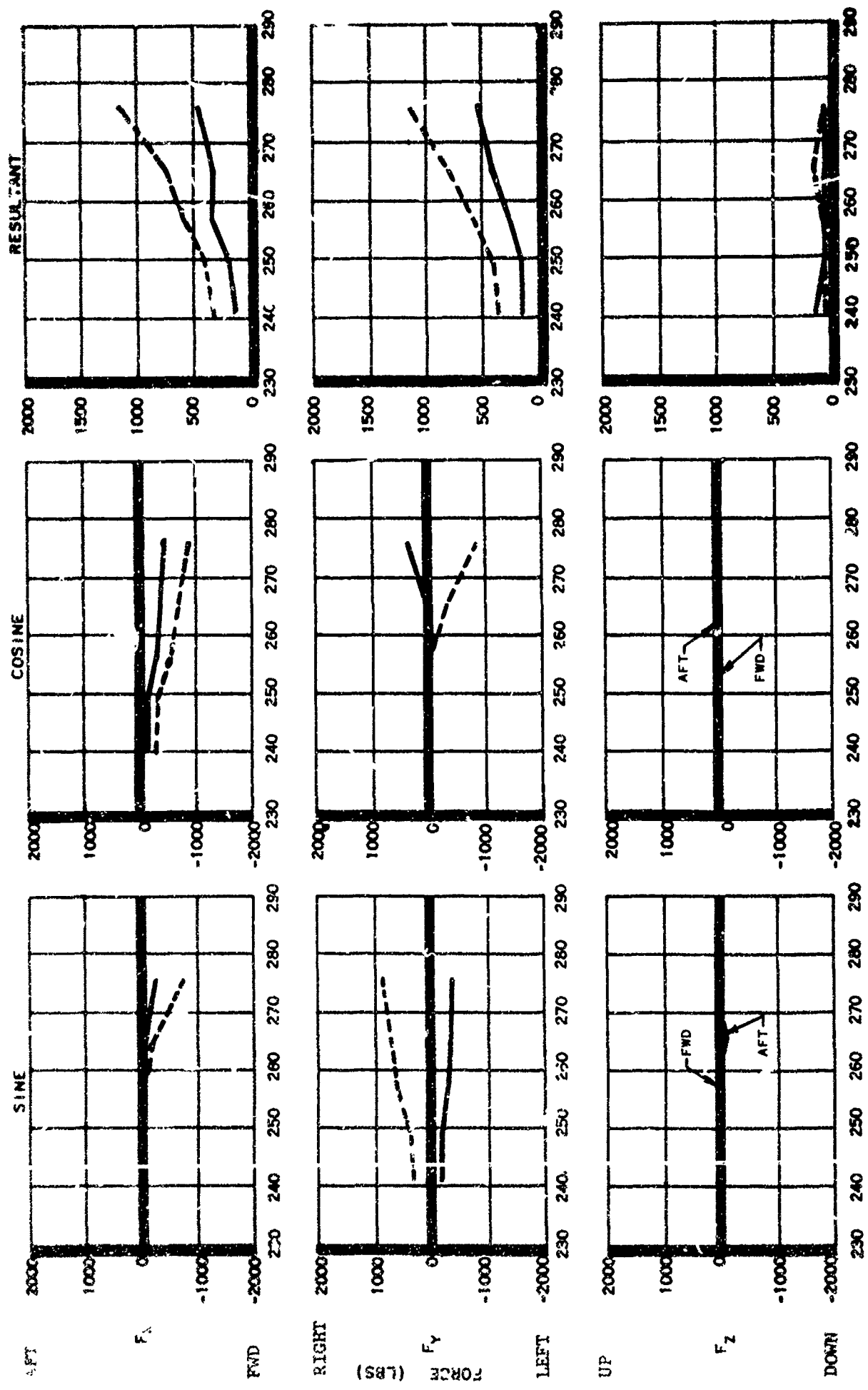


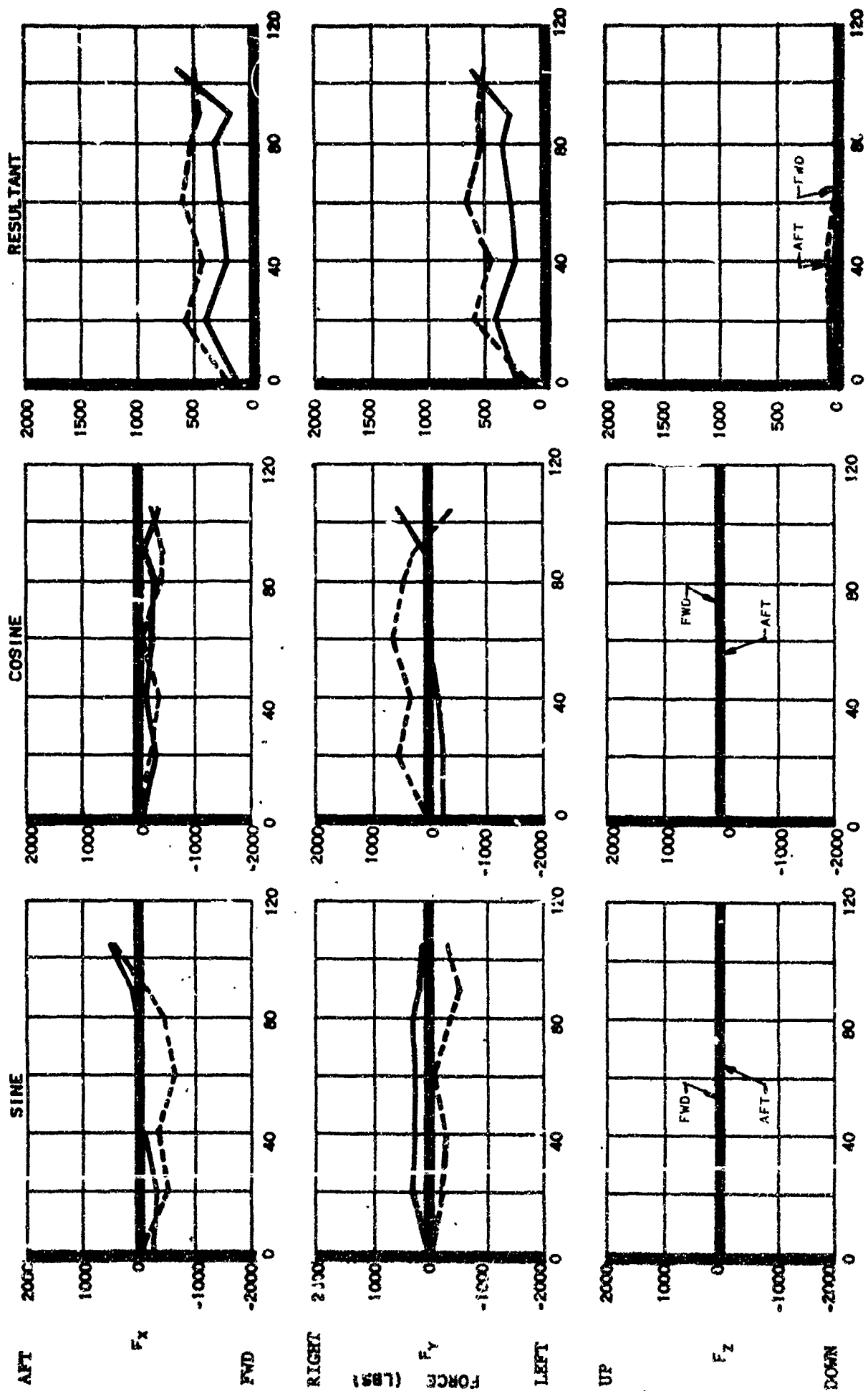
FIGURE 15c. ROTATING SYSTEM SECOND HARMONIC SHAFT LOADS
 RPM SWEEP AT 90 KNOTS

G.W. = 13,500 LBS.
C.G. = 19 IN. FWD.

FLT. H21C-96X121
WOOD BLADES

4TH HARMONIC
RPM - 258

FWD ROTOR
AFT ROTOR



AIRSPEED (KNOTS)

FIGURE 16a. ROTATING SYSTEM FOURTH HARMONIC SHAFT LOADS
AIRSPEED SWEEP AT 258 RPM

G.W. = 13,500 LBS.
C.G. = 19 IN. FWD.

FLT. H21C-96X121
WOOD BLADES

4TH HARMONIC
IAS = 40

FWD ROTOR
AFT ROTOR

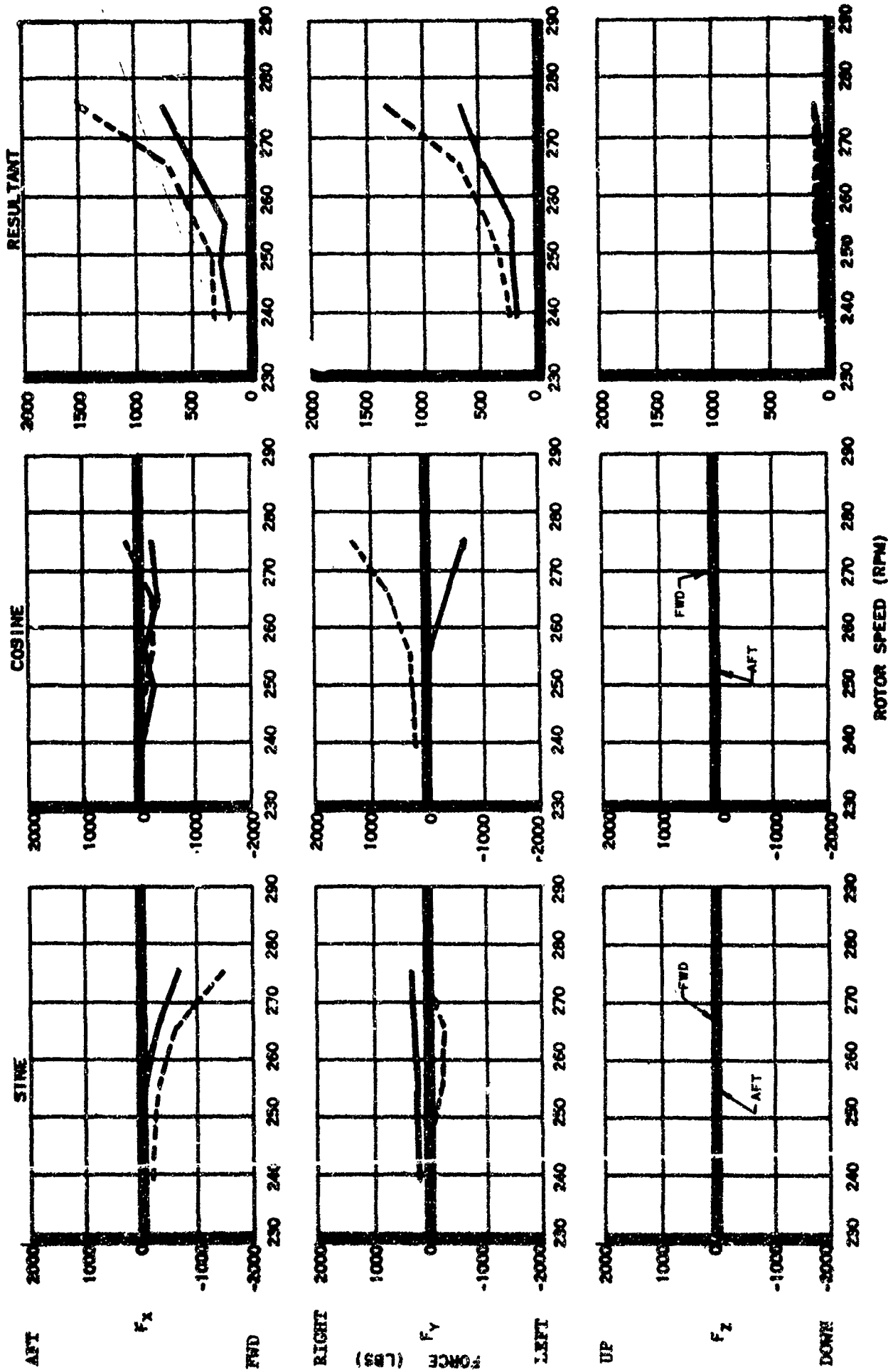


FIGURE 16b. POTATING SYSTEM FOURTH HARMONIC SHAFT LOADS
RPM SWEEP AT 40 KNOTS

G.W. = 13,500 LBS.
C.G. = 19 IN. FWD.

FLT. H21C-96X121
WOOD BLADES
IAS = 90

FWD ROTOR ———
AFT ROTOR - - -

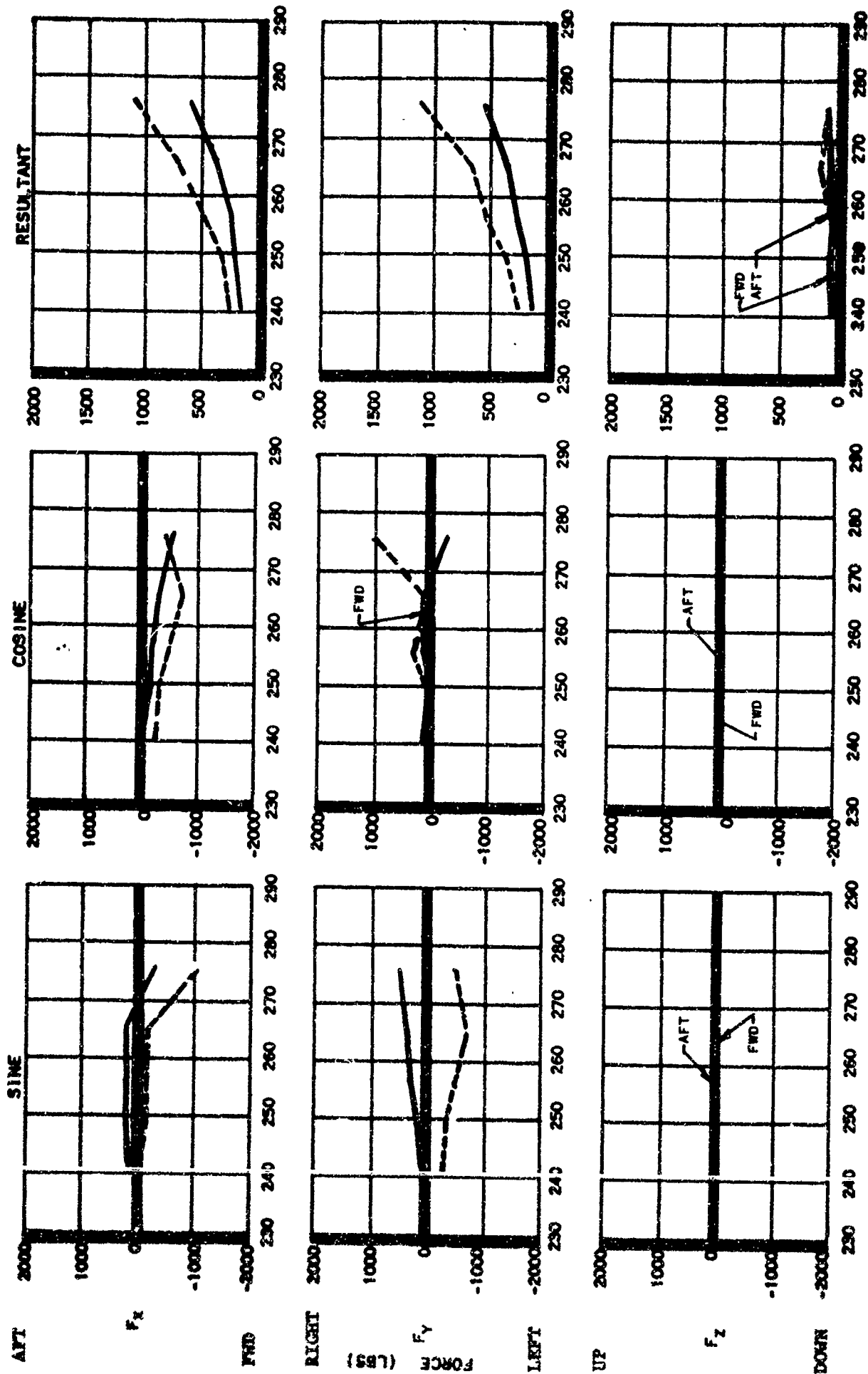


FIGURE 16c. ROTATING SYSTEM FOURTH HARMONIC SHAFT LOADS
RPM SWEEP AT 90 KNOTS

Conclusions

An extensive rotor hub load measurement program has been conducted, giving a complete picture of all the steady and oscillatory loads acting in the rotor shafts of a tandem helicopter. Shaft strain gage instrumentation was developed, calibrated and flown which had average accuracies of 6% for steady load and 4% for oscillatory load.

With a three bladed helicopter, third harmonic vibration levels are usually the dominant portion of the vibration environment, so that the third harmonic loads measured here are particularly important. Longitudinal shaft loads were the largest, averaging 800 lb at the forward rotor and 1300 lb at the aft; lateral loads averaged 250 and 500 lb forward and aft respectively; vertical loads averaged 200 and 400 lb forward and aft respectively. Both roll and pitch moments averaged 2,500 in. lb at the forward rotor and 5,000 in. lb at the aft rotor.

In-plane loads exhibited a trend with airspeed, low in hover, high at 20 knots transition, low at 80 knots cruise, and then a rise toward the top speed at 105 knots. Vertical loads differed; the forward rotor was high at hover and 105 knots, low at 60 knots; the aft rotor was low at hover and 105 knots, and peaks at 60 knots. Rotor speed sweeps at 40 and 90 knots indicated an extremely rapid load buildup with rpm for longitudinal load at both rotors and vertical load at the aft rotor. Lateral loads and the moments were not strongly affected by rpm.

Third harmonic vertical loads arise from direct addition of the vertical components of third harmonic blade root normal flap shears. Third harmonic in-plane loads come from second and fourth harmonic blade root lag shears and from horizontal components of second and fourth harmonic blade root normal flap shears. The measured second and fourth harmonic resultant rotating loads were the same in the longitudinal and lateral directions; in the rotating system these directions refer to the master hub spline azimuth and its perpendicular. The equality of these rotating longitudinal and lateral loads is a proof that the causative blade root shears are harmonically repetitive at each of the three blades. Second harmonic rotating loads averaged 500 lb at the forward rotor; 900 lb at the aft rotor. They displayed a tendency toward the high hover, low cruise, force levels which are characteristic of the fixed third harmonic airspeed sweep, and showed a definite increase with rotor speed. Fourth harmonic rotating loads averaged 250 lb at the forward rotor and 500 lb at the aft rotor. There were moderate changes with airspeed, but large increases with rotor speed. In converting to the fixed third harmonic system, second and fourth add to produce large longitudinal loads and subtract to produce small lateral loads.

**FULL-SCALE FLIGHT TEST DATA RELATING TO
ROTOR UNSTEADY AERCDYNAMICS**

Charles W. Ellis

Kaman Aircraft

FULL-SCALE FLIGHT TEST DATA RELATING TO ROTOR UNSTEADY AERODYNAMICS

**Charles W. Ellis
Chief Test Operations Engineer
Kaman Aircraft Corporation
Bloomfield, Connecticut**

INTRODUCTION

During the development of the HH-43B Huskie helicopter rotor system, which uses a servoflap-controlled, torsionally flexible rotor blade in a teetering hub configuration, the opportunity arose to obtain a limited amount of flight test data in areas related to rotor unsteady aerodynamics and dynamic loads. The data obtained allowed some insight into the significance of unsteady aerodynamics on forward flight rotor stability, of the influence of rotor stability margins on rotor loading in normal operating regimes, and of possible ground test methods for substantiating rotor flutter stability margins. This information is presented here in summary form.

BACKGROUND

During the conduct of the HH-43B structural demonstration program in 1959, flutter was encountered during the buildup to high-speed dive test conditions. Two distinct flutter modes were found, one involving servoflap bending and rotational deflection (against control system stiffness) and the other involving blade bending and servoflap rotational deflections. These flutter modes were found to be critically dependent on rotor lift coefficient and dynamic pressure, occurring only in high speed partial power descents.

Subsequent whirl testing at speeds well beyond normal overspeed whirl test requirements showed that it was possible to duplicate the in-flight occurrences during static whirling. This enabled standard flutter elimination techniques (mass balance, stiffness, and hinge moment changes) to be used to raise the flutter speed well above the operating range, and to substantiate this change prior to flight. Subsequent limit speed flights in the critical power ranges confirmed the satisfactory nature of the changes made, showing no re-occurrence of flutter in the entire flight envelope.

DISCUSSION

Figure 1 shows a typical variation of vibratory servoflap load with collective control position at constant airspeed. The data was obtained by establishing an airspeed in level flight and then slowly lowering collective while increasing rate of descent so as to maintain airspeed. Collective variation was sufficiently slow as to make each data point shown a quasi-steady state point. When the collective control position reached 48 percent of the level flight requirement, a very sudden increase in flap vibratory load was noted. Detailed examination of the oscillograph data shows this increase in load to have resulted from the sudden appearance of a new non-harmonic frequency in the loading. This frequency appeared each time the blade reached the maximum dynamic pressure (advancing blade) region, then damped out rapidly as the blade total velocity was reduced. Recovery was accomplished by a further reduction in power, which again returned flap loading to normal levels.

Whirl testing showed this particular flutter mode to be a coupling of rotor blade third symmetrical bending deflection with servoflap rotational deflection (against control system stiffness). Flutter only occurred when rotor loading was very close to zero lift (approximately $\pm 10\%$ of one "g" thrust). Flutter did not occur at integer multiples of Rotor speed nor at any fixed multiple of rotor speed.

Analysis of blade loading in flight also showed that the lift coefficient on the advancing blade at the flutter point was very close to zero. Flutter frequency was also equal to third symmetrical blade bending frequency. Apparently, then, a wake coupling existing in hover operation and showing a strong variation with lift coefficient persisted with similar lift coefficient effects out to advance ratios of at least 0.29.

Since standard flutter analysis methods showed extremely poor absolute correlation with the test results, the trends indicated to be significant by analysis were explored on the whirl test facility. Use of servoflap mass balance was shown to provide the most expeditious means of eliminating the flutter mode. This approach was substantiated on the whirl rig and then in flight, yielding the data shown in Figure 2. This plot shows the variation of maximum vibratory flap load with airspeed before and after the incorporation of the servoflap mass balance. Below the flutter speed point no influence of the flutter mode on vibratory flap loads can be detected, both the the original and the revised configuration showing identical loads. Similar trends were noted in blade torsional loadings.

It might be of interest to note here that flutter loadings were considerably higher during static whirl testing than in flight. This appeared to be due to the intermittent entry and departure from the flutter zone in flight as compared to the continuous penetration of the boundary during static whirl. The intermittent operation appeared to substantially limit flutter load buildup.

The incorporation of servoflap mass balance shifted the blade chordwise center of gravity aft. As predicted in Reference 1, this change in chordwise c.g. resulted in an increase in high speed rotor vibratory shear and bending moment. It was therefore necessary to add additional blade mass balance to compensate for the change produced by the flap counterweight. Figure 3 shows the effects of this change on blade root flatwise vibratory loading, and compares the results with the load variation predicted in Reference 1. Somewhat larger flight test variations are seen than were calculated. It should be pointed out that this change in blade root loading increased rapidly with airspeed, indicating the increasing importance of blade torsional deflections on flatwise loading as airspeeds are increased. Using cg-ac offset as a means of vibratory load reduction at high speed, as suggested by Reference 1, appears to be a powerful tool; a 1/2% change in cg-ac offset produced an 18% reduction in flatwise vibratory loading.

It has already been pointed out that static whirl testing was successful in reproducing the characteristic frequency and lift coefficient sensitivity of the in-flight flutter modes. It is interesting to also note, as shown in Figure 4, that whirl test flutter speeds and flight test flutter speed correlated well on a servoflap dynamic pressure basis. While this result appears to be somewhat different than results obtained on model rotors in the wind tunnel, and hence may only be applicable to rotor systems with localized control devices, it has provided a convenient means of providing successful ground substantiation of flutter integrity in subsequent servoflap rotor configurations. Flight test investigation on these rotor systems has continued to prove that freedom from flutter on the whirl rig means freedom from flutter in flight up to similar servoflap dynamic pressure. Combinations of overspeed and propeller slipstream velocity were used in achieving desired test "q". Additional testing to define the usefulness of this method for general flutter substantiation would be desirable.

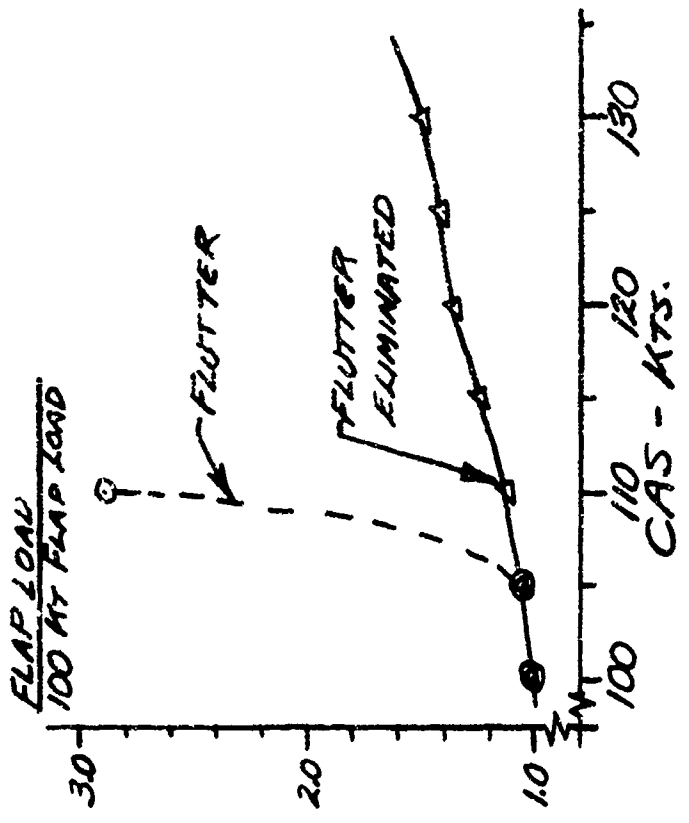
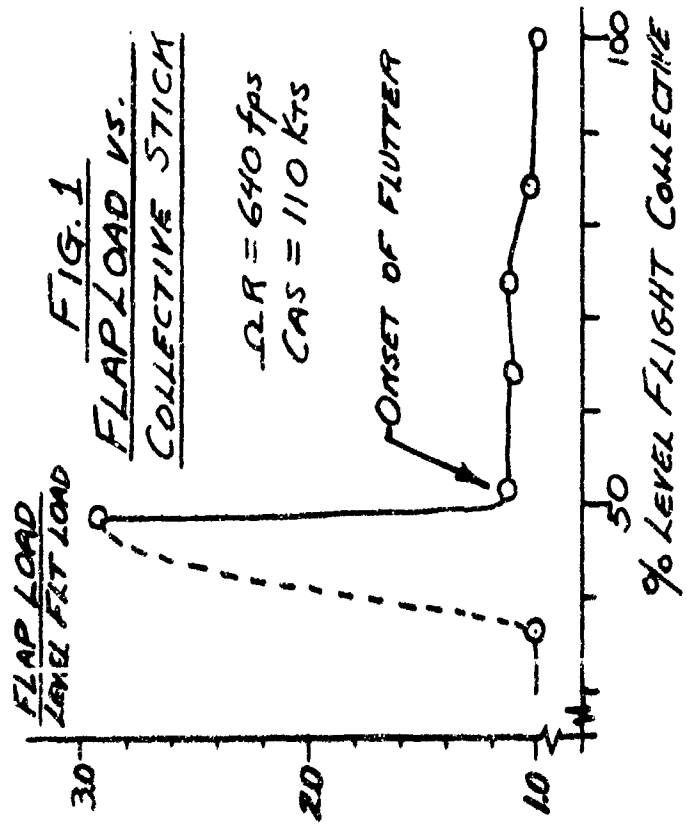
SUMMARY

In summary the data shown here indicates that:

1. Reduced damping at zero lift coefficient (wake effects) apparently persists at substantial advance ratios (up to 0.3)
2. Torsional coupling and relation between operating chordwise c.g. and flutter boundary can have a significant influence on blade vibratory loading.
3. Constant dynamic pressure testing offers some promise of providing a means for static flutter margin substantiation.

REFERENCES

1. Helicopter Blade Vibration and Flutter, R. H. Miller and C. W. Ellis, Journal of the American Helicopter Society, July 1956



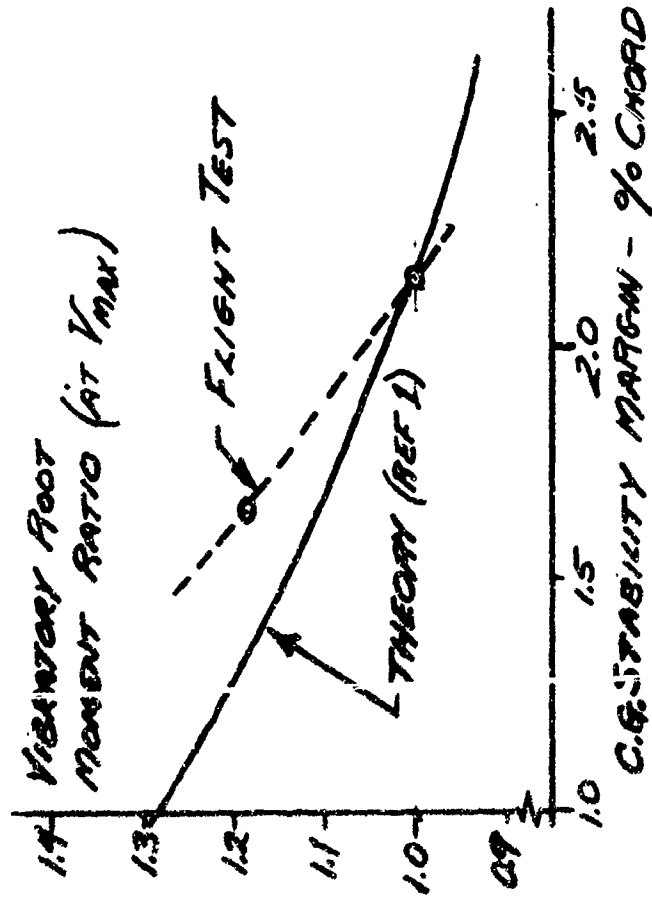


FIG. 3
EFFECTS OF CHORDWISE C.G. ON
BLADE VIBRATORY LOADING AT V_{max}

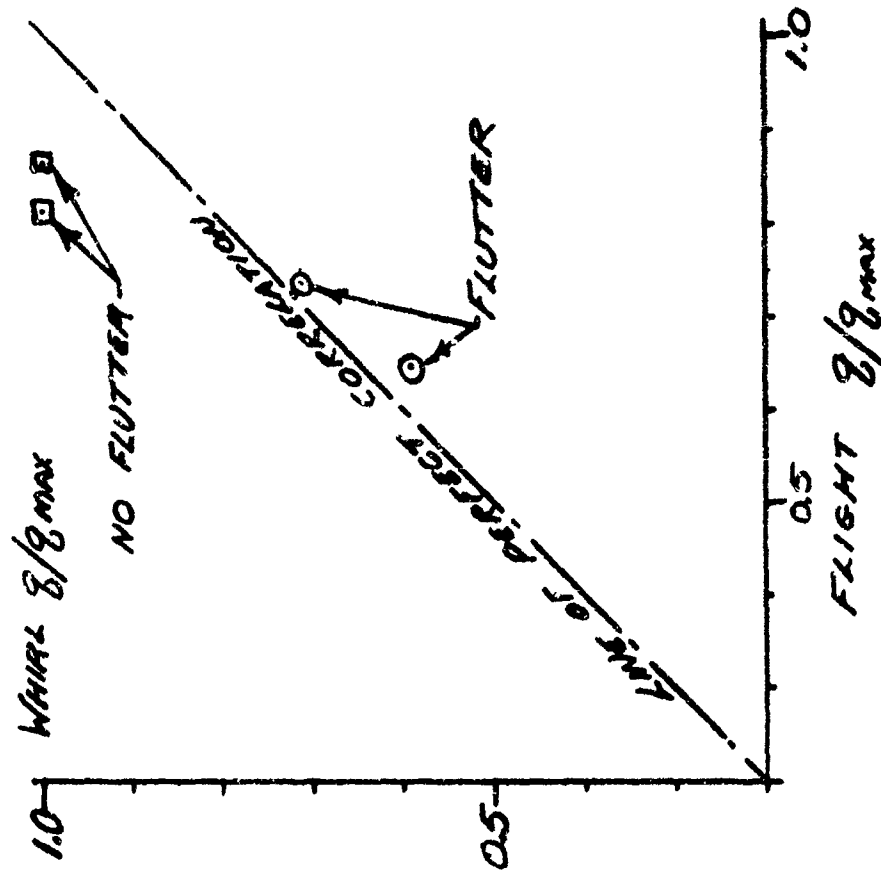


FIG. 4
COMPARISON OF FLIGHT AND
WHIRL TEST FLUTTER SPEEDS

**EXPERIMENTAL AND THEORETICAL STUDY
OF LOCAL INDUCED VELOCITIES
OVER A ROTOR DISC**

S. Tararine

Giravions Dorand, Paris, France

EXPERIMENTAL AND THEORETICAL
STUDY OF LOCAL INDUCED VELOCITIES
OVER A ROTOR DISC

by

V.S. TARARINE

GIRAVIONS DORAND - PARIS - FRANCE

ORAL VERSION

If we have to evaluate the aerodynamic loads over a helicopter rotor disc, we must take in account the effects produced by wake vortices issuing from the blades.

Our purpose is to define these wake vortices in permanent state by using results of tests performed in the wind tunnel. This will be done in three steps:

1. First we shall show the location of helix vortices.

2. Then we shall apply these results to a sample calculation in hovering flight.

3. Finally we shall give some results for the transient dynamic case.

The most extensive part of the results presented in this paper comes from the "Experimental and theoretical study of local induced velocities over a rotor disc for analytical evaluation of the primary loads acting on helicopter rotor blades". This work was carried out by "GIRAVIONS DORAND & Co." under the sponsorship of the EUROPEAN RESEARCH OFFICE U.S. DEPARTMENT OF THE ARMY.

I take here the occasion to thank the U.S.A. TRECOM who made it possible for this work to be accomplished and to be presented here to day.

All the wind tunnel tests were performed in the wind tunnel of the Institut de Mécanique des Fluides at Marseille.

LOCATION OF FREE VORTICES

Slide 1 shows the case where the circulation Γ is constant along the span but varies with time. The straight sides of the classical horseshoe vortices are now helix like curved lines. The radial vortices appear as the rate of circulation Γ changes with time.

Slide 2 shows the theoretical case where the circulation Γ varies along the span. The rapid rate of change of Γ at the tip of the blade, between points 2 and 3, produces a well located vortices which can easily be seen in wind tunnel. The slow rate of change of circulation Γ at the root of the blade between 1 and 2 gives a more diffused vortices.

Slide 3 offers a theoretical explanation.

Slide 4 shows the tip vortices. The helix is strongly deformed at the rear section under the disc.

Slides 5 and 6 show the root helix vortex which is moving in a turbulent region.

Slides 7 and 8 show the tip helix vortices. I have drawn the contour line of the root vortex. The interference between the two vortices is the cause of the strong deformation of the helix at the rear sector of the disc.

For this reason we can not assume a regular helix form and we are obliged to consider the real helix.

1.2 - Tip vortices

Slide 9. For an instantaneous azimuthal position $\psi = \Omega t$ of the blade we have measured the vertical distance $A_1 A_2, A_2 A_3$ between two successive vortices. In this way we know the correct distance of the vortices in the neighbourhood of the instantaneous blade position. This measurement was made on corresponding pairs of photos.

We have achieved this in two different ways.

In the first method smoke was emitted from the tip of the blade. We have already seen a pair of these photos.

In the second method (slide 10 and 11) the smoke emission was external and was directed so that the tip of the blade cut the smoke at different given azimuthal angles.

- For every "flight" we repeated the experiment for 24 different azimuthal values.
- We may write that the vertical distance $A_1 A_2$ is product of $V_{iz}(\psi)$ inflow velocity time the time interval which separate two successive vortices.

$$(1,1) \quad \begin{cases} A_1 A_2 = A_2 A_3 = \frac{T}{b} V_{iz}(\psi) \\ T = \frac{2\pi}{\Omega} \\ b = 2 \end{cases}$$

$V_{iz}(\psi)$ velocity is the inflow velocity induced by the wakes. This velocity is not the induced velocity to be introduced in the thrust formula but it helps us to locate correctly the wake vortices in the neighbourhood of the instantaneous blade position.

We have compared this inflow Velocity to the mean induced FROUDE velocity V_{im} given in the text book :

$$(1,2) \quad V_{iz}(\psi) = V_{im} \left[1 + \delta \overline{V_{iz}}(\psi) \right]$$

Slide 12 - The typical variation of non dimensionnal inflow velocity with azimuth is shown in slide 12.

Slide 13 shows the same variations around the disc.

1.3 - We have studied the different influences of :

- collective pitch
- tip speed ratio
- angle of attack of the rotor
(α is considered negative for nose up)
- cyclic pitch (pitch and roll)
- solidity
- Lock's constant.

Different curves are given in the text. The most important influences come from the tip speed ratio, angle of attack of the rotor and cyclic pitch. The collective pitch and solidity influence mainly the mean value V_{im} .

1.4 - We are now able to give coordinates of an element of a helix vortice.

Slide 14. Let us consider at time t a vortice element wich had left the blade τ_1 seconds ago that is to say at $t - \tau_1$

- For an element of tip vortice we propose :

$$(1,3) \quad \begin{cases} x_T = -V \cos \alpha \cdot (t - \tau_1) + R \cos \Omega \cdot (t - \tau_1) \\ y_T = R \sin \Omega \cdot (t - \tau_1) \\ z_T = -R \beta (t - \tau_1) + V_{iz}(\psi_1) \cdot (t - \tau_1) \\ \psi_1 = \Omega (t - \tau_1) \end{cases}$$

This means that after leaving the blade the vortice element has been taken by the resultant wind due to flow velocity plus $V_{iz}(\psi_1)$ (the inflow velocity is shown in the curves given in the text).

- For an element of helix vortice we propose the following formulae:

$$(1,4) \quad \begin{cases} x_R = -V \cos \alpha \cdot (t - \tau_1) + r_0 \cos \Omega \cdot (t - \tau_1) \\ y_R = r_0 \sin \Omega \cdot (t - \tau_1) \\ z_R = -r_0 \beta (t - \tau_1) + V_{im} (t - \tau_1) \end{cases}$$

After a period, r_0 is situated approximately at the center of gravity of the positive derivatives $\frac{\partial \Gamma}{\partial r}$ of the circulation.

1.5 - Slide 15 - The strengths Γ of the tip vortices are equal and opposite :

$$(1,5) \quad \Gamma_M = \left[\frac{1}{2} C_L \cdot c \cdot (\Omega r + V \sin \psi) \right]_{\text{Max}}$$

The Γ_M value can be developed as a FOURIER series and the first term can be estimated by the formula of MEIJER DREES.

1.6 - We may now calculate the location of wake vortices.

2 - EXAMPLE

2.1 - How may we apply the previous results to calculate aerodynamic loads along the blade.

Slide 16 - We shall treat the wake of the blade in two zones. The first zone is in the plane of the disc; it is defined by two azimuthal positions :

$$(2,1) \quad \left\{ \begin{array}{l} \text{instantaneous} \quad \psi = \Omega t \\ \text{and} \quad \psi = \Omega \left(t - \frac{T}{4} \right) \\ T = \frac{2\pi}{\Omega} \end{array} \right.$$

This zone can be treated by methods similar to those used for fixed wings.

- The second zone of the wake comprises two helix vortices and possibly radial vortices. We estimate that if the disc loading is great enough we can take into account only helix vortices with a constant Γ_0 circulation strength.

2.2 - As a numerical example we took the two blade rotor of Mr John R. RABBOTT Jr. (NACA T.N. 3688 July 1956, and we shall compare the theoretical results to the experimental results found by Mr RABBOTT.

Slide 18. The local circulation $\Gamma(r)$ at a station r along the A blade is given by the lift line equation :

$$(2,2) \quad \Gamma_A(r) = \frac{1}{2} \Omega r c \frac{dC_L}{d\alpha} \left(\theta_c - \frac{V_{iA}}{r} - \frac{V_{iB}}{r} \right)$$

The induced velocities are produced by the wake of blade A and blade B. The velocity produced by the wake of blade A is divided into two zones (1 and 2) the new equation can be written as follows :

$$(2,3) \quad \Gamma_A(r) = \frac{1}{2} c \frac{dC_L}{d\alpha} \Omega r c - \frac{1}{2} c \frac{dC_L}{d\alpha} \int_{r_0}^R \frac{\partial \Gamma}{\partial r_1} \cdot \frac{1}{11,4} \cdot \frac{dr_1}{r - r_1} \\ - \frac{1}{2} c \frac{dC_L}{d\alpha} (\overline{V}_{iA} + \overline{V}_{iB}) \Gamma_M$$

The unknown quantities are :

$$(2,4) \quad \left\{ \begin{array}{ll} \Gamma_A(r) & \text{a function of } r \\ \Gamma_M & \text{maximum value of circulation} \\ V_{im} & \text{inflow velocity} \end{array} \right.$$

The inflow velocity value is calculated by the elementary FROUDE strip formula at $\bar{r} = 0,5$.

- To resolve the equation we used an iterative method. We estimate the value of Γ_M and we calculate the $\Gamma_A(r)$ function. Then we draw the curve $\Gamma_A(r)$ to obtain a new maximum value; the process is repeated and in the case presently considered we found we required four iterations to obtain a good solution (Slide 19).

The comparison between the proposed method (Slides 20 and slide 21) and the experimental results is valuable. However it will be necessary to examine other examples to verify the theory.

3 - SOME RESULTS FOR THE TRANSIENT STATE AERODYNAMICS

- 3.1 - These a few underlying results of transient state aerodynamic will help us to propose a treatment which take into account the effect of radial vortices in permanent state.

- 3.2 - If we change the collective pitch from θ_{c0} to θ_{c1} (Slides 22, 23,) the response in thrust of the rotor can present very different aspects because there are many phenomena which may interfere.

- Primary factors seems to be :

- a) the rate of change of collective pitch
- b) flapping movement
- c) disc loading.

We shall now consider a few results experimentally observed.

- 3.3 - The two blade rotor had heavy blades (the LOCK constant was approximately 0.64). This enabled the wake aerodynamics to be observed. The flapping movement is small but poorly damped (Slides 24 and 25).

The circulation Γ around the blade is :

$$(3,1) \quad \Gamma = K \left(\theta_c - i_I - \sum i_{II} \right)$$

i_I is the induced angle by the first zone of the wake.

i_{II} is the induced angle by the second zones of the wake.

As the circulation Γ changes with time the tip helix vortices is fed with new vortices. These vortices can be seen in the wind tunnel by means of smoke tracers. Their number increases with the rate of change of collective pitch (Photos).

These vortices produce a double effect :

- 1 - They pass under the blade and may induce the LOEWY'S (Van VOOREN) effect.
- 2 - They deform the wake and change its intensity.

We have effected in hovering "flight" a slow rate of change of collective pitch, the distance between two successive vortices was greater than 1 - 1,5 chord lengths. Within boundaries of this experiment remarks.

- 1 - If we change collective pitch from θ_c to θ_{c1} the final permanent state is established after the vortices $\frac{\partial \Gamma}{\partial r}$ has travelled a vertical distance equal to approximatively one blade chord.
- 2 - The thrust variation with time is not exactly the same if we diminish or increase the pitch.
- 3 - If the change of pitch is sinusoidal having a frequency from 0.5 to 3.5 cps, there is phaselag between the pitch and thrust variation of about one period ($T = \frac{2\pi}{\Omega}$)

The thrust is proportionnal to :

$$(3,2) \quad \begin{cases} \theta_c - \Delta t \cdot \dot{\theta}_c = f(t - \Delta t) = f(t) - \frac{\Delta t}{1} \dot{f}(t) \\ \Delta t \neq T \end{cases}$$

3.4 - The influence of flapping may have two aspects :

- 1 - The flapping velocity changes the circulation Γ of the blade :

$$(3,3) \quad \Gamma = k \left(\theta_c - i_I - \sum i_r - \frac{1}{\Omega} \dot{\beta} \right)$$

- 2 - The flapping modifies the distance from the blade to the wake under the disc. This distance measured in half chords is :

$$(3,4) \quad \frac{2\beta r}{\alpha c} = \frac{\beta}{\alpha} \cdot \frac{b}{\pi r}$$

α angle of incidence of the blade

$\hat{\sigma}$ local solidity.

This distance can be quit great in two cases :

a) - light blades excited at frequencies between 0 and Ω ,

b) - all blades at the resonance frequency Ω .

The two previous phenomena are bound together. We can observe them on the slide (22). As the pitch has reached its final value there remains some time after only the movement of the blade it self.

Theoretically the thrust variation is proportionnal to : (Slide 36)

$$\frac{1}{\Omega} \dot{\beta}$$

(Slide 22) In fact the thrust oscillates with a period 30 % greater than $T = \frac{2\pi}{\Omega}$ period of revolution.

The damping of this oscillation is lower by about one half than theoretical one.

3.5 - Conclusion

We estimate that in usual permanent flight the effect of the variation of circulation $\frac{\partial \Gamma}{\partial r}$ which is attached to radial and helix vortices will be a corrective only. We suggest the following form :

$$\Gamma(t - \Delta t) = \Gamma(t) - \frac{\Delta t}{1!} \dot{\Gamma}(t)$$

4 - CONCLUSION

- 1 - We tried to define the wake vortices by using extensive experimental results in non dimensional form.
- 2 - The strong interference between the two helix deforms the regular curves and we are obliged to consider the real helix. This phenomenon is certainly influenced by the neighbourhood of the fuselage for low " μ ".

--oo000--

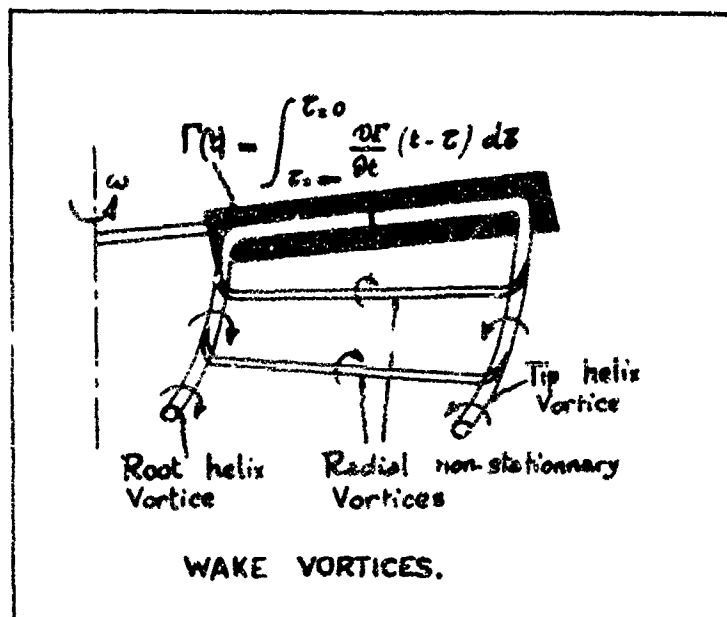


Fig. 1

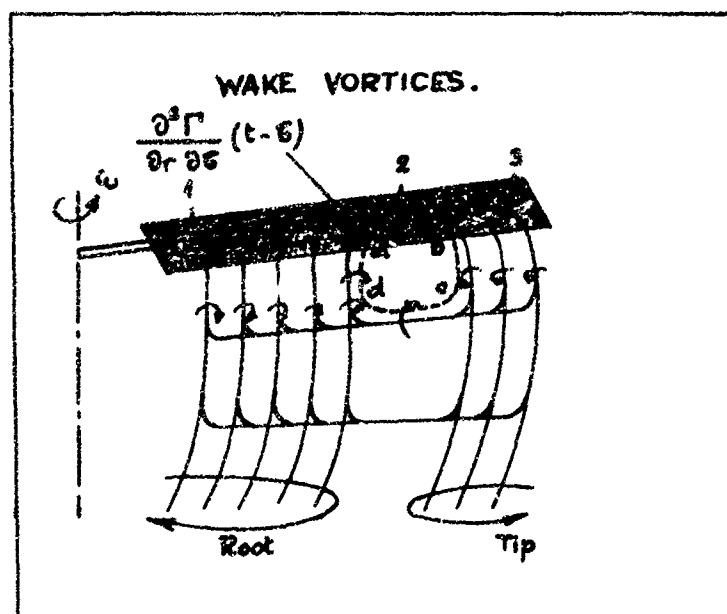


Fig. 2

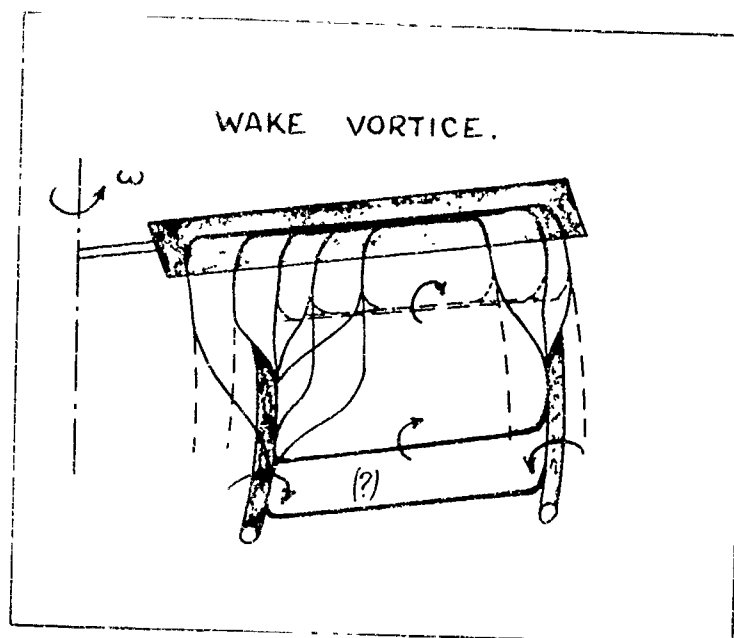


Fig. 3



Fig. 4

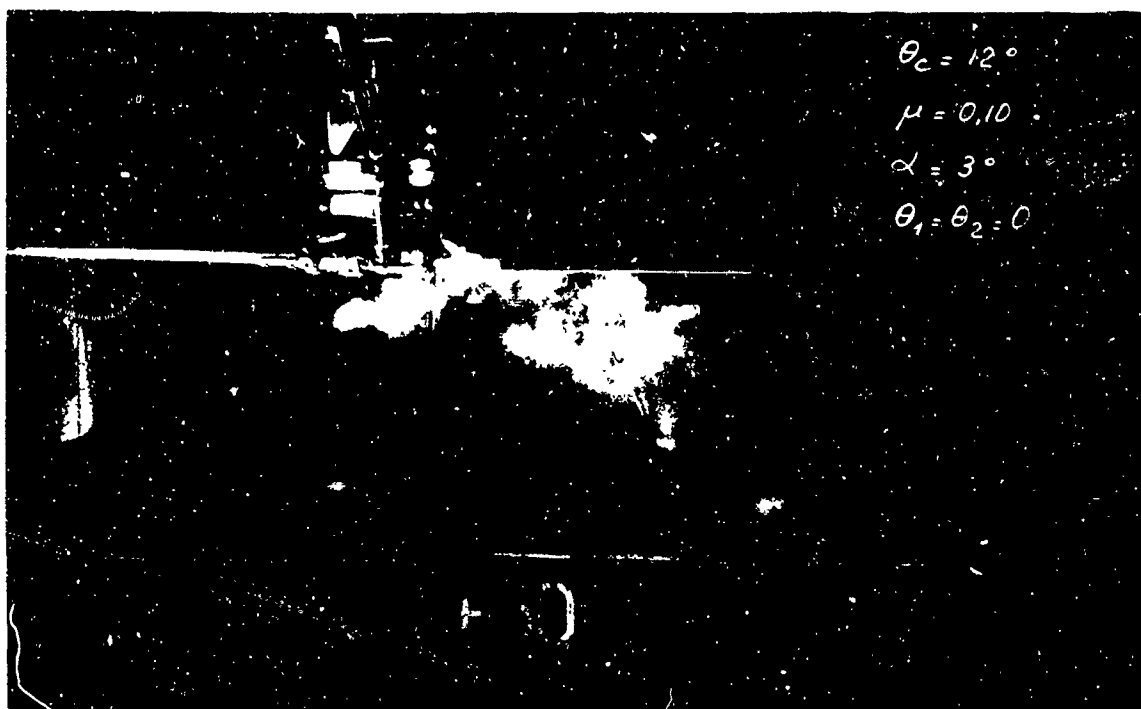


Fig. 5

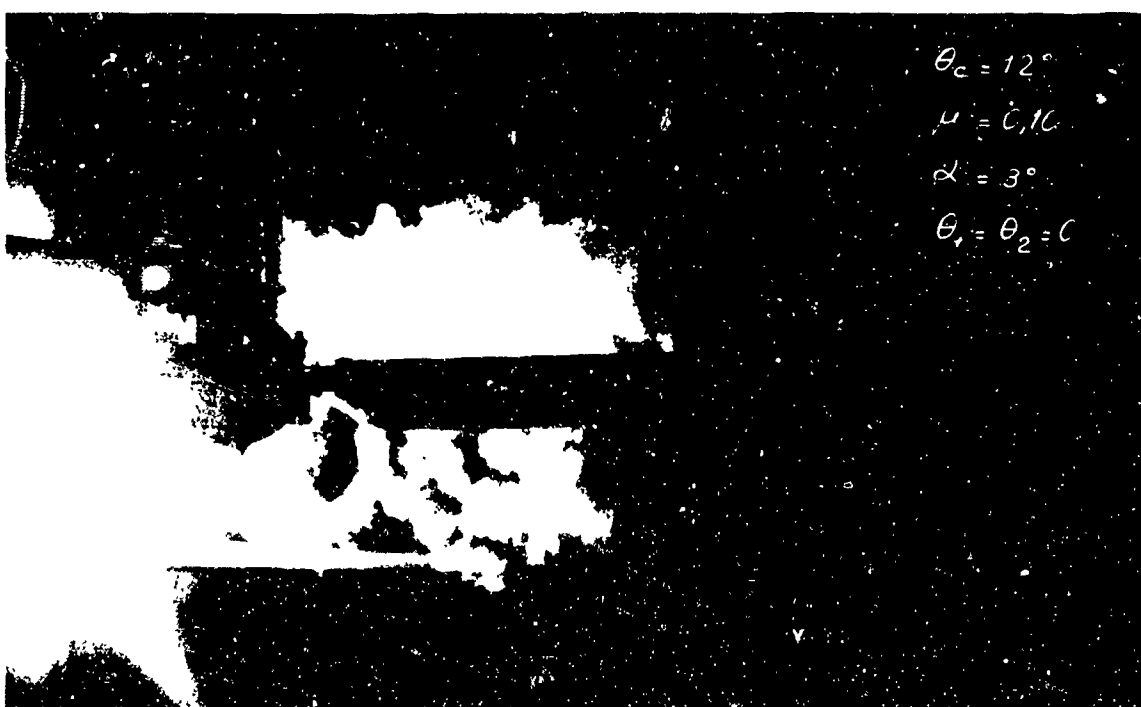


Fig. 6

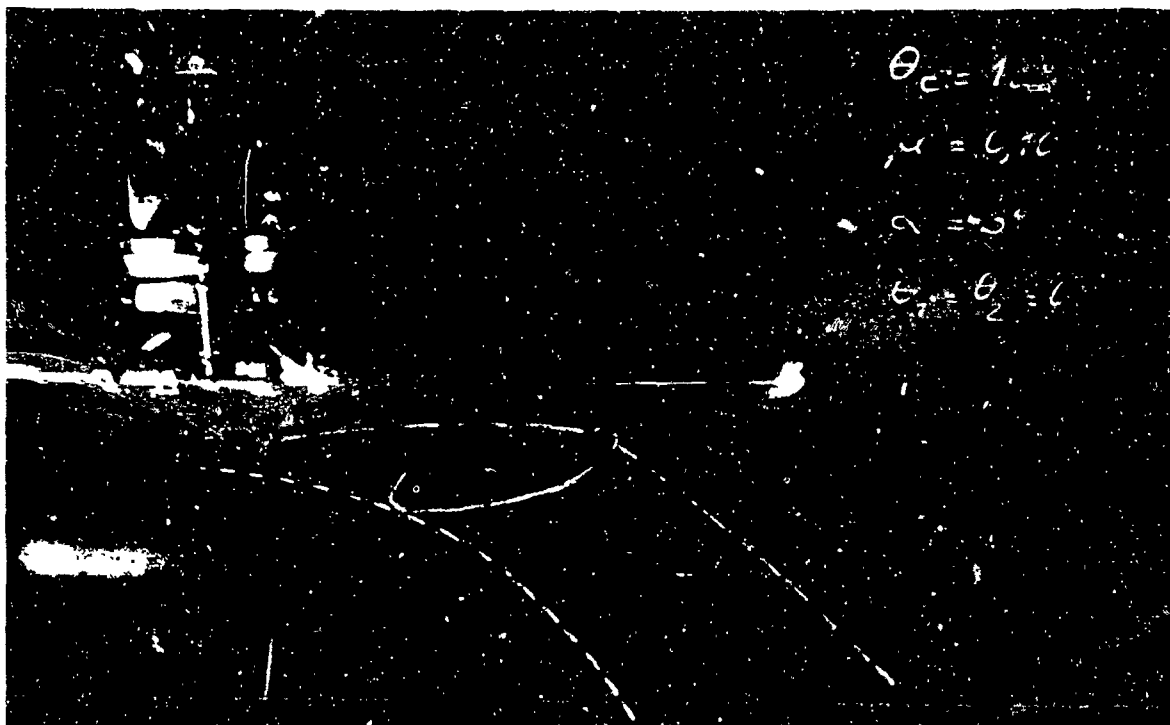


Fig. 7

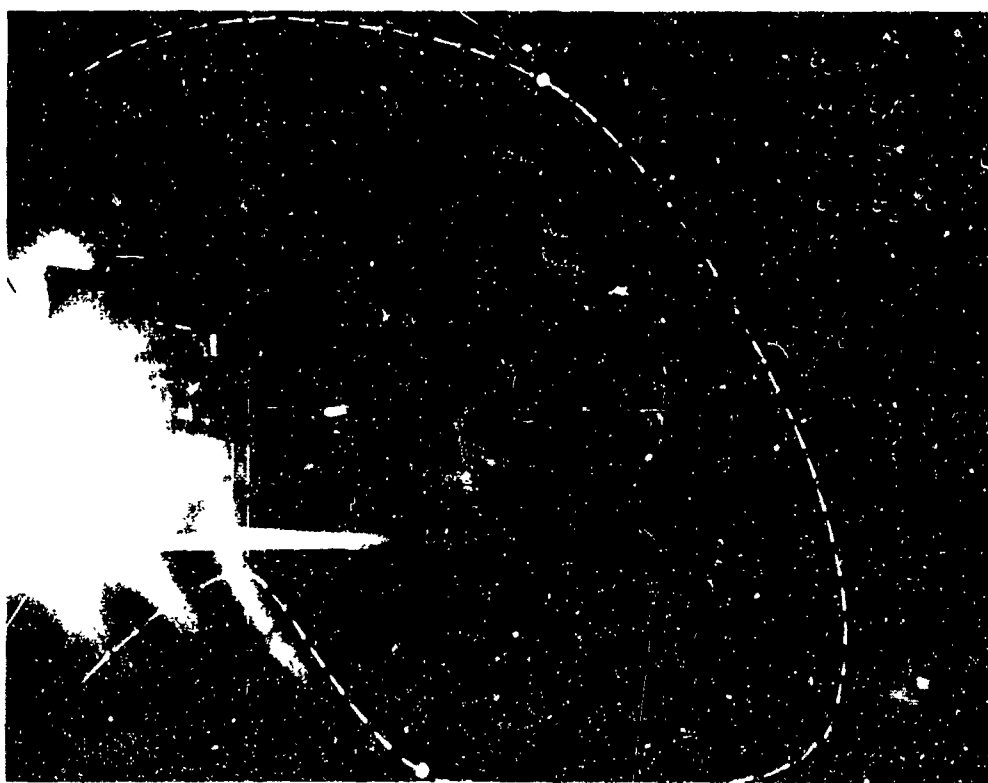


Fig. 8

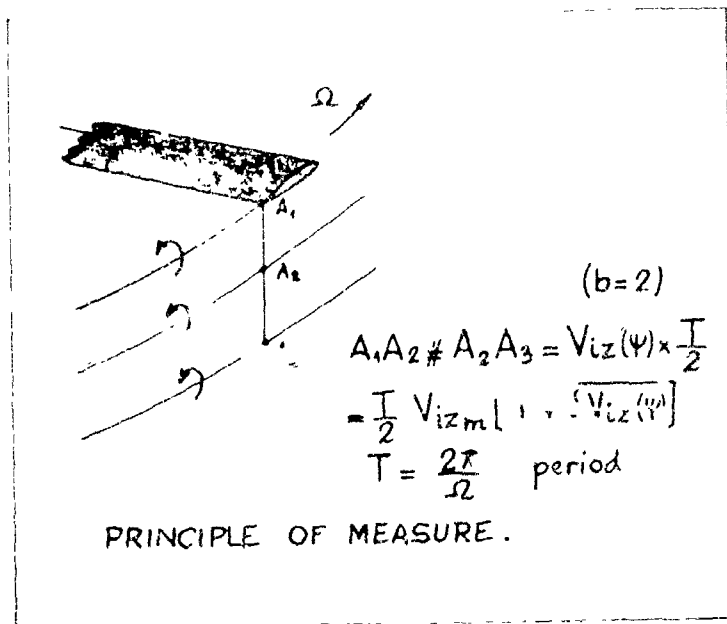


Fig. 9

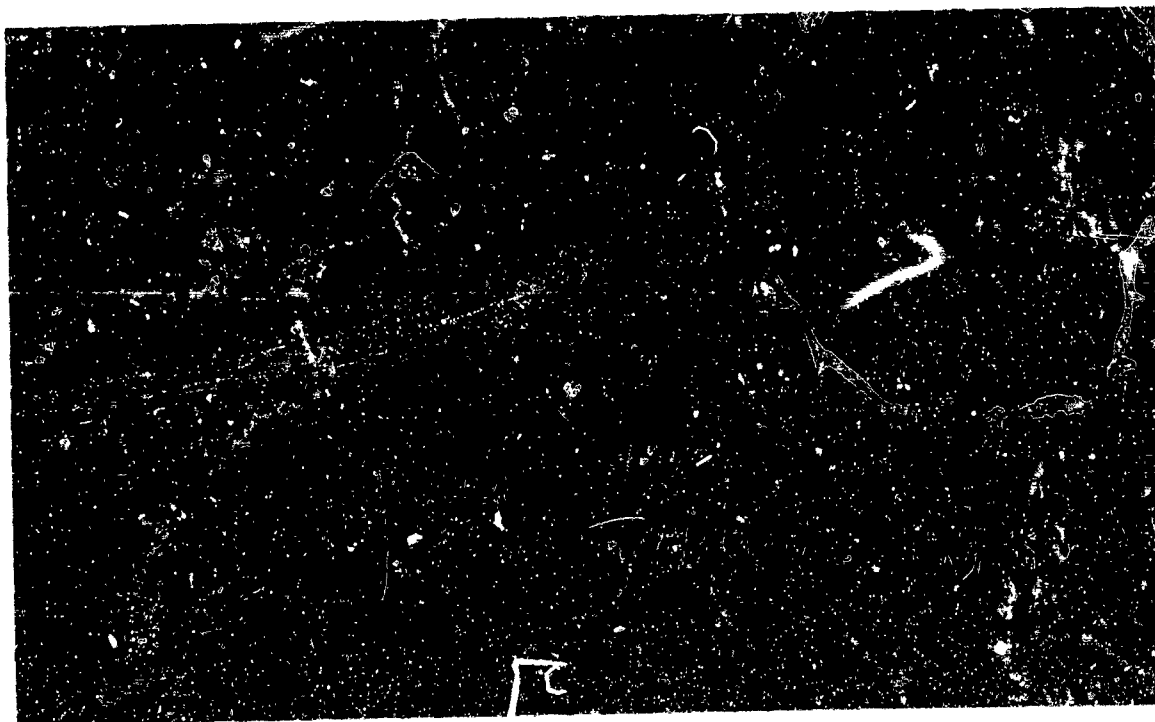


Fig 10



Fig. 11

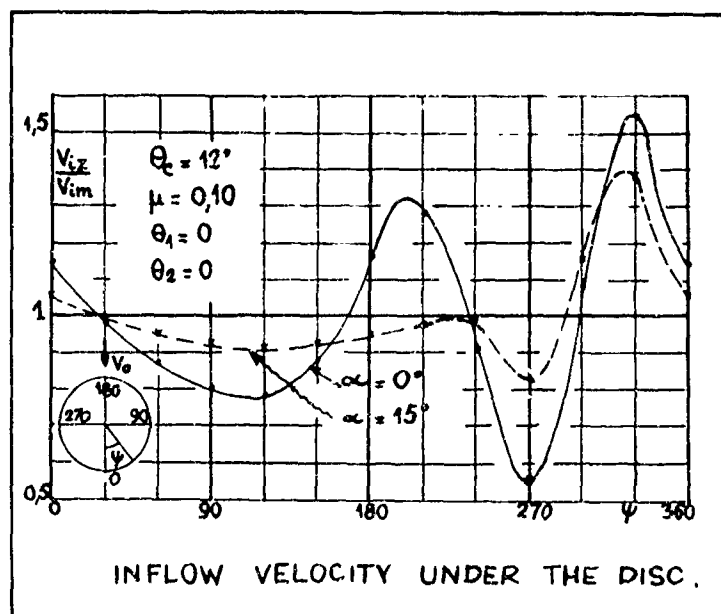


Fig. 12

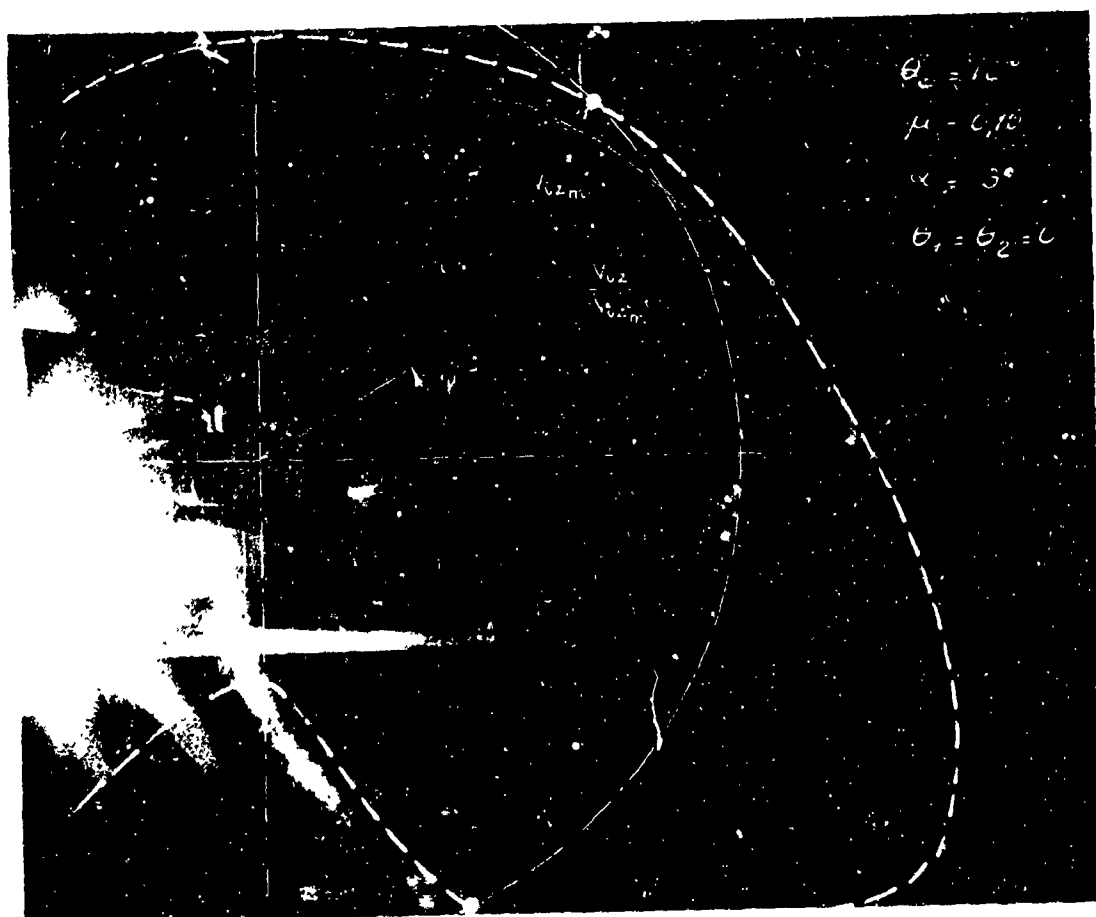
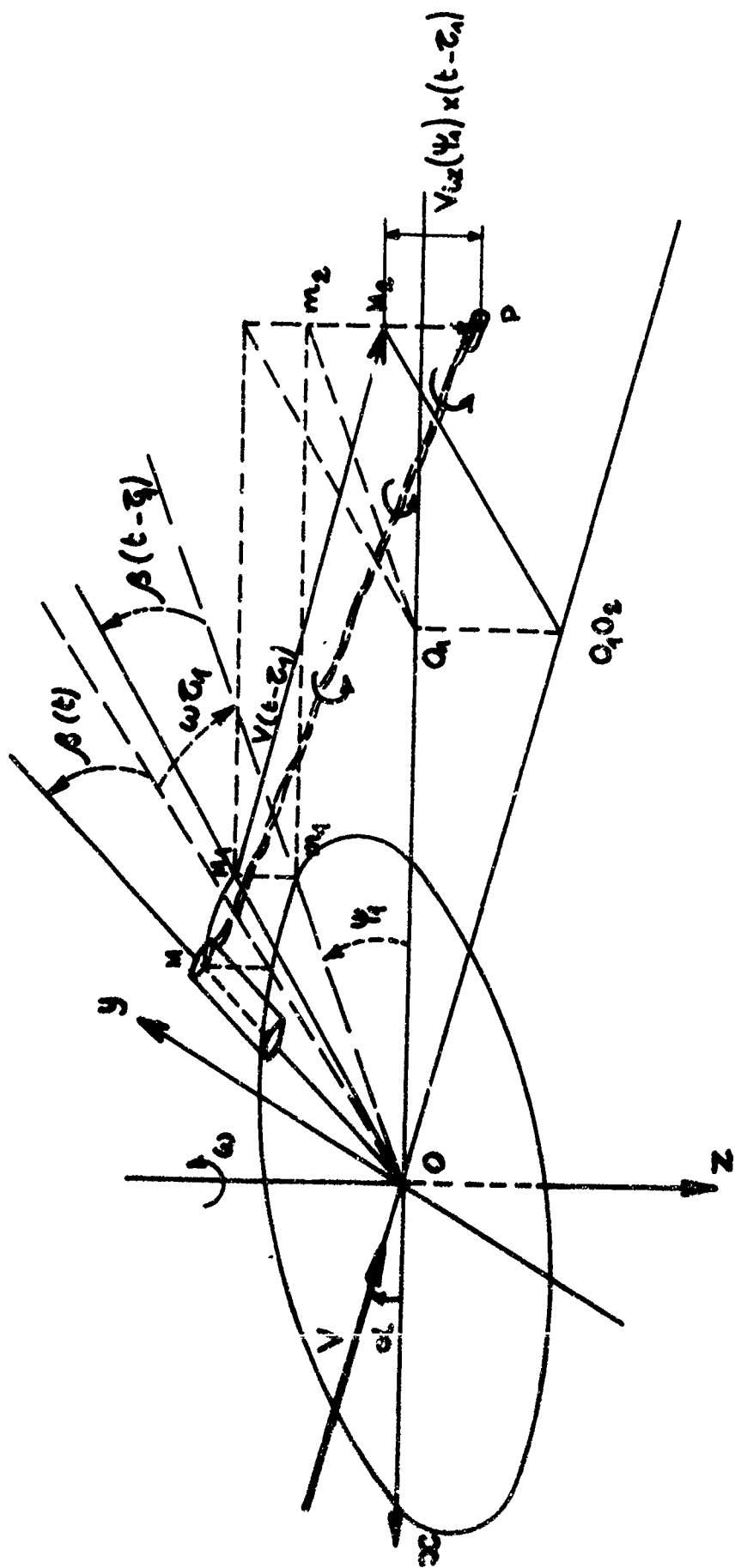


Fig. 13



$$-x_T = V_{imax} \cdot (t - \tau_1) + R \cos \omega(t - \tau_1)$$

$$y_T = R \sin \omega(t - \tau_1)$$

$$x_T = -R \beta(t - \tau_1) + V_{iz}(\psi_1)(t - \tau_1)$$

$$\psi_1 = \omega(t - \tau_1)$$

LOCATION OF HELIX VORTICE.

Fig. 14

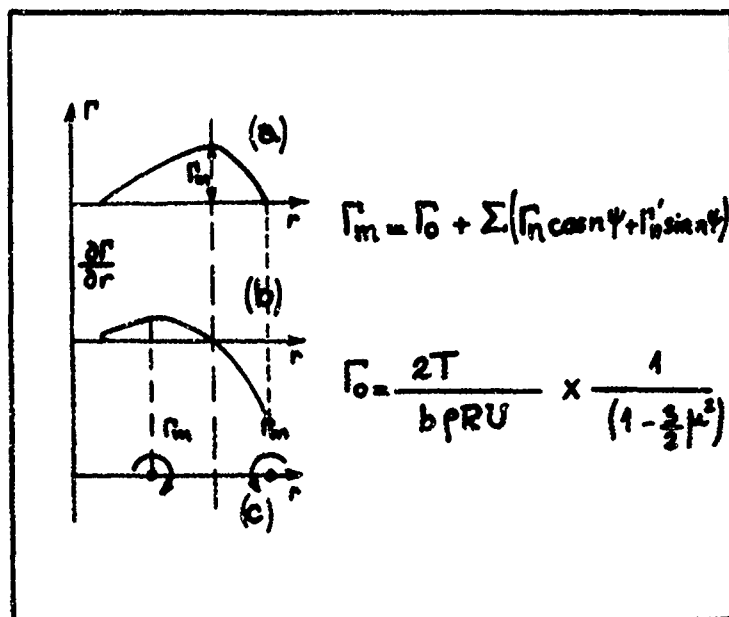


Fig. 15

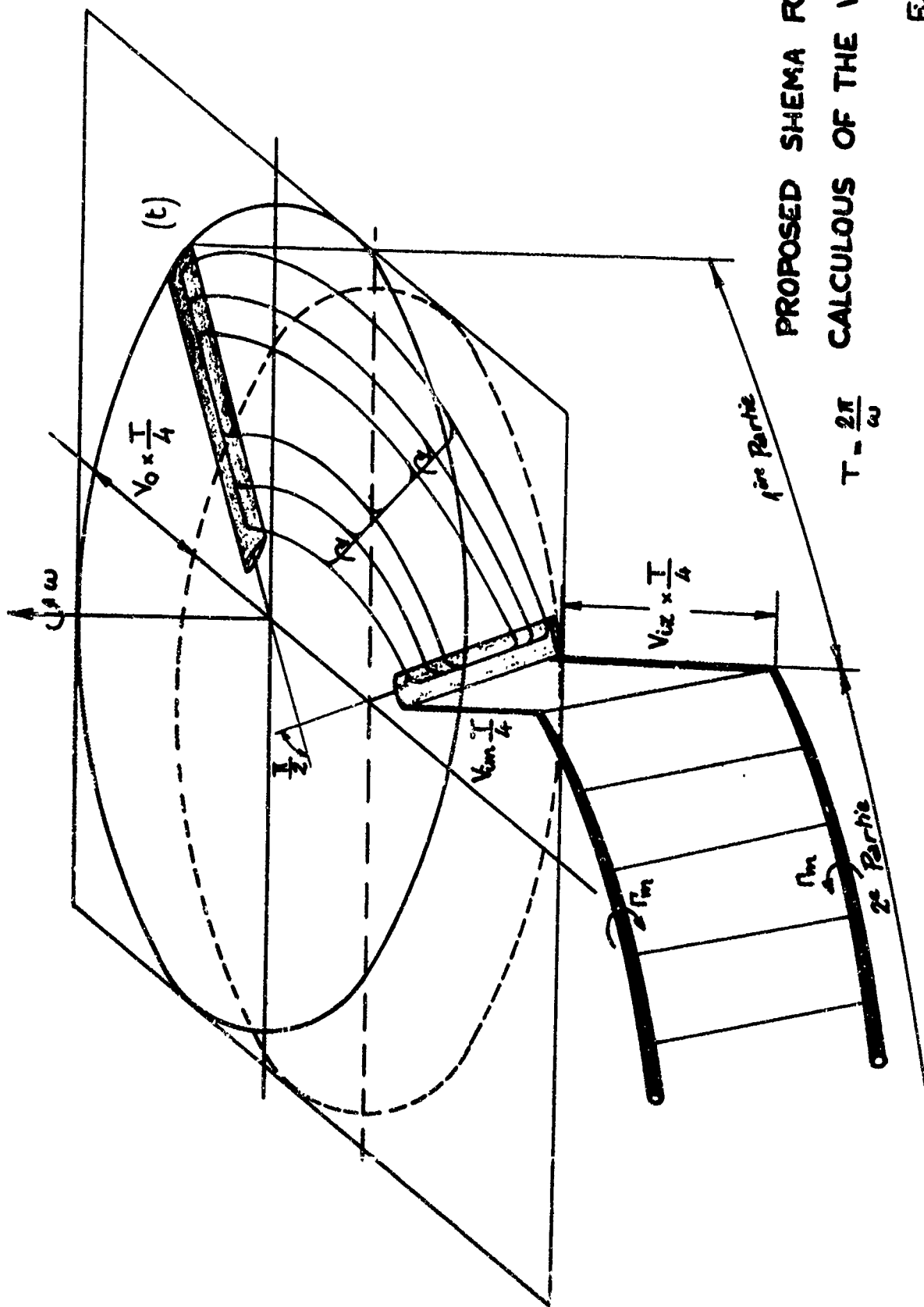
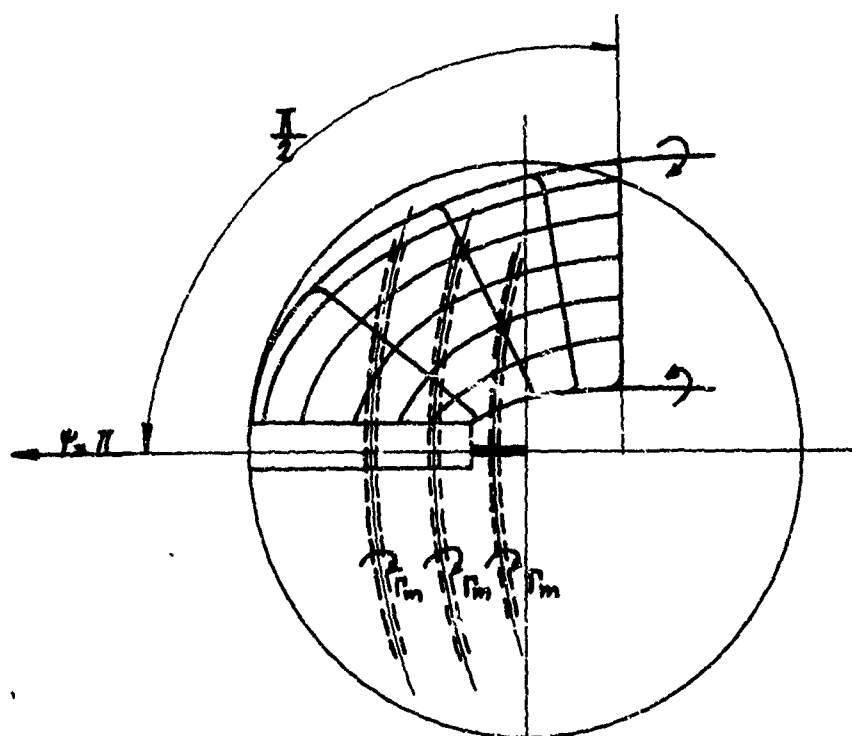


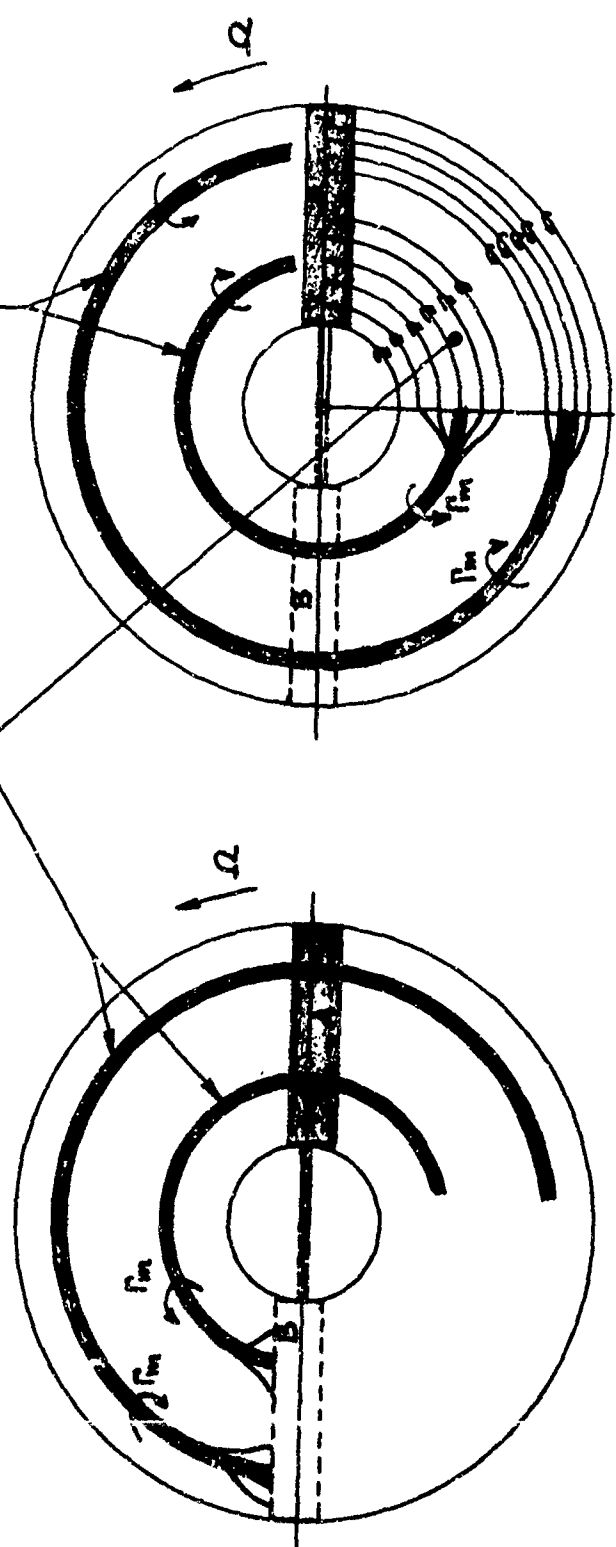
Fig. 16



SHEMA OF CALCULOUS.

Fig 17

$$\frac{1}{2} \frac{d\epsilon_i}{d\epsilon_i} \cdot \Gamma_A(r) = \Omega r \theta_i - \int_{r_0}^r \frac{\partial \Gamma_A}{\partial r} \cdot \frac{1}{11,4} \cdot \frac{1}{r-r_1} \cdot \frac{1}{r-r_2} dr - [\bar{V}_{iA} + \bar{V}_{iB}] \Gamma_M$$



CALCULOUS IN HOVERING .

Fig. 16

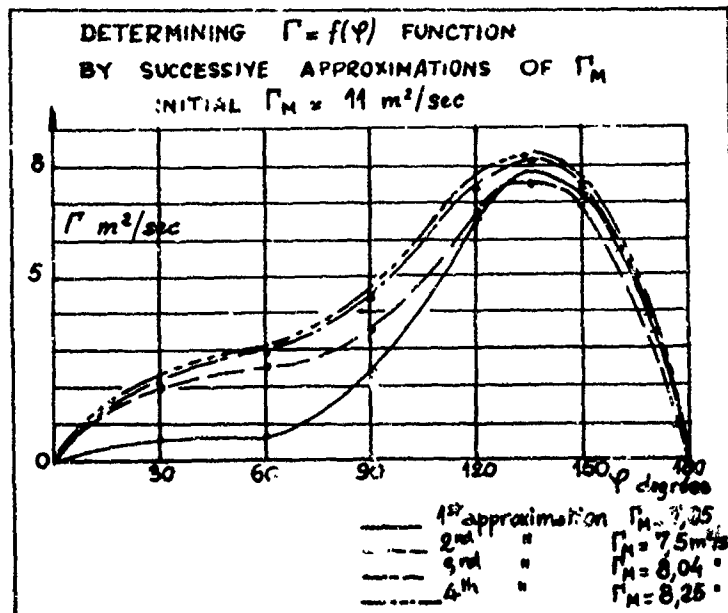


Fig. 19

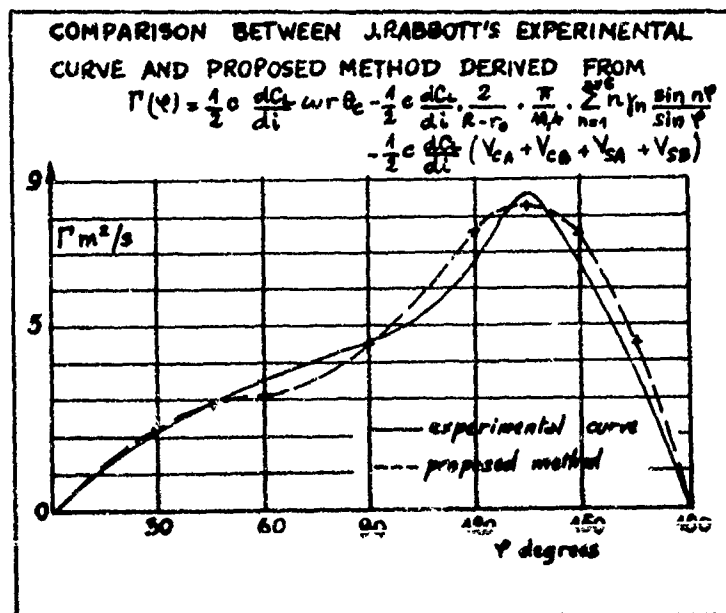


Fig. 20

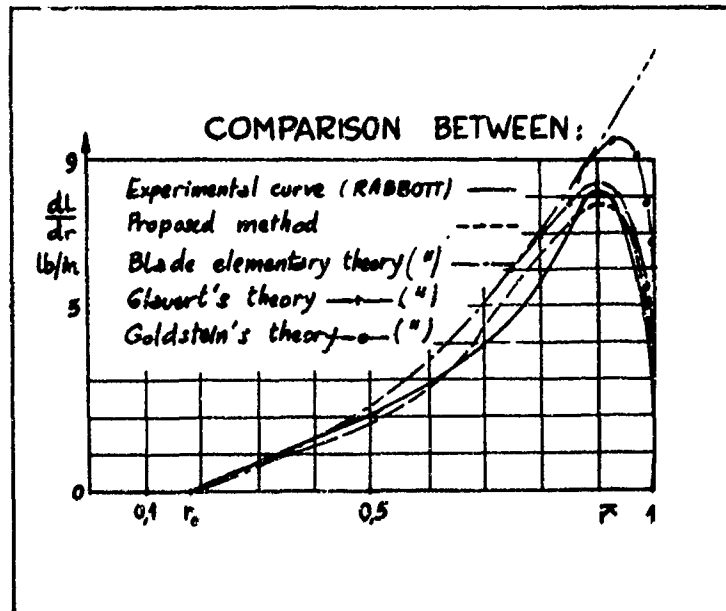
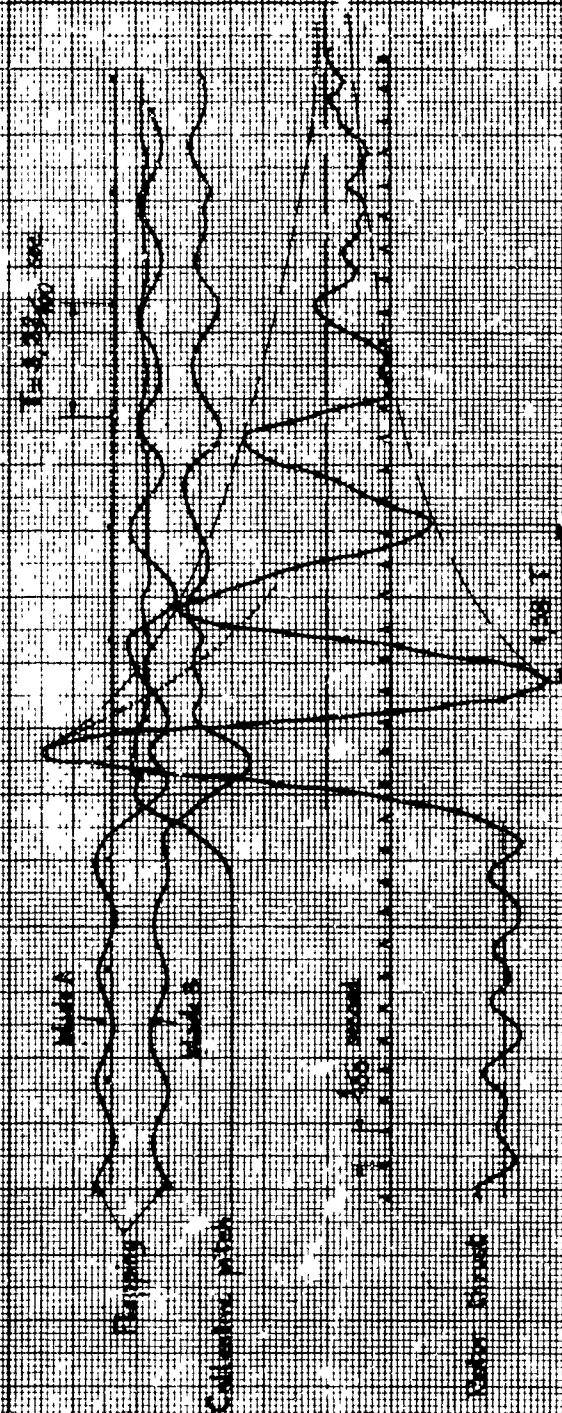


Fig. 21

TWO-BLADDED ROTOR - CONSTANT CHORD - NO TILT

$R = 1 \text{ m}$
 $\omega = 100 \text{ rad/sec}$
 $\Omega = 100 \text{ rad/sec}$
 $\Gamma = 0.0136$
 $\alpha = 0.104 \text{ rad}$
 $\beta = 0.0136$
 $\gamma = 0.0136$
 $\delta = 0.0136$
 $\epsilon = 0.0136$
 $\zeta = 0.0136$
 $\eta = 0.0136$
 $\theta = 0.0136$
 $\phi = 0.0136$
 $\chi = 0.0136$
 $\psi = 0.0136$
 $\omega = 100 \text{ rad/sec}$
 $\Omega = 100 \text{ rad/sec}$
 $\Gamma = 0.0136$
 $\alpha = 0.104 \text{ rad}$
 $\beta = 0.0136$
 $\gamma = 0.0136$
 $\delta = 0.0136$
 $\epsilon = 0.0136$
 $\zeta = 0.0136$
 $\eta = 0.0136$
 $\theta = 0.0136$
 $\phi = 0.0136$
 $\chi = 0.0136$
 $\psi = 0.0136$

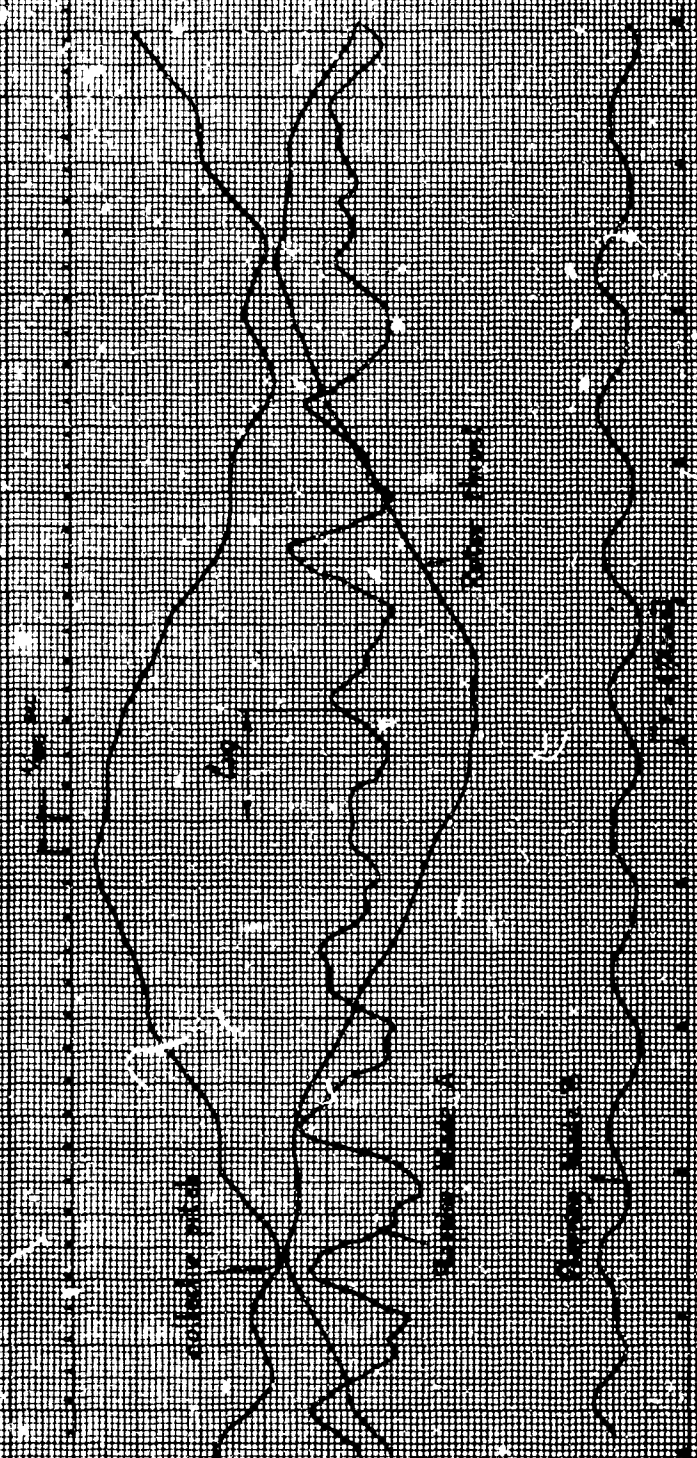


EXPERIMENTAL THRUST RESPONSE TO AN INPUT COLLECTIVE PITCH

(HEAVY BLADES)

Fig. 22

THE



FLAPPING RESPONSE TO HARMONIC INPUT FOR 3 VALUES OF LOCK'S CONSTANT

$$\ddot{\beta} + u \left(\frac{G_2}{I} \right) \dot{\beta} + u^2 \beta = u^2 \left(\frac{G_2}{I} \right) \cos \omega t$$

$\beta = f(u)$

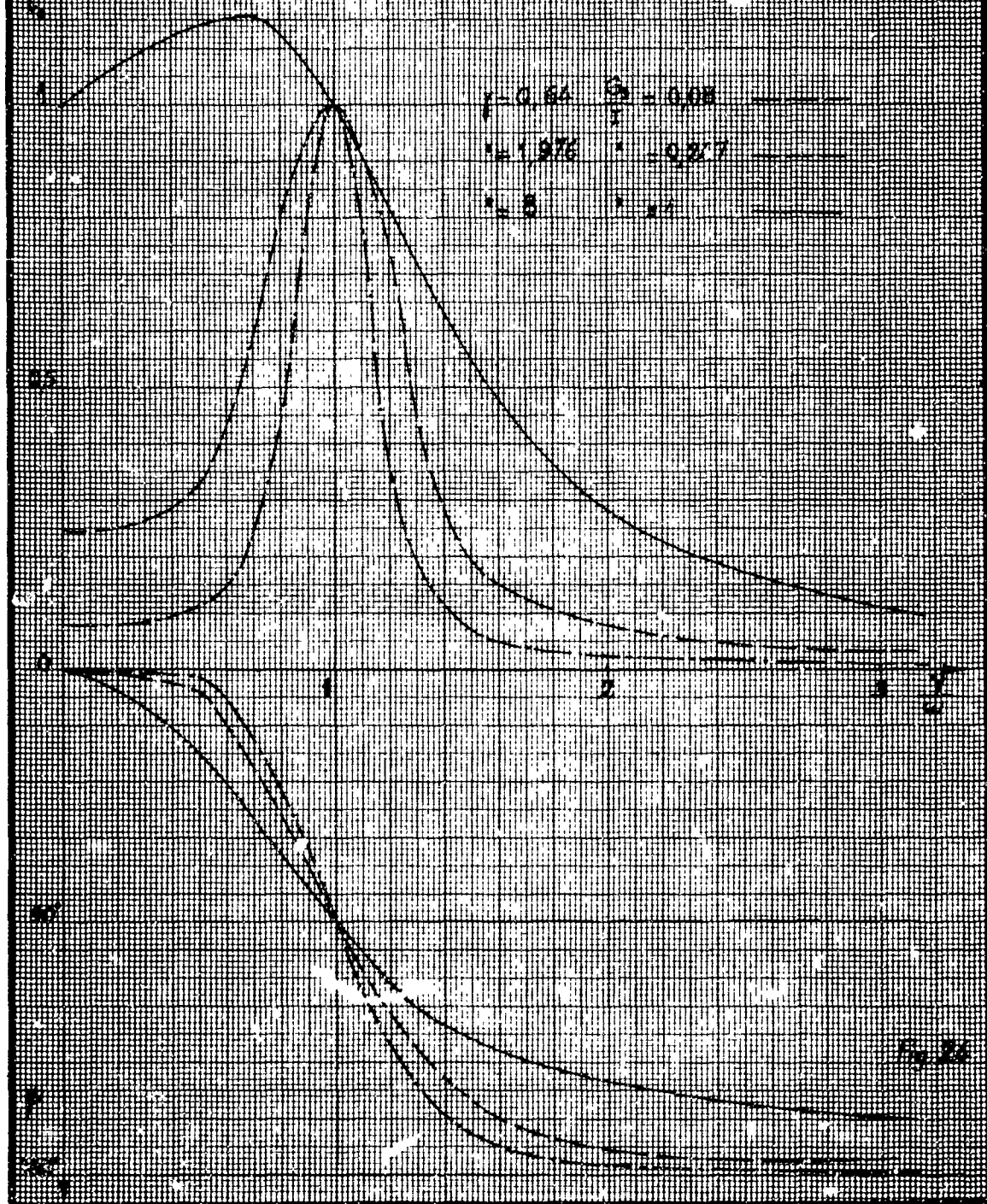
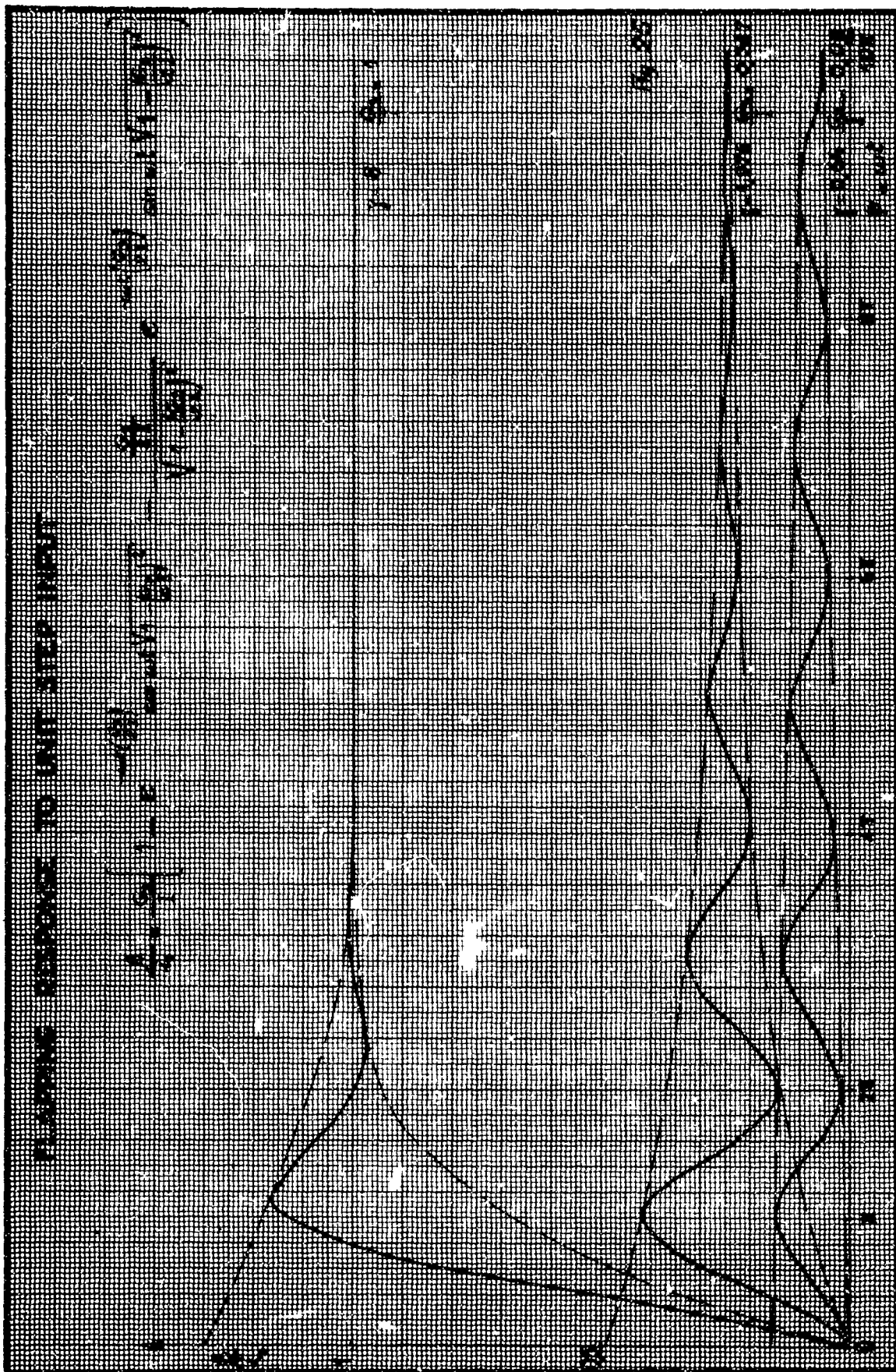


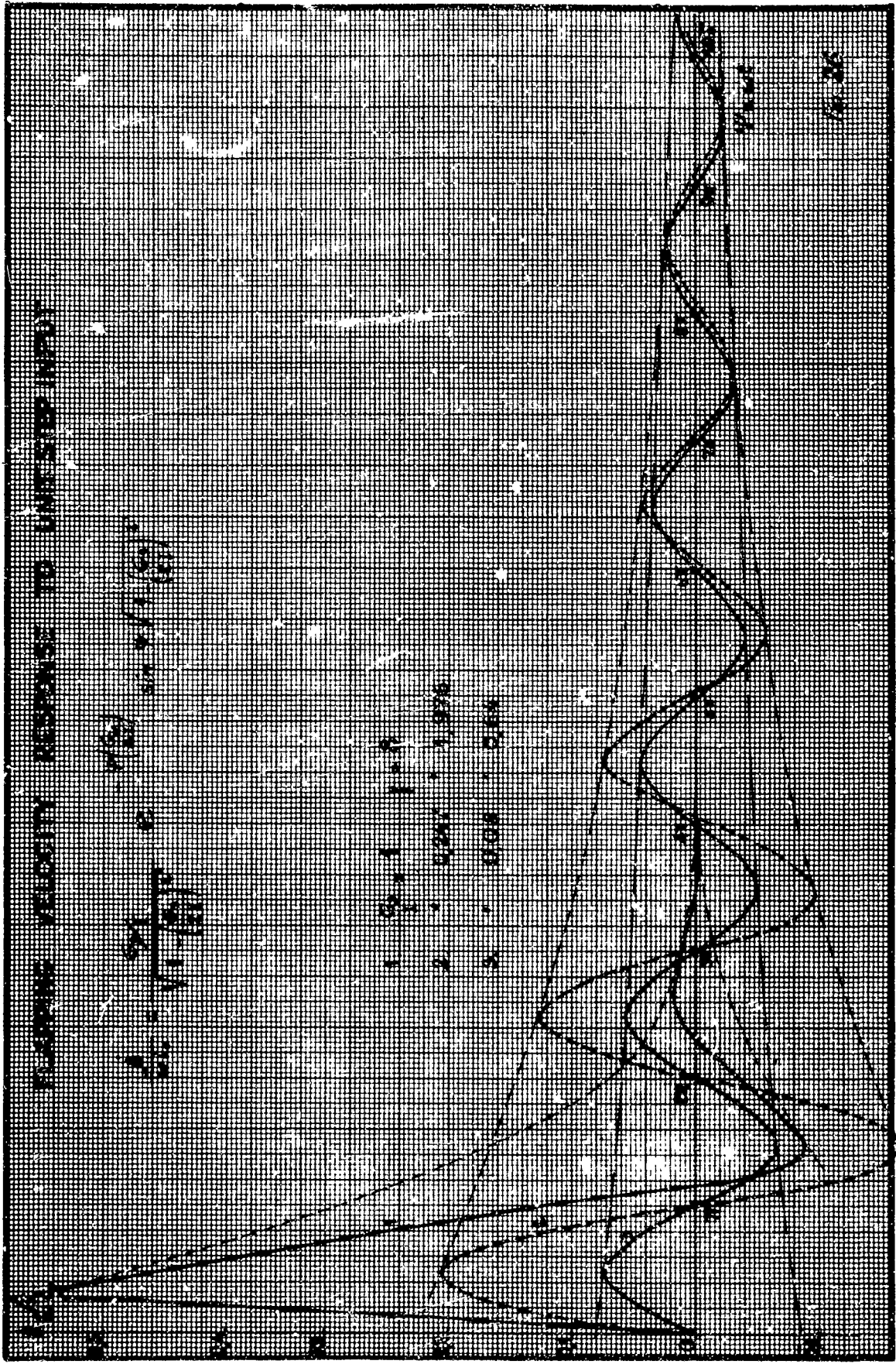
Fig. 26



FLARING VELOCITY RESPONSE TO UNSTEADY INLET

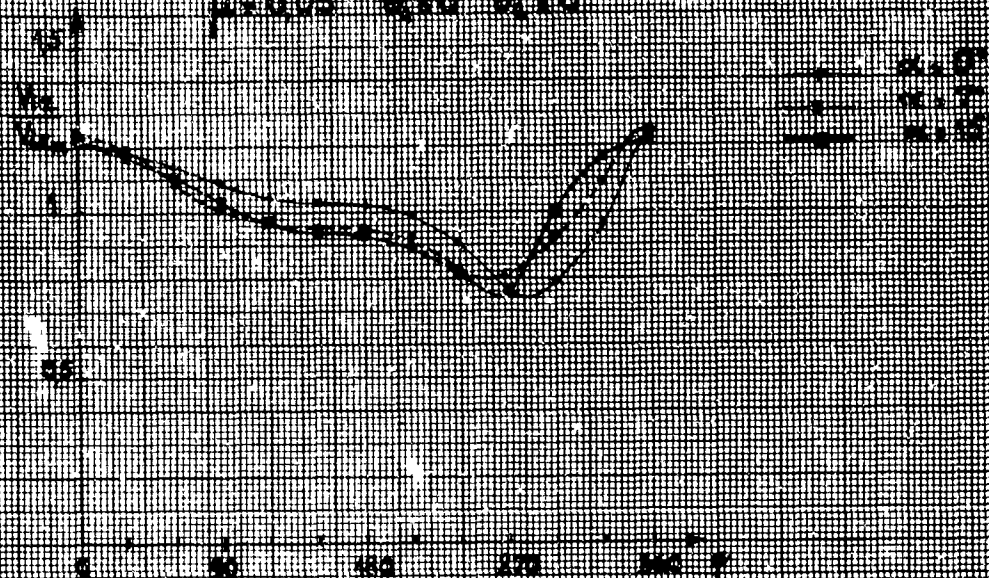
$$\frac{d}{dt} \left(\frac{V}{V_0} \right) = \frac{1}{V_0} \left(\frac{dV}{dt} \right)$$

- 1. $Q = 1.1 \times 10^{-4}$
- 2. $Q = 1.1 \times 10^{-4}$
- 3. $Q = 1.1 \times 10^{-4}$

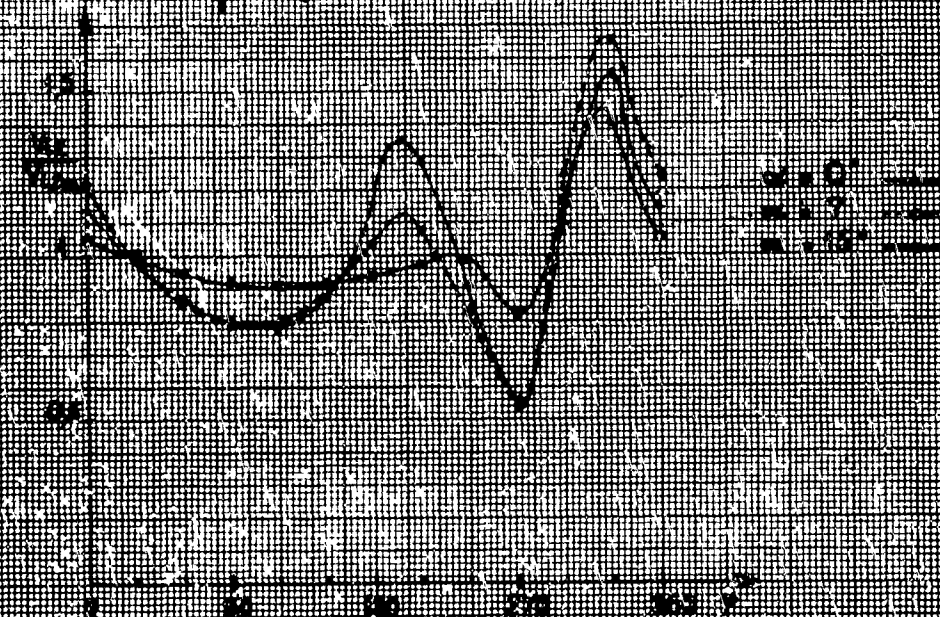


8.12

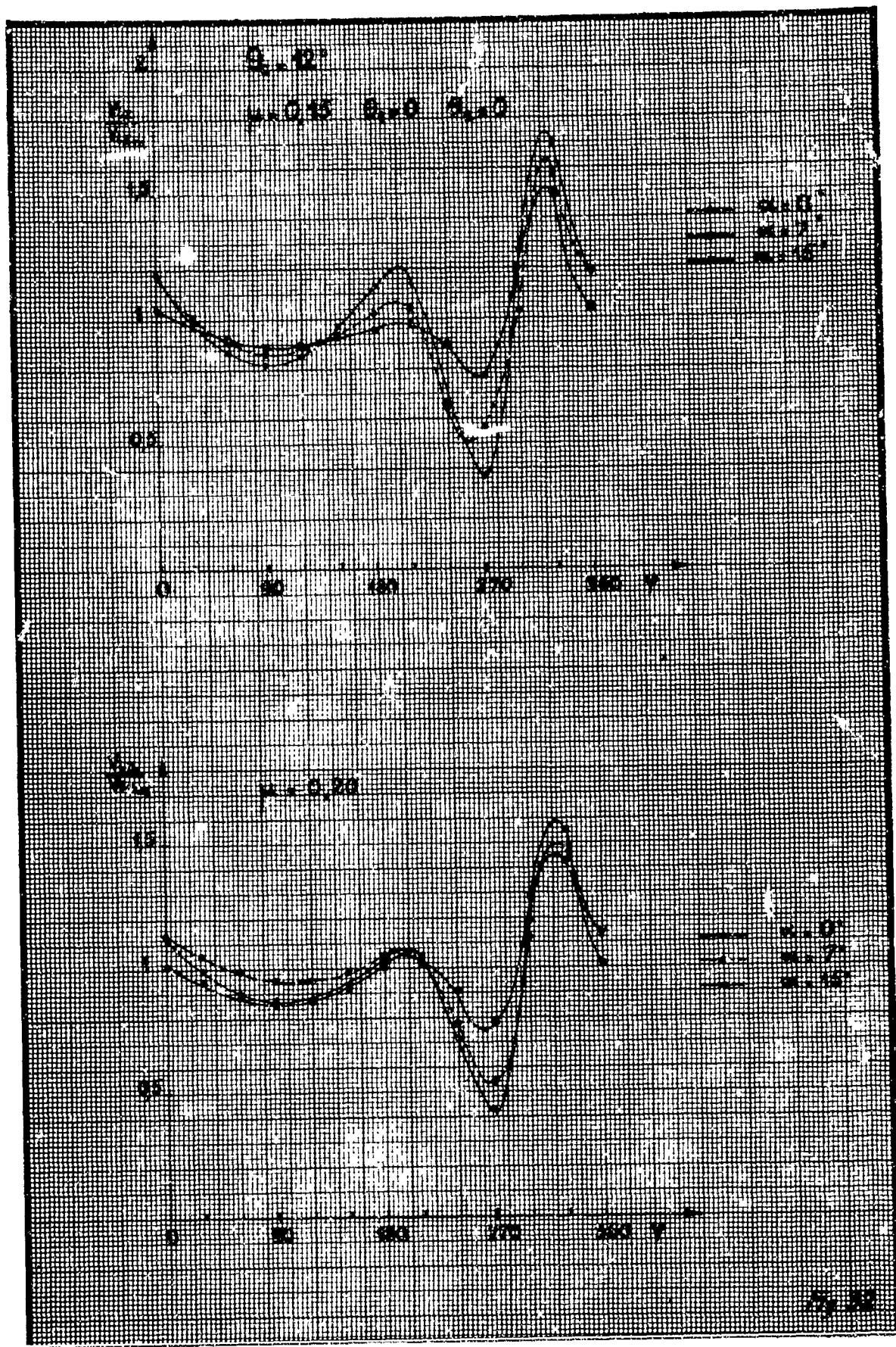
$\mu = 0.03$ 8.0 8.0

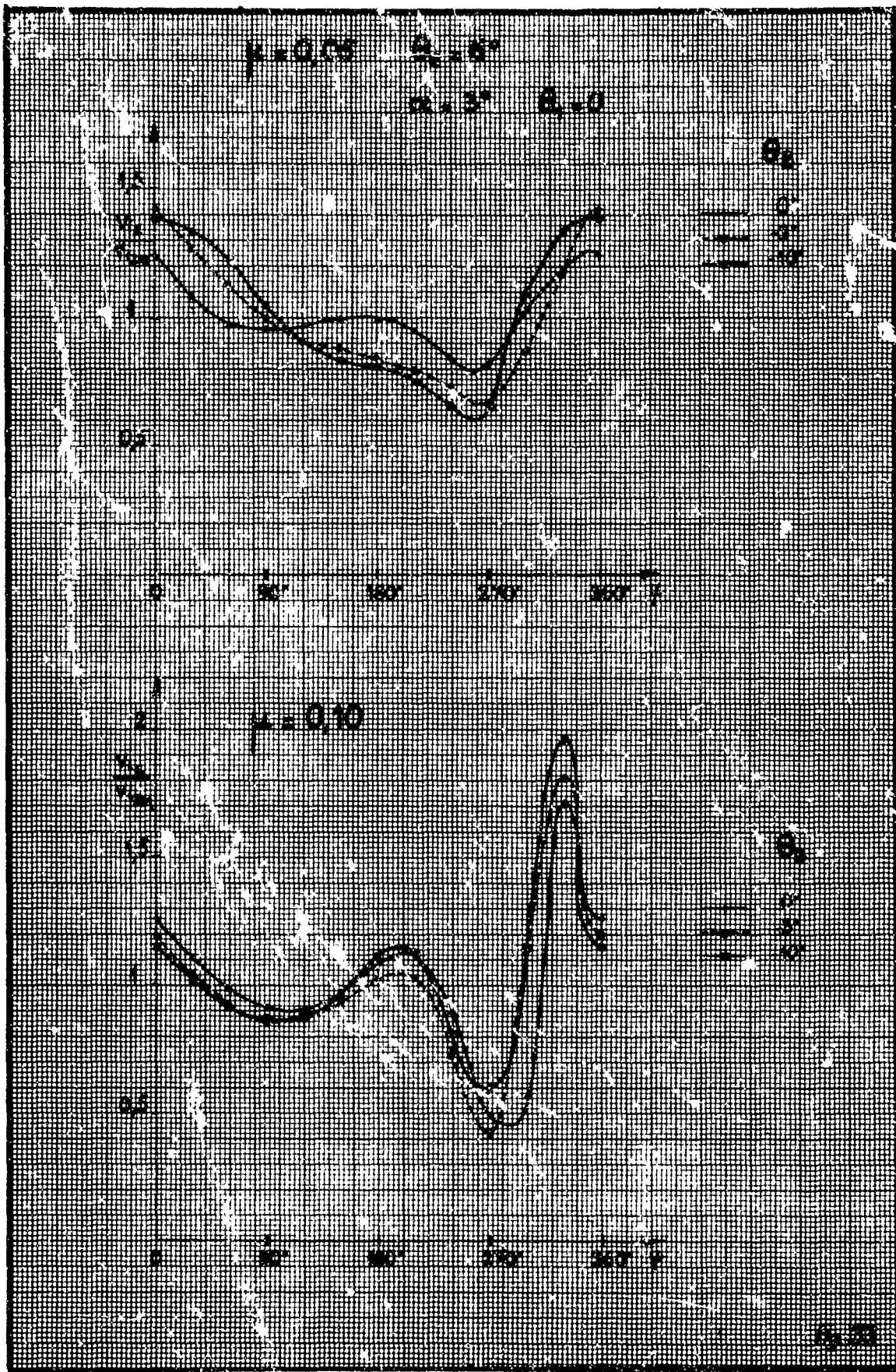


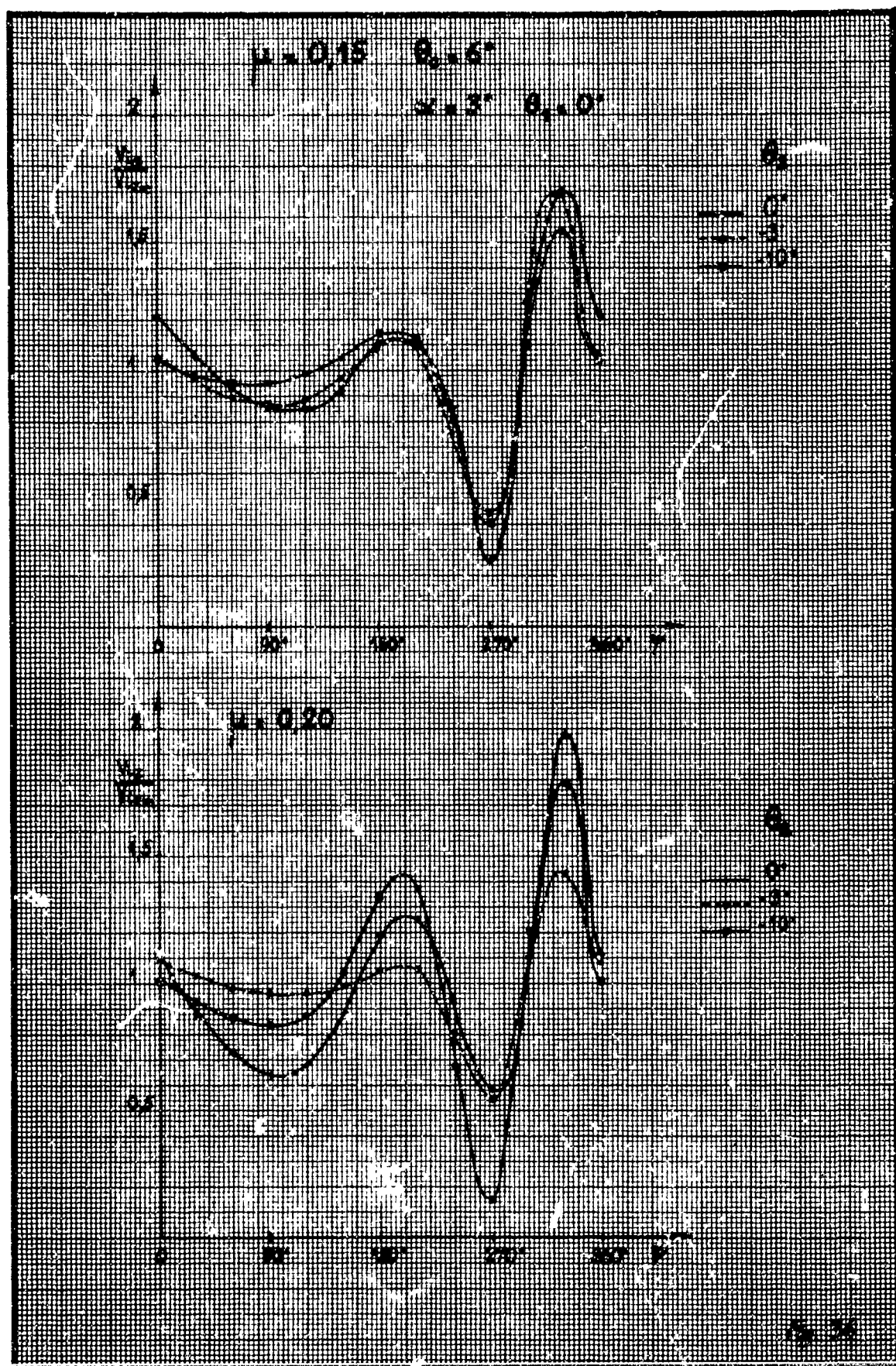
8.10



8.11







ROTOR AIRLOADS

R. Piziali, H. Daughaday, F. DuWaldt
Cornell Aeronautical Laboratory, Inc.

ROTOR AIRLOADS*

Raymond Piziali, Hamilton Daughaday, Frank DuWaldt
Cornell Aeronautical Laboratory, Inc.

INTRODUCTION

The problem of adequately predicting the aeroelastic response of rotating wings has been one of the most formidable problems to confront the aircraft industry. Industry has had to rely on expensive semiempirical methods and previous experience to design and develop these aircraft components. Such procedures do not provide the designer with a clear-cut rational approach to his problem and they provide little hope of optimizing the blade design to any given set of specifications.

The aeroelastic problem can be thought of as consisting of two closely related parts: the aerodynamic loading, and the dynamic response of the system. They are, of course, interdependent and related such that the aerodynamic loading excites the response of the structure and, at the same time, depends on it. In general, the dynamic response of the system will consist of fuselage motions and blade motions — i. e., rigid pitching, flapping, lagging, and all the coupled bending (both flapwise and chordwise) and torsion modes of the blades — while the aerodynamic loading will consist of the total reaction of the air on the blade sections. This aerodynamic loading will include the unsteady lift, induced drag, pitching moments, and profile drag which are appropriate for attached and separated flow conditions with the blade sections operating in normal and reversed flow.

The vortical wake of a rotating wing is quite complex; however, for steady-state translation of the rotor and as viewed from the wing in the rotating coordinate system, it is periodic. The wake-induced velocities at the wing will, therefore, also be periodic and these together with the periodic variation in the local tangential velocity (dynamic pressure) will cause the aerodynamic loading to be periodic. Thus, due to the time-varying airloading,

* This work was accomplished under the sponsorship of the U. S. Army TRECOM.

the vortical wake will consist of continuous distributions of shed and trailing vorticity which, at any instant, will be generally concentrated on a skewed and distorted helical surface; these distortions of the vortical wake from a skewed helical surface are, of course, the result of the time-varying three-dimensional induced velocity field of the wing and wake.

The above discussion points out the general complexity of the over-all aeroelastic problem for rotating wings and the interdependency of its various aspects. Any practical method of predicting this aeroelastic response will certainly make use of many simplifying assumptions. Some of these assumptions will be generally applicable; however, there will be others whose validity will depend on the particular wing and operating condition being analyzed. For example, in general, it will not be possible to neglect the aerodynamic coupling of the blade modes but for a specific problem this may be a valid assumption. Also, it will probably not be possible to compute the aerodynamic loading and the structural response independently; they will have to be computed simultaneously by satisfying the equations of motion or, possibly, by iterating between separate loading and response computations.

Any method of solution of the rotating wing aeroelastic problem must adequately predict the wake-induced velocities at the wing. However, it is very difficult to represent mathematically (or computationally) the wake effects; this, in the past, has been the prime obstruction to an adequate solution. The attempts of earlier investigators to solve this problem necessarily were based on relatively drastic simplifications of the wake in order to make the problem computationally feasible. Modern high-speed digital computing machines have now made it physically possible to account for much more of the realistic wake detail. It is, therefore, now possible to formulate a representation of the wake which will enable accurate computation of the wake-induced velocities.

This paper reviews our initial approach to the rotating wing aeroelastic problem and some of the results of this effort. A detailed discussion of this initial effort and the results are presented in References 1, 2, and 3. This is followed by a discussion of some of the remaining problems and the line of attack currently being followed in their solution.

THE INITIAL APPROACH TO THE PROBLEM

For the initial effort on this problem, it was felt that it would be advantageous to concentrate on only the aerodynamic loading aspect of it (i. e., to bypass, for the present, prediction of the structural response). This was facilitated by using measured dynamic response as a known input with the exception of the first harmonic flapping which was approximately forced to equilibrium by an iteration with the flapping equation of motion. Furthermore, an attempt was made to simplify the problem as much as possible for the initial effort by eliminating all but the most essential features and effects.

Each blade of the rotor was represented by a segmented lifting-line (bound vortex) located along the steady deflected position of the quarter-chord. The number of segments, n , and the length of each segment are arbitrary; they are each straight and of constant vortex strength. The lifting line is considered to advance in a stepwise manner through " N " equally spaced azimuth positions.

In the wake, the continuous distributions of shed and trailing vorticity of each blade are represented by a mesh of segmented vortex filaments; each segment is straight and of constant vortex strength. The segmented trailing vortex filaments emanate from each of the end points of the lifting-line segments. The segmented shed vortex filaments intersect the trailing filaments in a manner such that the end points of both are coincident (Figure 1).

The strengths, $d\Gamma/dt$, of the shed elements are equal to the change in strength of the bound vortex segments between successive azimuth stations and are deposited in the flow at each azimuth station of the bound vortex. The strengths, $d\Gamma/dr$, of the trailing vortex elements are equal to the differences in strengths of adjacent bound vortex segments and are deposited in the flow in a manner such that they connect the bound vortex end points to the shed vortex end points. The displacement time history of the wake elements is an input in this method; thus, any physically realistic distortion of the wake can be incorporated into the computation of the airloads.

For each azimuth position, the airloads are computed at the mid-points of the lifting-line segments. Thus, the airloads are computed at $(n)(N)$ points of the rotor disk. These points P_k of the disk are labeled as shown in the example of Figure 2; subscript, k , refers to position in the disk. The expression for the lift per unit span, for a blade section at any point, P_k , of the disk, is taken to be

$$l_k = \rho V_k \Gamma_k \quad (1)$$

where

$$\Gamma_k = a_k b_k |V_k| \left(\alpha_k - \frac{h_k}{V_k} + \frac{w_k}{V_k} \right) \quad (2)$$

The quantity in parentheses is the instantaneous "effective" angle-of-attack at the three-quarter-chord point, where α_k is the instantaneous geometric angle-of-attack with respect to the tip-path-plane, h_k the "effective" plunging velocity with respect to the tip-path-plane, and w_k the velocity component normal to the tip-path-plane induced by all the wake vorticity and the bound vorticity of other blades. The strengths, Γ_k , of the bound vortex elements are considered to be the unknowns for the method of solution developed.

The velocity component in a given direction induced at a point by an arbitrarily oriented straight vortex filament segment of constant strength is given by the Biot-Savart law as:

$$q = f \gamma \quad (3)$$

where γ is the constant vortex strength of the filament, and the coefficient f is a function only of the coordinates of the point where the velocity is being computed and the coordinates of the vortex filament end points. The velocity, w_k , of Equation (2) can be computed by summing the contributions (given by Equation (3)) of each individual vortex element of the blades and wake as indicated by Equation (4).

$$w_k = \sum_{\text{blades}} f \gamma + \sum_{\text{wake}} f \Gamma \quad (4)$$

However, each wake vortex element strength δ' of Equation (4) is just the difference in strength of two of the unknown bound vortex segment strengths, Γ_k (i. e., $\delta' = \Gamma_a - \Gamma_b$, where a and b are two values of the disk position subscript, k). These δ' relationships are depicted in Figure 1 relative to a point P_k of the rotor disk. If these differences are substituted for the δ' , Equation (4) can be expanded and the unknown Γ_k grouped and factored out. Thus, the w_k can be expressed as

$$w_k = \sum_{i=1}^{nN} \sigma_{ki} \Gamma_i \quad (5)$$

In Equation (5), the Γ_i are the unknown bound vortex strengths and each σ_{ki} is the sum of all the coefficients f of a common Γ_i in Equation (4). By substituting the w_k given by Equation (5) in Equation (2) and letting $I_k = a_k b_k (V_k \alpha_k - h_k)$, the following expression for Γ_k is obtained:

$$\Gamma_k = \frac{|V_k|}{V_k} \left[I_k + a_k b_k \sum_{i=1}^{nN} \sigma_{ki} \Gamma_i \right] \quad (6)$$

A set of linear simultaneous nonhomogeneous equations with constant coefficients is obtained when Equation (6) is written for each point, P_k , of the rotor disk at which the airload is to be computed. Thus, the airloads problem is reduced to obtaining the solution to this set of algebraic equations for which the unknowns are the $(n)(N)$ bound vortex strengths Γ_k .

The effects of stall were approximated by effectively limiting the lift coefficient to its value at the stall angle for effective angles of attack greater than the stall angle of the blade section. It is possible within the framework of this initial method to use more representative lift coefficient variations with angle of attack than the one chosen here. It should be noted, however, that incorporating stall in this manner assumes that the stalled section lift is all circulatory and there are, therefore, shed and trailing vortex elements in the wake with strengths determined by the stalled values of the bound circulation. In reality, the predominant part of the airload on the stalled section may be noncirculatory and due to the separated flow (i. e., analogous to the pressure drag on a flat plate at large angles of attack). Some indication of the magnitude

of the separated flow forces experienced may be obtained by using the measured airloads and dynamic pressure to compute the corresponding normal force coefficients; they are found to be extremely large for portions of the rotor disk where the blades are evidently stalled.

Reversed flow effects are accounted for in the computation approximately in that the sign of the lift force and the sense of the bound, shed and trailing vorticity are always consistent with the local tangential velocity, V , and the "effective" relative angle-of-attack of the section as it approaches and passes through the region of reversed flow. However, the wake remains attached to the bound vortex of the blade (although its position and orientation corresponds to the local inflow velocity) and the bound vortex remains at the quarter-chord while the blade approaches and passes through the region of reversed flow. In reality, when a section is operating unstalled in reversed flow, the center of pressure may be approximately at the three-quarter-chord; thus, the bound vortex should, possibly, be placed at that station and the induced velocity calculated at the quarter-chord.

Mach number and Reynolds number effects can be approximated as variations of lift curve slope of the local blade sections. For a given rotor and operating conditions, the Mach number and Reynolds number distributions over the rotor disk are fixed (known); thus, these effects can be incorporated into the computations by introducing the proper distribution of lift curve slope over the disk.

The sensitivity of the computed airloads to the number of revolutions of wake retained and the wake distortion was investigated computationally for the NASA model rotor (Reference 4) at an advance ratio of 0.15.

For this rotor and operating condition, three revolutions of wake accounted for practically all of wake-induced velocities; extending the wake to five revolutions only resulted in a maximum change of two percent in the magnitude of the lowest harmonics of the airloads (i. e. . the steady, first, and second harmonics). This was expected because the distant wake will have a relatively

uniform influence over the disk and, thus, affect primarily only the lowest harmonics of the results. The general conclusion is that the first few revolutions of wake are the most important with respect to dynamic airloads, and the amount of retained wake will depend on the rotor and operating condition being investigated.

Sensitivity of the computed airloads to distortions of the wake from a regular skewed helical surface was investigated for several relatively arbitrary distortions; the sensitivity experienced was moderate for this case. The only conclusion to be drawn from these results is that the wake distortion could possibly be important for certain specific rotors and operating conditions and that further investigation should be undertaken to determine and properly represent, at least to first order, these wake distortions. It should be remembered that the wake distortions are the result of a time-varying three-dimensional induced velocity field and cannot be properly determined by only the induced velocities at the blades or in the plane of the rotor. However, it is noted that reasonably good agreement with measured airloads has been achieved using a regular skewed helical wake which corresponds to a constant and uniform induced velocity field. Thus, for the cases computed, this is evidently a reasonable first approximation.

The measured and computed airloads are presented here for two different rotors and advance ratios. They are: (1) the NASA model, which was tested in a wind tunnel at $\mu = 0.15$ (Reference 4), and (2) a full-scale HU-1A helicopter rotor tested in flight at $\mu = 0.26$ (Reference 5). To emphasize the fact that apparent good agreement with respect to azimuthal distributions does not necessarily guarantee good agreement with respect to the harmonics, the following two forms of presentation are used: (1) the azimuthal distributions (i. e., time histories) at each radial station, and (2) the radial distribution of the sine and cosine components of each of the first eleven harmonics.

For the NASA model at $\mu = 0.15$, the computed and measured azimuthal airload distributions (time histories) are presented for five radial stations in Figure 3. The computed distributions have been adjusted to have the same

mean value as the measured distributions at each of the radial stations, so that the nonuniform parts of the loads can be directly compared. In general, the agreement appears to be good. A more stringent comparison is made in Figure 4 where the radial distributions of the sine and cosine component of each harmonic of the airloads are presented. It is, here, obvious that when the computed and measured radial distributions of the individual harmonics are compared, the correlation does not appear to be as good; it is, however, very encouraging.

For the HU-1A at $\mu = 0.26$, the airloads were computed with and without the measured motions of the blades; the computation without the measured motions did, however, have the steady blade deflections and the first harmonic rigid flapping motion. The measured motions used included the flapwise bending, rigid flapping, rigid pitching, and the torsion modes; only those harmonics of these motions which exceeded an equivalent recording trace deflection of 1/50 of an inch were retained. Presented in Figure 5 are the computed and measured azimuthal distributions of the airload at each radial station; the computed results in this figure are for the case with the elastic motions included and have been adjusted to have the same mean value as the measured results at each radial station. The agreement here appears to be quite good, although it is not as good as was obtained for the NASA model at $\mu = 0.15$. Also indicated on each airload time history in this figure is the azimuth range where the computed instantaneous effective angle of attack exceeded 14° (i. e., the azimuth range for which the lift coefficient was limited to a stalled value in the computations). It is interesting to note the change in character of these airloadings on the retreating side of the disk from the out-board radial stations to the inboard radial stations. This is evident in both the computed and measured results and is apparently the effect of stall occurring on the inboard blade sections. The radial distributions of the sine and cosine components of each harmonic of these measured and computed airloads are presented in Figure 6. Here, the results of both computations are presented, i. e., with and without the measured motions. The most significant differences between the two computed results appear in the first through the fifth harmonics

because, with the exception of the fourth harmonic motions, only the first five harmonics of the motions were of enough significance to be retained; the fourth harmonic motions were insignificant and, thus, neglected. It is interesting to note that even though there were no fourth harmonic motions used in the computation, a significant difference did appear between the fourth harmonic airloads obtained from the two computations which can only be attributed to the other harmonics of the motions. Here, as for the NASA model results, the correlation, based on the individual harmonics, does not appear to be as good as that based on the azimuthal distributions (i. e., time histories); the results are, however, very encouraging for this initial effort.

Some additional interesting results from the HU-1A computation which used the significant motions are presented in Figures 7 through 9. In Figure 7, the induced velocity distribution is presented as a contour plot over the rotor disk; these induced velocities at the various points of the disk are the velocity on the blade when it is at the point, i. e., they are the induced velocities in the rotating coordinate system. It should be noted that the contours are not of equal increments of the induced velocity. The two most interesting features evident in this figure are the nonuniformity of the induced velocity distribution, especially for an advance ratio of 0.26, and the large induced velocities and steep gradients on the retreating half of the rotor disk; the latter tend to alleviate the so-called retreating blade "tip-stall" by reducing the instantaneous effective angles of attack. This is evident in Figure 8 which presents a contour plot of the nondimensionalized, instantaneous, effective angle of attack over the rotor disk; the angle of attack has been nondimensionalized to an angle of 14° (the estimated stall angle for these blade sections). Experimental wind tunnel results obtained by the NASA (Reference 6) seem, in general, to confirm these results. The tuft patterns presented for operating conditions which are well into the stall region appear to indicate that the outboard portion of the blades remained unstalled. Further, it was observed in the tunnel tests that the total lift did not tend to fall off as the apparent stall area increased, and the variation of longitudinal flapping with advance ratio did not exhibit the change of slope that might be expected had there been progressive tip stall. The large induced velocities and steep gradients on the

retreating side of the disk and their absence on the advancing side are related to the concentration of the trailing vorticity near the blade tips and shifting of the airloading toward the tips on the retreating side. This shift of the airloading, which is influenced by the inboard area of stall, is evident in Figure 9 (a contour plot of the airloading over the rotor disk).

The induced drag and its harmonic analysis are also a part of the output of this program. For this case, the first through third harmonics of the induced drag are sizeable and resonance conditions could be troublesome at the higher harmonics. This induced drag distribution, when used to compute the induced power, yields a result which is approximately three times that obtained by a conventional method based on the uniform inflow assumption.* The conclusion to be drawn from these results is that more realistic induced velocity distributions will, in general, yield a higher induced power expenditure.** This is consistent with fixed-wing theory.

* These results are presented and discussed in more detail in Reference 3.

** A similar trend was noted by W. Castles and H. Durham (Reference 7).

GENERAL DISCUSSION AND RECENT WORK

In the initial approach which has been discussed, the dynamic response aspect of the problem was bypassed to facilitate concentration of effort on the development of the essential features of the computational procedure for determining the airloading. As mentioned previously, this procedure was possible since computed airloads were compared with loads measured in flight for configurations where the dynamic response was also measured. However, we must remember that our objective is to predict the aeroelastic response and airloads on a blade when our only known inputs are given flight conditions (i. e., cyclic pitch, collective pitch, advance ratio, etc.).

Two methods have been considered for solving for the aeroelastic response. One consists of an iterative procedure where the airloads would be computed for given inputs and dynamic response, and these airloads are then used to obtain a second estimate of the dynamic responses. The second method involves the simultaneous solution of the aerodynamic load and dynamic response problems.

It is clear that the iterative procedure has some fundamental difficulties from a theoretical standpoint, although it may be adequate in some cases. The airloads computed at any step of the iteration are based on the prescribed inputs and dynamic responses of the preceding iteration, and they include the corresponding aerodynamic damping loads. There appears to be no exact method available for separating the aerodynamic damping from this total airloading, although an approximate estimate of the damping can be made with quasi-static aerodynamics.

The dynamic response for the next step of the iteration can be computed treating the total aerodynamic force (including aerodynamic damping) as the exciting force. In this case, the responses near resonances are very large, being only limited by the comparatively small structural damping, and it would be expected that the convergence of the procedure would be poor. An improved convergence can be obtained by, first, approximately estimating the aerodynamic

damping and subtracting it from the total computed airloading to obtain the forcing function. Now, the same approximate treatment of aerodynamic damping would be included in the computation of the dynamic responses for the next step of the iteration.

Currently, we are evaluating the advantages of the exact treatment of the problem which closes the loop on the airload and response calculations. It turns out that the general technique which has been described for handling the airloads problem alone can be extended to include the determination of the dynamic responses.

In steady flight, the response in each of the dynamic modes of interest can be expressed as a Fourier series with the fundamental period of one rotor revolution. Thus, for example, the amplitude velocity, and acceleration in the q^{th} dynamic mode can be written,

$$\dot{q} = \sum_n (a_n \cos n\Omega t + b_n \sin n\Omega t), \quad \ddot{q} = n\Omega \sum_n (-a_n \sin n\Omega t + b_n \cos n\Omega t)$$

$$\ddot{q} = -n\Omega^2 \sum_n (a_n \cos n\Omega t + b_n \sin n\Omega t)$$

However, this harmonic description of the response is incompatible with the time domain description which is used in the airload computation discussed earlier. The situation is easily remedied by expressing the a_n and b_n coefficients in terms of the N values of q at the N azimuth positions used in the airload determination. By this means, the velocity, \dot{q} , and acceleration, \ddot{q} , at a given azimuth position, can be written in terms of the q 's at all N azimuth positions. It also proves possible to express the structural damping in each mode in terms of the N q 's.

When the dynamic response is considered simultaneously with the airloads, an equation of motion is added for each of the S modes considered which must be satisfied at each of the N azimuth positions. Thus, there are N times S new variables to be included in the machine calculation. In addition to the new equations of motion obtained, Equation (6) is also modified when the dynamic response is determined simultaneously. Some of the prescribed inputs, I_R , become linear functions of the new variables. However, the revised equations can still be arranged in the same form and solved in an analogous manner.

It has been found conceptually convenient to view the aerodynamic loading aspect of the over-all aeroelastic problem in the following manner: The wing and its "immediate" attached wake can be thought of as a "wing-wake system" for generating a force. This system will have a characteristic transfer function which will describe the variation of the output (i. e., the airloading) with the frequency of the input (which is a time-varying angle of attack). The remainder of the wake, which is the returning wake of the wing and all the wake of the other wings in the rotor, and the motions of the wing are then thought of as providing the input to this system. For example, when the classical two-dimensional oscillating wing problem is viewed in this way, the wing section and its entire wake will make up the wing-wake system, and the inputs are just due to the motions of the wing. When the immediate wake of the rotating wing is considered as part of the system, it will influence the system transfer function and, therefore, be effective in controlling the system response to the inputs rather than functioning as part of the input source. The point of division between the immediate wake and the remainder of the wake is, here, unimportant because the model is used only as a convenient way of thinking about the problem and not as a basis for computation. The problem is, thus, conceptually divided into two parts: the first part being the inputs to the wing-wake system, and the second part the wing-wake system itself.

The displacement time history of the wake will certainly influence the inputs to the wing-wake system, and it has been determined that the airloading can be sensitive to this displacement time history. At any instant of time, the wake will appear to be a skewed and distorted helical surface. The skewed helical surface upon which the distortions can be thought to be superimposed is determined by the rotor translational velocity, the tip-path-plane angle, and the rotational velocity of the rotor. The deviation of a particular wake element from this surface at any instant of time depends on the induced velocities it has encountered since it left the wing. Because the first revolution of wake is the strongest source of input to the wing-wake system, it should be positioned

with the greater precision. Although the computational procedure of the initial effort is capable of accounting for any rather general wake displacement time history, there still remains the question of the correct displacement time history. To determine this exactly would require that the total induced velocities be computed throughout the wake for each instant of time and that the wake elements be moved according to their local induced velocities for each increment of time; such a procedure becomes computationally impractical, even on a high-speed digital computer. A possible approximation which is being attempted would require repeating the loads computation at least once (i. e., at least one iteration) to determine the proper wake distortion. First, the wake displacement time history would be assumed as it is now for the initial method. The velocity time histories of selected wake elements would then be computed as well as the velocities at the blades. These wake element velocities would then be used to generate the wake displacement time history for the second computation. It is anticipated that the position deviation from the assumed displacement time history will not significantly alter the induced velocity at each wake element; therefore, the convergence of the position should be rapid. Additional iterations would be carried out to test this postulated behavior.

In addition to having an adequate representation of the input source for the wing-wake system, a successful computational procedure must have an adequate representation of the wing-wake system itself. In the initial approach, the wing was represented by a single bound vortex at the quarter-chord, satisfying boundary conditions at the three-quarter-chord and the immediate wake was represented by a system of concentrated vortex filaments shed at equal increments of time. The major approximations involved in this initial approach are: (1) the boundary conditions are satisfied at only one point on the chord, and (2) the immediate wake is represented by concentrated vortices equally spaced in time from the trailing edge. These approximations of the wing-wake system seem relatively drastic, but they produce relatively good results. The apparent good results thus far obtained using this representation may be due to the relatively low reduced frequency range of the predominant part of the airloading and/or may also be the result of compensating errors arising from the approximations.

From a mathematical point of view, the boundary condition at any instant of time over the chord, to be satisfied by a distribution of singularities on the chord, is the sum of all the velocities normal to the chord at that instant of time. This boundary condition, which is termed the "instantaneous effective" boundary condition, is composed of the normal velocities due to the angle of attack, camber, gusts, etc. (i. e., due to all the inputs to the wing-wake system), plus the normal velocities induced by the immediate wake; thus, it is through this influence on the instantaneous effective boundary condition that the immediate wake is effective in controlling the wing-wake system response. In the airfoil problem, this instantaneous effective boundary condition is, of course, related to past history of the singularity distribution, i. e., the airfoil problem is a succession of related boundary value problems.

If the singularity distribution (i. e., the distribution of bound vorticity) is expanded in a Glauert series and the instantaneous effective boundary condition in a cosine series, the corresponding coefficients of the two series can be shown to be directly proportional to each other. Because the lift and moment are functions of only the first four terms of the Glauert expansion, they therefore depend only on the first four terms of the instantaneous effective boundary condition expansion. Thus, to predict the lift and moment, the wake representation need only represent adequately the first four terms of the expansion of the wake-induced velocity distribution (i. e., the low order part of the distribution) and then the wing representation should be capable of satisfying this boundary condition over the entire chord.

The amount of improvement in the computed lift which would result from the use of such improvements in the computational model is not clear. However, it is believed it would yield much more realistic aerodynamic moments; thus, such improvements are being implemented to determine their benefits.

The chordwise boundary condition will be satisfied over the entire chord by directly computing, for each element of wake vorticity, its contribution to each of the first four Glauert coefficients (instead of computing the induced velocity at the three-quarter-chord due to each element as in the initial approach).

This is accomplished by the use of Glauert's well-known integral which is transformed to apply to the problem coordinate system. This amounts to determining the first four terms of the cosine expansion of the chordwise induced velocity distribution due to an element of vorticity arbitrarily oriented with respect to the blade chord. It is clear that the more distant a wake element is from the chord, the less will be its contribution to the higher-order terms of its cosine expansion. Thus, most of the wake (specifically that part functioning as the input source to the wing-wake system) will contribute significantly only to the first two Glauert coefficients (those which correspond to the linear and constant part of the instantaneous effective boundary condition over the chord). The immediate wake (that part which functions as part of the wing-wake system) will, of course, contribute significantly to all four of the Glauert coefficients.

There are two possibilities for the representation of the immediate wake. First, there is evidence from some of our earlier computations that by proper choice of the distance of the first concentrated shed wake element from the trailing edge, it may be possible to reproduce the first four terms of the expansion of the wake-induced velocity distribution with sufficient accuracy to enable computation of the lift and moment adequately for the reduced frequency range of interest. The second possibility is a formulation which has been developed wherein the shed wake is effectively made a continuous distribution behind the wing from the trailing edge back as far as deemed necessary. This distribution is not fixed; for each azimuth position of the blade, this distribution will be a function of the total circulation about each blade section for each of the azimuth positions. Both of these wake representations, together with the above method of satisfying the chordwise boundary conditions, are being tried on the two-dimensional oscillating wing problem in order to determine their adequacy.

In the initial approach, the mesh of shed and trailing vortex filaments was maintained for the entire retained wake. It is now believed that it may be possible to eliminate all the shed vorticity for most flight conditions, except that in the immediate part of the wake; this could reduce the computation time by approximately one-half.

CONCLUDING REMARKS

It should be remembered that the over-all problem is an aeroelastic problem and the airloading is but one aspect of it. Because of the interdependency of the airloading and structural response, it may be necessary to compute them simultaneously in order to obtain satisfactory results. Direct application of such a formulation to aeroelastic stability analyses is evident. Another interesting area of application for this work is the maneuvering or transient flight conditions of the rotor.

The work accomplished thus far indicates that a practical solution to the aeroelastic problem is feasible. However, there are many possible approximations and assumptions which may be utilized, and those which are permissible are not yet clearly defined. Thus, it may still be possible to improve the results while simplifying or, at least, shortening the computation.

REFERENCES

1. Piziali, R. A. and DuWaldt, F. A. Computation of Rotary Wing Harmonic Airloads and Comparison with Experimental Results Presented at AHS Meeting May 1962
2. Piziali, R. A. and DuWaldt, F. A. A Method for Computing Rotary Wind Airload Distributions in Forward Flight TRECOM Report No. TCREC TR 62-44 November 1962
3. Piziali, R. A. and DuWaldt, F. A. Computed Induced Velocity, Induced Drag, and Angle of Attack Distributions for a Two-Bladed Rotor Presented at AHS Meeting May 1963
4. Rabbott, J. P., Jr. and Churchill, G. B. Experimental Investigation of the Aerodynamic Loading on a Helicopter Rotor Blade in Forward Flight NACA RM L56107 25 October 1956
5. Burpo, F. B. Measurement of Dynamic Air Loads on a Full-Scale Semirigid Rotor TRECOM Report No. TCREC TR 62-42 December 1962
6. Sweet, G. E., Jenkins, J. L., Jr. Results of Wind-Tunnel Measurements on a Helicopter Rotor Operating at Extreme Thrust Coefficients and High-Tip-Speed Ratios Presented at IAS Meeting January 1963
7. Castles, W., Jr. and Durham, H. L., Jr. The Computed Instantaneous Velocities Induced at the Blade Axes by the Skewed Helical Vortices in the Wake of a Lifting Rotor in Forward Flight ASTIA Document No. AD-210613 May 1959

NOMENCLATURE

- a - Lift curve slope: $dC_l/d\alpha_e$
- b - Blade semichord at each radial station,
- h - "Effective" plunging velocity of the blade section; includes the component of the free stream velocity, V_∞ , normal to the local blade sections (i. e., the effects of the local blade slopes).
- k - Subscript indicating position in the rotor disk.
- L - Lift per unit span.
- n - Number of radial bound vortex segments representing blades.
- N - Number of equally spaced azimuth positions at which the airloads are computed; must be multiple of the number of blades in the rotor.
- P - The point of the rotor disk where the airloads are computed.
- r - The radial coordinate of the rotor.
- R - Blade radius.
- V - Tangential velocity in tip-path-plane: $V = \Omega r + V_\infty \cos \alpha_T$
- V_∞ - Free stream velocity due to rotor translation.
- w - The induced velocity component normal to the tip-path-plane at the three-quarter-chord of the section.
- α - Instantaneous geometric angle of attack with respect to the tip-path-plane.
- $\hat{\alpha}$ - Stalling angle of attack for the blade sections.
- α_e - Instantaneous effective angle of attack with respect to the tip-path-plane: $\alpha_e = \alpha - h/V + w/V$
- α_T - Longitudinal tip-path-plane inclination with respect to the free stream velocity, V_∞ .
- Γ - The unknown strength of the bound vortex segment representing the blade section.

μ - Advance ratio: $\mu = V_f \cos \alpha_T / \Omega R$

ρ - Air density.

ψ - Azimuthal position.

Ω - Rotational speed of the rotor

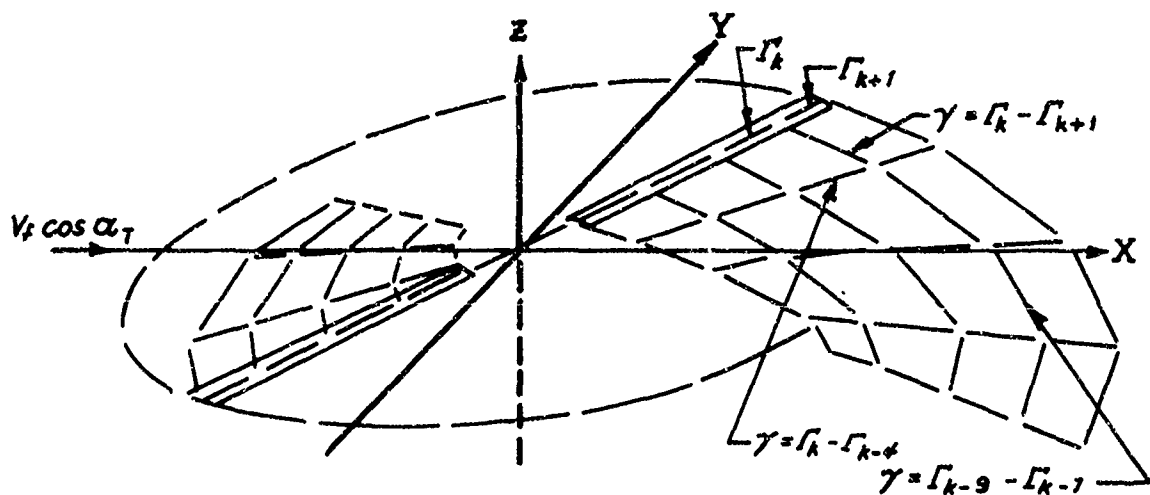


Figure 1 PICTORIAL EXAMPLE OF THE INITIAL PORTION OF THE WAKE OF A TWO-BLADE ROTOR DIVIDED INTO FOUR (i.e. $n = 4$) RADIAL SEGMENTS

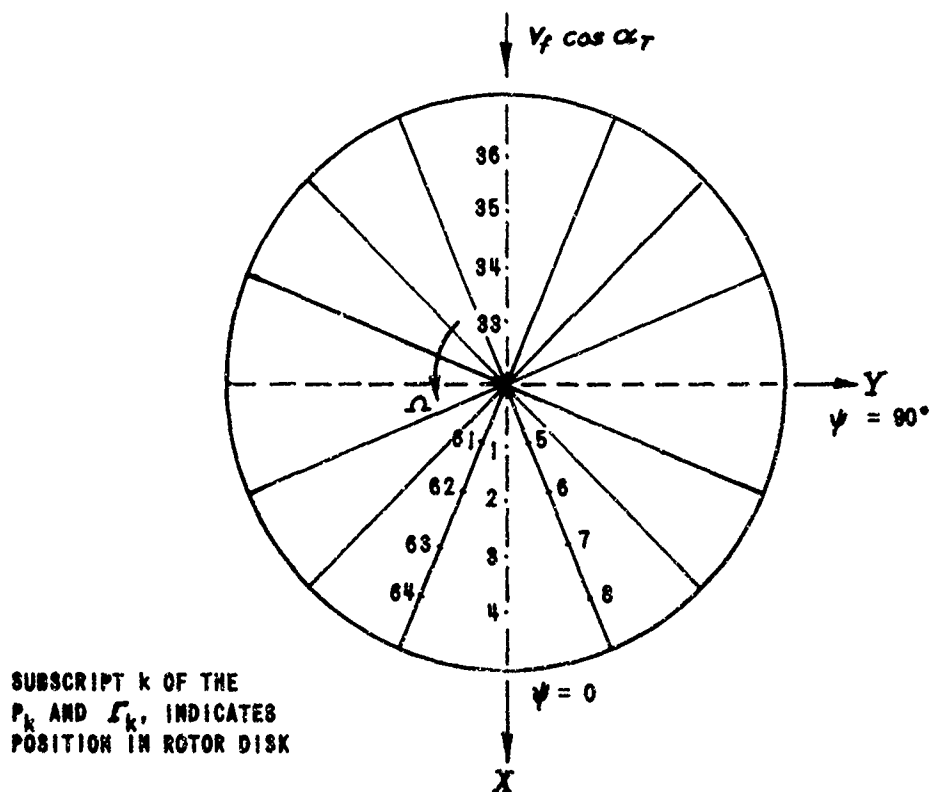


Figure 2 SAMPLE MAP OF COMPUTATION CONTROL POINTS IN TIP PATH PLANE FOR $n = 4$, $N = 16$

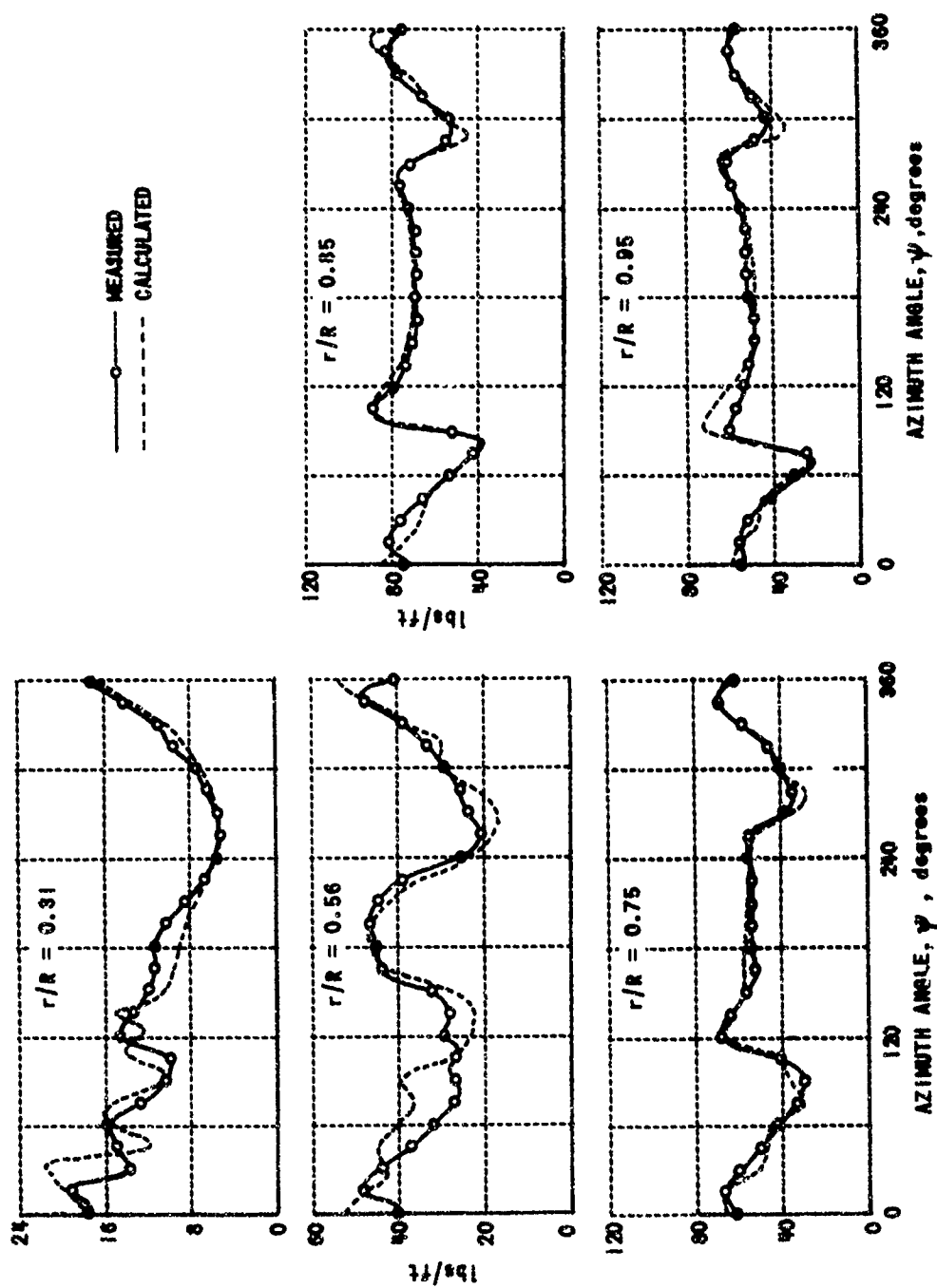


Figure 3 AZIMUTHAL VARIATION OF AIRLOADS FOR NASA MODEL ROTOR; $\mu = 0.15$

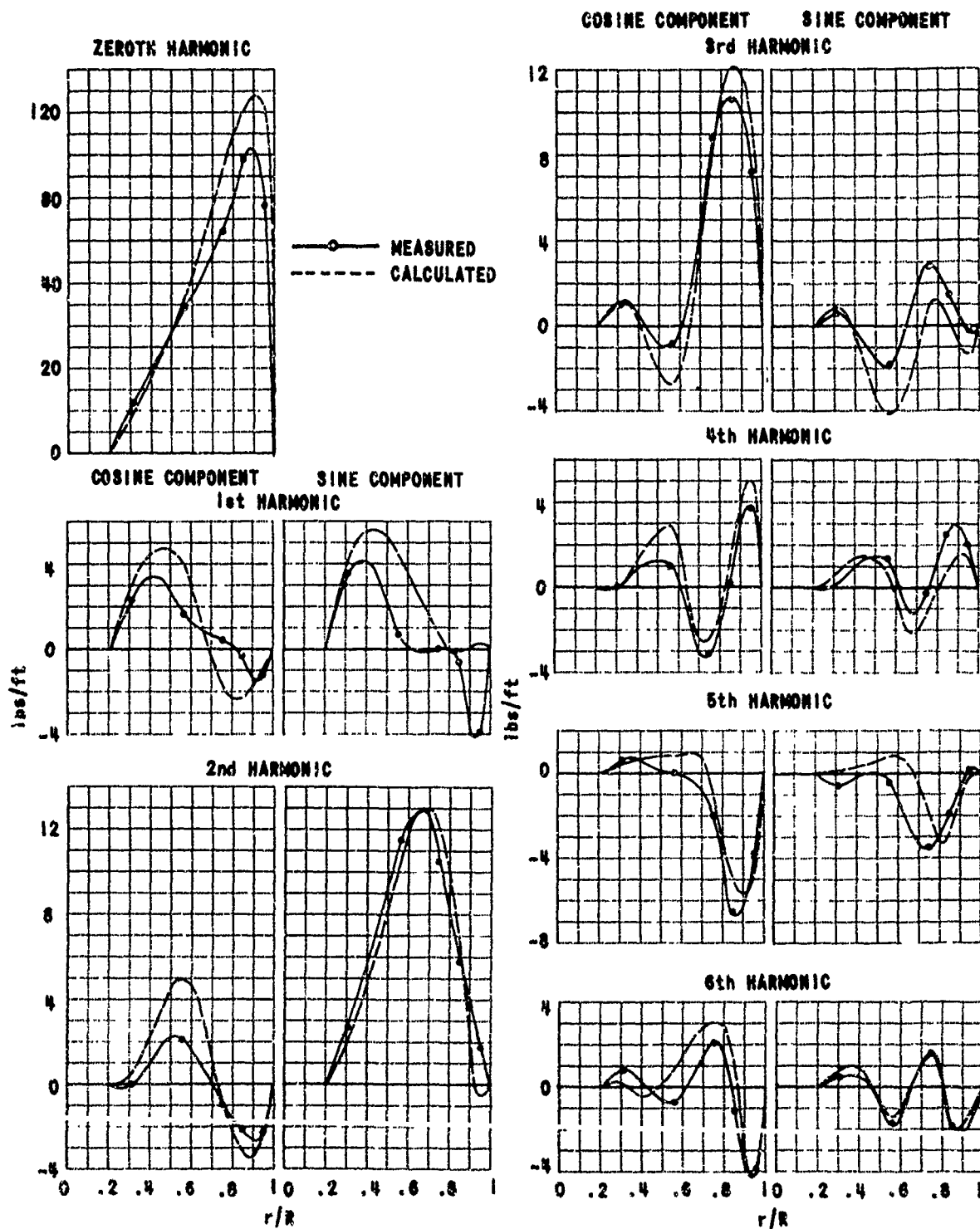


Figure 4 SPANWISE DISTRIBUTIONS OF THE HARMONICS OF THE MEASURED AND COMPUTED AIRLOADS FOR THE NASA MODEL ROTOR; $\mu = 0.15$

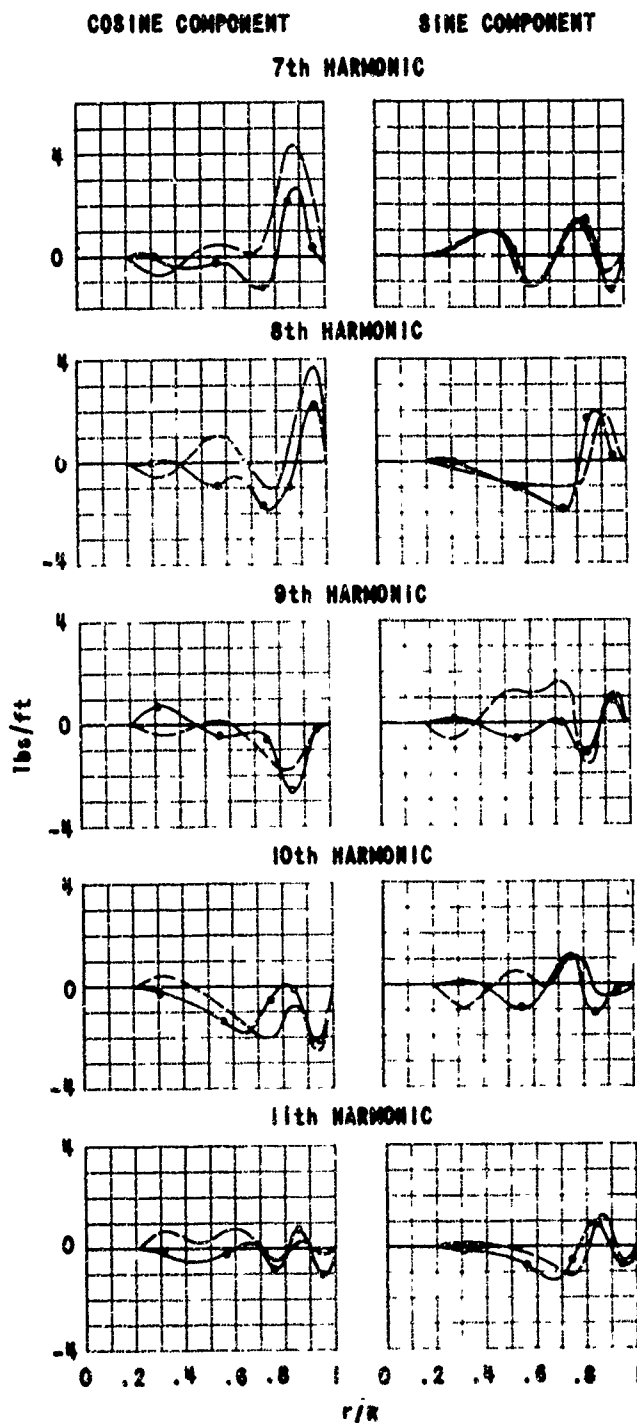


Figure 4 (cont'd)

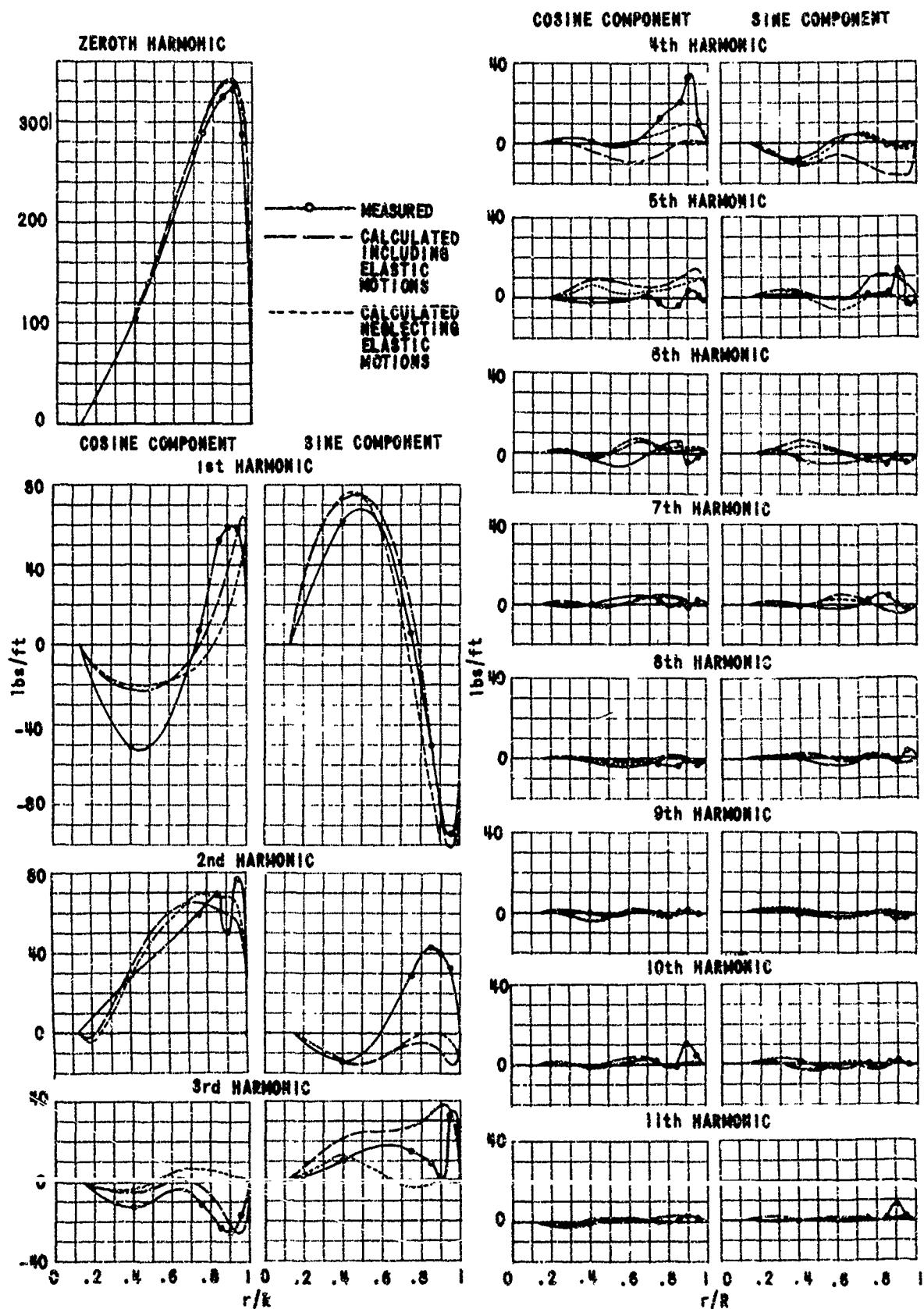


Figure 6 SPANWISE DISTRIBUTIONS OF THE HARMONICS OF THE MEASURED AND COMPUTED AIRLOADS FOR HU-1A; $\mu = 0.26$

REVERSE FLOW

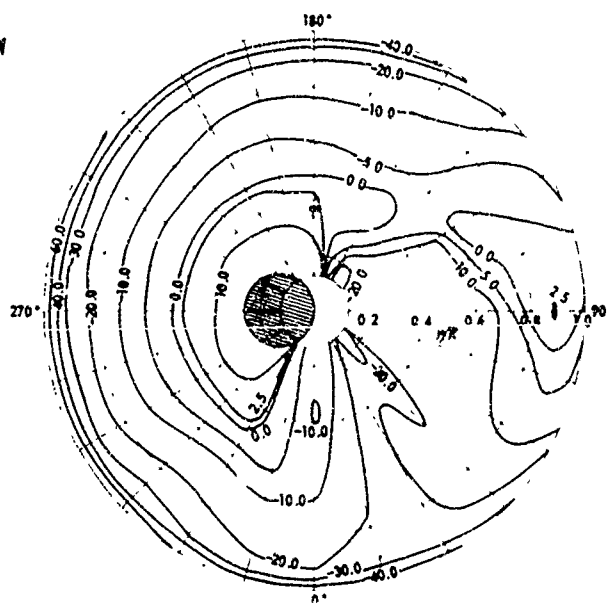


Figure 7 INDUCED VELOCITY DISTRIBUTION
IN THE ROTATING COORDINATE
SYSTEM; ft/sec; HU-1A; $\mu = 0.26$

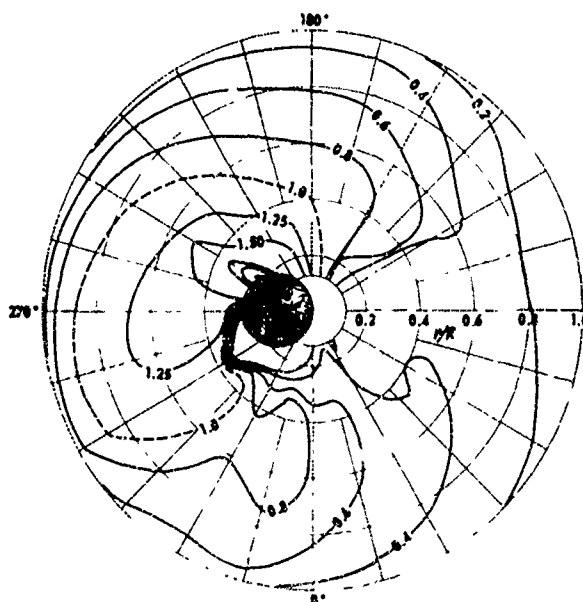


Figure 8 DISTRIBUTION OF EFFECTIVE
ANGLE OF ATTACK, NORMALIZED
TO 14 DEGREES; HU-1A; $\mu = 0.26$

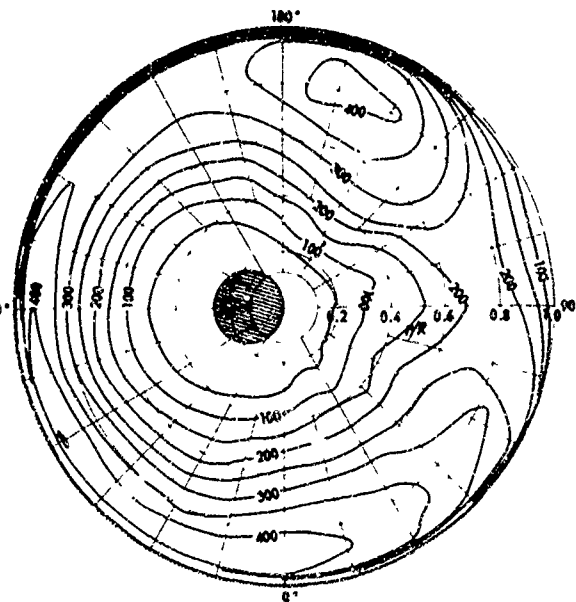


Figure 9 AIRLOAD DISTRIBUTION; lbs/ft;
HU-1A; $\mu = 0.26$

**COMPARISON OF FLIGHT MEASURED
HELICOPTER ROTOR BLADE
CHORDWISE PRESSURE DISTRIBUTIONS AND
TWO-DIMENSIONAL AIRFOIL CHARACTERISTICS**

**James Scheiman and Henry Kelley
NASA, Langley Field, Hampton, Virginia**

COMPARISON OF FLIGHT MEASURED HELICOPTER
ROTOR BLADE CHORDWISE PRESSURE DISTRIBUTIONS
AND TWO-DIMENSIONAL AIRFOIL CHARACTERISTICS

By James Scheiman and Henry L. Kelley
NASA Langley Research Center

For Presentation at the CAL-TRECOM Symposium on
Dynamic Loads Problems Associated With Helicopters
and V/STOL Aircraft, Buffalo, New York,

June 26-27, 1963

COMPARISON OF FLIGHT MEASURED HELICOPTER
ROTOR BLADE CHORDWISE PRESSURE DISTRIBUTIONS
AND TWO-DIMENSIONAL AIRFOIL CHARACTERISTICS

By James Scheiman and Henry L. Kelley
NASA Langley Research Center

SUMMARY

A comparison is made between airfoil chordwise pressure distributions from helicopter rotor flight tests and static two-dimensional wind-tunnel tests. Differences in actual and two-dimensional-airfoil pressure distributions are shown to exist. These differences in airfoil characteristics are expected to amplify the blade flapwise and torsional vibratory forces determined from two-dimensional-airfoil data. Possible reasons for these airfoil differences are briefly discussed. The point is made that in endeavoring to confirm current refined theories of calculating section angle of attack, it is essential, in making data comparisons, that care be used to prevent these differences between actual and static two-dimensional-section data from obscuring the effectiveness of the angle-of-attack calculations.

INTRODUCTION

Experience has shown that the ability to perform an adequate structural dynamic analysis of the rotor blade is marginal. This lack of ability has generally been viewed as attributable to unknown air loads and in particular to unknown inflow velocities rather than to the applicability of two-dimensional-airfoil characteristics. This view has tended to be confirmed, for example, by the results of rotor test inflow velocity measurements and by the adequacy of predicting

helicopter performance by use of two-dimensional airfoil data. In any case, both inflow velocities and actual airfoil characteristics must be known in order to perform a reasonably accurate dynamic blade analysis.

In regard to the inflow velocities, it is believed that the capability of theory to predict these velocities for trim level flight has significantly improved recently. With these new theories the danger exists for blaming the remaining inadequacy of the inflow theory for any lack of correlation between test and theory, when the differences may actually be caused by airfoil characteristic discrepancies.

The validity of two-dimensional data has been given little detailed attention because of a lack of actual operating test data. Partly to help fill this gap, the NASA Langley Research Center has recently completed a helicopter flight-test program which has utilized extensive blade pressure instrumentation. These data provide a comparison of the actual and two-dimensional-airfoil chordwise pressure distributions to the extent needed to illustrate that important airfoil characteristic discrepancies do occur in the flight conditions sampled.

Portions of the flight measured chordwise pressure distributions for two flight conditions are discussed. Samples of these distributions are directly compared with two-dimensional full-scale data (see ref. 1) by equating the two normal force coefficients. The chordwise pressure distribution for other flight conditions and the movement of the blade center of pressure are discussed.

All reference to two-dimensional-airfoil characteristics in this paper refers to static two-dimensional characteristics in distinction to oscillating unsteady two-dimensional characteristics.

SYMBOLS

c	airfoil chord
C _N	normal-force coefficient
Δp	differential pressure measured on the airfoil
q	dynamic pressure
r	radial distance to blade element measured from center of rotation
R	blade radius measured from center of rotation
V _F	forward speed
x	chordwise distance measured from blade leading edge
\bar{x}	center of pressure of airfoil section measured from leading edge
μ	nondimensional tip-speed ratio, $\frac{1.69V_F}{\Omega R}$
ψ	blade nominal azimuth angle, measured from downwind position in the direction of rotation and disregarding blade lag motion
Ω	rotor angular velocity

DISCUSSION

Normal-Force Coefficient for Flight

With Blade Section Stall

A plot of the local normal-force coefficients C_N along the blade radius for different azimuth positions is shown in figure 1. The flight condition is for a trim, level-flight-cruise forward speed and a reduced rotor rotational speed and is thus for a flight condition expected to produce local blade-section stalling. Further details of this flight condition are available in table IV of reference 2.

Notice the high values of normal-force coefficient in the area of $r/R = 0.55$, $\psi = 210^\circ$ to $\psi = 240^\circ$ and for $r/R = 0.75$, $\psi = 250^\circ$. These coefficients correspond to dynamic pressures of approximately 50 pounds per square foot at $r/R = 0.55$ and 100 pounds per square foot at $r/R = 0.75$. The normal-force coefficient values, in these areas of the rotor, correspond to values above the maximum static two-dimensional values of C_N . Just prior to these high normal-force coefficients a rapid rate of change in the normal-force coefficient is noted. This change in C_N can be directly related to a two-dimensional-airfoil angle-of-attack change and the corresponding high rates of angle-of-attack change can be explained, for example, by the rapid changes in local inflow velocities through the rotor. In this instance an estimate based on successive normal-force coefficients, in the previously mentioned high angle-of-attack area of the rotor, indicates a rate of roughly 100° per second or 1° per $2\frac{1}{2}$ blade-chord lengths. This rapid angle-of-attack increase will

provide a partial explanation for the lack of chordwise-pressure-distribution correlation explored further in this paper.

The circles on this figure are points where chordwise pressure distributions are discussed in figures 2 to 4; the solid circles are points where two-dimensional and flight data are compared.

Chordwise Pressure Distributions for Flight With Blade Section Stall

Figures 2 to 4 are for the same flight condition as figure 1, which was selected with the expectation of producing local blade-section stalling. A plot of the chordwise pressure coefficient distribution for $r/R = 0.55$ and $\psi = 165^\circ, 195^\circ, 210^\circ, 225^\circ$, and 255° is shown in figure 2. The blade-azimuth position, integrated normal-force coefficient, and the centers of pressure are as indicated. At $\psi = 165^\circ$, the flight-test distribution agrees with the two-dimensional data; the center of pressure is close to (slightly aft of) the quarter chord. The normal-force coefficient is below the two-dimensional stall point. At $\psi = 195^\circ$ the normal-force coefficient of 1.3 is above the two-dimensional stall value but the pressure distribution appears unstalled. At the remaining azimuth locations the normal-force coefficient is above the airfoil section two-dimensional stall point and no two-dimensional data are available for comparison. The pressure distribution is such as to correspond to some separation and, therefore, the section can be viewed as exhibiting stall characteristics although the details of the distribution have no counterpart in two-dimensional data. Based on examination of the contours of figure 1, this increased maximum C_N

is expected to increase the vibratory amplitude of the actual airfoil blade loads as compared with the predicted two-dimensional air loads.

It may be of interest that some variations in pressure occurred between rotor revolutions for these last three plots (average values are shown); however, the distribution shapes are believed representative. These variations in themselves suggest a stalled type of flow.

Sample pressure distributions for $r/R = 0.75$ are shown in figure 3; these distributions are for the same flight condition shown in figures 1 and 2. For $\psi = 165^\circ$ and 195° the distribution shows good agreement with two-dimensional data. As the azimuth angle increases from $\psi = 195^\circ$ to 240° , the normal-force coefficients again increase to values above the two-dimensional stall point, although the actual airfoil retains the unstalled two-dimensional pressure distribution.

The pressure distribution for $r/R = 0.95$ is shown in figure 4. The normal-force coefficients are all below the static two-dimensional stall point and therefore good pressure-distribution correlation would be expected. For $\psi = 45^\circ$ and 75° the agreement between the flight and two-dimensional data is indeed reasonable, but at $\psi = 90^\circ$ and 120° the correlation is not so good. Thus, while a large part of the rotor does behave in accordance with two-dimensional data, figures 2 to 4 show that poor correlation can occur to a degree which would be expected to have a major effect on periodic blade loads.

Chordwise Pressure Distributions for Flight

With High Blade-Tip Mach Numbers

The next trim level flight condition discussed for flight at a high tip Mach number, for which the maximum blade-tip Mach number was 0.76. The chordwise pressure distribution for the 0.95 blade station is shown in figure 5. The normal-force coefficients are all below the two-dimensional-airfoil stall point and good correlation would be expected. The centers of pressure, however, are all farther forward than would be expected, even for high Mach number operation of a two-dimensional airfoil. For $\psi = 30^\circ$ there is reasonable agreement between the flight and two-dimensional distributions, although for $\psi = 75^\circ, 90^\circ$, and 105° the flight data depart from the two-dimensional data.

The 0.75-radius station shown in figure 6 is for the previously described high tip Mach number flight. The flight-measured chordwise pressure distributions, the centers of pressure, and normal-force coefficients are typical of unstalled two-dimensional data. The correlation shown is good.

The high tip Mach number test for the 0.55-blade-span station is shown in figure 7. Again the normal-force coefficients, centers of pressure, and the distribution are typical of two-dimensional data. The correlation with two-dimensional data is again good.

In summary, figures 5, 6, and 7 for the high tip Mach number flight indicate that a large percentage of the actual chordwise pressure distributions are in agreement with two-dimensional airfoil data. Only a

small (though important) percentage of the pressure distributions are not in agreement. Since the disagreement in this case is primarily in the high Mach number regions, it appears that with careful selection of the flight test conditions, it will be possible to find cases that warrant comparison with theories using the two-dimensional data to study the adequacy of new angle-of-attack prediction theories.

Other Flight Conditions

A small portion of the chordwise pressure distributions for a number of other trim level-flight conditions have been reviewed and the results were similar to the results of the previous two flight conditions discussed in detail in this paper; namely, that portions of the actual operating helicopter blade do not behave in accordance with two-dimensional airfoil data. Because there are these cases where important differences do arise, an exact knowledge of the rotor inflow velocities is not necessarily sufficient to describe the exact rotor blade loading. Caution should therefore be exercised in interpreting the correlation of flight measured and theoretical rotor-blade spanwise loadings.

Measured Center-of-Pressure Movement

In an attempt to generalize the actual airfoil center-of-pressure movement, a plot was made of the center of pressure as a function of the blade azimuth angle for three different flight conditions, and this plot is shown in figure 8. Note the forward shift in center of pressure on the advancing side of the rotor for all three flight

conditions and the rearward center of pressure on the retreating side of the rotor for the first flight condition (flight with blade section stall discussed previously). The forward shift in center of pressure could not be explained by Mach number effects.

The flight-test blade was a modified NACA 0012 airfoil (ref. 1) and hence had no camber. The interesting possibility thus arises that if a small amount of camber, which would tend to add a constant moment coefficient with varying angle of attack below stall were added, the variations in dynamic pressure with azimuth would then modify the measured centers of pressure in such a way as to result in reduced one-per-revolution aerodynamic control forces. In other words, the added source of moment variation with azimuth would be expected to have a phase angle such as to offset partially the measured variations.

Discussion of Actual and Two-Dimensional-Airfoil

Pressure-Distribution Differences

The reasons for the differences found between actual and two-dimensional airfoil data are not completely understood. As is well known, the flow conditions on a rotor are highly complex and many potential contributing explanations have long been at hand should such problems arise. Since the problem has now been verified in tangible form, an effort is being made to sort out some of these possibilities.

As one example, the fact that a high rate of increase in angle of attack can give higher than static $C_{N_{max}}$ values is well known (for example, ref. 3), and this effect has long been looked for in

rotor measurements. In some early investigations this effect was apparently negligible, that is, stall was evidenced roughly where expected. Apparently the other complexities of rotor inflow, and the specific design details, prevented any significant occurrence of higher than static $C_{N_{max}}$ values. In several more recent investigations, including the present one, the opposite has been true. Dynamically, this effect would be expected to increase the actual amplitude of the oscillating air loads as compared to the calculated loads based on two-dimensional data.

It should be noted that the most drastic source for high rates of change of angle of attack is likely to be the striking of the tip vortex from the previous blade. Consequently, the high rates of change and the C_N values in excess of static two-dimensional values may occur in specific cases in basically mild flight conditions as well as in the low rotor speed or high forward velocity conditions normally associated with blade-section stalling.

Time-varying blade yaw angles, spanwise flow on the blade, and nonuniform velocity gradients in front of the airfoil are other possible factors that may cause disagreement between actual and two-dimensional airfoil characteristics.

CONCLUDING REMARKS

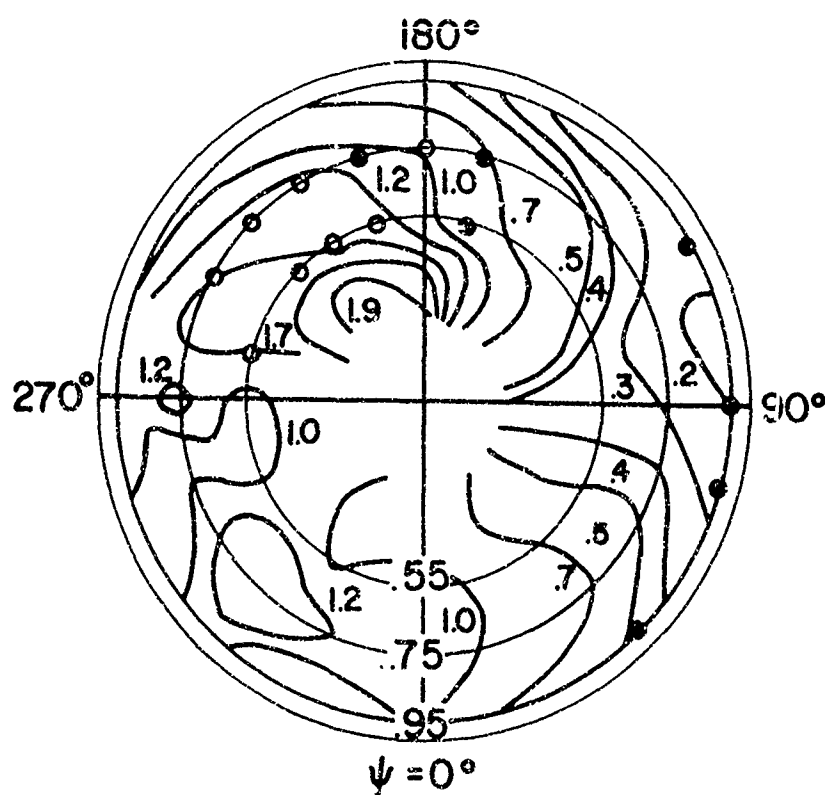
It has been shown that the actual helicopter rotor blade does not always behave in accordance with two-dimensional airfoil data. These airfoil-characteristic differences are expected to amplify both the

applied and torsional blade oscillating loads. Possible reasons for these differences were briefly explored. The point is made that when loads are predicted from refined inflow theories as compared with experimental loadings, caution should be exercised in interpreting differences in blade loading, since these may arise because of the applicability of two-dimensional data rather than inadequacies of inflow theory. Thus, before comparisons of actual and predicted loads are used to determine validity of angle-of-attack calculations each experimental case used must be reviewed for evidence of presence or absence of discrepancies between the actual section aerodynamic characteristics as reflected by chordwise pressure distribution and the section characteristics being assumed in the analysis.

REFERENCES

1. Lizak, Alfred A.: Two-Dimensional Wind Tunnel Tests of an H-34 Main Rotor Airfoil Section. TREC Tech. Rep. 60-53 (SER-58304), U.S. Army Transportation Res. Command (Ft. Eustis, Va.), Sept. 1960.
2. Scheiman, James, and Ludi, LeRoy H.: Qualitative Evaluation of Effect of Helicopter Rotor-Blade Tip Vortex on Blade Airloads. NASA TN D-1637, 1963.
3. Silverstein, Abe, and Joyner, Upshur T.: Experimental Verification of the Theory of Oscillating Airfoils. NACA Rep. 673, 1939.

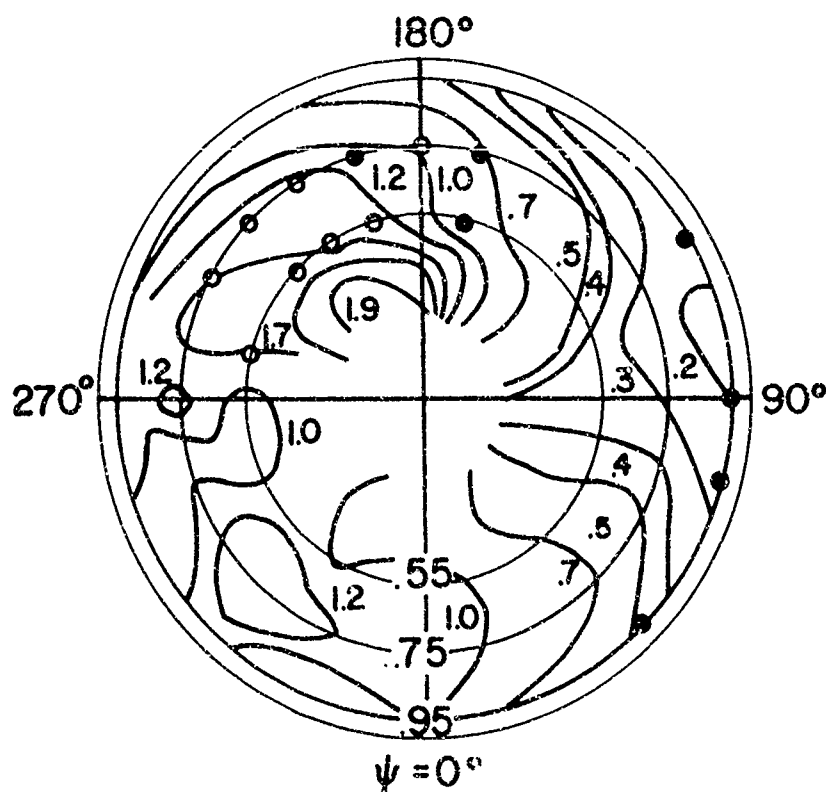
- FLIGHT AND 2-DIM. TUNNEL } CASES FOR CHORDWISE PLOTS
- FLIGHT ONLY



NASA

Figure 1.- Local normal-force coefficients from flight data, $\mu = 0.23$.

- FLIGHT AND 2-DIM. TUNNEL } CASES FOR CHORDWISE PLOTS
- FLIGHT ONLY



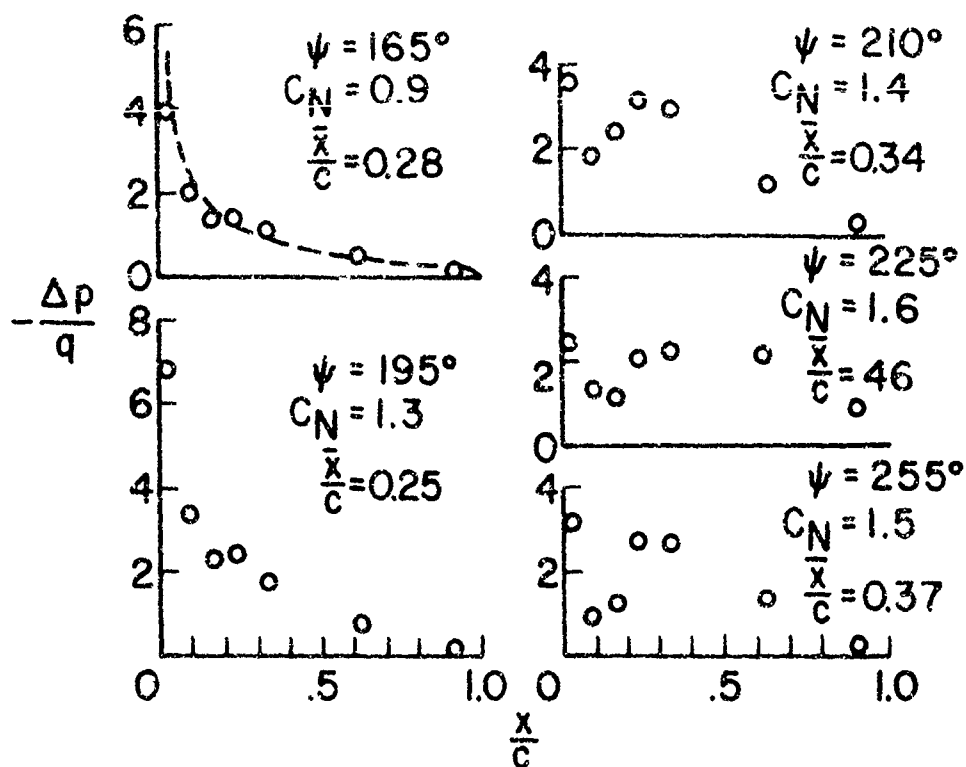
NASA

Figure 1.- Local normal-force coefficients from flight data, $\mu = 0.23$.

$$\mu = 0.23, \frac{r}{R} = 0.55$$

○ FLIGHT DATA

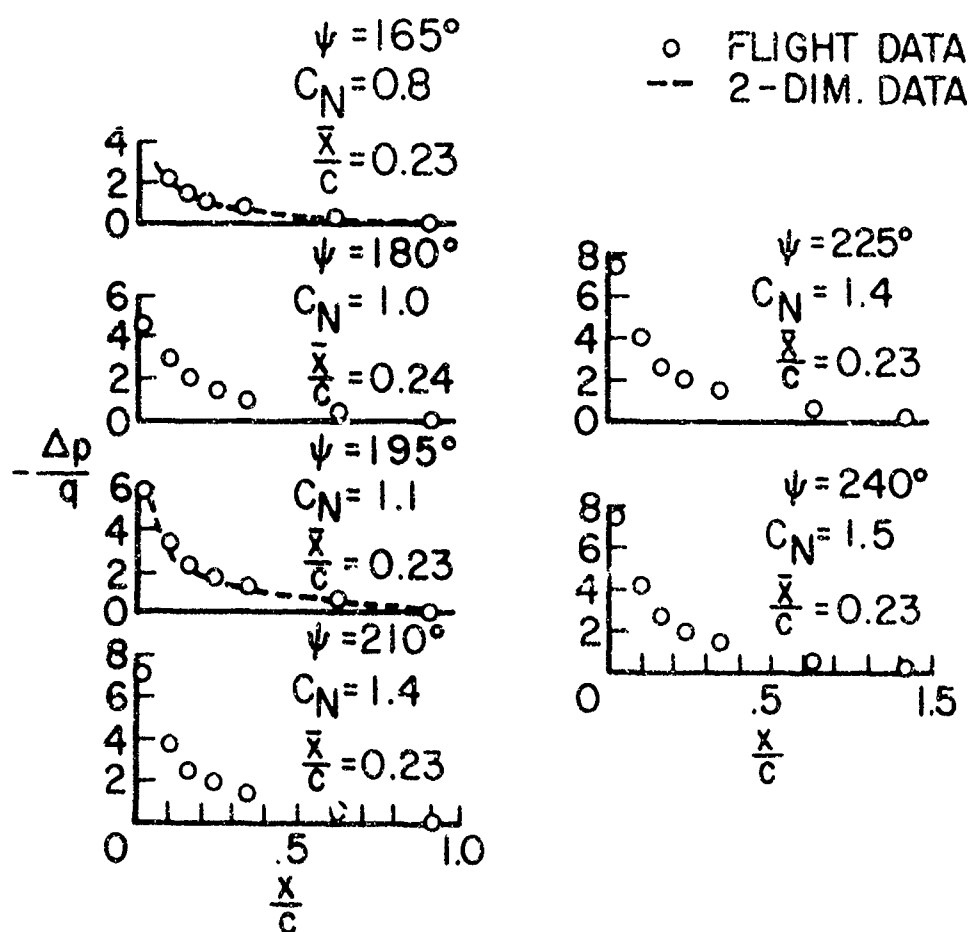
--- 2-DIM. DATA



NASA

Figure 2.- Chordwise pressure distributions.

$$\mu = 0.23, \frac{l}{R} = 0.75$$

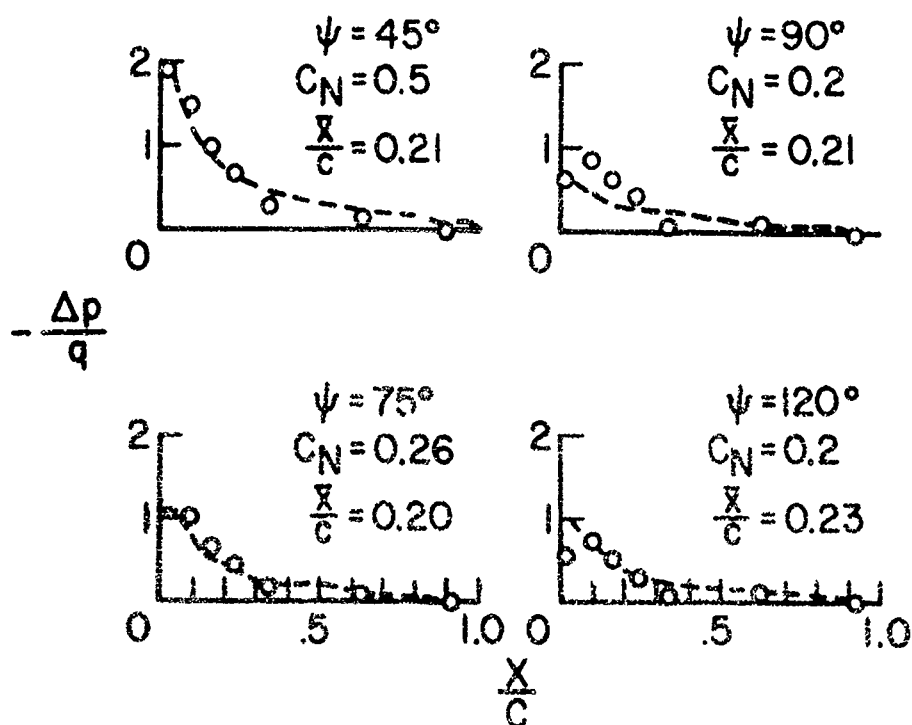


NASA

Figure 3.- Chordwise pressure distributions.

$$\mu = 0.23, \frac{r}{R} = 0.95$$

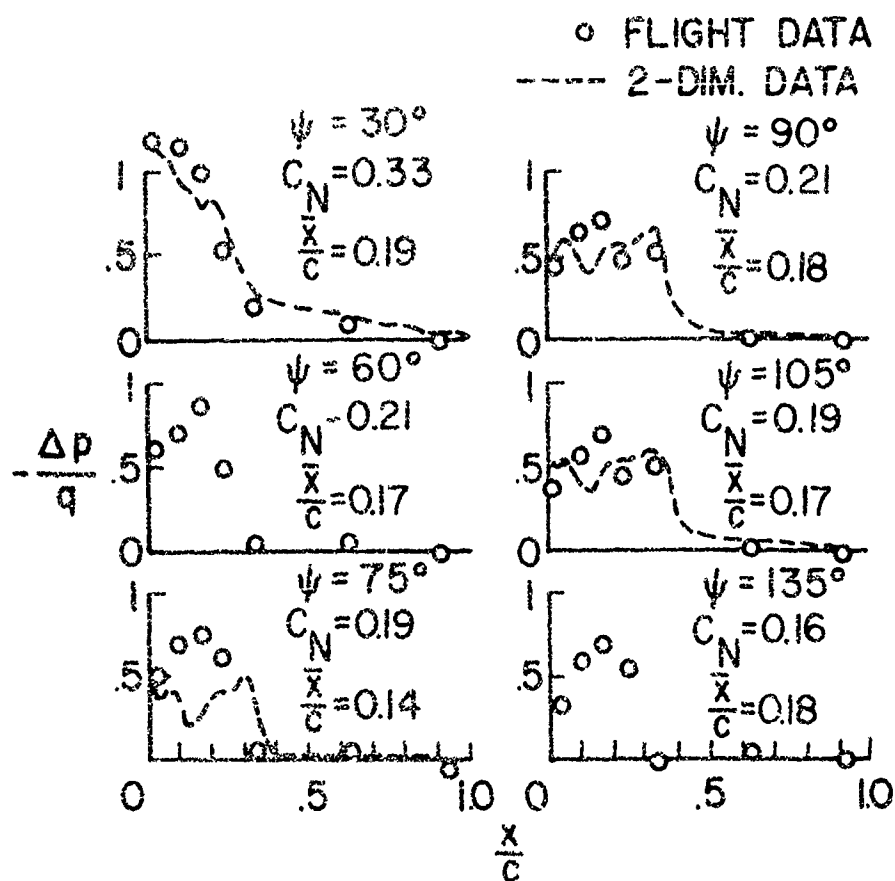
○ FLIGHT DATA
 --- 2-DIM. DATA



NASA

Figure 4.- Chordwise pressure distributions.

$$\mu = 0.24, \frac{r}{R} = 0.95$$

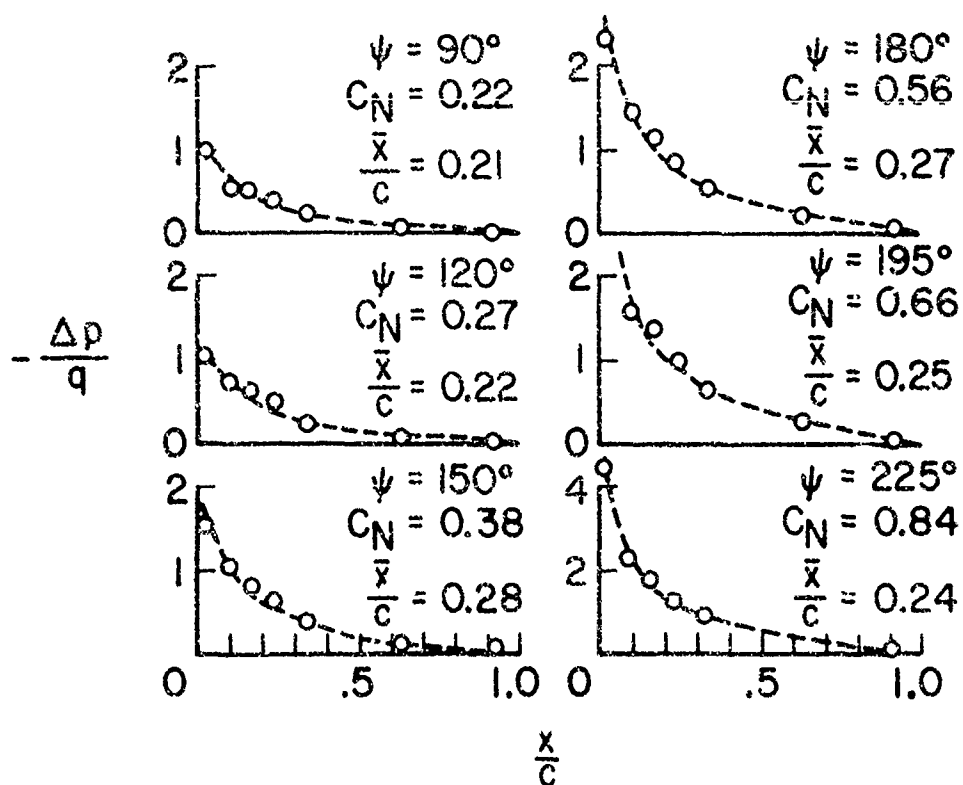


NASA

Figure 5.- Chordwise pressure distributions.

$$\mu = 0.24, \quad \frac{r}{R} = 0.75$$

○ FLIGHT DATA
 --- 2-DIM. DATA



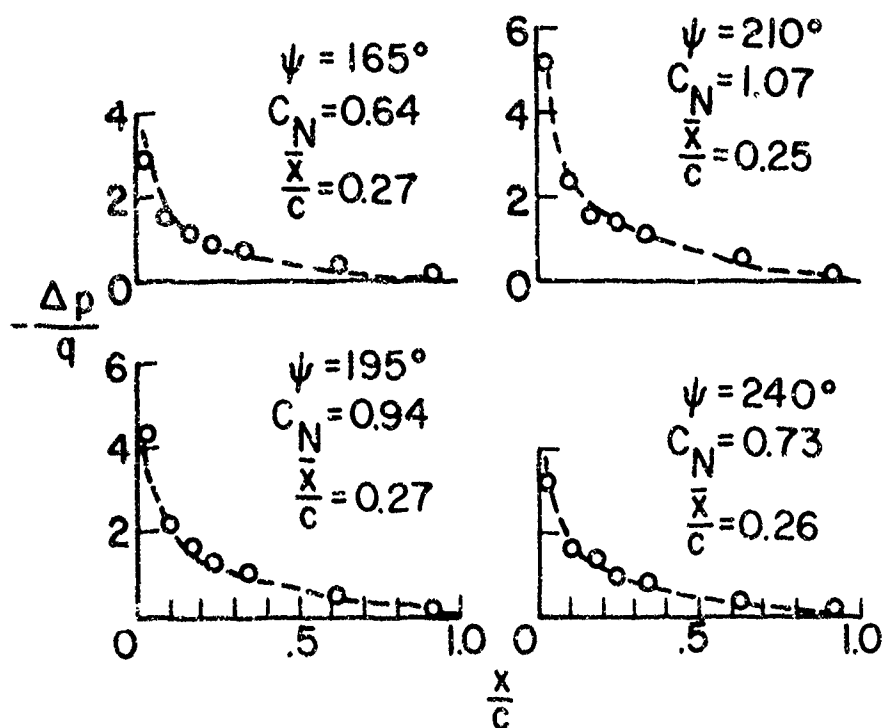
NASA

Figure 6.- Chordwise pressure distributions.

$$\mu = 0.24, \frac{r}{R} = 0.55$$

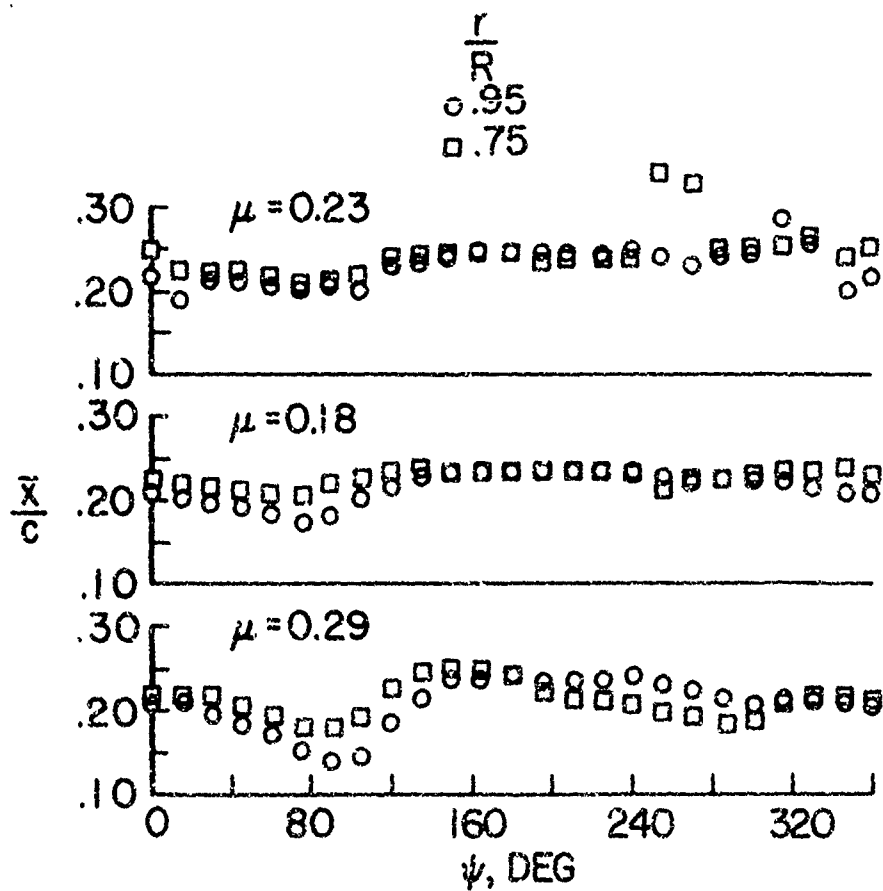
○ FLIGHT DATA

--- 2-DIM. DATA



NASA

Figure 7.- Chordwise pressure distributions.



NASA

Figure 8.- Centers of pressure.

**A DISCUSSION OF ROTOR BLADE
HARMONIC AIRLOADING**

R.H. Miller

MIT

A DISCUSSION OF ROTOR BLADE HARMONIC AIRLOADING

R. H. Miller

Department of Aeronautics and Astronautics
Massachusetts Institute of Technology

Introduction

The subject of this symposium covers one of the most important and yet in many ways one of the most neglected areas of V/STOL technology. Certainly in an engineering sense the subject cannot be said to have been neglected since the problems of helicopter vibration and fatigue (both human and structural) must be reduced to manageable proportions by the exercise of ingenuity and much time and expense during the engineering development stages, and this has been the history of V/STOL development since the first practical helicopter flew in the 1930s.

However the basic research which could lead to a better understanding of the physical phenomena of VTOL dynamics and hence to a more rational solution of the associated problems has been neglected in the past and the result has been a containment of the problems rather than their solution. There are many valid reasons for this lag in research, the most obvious being the extreme complexity of the system. However we now have both experimental and analytical techniques available to us which could permit rapid investigation of the aerodynamics and dynamics of V/STOL aircraft and which could lead to a better understanding of the basic phenomena. It is axiomatic that without this understanding control of these phenomena will never be possible except on a hit and miss basis.

The decision to hold a symposium on this topic is therefore most welcome and timely. In responding to the invitation to present a discussion at this meeting on work conducted at MIT on rotor dynamics, a selection was made from the projects conducted during the past few years and only those pertinent to the title of this paper and of current interest were selected. Research by others in the same area will not be referred to in the interests of time and because a fairly complete coverage has previously been included in Ref. 1.

Early Investigation of Airloads by Meyer and Falabella

From 1947 to 1952 a series of wind tunnel tests were conducted on the aerodynamic loading of rigid and flapping rotor blades. The initial studies (Ref. 2) were confined to the measurements of bending moments. One of the most interesting results was the demonstration of the critical effects of blade resonance combined with the very low aerodynamic damping, clearly evident from Fig. 1. Reasonable overall agreement between computed and measured bending moments was obtained for both the flapping and rigid rotor but it was concluded that information regarding the actual aerodynamic loading or induced flow was needed to establish the higher harmonic loadings.

Consequently a new program was started in which the blade airloads were measured directly by means of a pressure transducer. Fig. 2, from Ref. 3 presents one of the results of this investigation and shows the downwash distribution at the rotor disc deduced from the measured airloads. These results are useful for verification of more recent theoretical calculations of the downwash distribution and at the time provided experimental evidence of the highly non uniform character of the rotor inflow which is now recognized as being one of the primary sources of the periodic excitation of helicopters.

It was during this program that the pronounced effect of flapping hinge offset on the airload distribution of the rotor was noticed. This led to the conclusion that the effect of a rigid rotor could be achieved without the need for providing a high degree of structural stiffness; that is a hinged rotor could be designed to carry large first harmonic bending moments at the hub by offsetting the flapping hinge appreciably from the center of rotation. Of interest here is the pronounced influence of this first harmonic load variation on the inflow through the rotor, as shown in Fig. 3. A much more uniform downwash distribution was obtained which would suggest that an equivalent rigid propeller carrying large first harmonic moments in forward flight would be smoother than a flapping rotor. Structural and design considerations determine the degree to which such moments could be tolerated in an actual vehicle. This point is discussed further in Ref. 4.

Direct Measurement of Hub Loading

The investigations described above clearly indicated that appreciable higher harmonic excitations were occurring on the rotor. Simple rotor blade aerodynamic theories using uniform downwash indicated that these loads would decrease rapidly with advance ratio. However this clearly did not fit the observed facts. Consequently a program in which hub loads were directly measured was initiated in order to explore this phenomenon more fully. The program was conducted in two parts. In the first the rotor was subjected to forced oscillations and the results substantiated the large reduction in damping predicted by Loewy due to unsteady aerodynamic effects. In the second part the rotor was used as a mechanical amplifier for the aerodynamic harmonic load by placing the blade in resonance with the harmonic to be investigated and measuring the resultant hub shears. As a result of this series of tests it was obvious that a mechanism existed which produced high periodic airloads on a rotor blade at integers of the rotor speed, that existing methods for predicting these loads were inadequate and that unsteady aerodynamic effects in the presence of these oscillatory airloads were of prime importance. (Refs. 11 and 12)

The experimental program was continued in order to investigate more harmonics, particularly the third which had not been covered in the earlier investigation and in order to determine the effects of tandem rotor geometry on the vibration level. Because of the obvious difficulty of changing geometry for such purposes in a flight test program results of this nature are most conveniently obtained from wind tunnel tests. This program, conducted by Duvivier, produced the results shown in Fig. 4, taken from Ref. 5 in which the pronounced effects of geometry on tandem rotor vibration are evident.

During this program techniques were developed for measuring blade airloads directly by means of single pressure pickups located at various spanwise stations along the rotor blade. This permits the investigation of many interesting phenomena with relatively small models in the wind tunnel and forms the basis of a continuing program involving the direct measurement of rotor blade airloads under various simulated flight conditions and airframe geometries. Because of the difficulties of covering a wide variation of trim conditions and geometry on a full scale vehicle such testing techniques are of value in providing a better understanding of rotor aerodynamic loading. This work is sponsored by TRECOM, U. S. Army.

Aeroelastic Investigations

Simultaneously research was being conducted on the flutter characteristics of rotor blades. Much of this work is not pertinent to this meeting, however two items are of interest and will be briefly discussed.

Stall flutter of propellers, rotors and compressors has been a problem for years because of the high angle of attack at which these operate. On a rotor blade this phenomenon is believed to be one of the causes for the very high pitching moments experienced at high advance ratios. Investigations by Ham (Ref. 6) defined the parameters which govern this phenomenon and provided a valuable criterion by which its presence can be detected. For example Fig. 5 taken from Ref. 6 shows the great dependence of stall flutter amplitude on the amount of stalled area in the rotor disc regardless of advance ratio.

Another aeroelastic phenomenon which is of importance in establishing the harmonic loading of rotor blades is that arising from the deflections of the blade out of the plane of rotation and out of the plane of its twist axis. The effects of this phenomenon on flutter are discussed in Ref. 7. Its potential significance for blade loading is discussed in Refs. 1 and 8 and may be demonstrated by a simple illustration. In Fig. 6 a blade is shown with its normal elastic deflection. Primary torsional flexibility for simplicity is assumed to occur at the feathering hinge located near the blade root. As the blade twists about the feathering hinge components of centrifugal force act to increase this twist. That is, a rotor blade bent out of its plane of rotation is not in static equilibrium. Since the centrifugal force is several times the gross weight of the ship, clearly powerful blade twisting moments can be produced by this mechanism. In Ref. 7 it was shown that in certain cases these moments could be equivalent to those produced by a 6% shift in chordwise CG of the rotor blades.

Since rotor blades must bend elastically in the presence of aerodynamic lift, the centrifugal force component as well as the steady state drag will cause periodic twisting moments due to the periodic changes in blade bending deflection caused by the higher harmonic airloads. In addition, periodic changes in induced drag due to the higher harmonic content of the downwash will combine with the steady state elastic deflection of the blade to produce another source of periodic twisting moments. Twisting moments from these two sources will cause harmonic changes in angle of attack and are therefore of considerable importance in establishing the blade loads.

Theoretical Prediction of Blade Airloads

The tests discussed above clearly indicated the need for an analytical tool for computing blade downwash velocities which would take into account the individual blade wake geometry and also introduce the effects of unsteady aerodynamics. Attempts to obtain a closed form solution to this problem, or one based on tabulated integrals, were not successful and it was evident that extensive computer facilities would be required to explore this problem and, hopefully, to provide a basis for obtaining simplified solutions suitable for engineering applications. In 1960 the availability of an IBM 709 computer at the MIT Computation Center and funds from a Carnegie grant permitted initiation of such a program. This is a continuing investigation under BuWeaps sponsorship. The results to date have been published in Ref. 1, 8 and 9 and therefore only the intent of the research and the current status will be summarized here.

It was decided that an attempt would be made to construct the program of research in such a way as to lead primarily to an understanding of the basic phenomena involved and to include insofar as possible a rigorous treatment of the unsteady aerodynamics. In order to accomplish both these purposes the following approach was followed.

1. The computer program was developed in such a way that the rotor inflows could be obtained independently, if possible, of blade motions.
2. The classical approach in which the trailing and shed wakes were treated independently and the unsteady aerodynamic effects determined separately was followed.
3. The program could be modified to a lifting surface rather than a lifting line approach when necessary.
4. Since the program was to be used primarily for research, numerical precision of the different integrations would be varied over wide limits and over the different elements of the program as required.
5. The classical assumptions of a rigid wake of propeller vortex theory would not be accepted.

It was hoped that this approach in addition to clarifying the physics of the problem would also lead to a much simplified computer program.

Computer solution times vary widely depending on the degree of accuracy desired. Fig. 7 shows a comparison of the correlation between theory and experiment as a function of the number of stations used in establishing the trailing vortex pattern for a harmonic of general interest. The large number of stations of Fig. 7a are required to define the tip loading accurately but the smaller number of stations of Fig. 7b would probably be sufficiently accurate for most engineering purposes. The two station solution (Fig. 7c) is useful for demonstrating many of the phenomena of rotor blade loading and is a valuable research tool. At moderate speeds the bound circulation on the blade does not vary radically over the outer 50% span, regardless of twist, from the minimum energy condition of constant circulation and hence much qualitative information may be quickly obtained by observing behavior of a hypothetical "ideally" twisted blade, as was done in Ref. 1, having a tip vortex and a root vortex located at a representative inboard station.

The degree of accuracy shown in Fig. 7a is by no means typical for all rotors and harmonics. For certain conditions more accurate solutions are required using much closer intervals, a reiteration for non-rigid wake effects and a lifting surface theory rather than the lifting line approximations. Such solutions and the conditions under which they are used will be discussed later. The ideal fluid potential flow model used in these solutions has, however, certain fundamental limitations and there is some question as to the degree of ultimate computation accuracy which would be meaningful in view of both these limitations, and the difficulty of obtaining equally accurate test results or actual rotors under known conditions. It is believed that, as in the case of fixed wings, this theory is of most value as a research tool in order to clarify physical phenomena and to aid in the interpretation of test results.

The decision to separate the blade motions from the computer solutions for downwash resulted from the previously discussed experimental evidence of the pronounced effect of blade elasticity on the airloads. If it could be assumed that the blade responded to an aerodynamic input which, to first order, would not be modified by this response then the problem could be considerably simplified since the solution for blade airload and for blade response to that airload could be separated. The basis for this hypothesis came from the investigations reported in Ref. 1. From this study it was evident that interharmonic coupling effects could to first order be neglected. That is, for example, the n th component of downwash generated by an m th harmonic lift variation was an order of magnitude less than

that generated by the n th harmonic lift variation. Furthermore higher harmonic airloads are an order of magnitude less than the steady state load acting on the ship. Consequently their contribution to the downwash distribution at the rotor disc will be two orders of magnitude less than that contributed by the spiral wake generated by steady state blade lift and this downwash is readily computed for any gross weight and mean inflow.

Having established the nature of the downwash variation around the rotor disc the next step is to compute the airload variation corresponding to this downwash distribution. Quasi-static lifting line solutions give reasonable estimates of these loads but introduce appreciable errors both in magnitude and phase. It is therefore necessary to introduce the classical lift deficiency functions of unsteady aerodynamics. In Ref. 1 a closed form solution was obtained for this lift deficiency function, $C(k) = F + iG$ (to use standard nomenclature) for hovering flight and for an infinite number of blades and it was shown that F and G reduced to the following simple expressions, independent of frequency,

$$F = \frac{1}{1 + \frac{\sigma\pi}{4\lambda}} \quad G = 0$$

This result leads to the hypothesis that over all approximate values of the lift deficiency function F and the corresponding phase shift G/F could also be obtained for the forward flight case. Consequently typical values were computed some of which are shown in Fig. 8. A more marked variation with frequency was apparent than for the hovering flight case; also the lift deficiency function gradually increases with μ and eventually approaches the two dimensional classical value. Similarly G increases from a value very close to zero and again approaches the two dimensional value away from the blade tip. G , which determines the phase shift cannot be predicted by using lifting line theory because of the singularities involved as the shed wake approaches the trailing edge of the surface, and lifting surface theory must therefore be used in obtaining these results. An approximate means of determining this while still retaining the convenience of lifting line theory in the computer solutions was suggested in Ref. 8 in which an equivalent upper limit for the shed wake integrations was established. Lift deficiency functions obtained by these means are highly accurate in comparison with the formal approach using lifting surface theory given in Ref. 1.

Computation of the rotor blade airload thus proceeds in the following steps:

1. Compute the downwash distribution at the rotor disc due to a trailing vortex system of constant unit strength originating from as many spanwise stations as desired along the blade. The use of unit vortex strength permits tabulating this downwash distribution for various values of mean inflow λ_0 , advance ratio, μ , and the number of blades. This tabulation is currently being started.
2. The actual downwash is then computed from the known blade geometry and aircraft trim by inversion of the matrix obtained from Eq. 17 of Ref. 8 in the manner described in that reference.
3. Knowing this downwash distribution quasi static airloads may be obtained from Eq. 14 of Ref. 8 and the actual airloads obtained by suitably modifying the quasi static airloads by the appropriate F and G functions, similar to those given in Fig. 8.

Steps 2 and 3 are trivial solutions for the computer, the bulk of time being required for the integration of step 1, hence the attempt to tabulate these results.

The limitations of the lifting line theory will now be discussed using for illustration the simple two dimensional case. Fig. 9 is a sketch of an airfoil in two dimensions in the presence of an element of vorticity $\gamma d\xi$ at a distance ξ from the airfoil. The normal velocity w induced at this airfoil at a chordwise station x due to $\gamma d\xi$ is

$$w(x) = \frac{\gamma d\xi}{2\pi(\xi - x)}$$

When $\xi \gg b$, i.e., when the element of vorticity is relatively far from the blade then $\xi \gg x$ and w is substantially constant with x . A mean value of w may then be used and this is the basis for the well known lifting line theory. When ξ is not large compared to b lifting surface theory must be used. This requires that w be expressed as a Fourier series in terms of the blade chord. The first two components of the series and their tip variations define the blade lift. These steps have been described in detail in Ref. 1. Evidently computer time for such a solution would be several times more than that required for the lifting line solution, depending on the number of chordwise stations required to define $w(x)$ adequately. Fortunately there are only a few instances where such an approach would be required and, as is evident from the above discussion, the multiple chord station computations need be performed only over a short segment of the wake in the vicinity of the airfoil, using equations 4 and 5 of Ref. 1. Two cases requiring this more rigorous lifting surface theory will now be given as illustration.

The first is in the computation of the lift deficiency function $C(k) = F + iG$ referred to above. As the shed wake approaches the airfoil or $\xi \rightarrow b$, a singularity at the trailing edge of the airfoil develops which can not be ignored if G , which determines the phase shift, is to be correctly evaluated. This requires the use of lifting surface theory. For reasons discussed in some detail in Ref. 8, F can be closely approximated for the low reduced frequencies of interest in rotor dynamics by ignoring this singularity and using mean values of $w(x)$ as in lifting line theory. However G is always critically dependent on the chordwise variation of $w(x)$. This was the reason for introducing the concept of a "near" and a "far" wake in Ref. 1 and using lifting surface theory in the near wake. In hovering flight, $\mu = 0$, the near and far wakes contribute about equally to the final value of G but as μ increases the effect of the far wake gradually diminishes until at a μ of about .3 only the effect of the near wake on G is significant. Again this follows from the above discussion.

In Fig. 10 the build up of the lift deficiency function is shown for a typical case. Subscript 1 refers to the lift deficiency function generated by the near shed wake where the near wake is defined as being that portion extending from the rotor blade aft over the first quarter azimuth. This portion of the lift deficiency function generally is close to the two dimensional classical value. Subscript 2 refers to the lift deficiency function obtained from both the near and far shed wakes. Subscript 3 refers to the lift deficiency function as obtained from both the far shed and near shed wakes and the complete trailing wake system. It is evident that as the advance ratio increases the near shed wake dominates. At the blade tip, however and for loadings concentrated over a short segment of the span, the three dimensional value of G becomes appreciably smaller than the two dimensional value. Frequently its effect at least for blade loading computations, will not be of great significance and lifting line solutions may therefore provide good approximations to this loading.

Another case of interest in which lifting surface theory must be used is found when the blade approaches close to the trailing wake. This can occur when non-rigid wakes are intro-

duced into the computations at low advance ratios as discussed in Ref. 10. It may also occur at any advance ratio in the case of a rotor with a large number of blades operating at low thrust coefficients and hence having low mean inflow velocities. The intense tip vortex, characteristic of rotors, generated by any one blade will come close to the following blade and lifting line theory then predicts erratic and unreliable lift variations.

An interesting conclusion drawn from an examination of the time history of airloads both experimental and analytical is the very pronounced higher harmonic content of this load close to the 90° azimuth value. Figure 16 of Ref. 1 showed the very rapid change in downwash occurring near this point as the blade passes over the leading edge of the vortex spiral and the resulting lift is almost in the nature of an impulse. It was found that even nine harmonics were insufficient to describe this rapid change of lift and good agreement with test was only obtained in this regime when the computer solution as obtained prior to harmonic analysis was used. The significance of this result lies in the fact that a vibratory input from the rotor of frequency equal to the number of blades times the rotor speed will always occur regardless of the number of blades used. Since this type of vibratory input arising from an impulse is particularly unpleasant any rotor modification which reduces the impulsive nature of the lift would be desirable.

It may well be asked at this point what modifications are indicated which would improve the vibration characteristics of the rotor. Certainly twist appears to have a profound effect on the airload distribution with the non-twisted blade having a higher downwash at the tip than the twisted blade. This would tend to move the wake further away from the rotor as each subsequent blade passes over it. Another factor is the effect of blade modifications on the higher harmonic spanwise load distribution. The response of a rotor blade to a given input depends on the generalized force and, if the spanwise airload distribution is known, this response can be modified by suitably varying the spanwise mass distribution. The value of a better understanding of rotor aerodynamics in forward flight will become more evident once a working theory has been developed and extensively used.

Summary

It has been shown how experimental investigations over a period of years have led to the development of analytical tools for the determination of rotor blade dynamic loading and how these tests have helped in defining objectives for the analytical solutions. This work represents a small part of a larger effort over a period of years by many organizations. However this total effort is still small compared to the magnitude of the problem and it is hoped that the discussions in this paper and the results reported by other investigators will stimulate greater effort in this important area.

In particular, refinements in the theory are needed to permit rigorous treatment of special cases. The effects of blade twist on the harmonic load need clarification. Simplified engineering solutions must be developed, possibly the effect of a viscous vortex core introduced and the effects of rotor/rotor interference determined analytically. Stall flutter and other potential instabilities at high advance ratios due to the elastic deflection of the blade out of the plane of rotation must be further investigated preparatory to the proposed increases in helicopter speeds during the next decade.

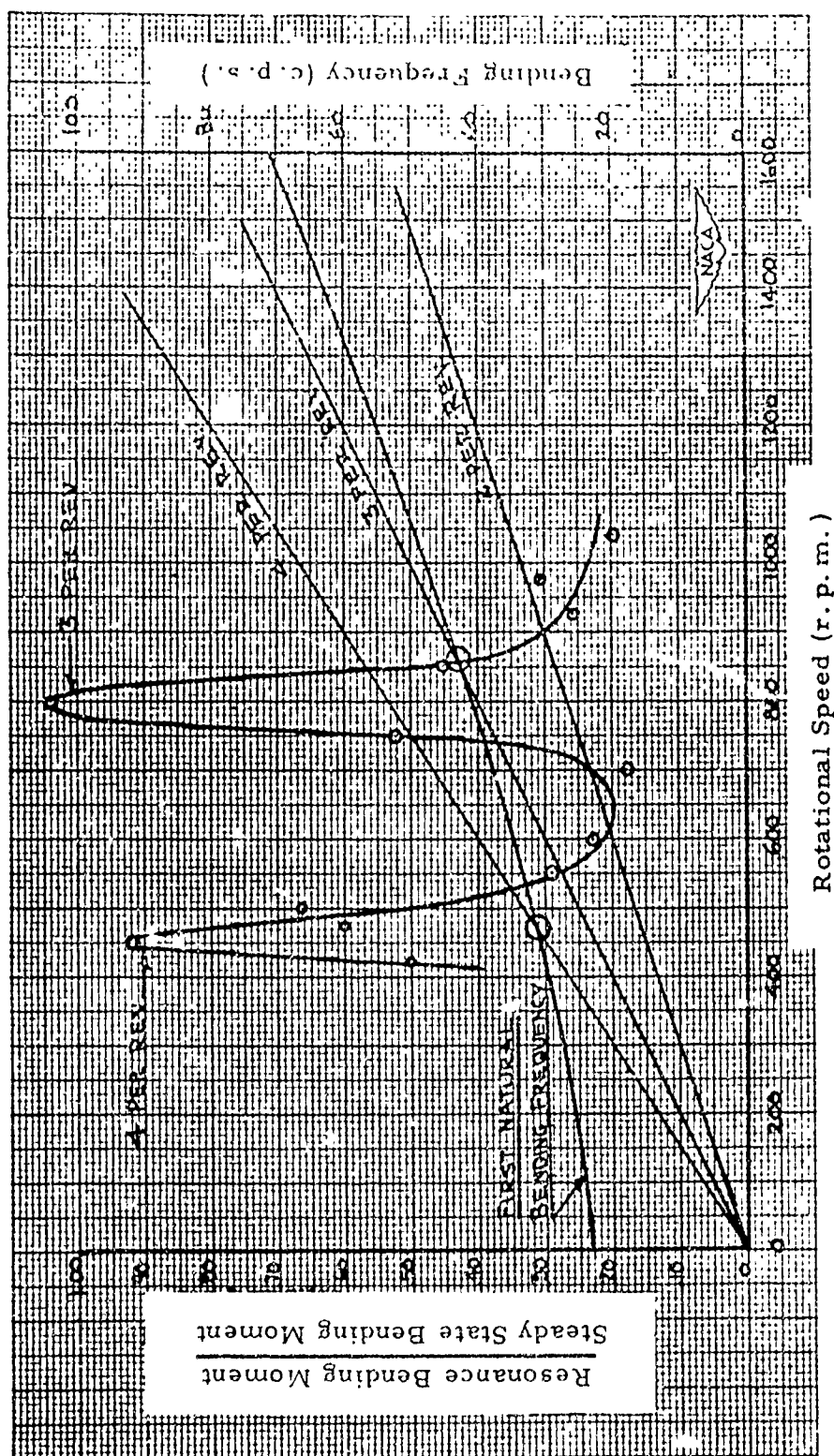
Such problems are among the most interesting and challenging ones yet presented to the aeroelastician. Progress to date indicates that rational solutions to these problems will eventually be found and in a time frame depending only on the level of effort expended.

References

1. Miller, R. H., Rotor Blade Harmonic Airloading, IAS Preprint No. 62-82, January 1962.
2. Meyer, J. R., Jr., An Investigation of Bending-Moment Distribution on a Model Helicopter Rotor Blade and a Comparison with Theory, NACA Technical Note 2626, February 1952.
3. Falabella, G., Jr. and Meyer, John R., Jr., Determination of Inflow Distributions from Experimental Aerodynamic Loading and Blade-Motion Data on a Model Helicopter Rotor in Hovering and Forward Flight, NACA Technical Note 3492, November 1955.
4. Miller, R. H., "Some Factors Affecting Helicopter Design and Future Operations", Proceedings of the Fourth Anglo-American Aeronautical Conference, London, 1953.
5. Duvivier, J. F., Study of Helicopter Rotor-Rotor Interference Effects on Hub Vibration, Technical Documentary Report No. ASD TR61-601, June 1952, Wright-Patterson Air Force Base, Flight Dynamics Laboratory.
6. Ham, N. D., An Experimental Investigation of Stall Flutter, Journal of the American Helicopter Society, Vol. 7, No. 1, January 1962.
7. Miller, R. H. and Ellis, C. W., Blade Vibration and Flutter, Journal of the AHS, July 1956, Vol. 1, No. 3.
8. Miller, R. H., On the Computation of Airloads Acting on Rotor Blades in Forward Flight, AHS Journal, Vol. 7, No. 2, April 1962.
9. Miller, R. H., Aerodynamics in the Next Decade, Canadian Aeronautics and Space Journal, Vol. 9, No. 1, January 1963.
10. Ham, N. D., An Experimental Investigation of the Effect of a Non-Rigid Wake on Rotor Blade Airloads in Transition Flight, Cal/TRECOM Symposium on Dynamic Load Problems associated with Helicopters and V/STOL Aircraft, June 26-28, 1963.
11. Zvara, J., Ham, N. D. and Moser, H. H., Investigation of Rotor Response to Vibratory Aerodynamic Inputs -- Experimental Results and Correlation with Theory, WADC Report 58-87, Part I.
12. Ham, N. D. and Zvara, J., Experimental and Theoretical Analysis of Helicopter Rotor Hub Vibratory Forces, WADC Technical Report 59-522, October 1959.

Acknowledgement

The work discussed in this paper has been supported at various times by the NACA, WADC, ONR, and most recently by TRECOM and BuWeaps. Assistance from the Carnegie Foundation and the MIT Computation Center, where the programs used were developed, is also gratefully acknowledged.



(a) $EI = 3000$ pound-inches².

Figure 1 ROTOR-BLADE RESONANCE STUDY. HOVERING, HINGED-AT-ROOT CONDITION; $\theta = 12^\circ$

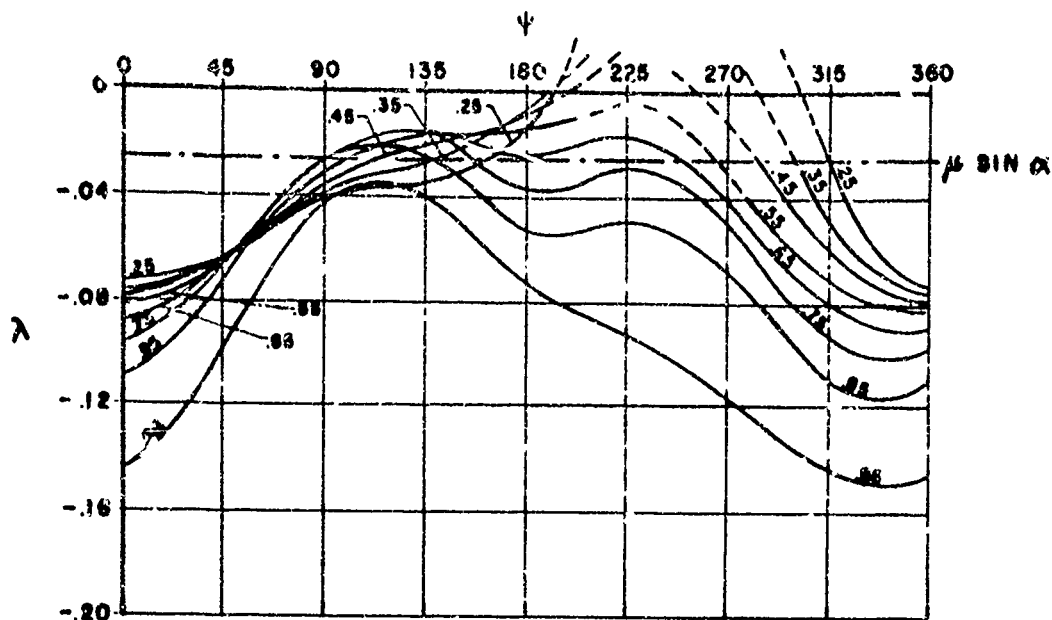


FIG. 2 INFLOW VARIATION OVER ROTOR DISC AS DETERMINED EXPERIMENTALLY. CONVENTIONAL ROTOR WITHOUT FLAPPING HINGE OFFSET; $\mu = 0.30$

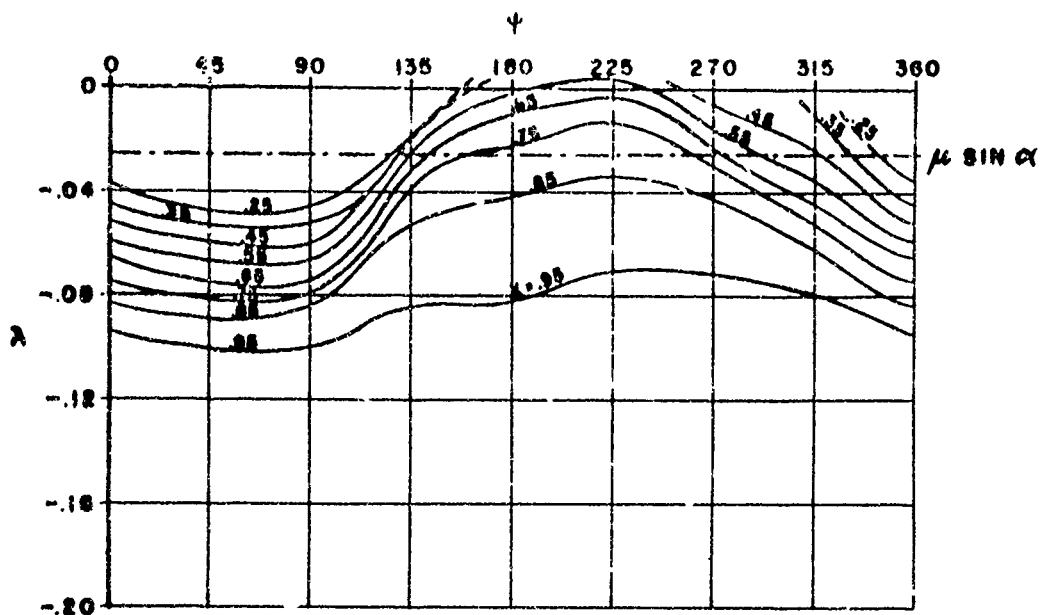


FIG. 3 INFLOW VARIATION OVER ROTOR DISC AS DETERMINED EXPERIMENTALLY. FLAPPING HINGE OFFSET = $0.13R$; $\gamma = 1.8$

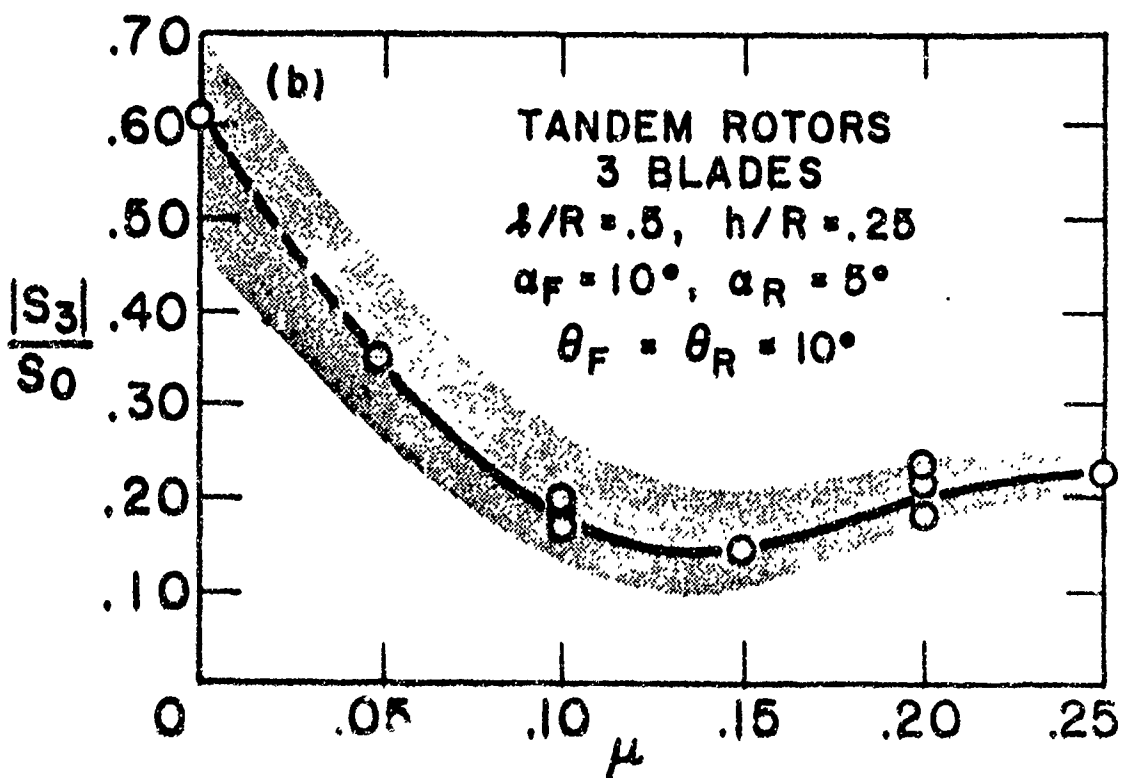
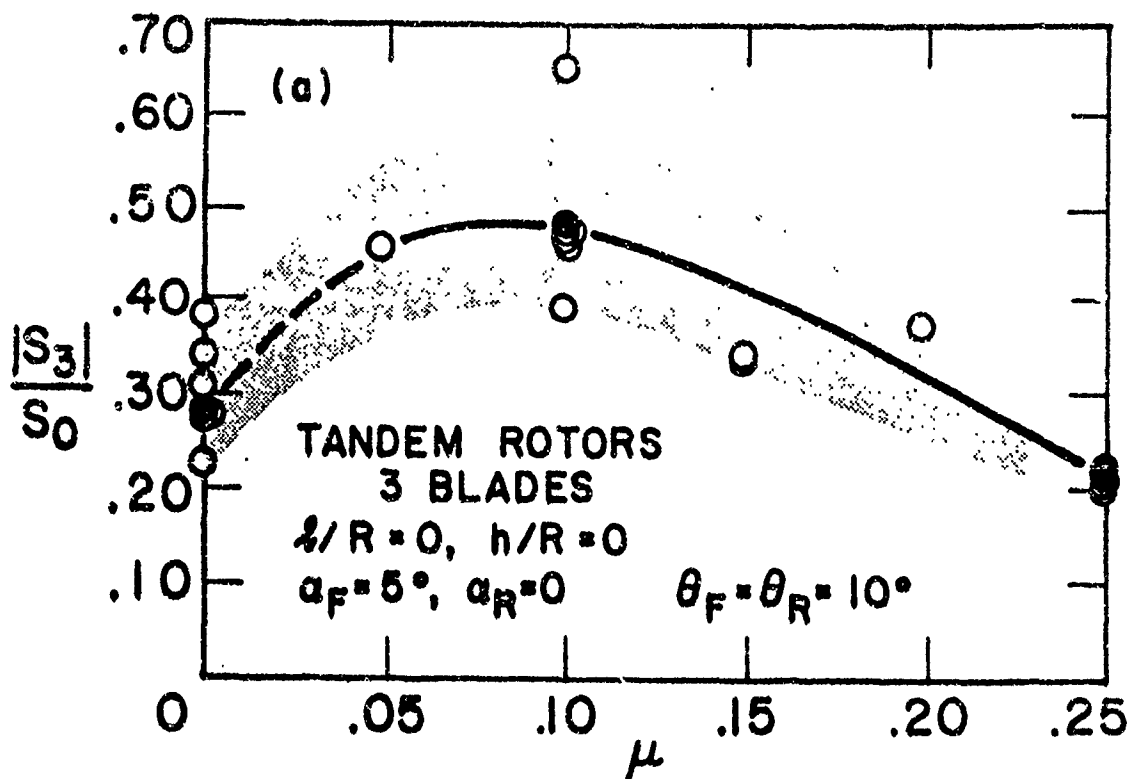


FIG.4 REAR ROTOR THIRD HARMONIC
VERTICAL SHEAR

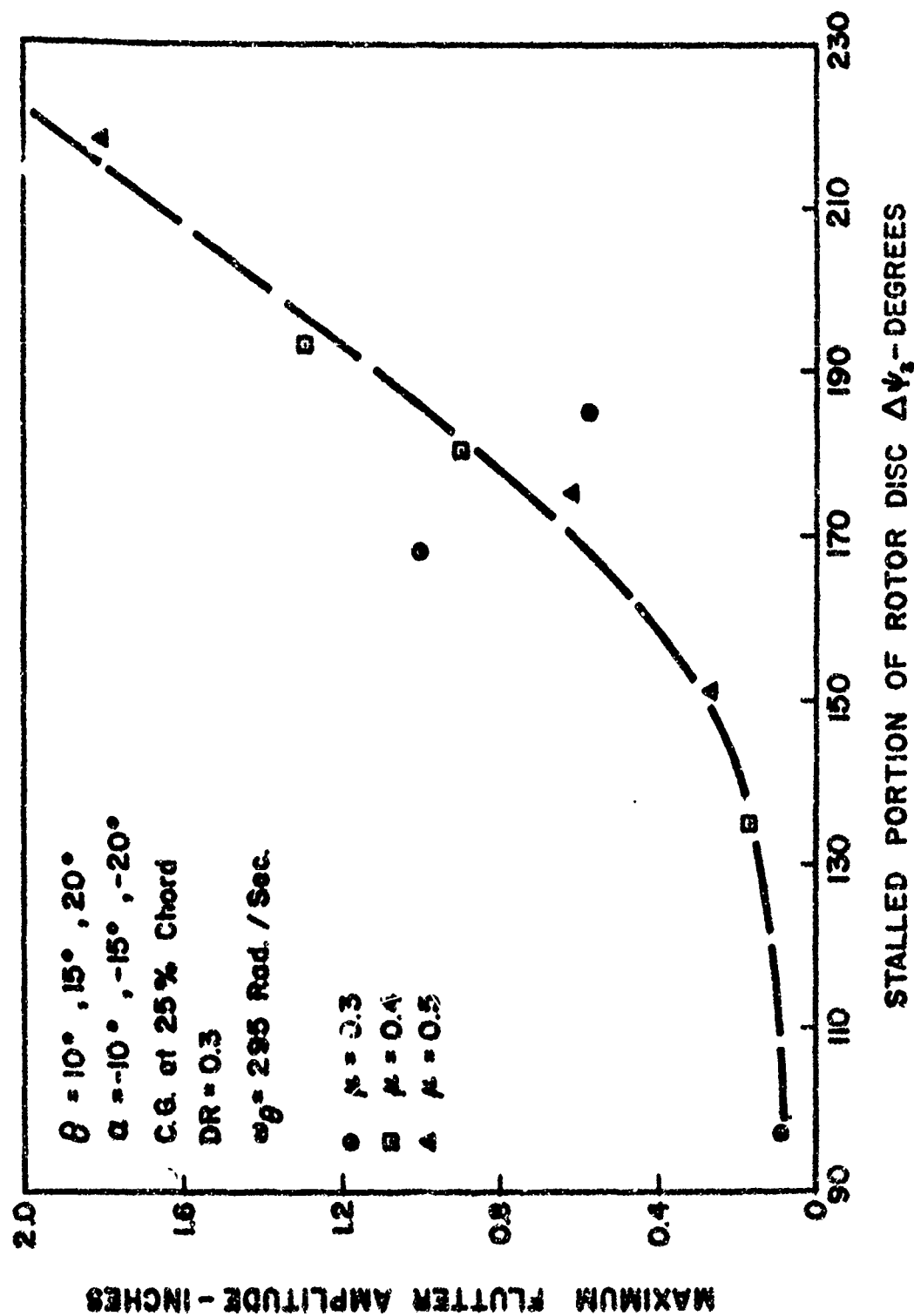


FIG. 5 EFFECT OF DEGREE OF STALL ON MAXIMUM FLUTTER AMPLITUDE

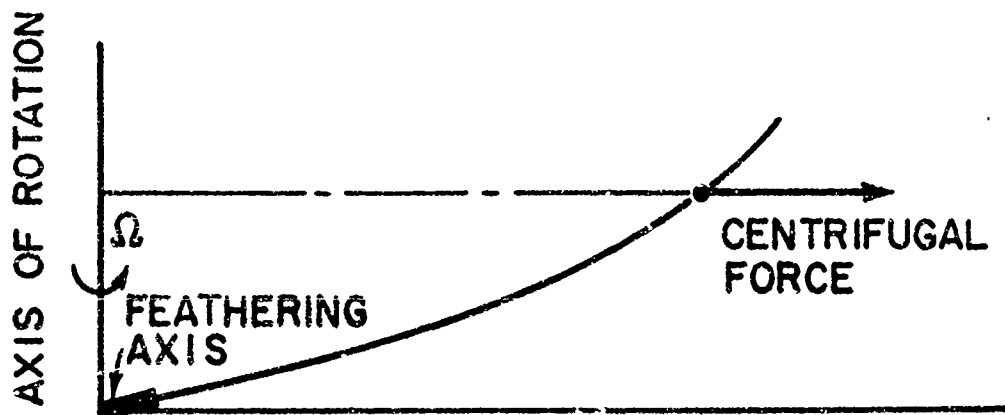


FIG. 6a BLADE DEFLECTED OUT OF PLANE OF ROTATION

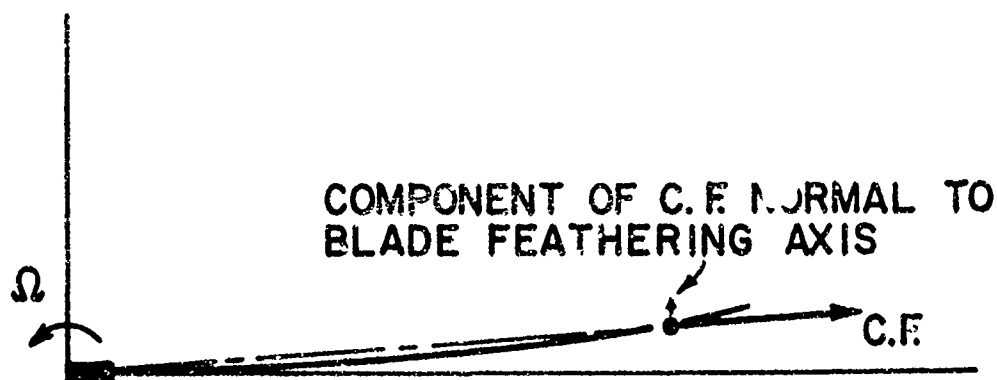


FIG. 6b PLAN VIEW OF BLADE DEFLECTED OUT OF PLANE OF ROTATION AND TWISTED ABOUT FEATHERING AXIS SHOWING COMPONENT OF CENTRIFUGAL FORCE NORMAL TO FEATHERING AXIS AND CAUSING FURTHER TWISTING

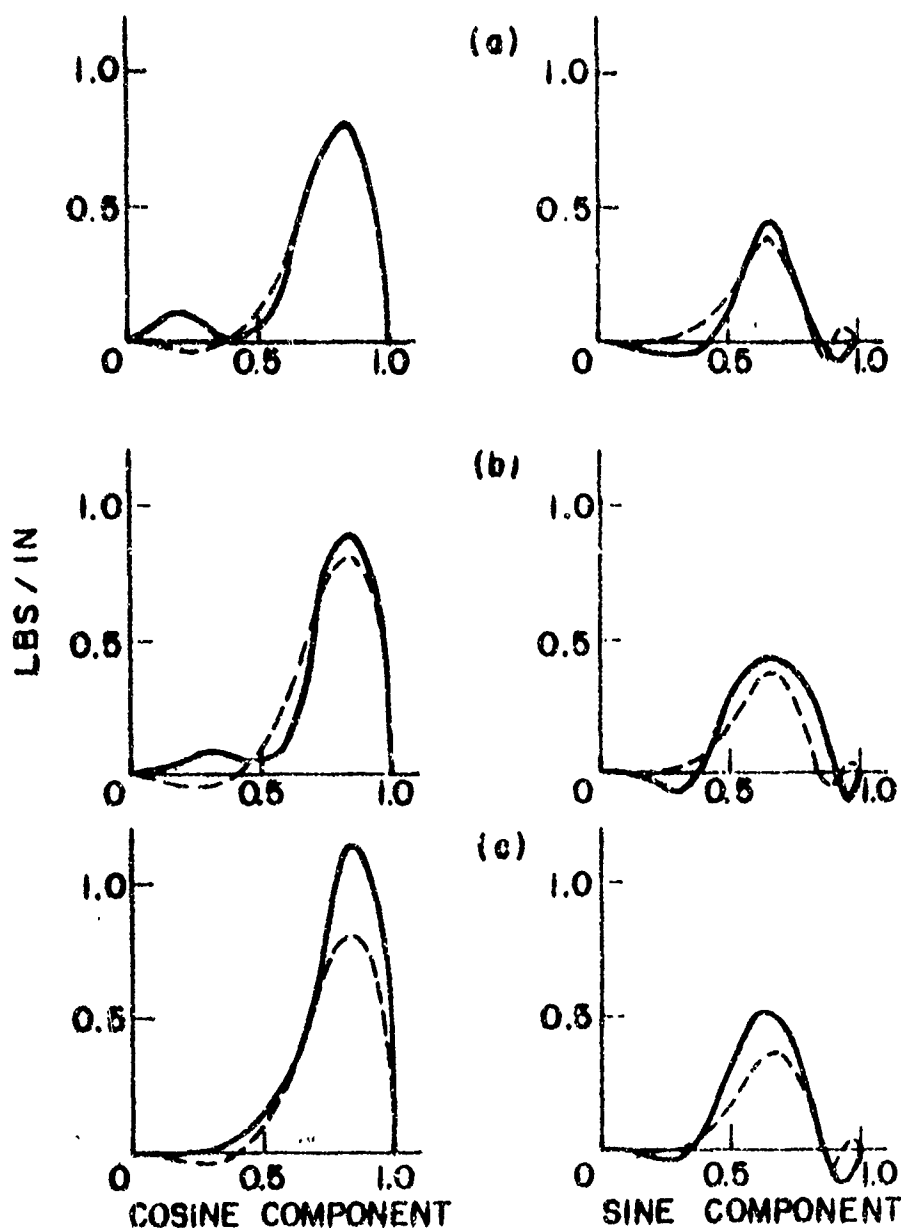


FIG. 7 CORRELATION BETWEEN THEORY AND TEST
 AS A FUNCTION OF THE NUMBER OF SPANWISE
 STATIONS USED IN SOLUTION. THIRD HARMONIC
 SPANWISE DISTRIBUTION 2 BLADES $\mu = .2$
 3 SPIRALS 15° INTERVALS
 ---- EXPERIMENTAL RESULTS FROM NACA
 RM 1.66107
 ——— THEORY

(a) 10 STATIONS-SOLUTION TIME 17 MINS
 (b) 6 STATIONS-SOLUTION TIME 10 MINS
 (c) 2 STATIONS-SOLUTION TIME 4 MINS

ON IBM
 7090

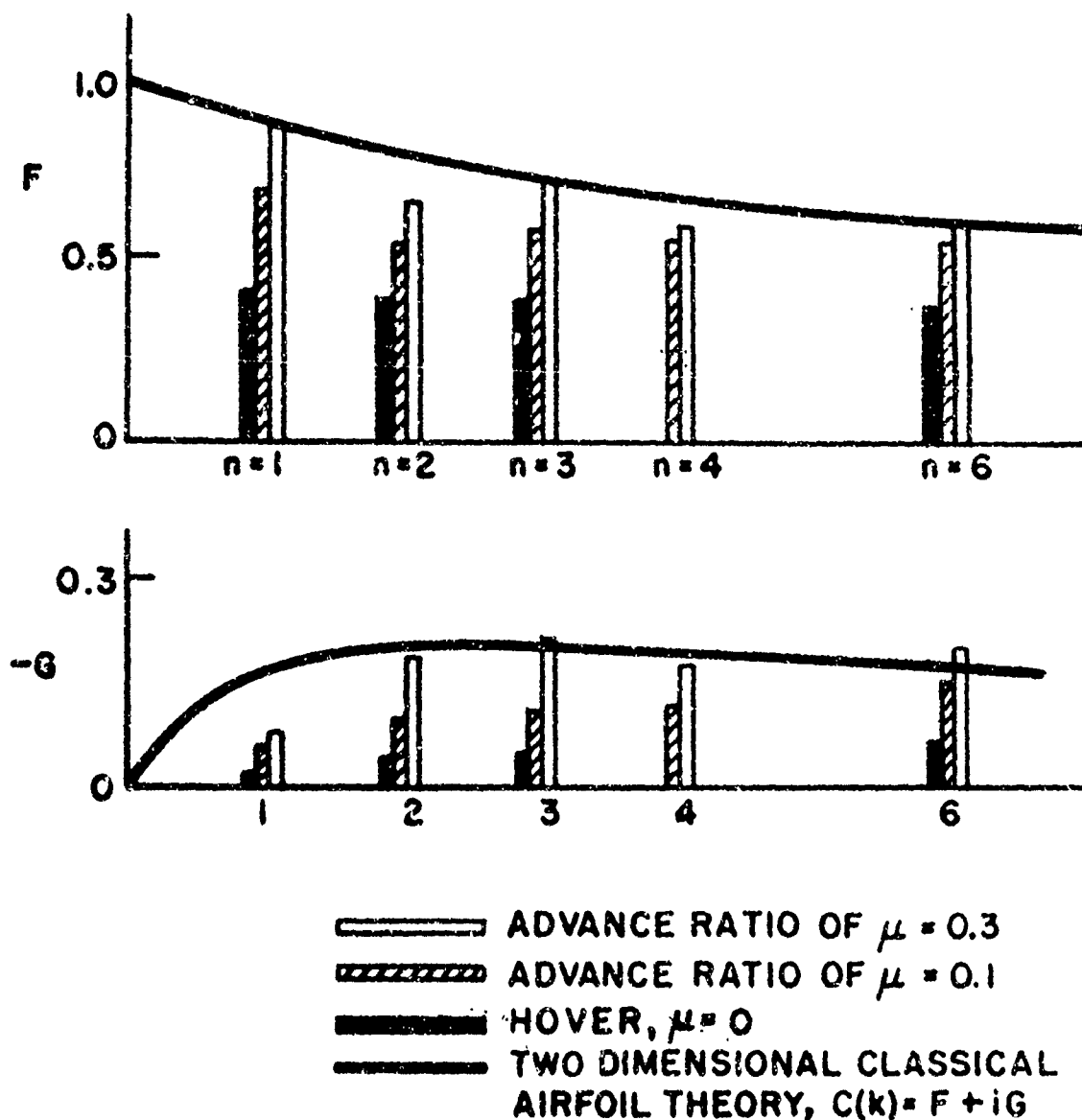


FIG. 8

THREE DIMENSIONAL LIFT DEFICIENCY F , AND
 PHASE SHIFT, G/F AS A FUNCTION OF HARMONIC
 n OF ROTATIONAL SPEED. THREE BLADES, ASPECT
 RATIO OF BLADES 10. INFLOW RATIO $\lambda = 0.05$

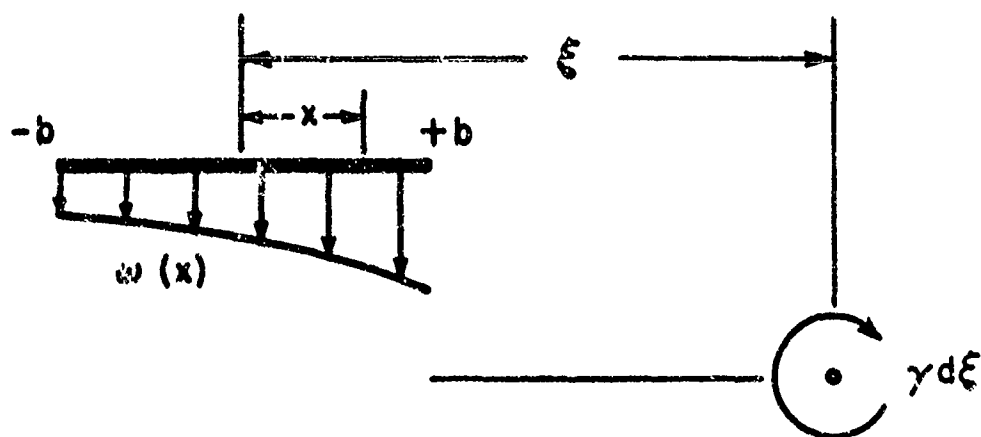


FIG. 9 TWO DIMENSIONAL INDUCED FLOW ON
AIRFOIL DUE TO ELEMENT OF VORTICITY
IN WAKE

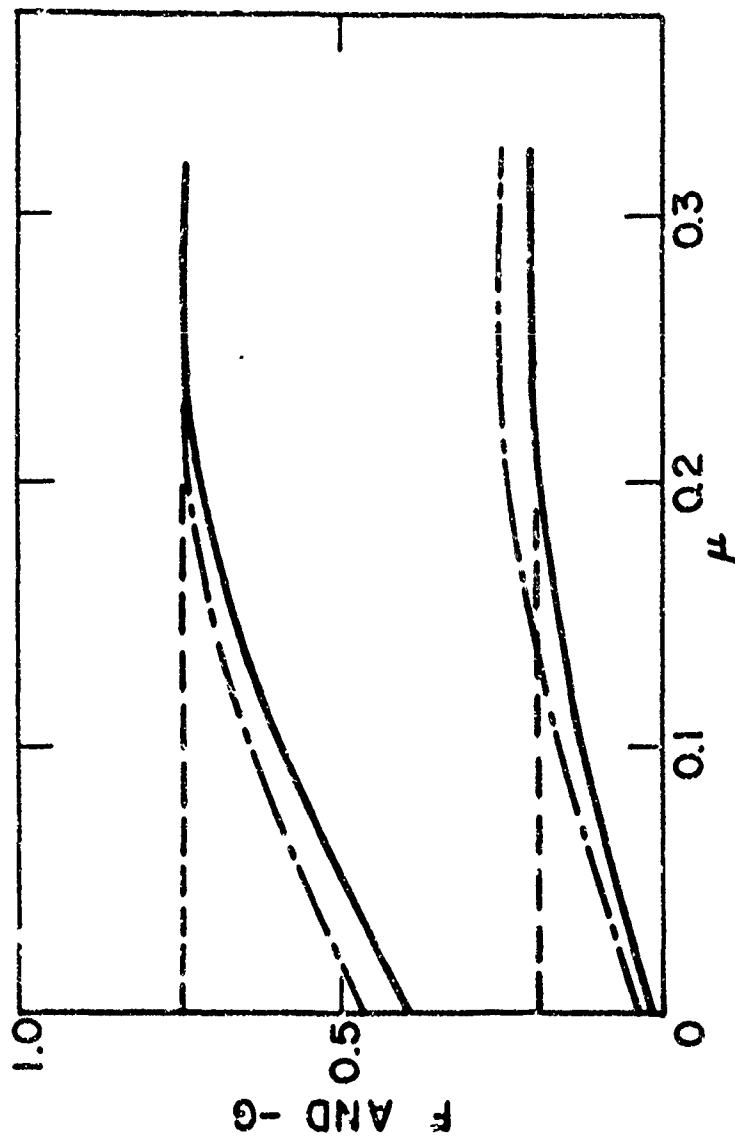


FIG. 10 EFFECT OF ADVANCE RATIO ON REDUCTION IN LIFT F AND PHASE SHIFT $\tan^{-1} \frac{G}{F}$ DUE TO THREE DIMENSIONAL UNSTEADY AERODYNAMIC EFFECTS. RESULTS FOR THREE BLADED ROTOR, ASPECT RATIO OF 10, AT 80% SPAN STATION, MEAN IN FLOW $\lambda_0 = .05$ THIRD HARMONIC. ($k = .1875$)

- COMPLETE SOLUTION
- - - SHED WAKE ONLY
- · - NEAR SHED WAKE ONLY

**AN EXPERIMENTAL INVESTIGATION
OF THE EFFECT OF A NON-RIGID WAKE
ON ROTOR BLADE AIRLOADS
IN TRANSITION FLIGHT**

Norman Ham

MIT

An Experimental Investigation of the Effect of a Non-Rigid Wake on Rotor Blade Airloads in Transition Flight*

Norman D. Ham
Department of Aeronautics and Astronautics
Massachusetts Institute of Technology

1. Introduction

Recent theoretical work at M. I. T. on rotor blade harmonic air loading, Refs. 1 and 2, has indicated the possibility of a portion of a blade tip vortex being drawn up into the leading edge of the rotor disc under certain flight conditions with consequent major effects on the blade local air loading. It is believed that these effects contribute significantly to the vibration level of the rotor during the associated flight conditions. However no experimental confirmation of the existence of the phenomenon has been available.

It is the purpose of the present paper to first discuss the theoretical results indicating the possible existence of this phenomenon, then indicate how these results can be utilized in establishing those test conditions that will permit observation of the phenomenon, and finally to present the experimental evidence to date of the occurrence of the phenomenon in terms of blade measured air loading.

2. Theoretical Background

Figures 1 and 2 illustrate the path of the blade tip vortices for two selected advance ratios corresponding to the so-called transition regime of a typical helicopter. Note the several intersections of the forward blade by the tip vortices of all three blades. In most flight conditions the rotor downwash is sufficiently large to carry these tip vortices well below the rotor disc. However under certain transition conditions a pronounced upwash occurs at the leading edge of the disc which may carry the intersecting tip vortices up through the disc and back down again farther downstream as suggested in Ref. 3. A typical example is shown in Figure 3.

At any point (x, y) on the trajectory of that segment of the tip vortex at $\psi = 180^\circ$,

$$\frac{dy}{dx} = \frac{V \sin i + v(x)}{V \cos i}$$

Then assuming that near the disc $v(x)$ does not vary significantly with y ,

*This research supported in part by the Headquarters, U. S. Army Transportation Research Command and by the Bureau of Weapons, U. S. Navy. Reproduction, translation, publication, use and disposal in whole or in part by or for the U. S. Government is permitted. Computer time was made available by the MIT Computation Center.

$$\begin{aligned}
 y &= \int_0^x \frac{dy}{dx} dx \\
 &= \frac{1}{V \cos i} \int_0^x [V \sin i + v(x)] dx \\
 &= \frac{1}{\mu} \int_0^x \lambda(x) dx
 \end{aligned}$$

and the condition for vortex intersection of the disc is given by the integral equation

$$\int_0^{x_i} \lambda(x) dx = 0$$

where x_i is the value of the x-coordinate of the trajectory when intersection occurs, measured along the disc fore-and-aft axis from the leading edge. The trajectory is readily obtained graphically as shown in Fig. 3. Therefore theoretical plots of rotor downwash at $\psi = 180^\circ$ can be used to predict possible intersections of the rotor disc by a tip vortex at $\psi = 180^\circ$. Note that disc incidence i is of prime significance in determining the intersection point.

Downwash distributions for advance ratios of .05 and .10, for a three bladed rotor with twisted blades are shown in Figures 4 and 5. These distributions were calculated using the theory of Refs. 1 and 2.

Two types of rotor wake geometry were considered in the inflow analysis. The first type, (1), that of the so-called "non-rigid" wake, is based on the assumption that the tip vortex moves with the local resultant velocity it experiences at the instant of shedding. The second type, (2), also that of the "non-rigid" wake is based on the assumption that the tip vortex moves with the mean local resultant velocity it experiences over an interval. Inflows resulting from both assumptions are shown in the figures. Note the effect of a non-rigid wake on the distributions. Under the given conditions the non-rigid wake geometry leads to a large predicted upwash near the leading edge of the rotor disc.

Application of the above inflow distributions to calculation of the trajectories of tip vortices at $\psi = 180^\circ$ indicates that vortex intersections should occur near the 80% radius of the blade, as shown in Figures 6 and 7.

3. Experimental Technique

The experimental equipment used in the present study was that described in Refs. 4 and 5, modified in the present case to permit remote control of the angle of shaft tilt while the rotor

was operating. A general view is shown in Fig. 8. Available blades had pressure transducers mounted at 49%, 83%, and 93% of blade radius. The experimental technique involved the recording of a timing signal and the pressure signal from the pressure transducer at the 83% station on an Offner pen recorder for a test condition having parameters corresponding to those for a theoretically predicted upwash at the leading edge of the disc, while varying shaft angle in the range indicated by the theory of Section 2 to lead to vortex intersections of the forward blade near the 83% pressure station. When the pressure trace showed peaks indicating the occurrence of the predicted intersection of the tip vortex with the blade near the 83% radius point (see Fig. 8), a complete record was taken on a Heiland oscillograph. This record showed the signals from all three pressure transducers as well as a timing signal, and a blade flapping signal. Typical Offner pressure records are shown in Figs. 9 and 10.

4. Results and Discussion

The experimental results of Figure 9 indicate the occurrence of a large local pressure fluctuation at the 83% blade pressure station for rotors having three twisted or untwisted blades in simulated transition flight at $\mu = .05$. The pressure peak occurs at an azimuth position of approximately 200° . Since the upwash conditions theoretically predicted for the given flight condition and twisted blades indicated a tip vortex intersection with the rotor disc in the neighborhood of $\psi = 180^\circ$, it is concluded that the observed pressure fluctuation is due to the tip vortex shed by the second preceding blade passing near the 83% pressure station of the instrumented blade. Note that the effect has approximately the same intensity for both twisted and untwisted blades, though the shaft angles differ for the two cases.

The results presented in Figure 10 for $\mu = .10$ are less clear, but are believed to show the effects of the presence of a tip vortex near the 83% pressure station. It is suspected that in this case the tip vortex from the immediately preceding blade passes close to the 83% pressure station over a much larger portion of the disc than in the $\mu = .05$ case. Hence the effect appears as a small dip at $\psi = 130^\circ$ approximately and as a general increase in pressure loading in the $\psi = 150^\circ$ to 220° region. Again the results are approximately the same for both the twisted and untwisted blade.

The following explanation is advanced for the distributed nature of the effect. Examination of the calculated downwash field for the rotor with twisted blades in the $\mu = .10$ flight condition revealed the presence of an upwash occurring at the $\psi = 127.5$ azimuth position, as shown in Figure 11. It is suspected that a region of upwash exists between this azimuth position and that at $\psi = 180^\circ$ and between blade stations at 80% and 95% radius. Unfortunately the chosen computation points for the theoretical downwash field calculation did not include this region. However, existing information permits the construction of Figure 12. The two plotted points represent possible disc intersections by the tip vortex shed from the immediately preceding blade. It is assumed, but not shown, that a locus of intersections exists between these two points. The solid curve represents the instantaneous position of the tip vortex shed by the preceding blade when the instrumented blade is at the corresponding azimuth position. Finally the path of the 83% blade pressure station is shown by the dash-dotted curve. It is seen that the tip vortex is close to, and ahead of, the instrumented pressure station in the region $\psi = 130^\circ$ to 150° , and close to, and behind, the pressure station in the region $\psi = 150$ to 180° . The observed harmonic pressure fluctuations in the same azimuth regions and at the given pressure station are of a form consistent with the above hypothesis, i. e., first a down loading due to the downwash of an arriving vortex and then an up loading due to the upwash of a departing vortex. The

above discussion is speculative only and awaits quantitative comparison between theoretical and experimental harmonic airloading for the given flight conditions. It is hoped to obtain such comparisons in the near future.

5. Conclusions

The existence of rotor blade impulsive airloading due to the impingement of tip vortices from preceding blades is now believed to be confirmed. The practical significance of the effect includes the increase of rotor operating vibration levels, particularly if the impulse is applied to the anti-node of a blade bending mode. Flight conditions where the effect is experienced by helicopters include transition flight, and hovering in ambient winds, for example while performing plane guard or sonar dipping duties.

Possible means of eliminating such impulsive loading include rapid acceleration through transition, since large disc incidences and rotor inflows prevent the occurrence of the upwash field at the leading edge of the disc. Another approach is distribution of the tip vortex strength by appropriate tip geometry or by tip blowing, as suggested in Ref. 3.

Finally, the tip vortex interference effects demonstrated by the model rotor of the present paper are likely to influence the airloads currently being measured on full scale rotors in corresponding flight conditions and should be considered when evaluating such airload measurements.

References

1. Miller, R. H., Rotor Blade Harmonic Air Loading, I. A. S. Paper No. 62-62, 1962.
2. Miller, R. H., On the Computation of Airloads Acting on Rotor Blades in Forward Flight, A. H. S. Journal, April, 1962.
3. Brandt, D. E., Investigation of Rotor Blade Dynamics During Equilibrium Transition Flight, S. M. Thesis, M. I. T., 1962.
4. Ham, N. D. and Zvara, J., Experimental and Theoretical Analysis of Helicopter Rotor Hub Vibratory Forces, WADC - TR-59-522, 1959.
5. Duvivier, J., Study of Helicopter Rotor-Rotor Interference Effects on Hub Vibrations, ASD - TR-61-601, 1962.

Model Rotor Characteristics

Blade Radius	$R = 4 \text{ ft.}$
Number of Blades	3
Blade Chord	5 in.
Airfoil Section	NACA 0012
Solidity	0.1

Symbols

Standard NASA nomenclature is used throughout except for:

$\theta_{.67R}$ = blade pitch angle at $.67R$ radius

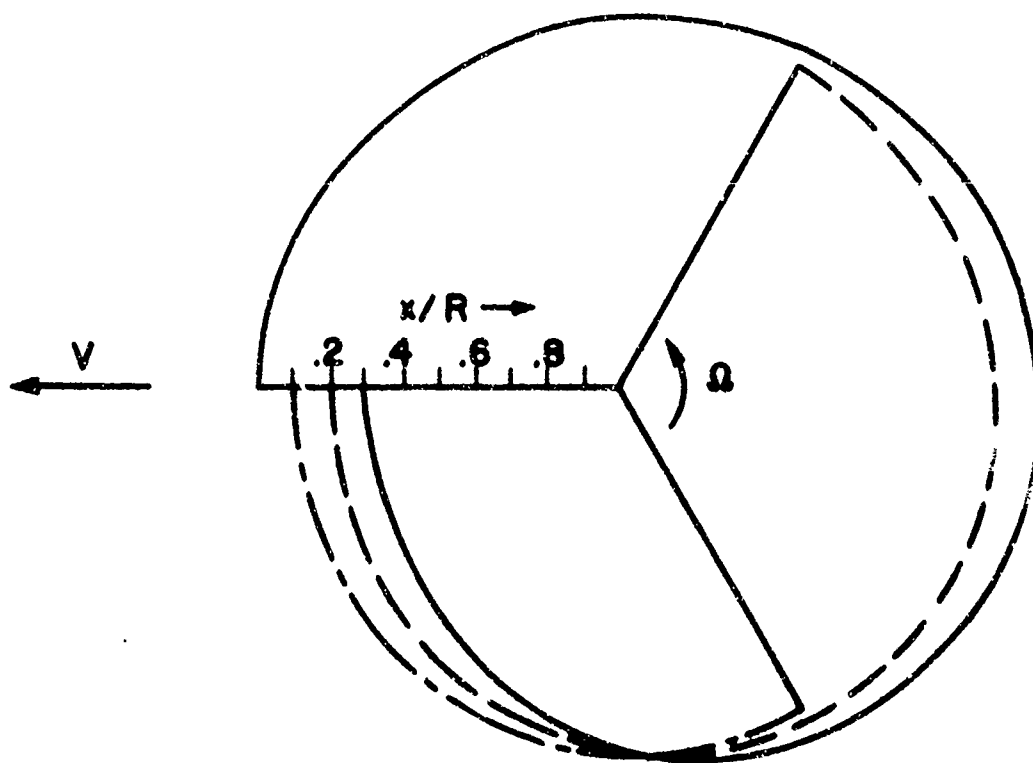


FIG. 1 TIP VORTEX PATTERN FOR THREE
BLADES: $\mu = .05$

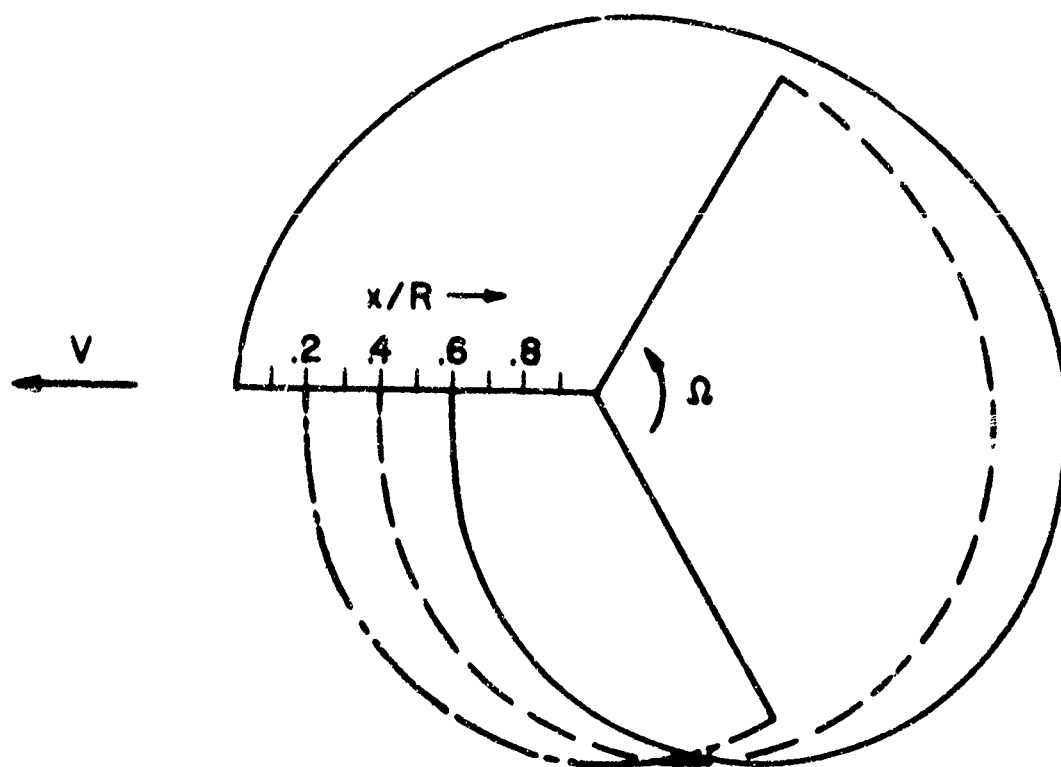
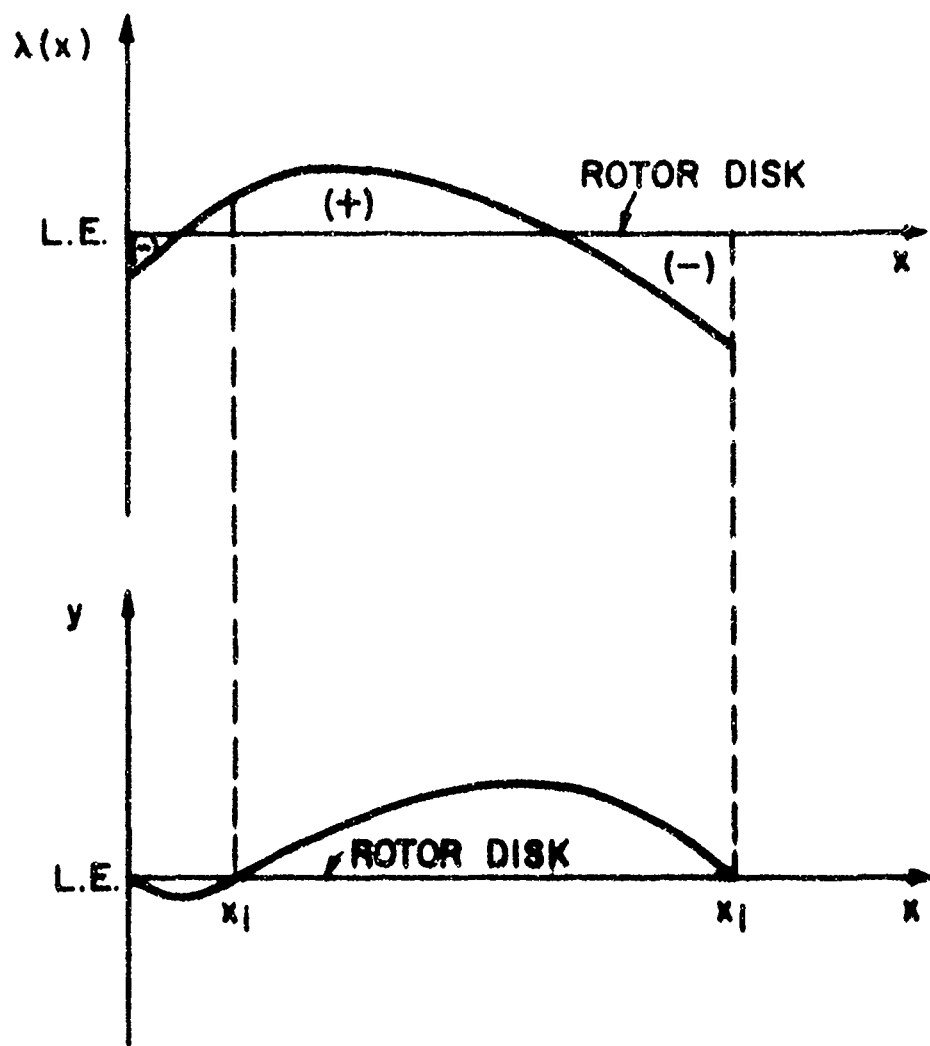


FIG. 2 TIP VORTEX PATTERN FOR THREE
BLADES: $\mu = .10$



$$\frac{dy}{dx} = \frac{V \sin i + v(x)}{V \cos i} = \frac{\lambda(x)}{\mu}$$

$$\therefore y = \int_0^x \frac{dy}{dx} dx = \frac{1}{\mu} \int_0^x \lambda(x) dx$$

$$\therefore \int_c^{x_1} \lambda(x) dx = 0$$

FIG. 3 CALCULATION OF TIP VORTEX TRAJECTORY

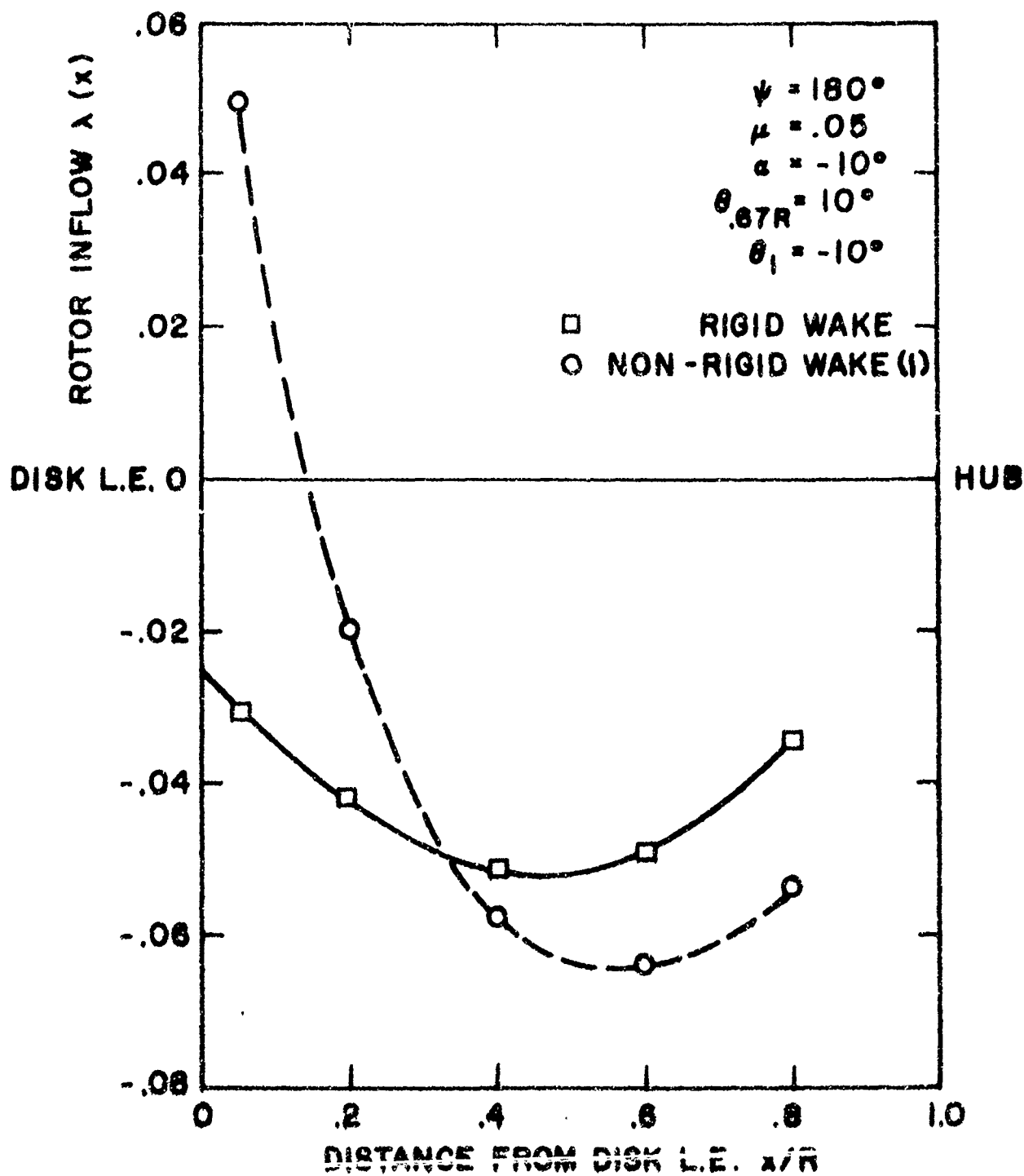


FIG. 4 INFLOW DISTRIBUTIONS FOR $\mu = .05$

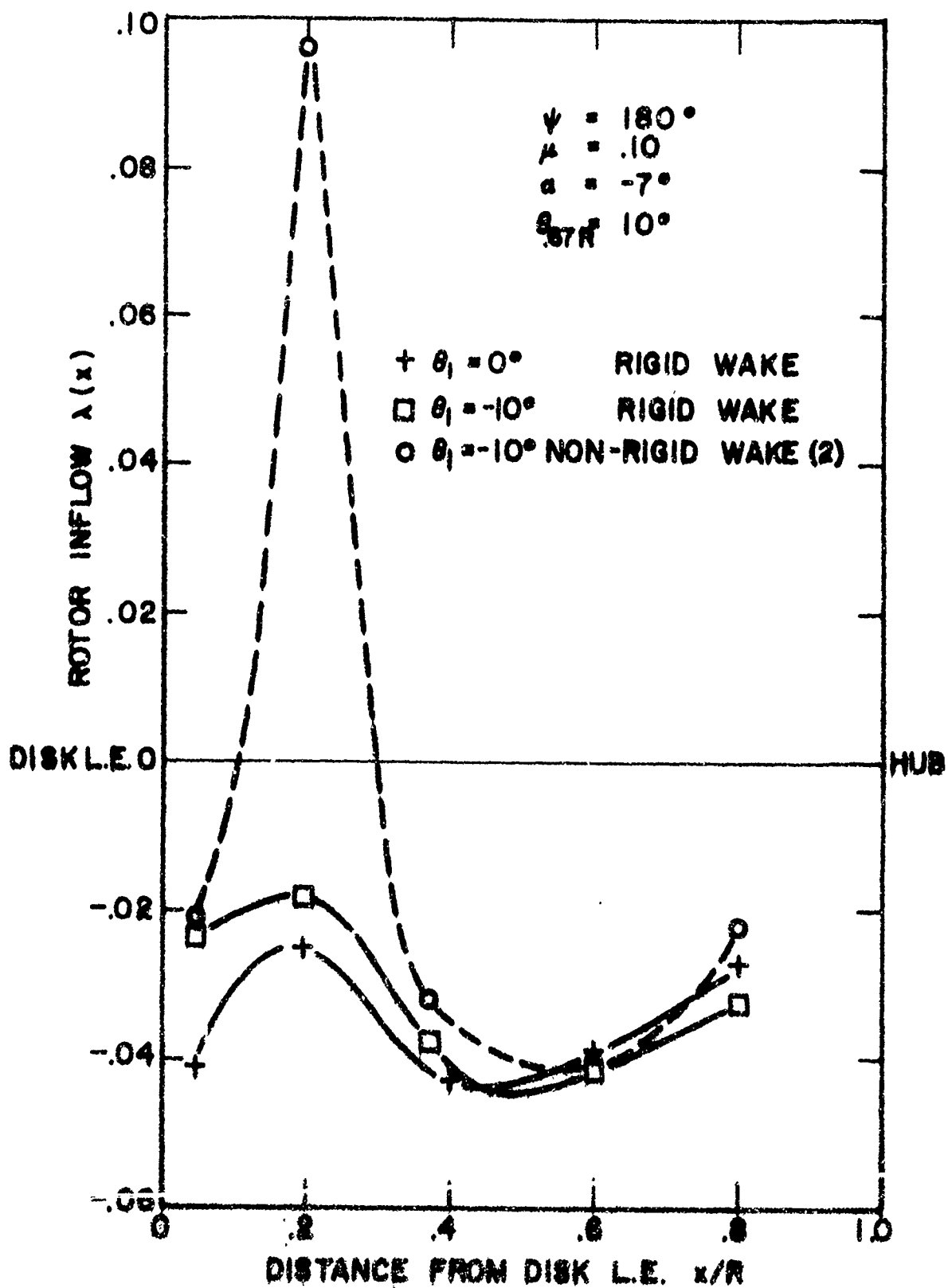


FIG. 5 INFLOW DISTRIBUTIONS FOR $\mu = .10$

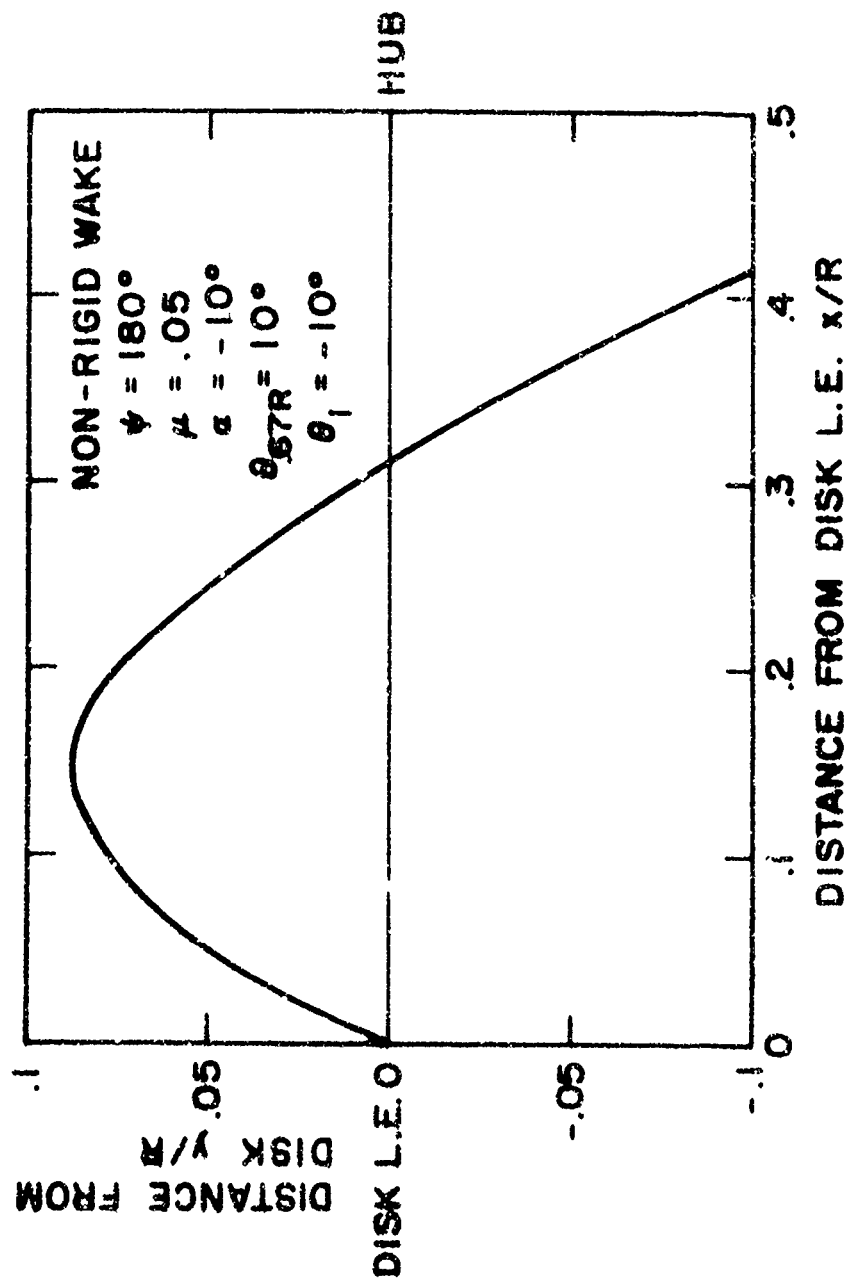


FIG. 6 TIP VORTEX TRAJECTORY $\mu = .05$

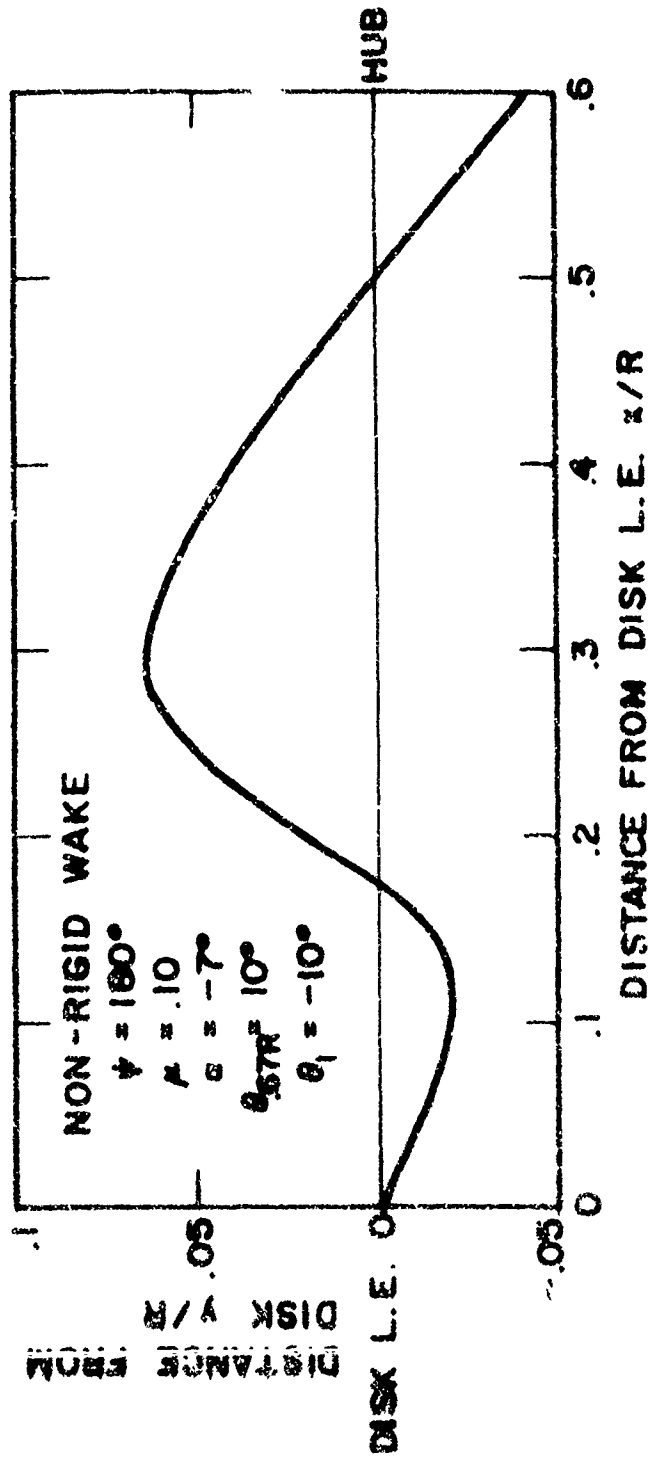


FIG. 7 TIP VORTEX TRAJECTORY $\mu = .10$

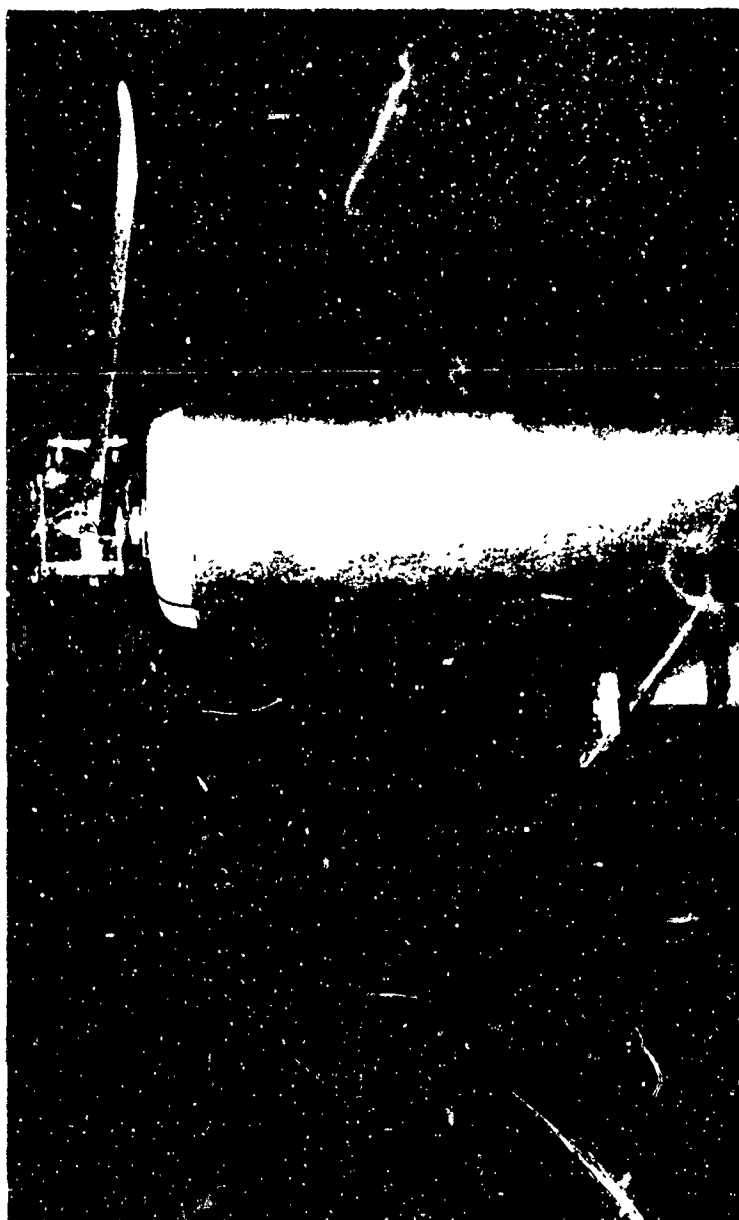
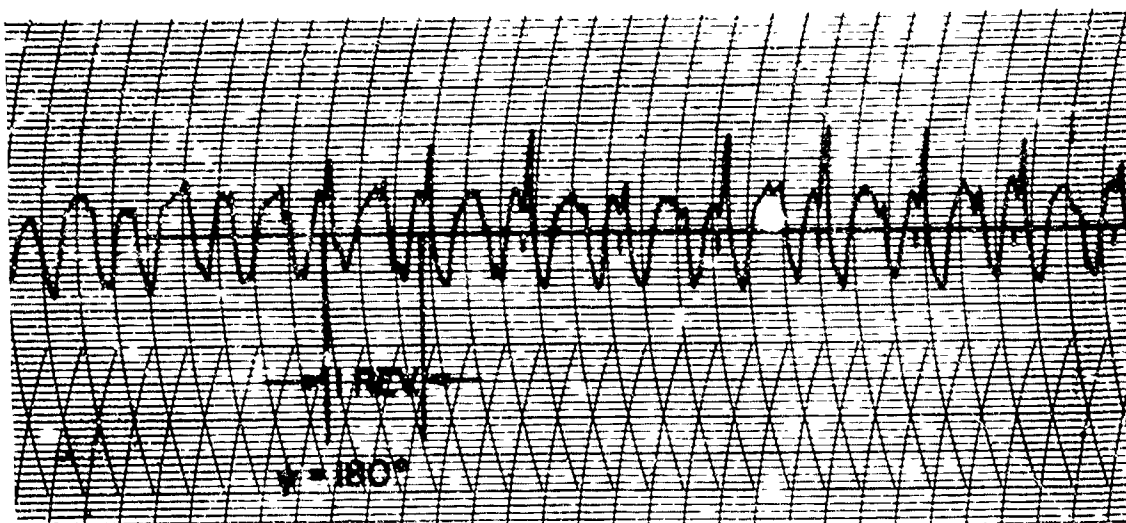
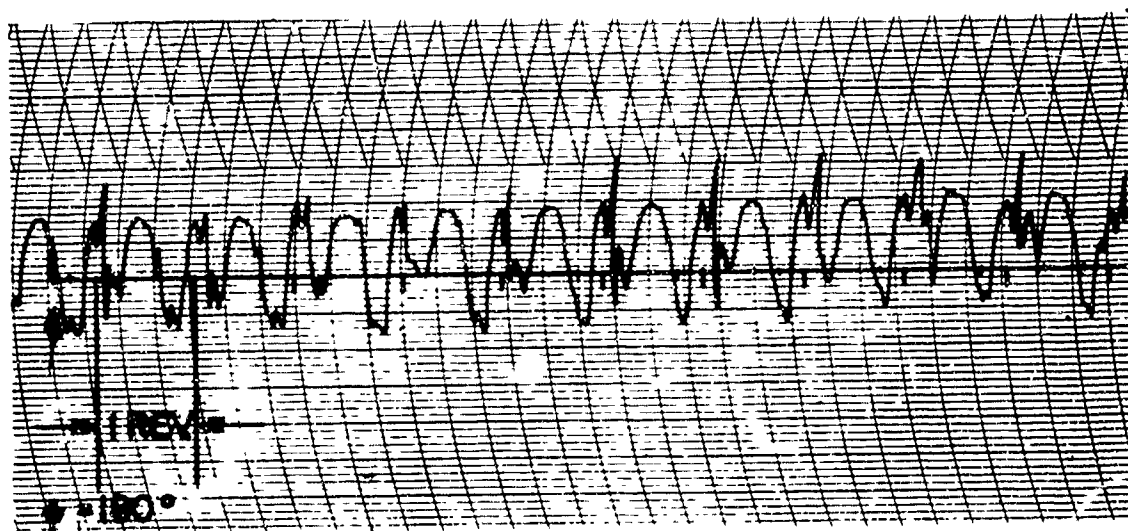


FIG. 8 ROTOR TEST STAND

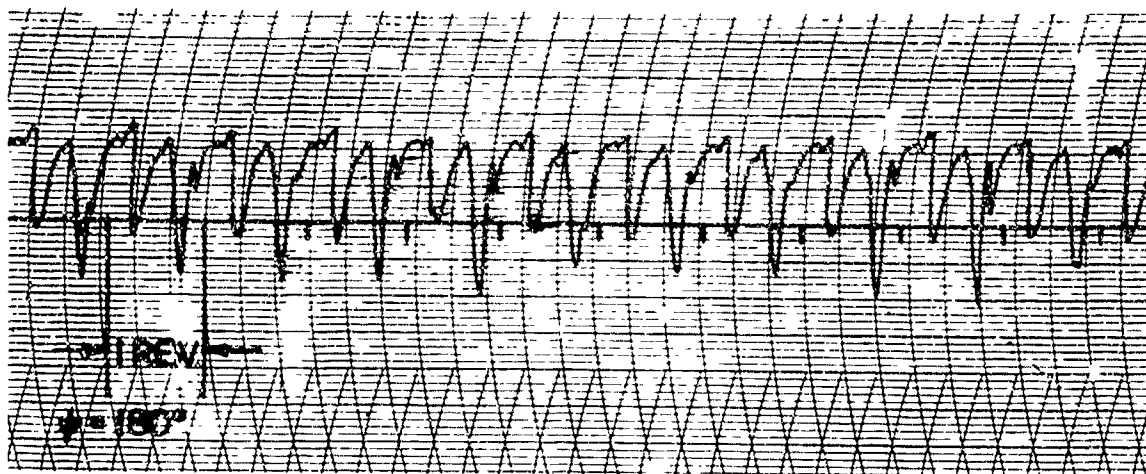


(a) TWISTED BLADE $\theta_1 = -10^\circ$ $\alpha = -10^\circ$



(b) UNTWISTED BLADE $\theta_1 = 0^\circ$ $\alpha = -7^\circ$

FIG. 9 EXPERIMENTAL AIRLOAD VARIATION WITH
AZIMUTH AT THE 83% BLADE STATION
 $\mu = .05$ $\theta_{67R} = 10^\circ$



(a) TWISTED BLADE $\theta_1 = -10^\circ$



(b) UNTWISTED BLADE $\theta_1 = 0^\circ$

FIG. 10 EXPERIMENTAL AIRLOAD VARIATION WITH
AZIMUTH AT THE 83% BLADE STATION

$$\mu = .10 \quad \theta_{.67R} = 10^\circ \quad \alpha = -7^\circ$$

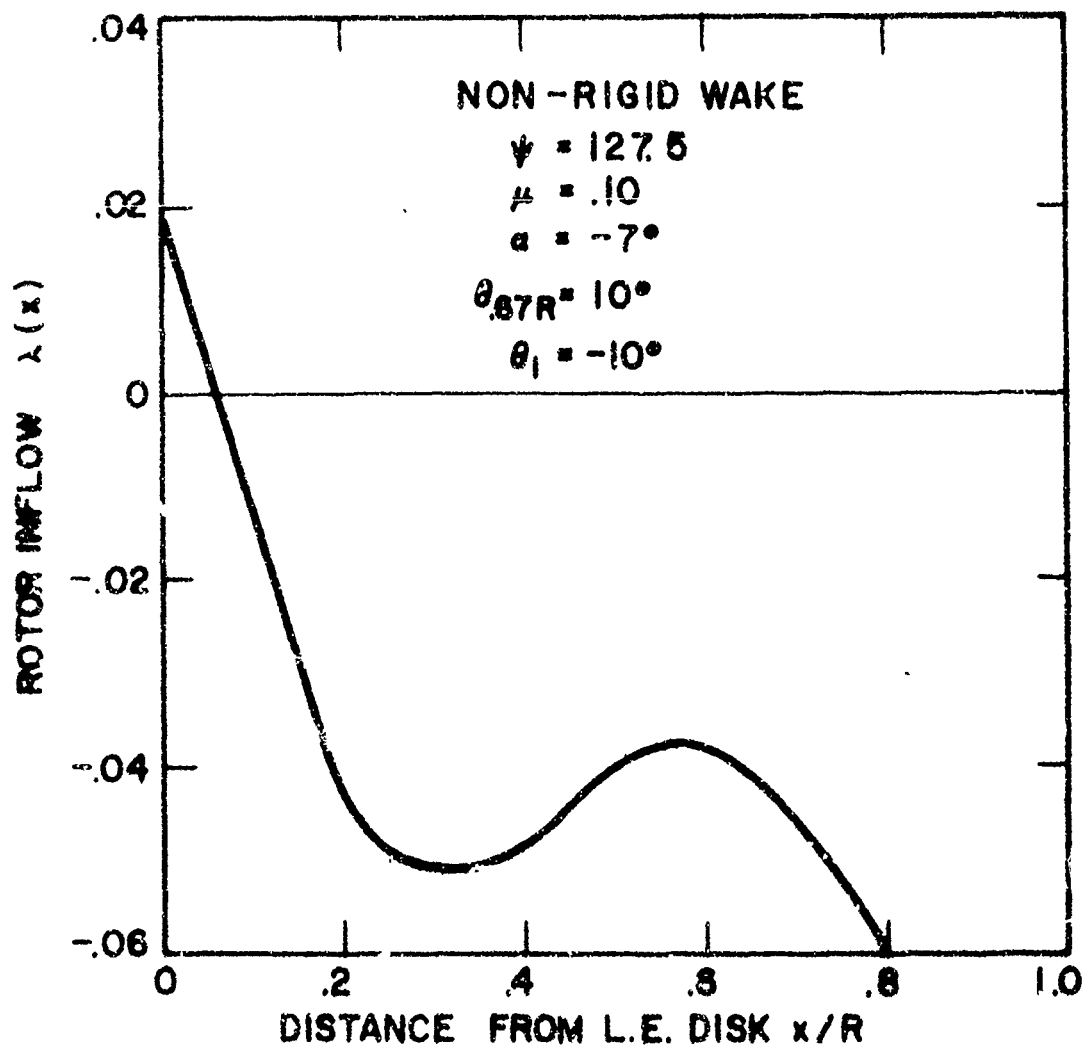


FIG. II INFLOW DISTRIBUTION AT $\psi = 127.5^\circ$

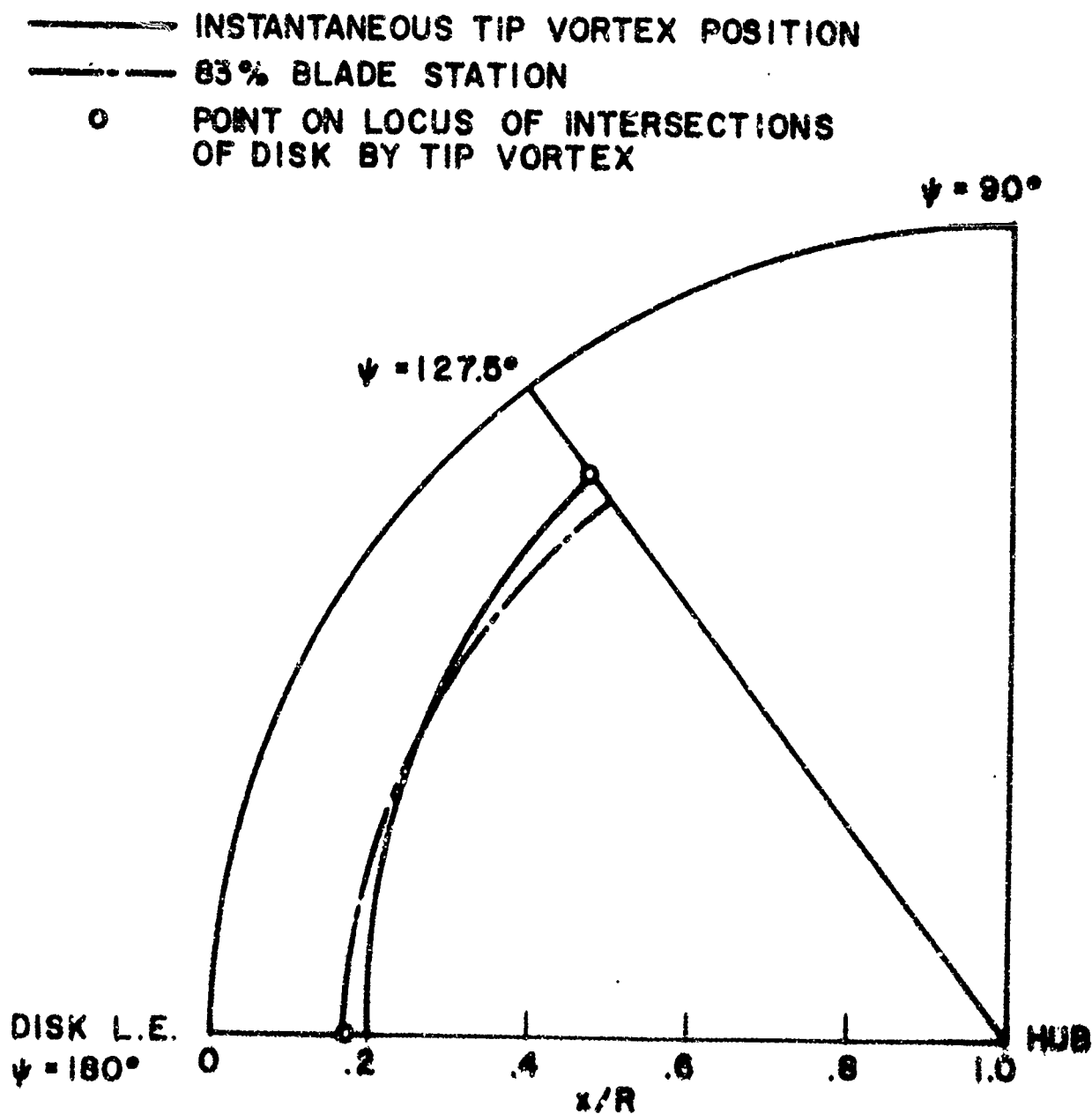


FIG. 12 INSTANTANEOUS TIP VORTEX POSITION FOR NON-RIGID
 WAKE $\mu = .10$ $\alpha = -7^\circ$ $\theta_{57\%} = 10^\circ$ $\theta_1 = -10^\circ$